Etude de l'optimisation et de la cinétique de formation de conducteurs supraconducteurs Nb3Sn obtenus par la méthode de l'étain interne

Chaowu Zhang

Année 2007

Thèse

Pour obtention du grade de
Docteur de L'Université Joseph Fourier de Grenoble 1, France
Spécialité : Physique

Et de
Shaanxi University of Science and Technology, Xi'an, China
Speciality : Material Sciences

SUPERCONDUCTIVITY OPTIMIZATION AND PHASE FORMATION KINETICS STUDY OF INTERNAL-Sn Nb_3Sn SUPERCONDUCTING WIRES

Zhang Chaowu

Under the supervision of

Professor Zhou Lian at Shaanxi University of Science and Technology, Xi'an, China

And

Dr. André Sulpice at University Joseph Fourier, Grenoble, France

Dr. Jean-Louis Soubeyroux at University Joseph Fourier, Grenoble, France

Date: July 19th, 2007

JURY

Rapporteur:	M. Roland TAILLARD, Professeur, Université de Lille, Fr
Rapporteur:	M. Bingbo WEI, Professeur, Northwestern Polytechnical University
	M. Lian ZHOU, Professeur, Northwestern Polytechnical University
	M. Gia Ky HOAN, Dr., ALSTOM MSA, Belfort
	M. André SULPICE, Dr. CNRS Grenoble
	M. Jean-Louis SOUBEYROUX, Dr. CNRS Grenoble

ACKNOWLEGEMENTS

I have spent three years in China and in CNRS/Grenoble for which I am really grateful and enjoyable. There are many people I would like to thank during my PhD research period. Foremost, I should give my sincere thanks to my advisors, Prof. Zhou Lian, Dr. Andre Sulpice and Dr. Jean-Louis Soubeyroux, for providing me with many opportunities and for their understanding, encouragement and advices. I especially need to acknowledge Prof. Tang Xiande, who is the leader of Nb_3Sn group in NIN, for his arrangement and guidance in wire manufacturing. I have truly appreciated CRETA, CRTBT, LCMI, CRISTALLOGRAPHIE / CNRS, ILL/Grenoble and SMRC, Analysis Center/NIN for their help and assistance in my experiments and measurements. Truly thanks to SMRC, WST/NIN and MSA/Alstom for funding me this research and for providing high quanlity multifilament superconductor wires examined in this thesis.

Many thanks to Prof. Zhang Pingxiang, Prof. Lu Yafeng and Prof. Feng Yong in NIN, and Dr. Christophe Verwaerde and Dr. Gia Ky Hoang in Alstom for their support and for providing convenience to me during the three years study. I also thank Yang Ming, Li Chunguang and the whole Nb_3Sn research group in NIN for helping me to fabricate mono-element wires. I am deeply indebted to Brosse-Maron Pierre and Balay Joel for their painstaking work in my sample preparation. I am also grateful to Pairis Sébastien, Miss Sophie Rivoirard in CNRS and Chen Shaokai in NIN for their excellent microscopy skills. I should also sincerely thank Dr. Eric Mossang in LCMI for help and convenience in critical current measurements. Specifically, I am very thankful to Dr. Robert Tournier for his helpful advice and much concern when I was in Grenoble. Deep thanks to Dr. Li Chengshan and Dr. Yan Guo for the assistance and discussion in CNRS. I also thank Dr. Hu Rui, Dr. Yu Zeming, Dr. Li Jinyong and the colleagues in NIN and in CRETA for many helpful discussions. Thanks to Ms. Sun Mingxia for assisting me going abroad. I also would like to express my sincere thanks to my doctoral committee for their excellent instruction for my PhD dissertation refereeing and oral examination.

Lastly, I am forever grateful to my wife and my family for their love, support, understanding and encouragement during my extensive PhD career.

SUPERCONDUCTIVITY OPTIMIZATION AND PHASE FORMATION KINETICS STUDY OF INTERNAL-Sn Nb_3Sn SUPERCONDUCTING WIRES

Zhang Chaowu

Under the supervision of

Professor Zhou Lian at Shaanxi University of Science and Technology, Xi'an, China

And

Dr. Andre Sulpice at University Joseph Fourier, Grenoble, France

Dr. Jean-Louis Soubeyroux at University Joseph Fourier, Grenoble, France

Nb_3Sn wire is one of the most applicable cryogenic superconducting materials and the best choice for high-field magnets exceeding 10T because of its superior high-field performances. In order to systematically investigate the superconductivity optimization and the phase formation kinetics of internal-Sn Nb_3Sn superconducting wires, two ITER-type MF wires from MSA/Alstom and WST/NIN were selected, and four sets of ME wires were designed and fabricated in this study. The two MF wires had high-Cu composite designs with smaller number of sub-elements and non-reaction diffusion barrier, and manufactured with RRP internal-Sn technology. The four sets of ME wires had different Sn ratios and one of them had Zr alloyed Nb.

Four modern measurement techniques were utilized in the experiments. The transport critical current measurement was used to determine the non-Cu J_C, the engineering J_E and the flux pinning force F_P (reflected by $J_C \times B$) as a function of the applied field. The in-situ and off-situ neutron diffraction examinations were arranged for two purposes: dynamically observing the variation of various CuSn phases with the HT progress, and more importantly searching for the variation rule of Nb_3Sn phase development. Two SQUID magnetization methods were applied, cycling the temperature at a fixed field and cycling the field at a

constant temperature. The former was to determine $T_C(B)$, irreversibility temperature T*(B) and T_C transition curves. The later was to obtain hysteretic loops, and then flux pinning force F_P and irreversibility field H*. Microstructure observation and microchemistry analysis were employed in exploring A15 grain configuration, crystalline morphology and Sn concentration distribution, and especially the A15 layer thickness variation with the HT process.

The measurement results of the two ITER-type MF wires can be summarized as the followings. (1) The transport critical current measurements have shown that the non-Cu J_C, and the calculated flux pinning force F_P were promoted to the highest and then reduced with the increase of HT temperature and time. On the contrary, the irreversibility field H* which reflects the high-field performance had no such a decrease. (2) The in-situ neutron diffraction measurement has demonstrated that the Cu-Sn alloying process started to develop η phase at ~210°C, and then transformed into ε phase and δ phase. The γ phase became increasing at the expense of δ phase decrease. The Nb_3Sn phase formation started at ~600°C and kept increasing with the prolongation of reaction time. (3) The SQUID magnetization measurements have exhibited that the $T_C(B)$ and T*(B) values, the T_C and M-T transition curves were all increased with the increase of HT time, and maintained nearly no change after complete reaction. These T_C-related superconducting properties had no obvious variation at different HT temperatures for complete reaction, indicating that the A15 phase composition of Nb_3Sn wire is temperature-independent. The ΔM-B curves and the (ΔM × B)-B curves, reflecting the flux pinning situation of A15 phase, were also increased with the increment of HT temperature and time, approached the highest position before lowering down, whereas the irreversibility field H* maintained the high values. (4) The microstructure observation and microchemistry analysis have indicated that the NIN wire had faster reaction rate and lower reaction temperature, and more equiaxed crystals in its crystalline morphology at the same HT conditions. Comparatively, AST wire needs a higher reaction temperature to increase the reaction rate and to improve the A15 phase configuration distribution.

It can be generalized from the two MF wire results that the NIN wire is suitable to be heat-treated at lower temperature because the Ti alloyed in Sn effectively accelerates the Sn diffusion and reaction, reduces the reaction temperature and promotes the phase formation. However, the AST wire is preferable a higher HT temperature to achieve its best

superconducting performances. The HT optimization of the two wires has been acquired as: NIN wire, 650°C~675°C for 128hrs and AST wire, 675°C~700°C for 128hrs.

The measurement results of the four sets of ME wires can be concluded as the follows. (1) The SQUID magnetization measurement has shown that the package J_C and package F_P of ME wires reflected by the ΔM-B and the (ΔM × B)-B curves became increasing with the increase of HT temperature and time and the Sn ratio, and with the addition of third-element Zr, while the A15 layer F_P and the A15 layer J_C changed very little at lower field, but expanded to high field. (2) The off-situ neutron diffraction measurement has demonstrated that the phase formation rate of ME wire is affected by the three factors: first, the increase of Sn ratio enlarges the Sn source supply and then increases the phase formation rate; second, the elevation of HT temperature activates the Sn diffusion and reaction and then accelerates the phase formation rate, especially from 675°C to 700°C; third, the combination of Ti alloyed in Sn and Zr alloyed in Nb is very effective in promoting the A15 phase formation. (3) The microstructure and microchemistry analysis have exhibited that the A15 phase amount was obviously increased with the increase of reaction temperature and time and the Sn ratio, and with the addition of Zr. However, these phase-improving factors only alter the A15 phase quantity, but do not vary the A15 phase quality or equilibrium composition.

Specifically in this study, the A15 layer thicknesses of various ME samples were measured and were carried out linear and non-linear fits by means of two model equations. The results have demonstrated that the phase formation kinetics of Nb_3Sn solid-state reaction is in accordance with an n power relation and the n value is increased with the increase of HT temperature and the Sn ratio in the wire composite.

CONTENTS

1. INTRODUCTION

1.1 Research Motivation

With the development of science and technology, the demand for magnets of ever-increasing magnetic field is growing strongly. For instance, Very Large Hadron Collider (VLHC), next-generation accelerators, as well as International Thermonuclear Experimental Reactor (ITER) require fields exceeding 10 tesla(T) [1]. Over the last ten years much attention has been paid to high-field superconductors in order to meet the magnet requirements [2]. Multifilament Nb_3Sn wire is one of the most practical cryogenic superconducting materials, which has high critical temperature T_C (18.3k), high upper critical field H_{C2} (>30T) and high critical current density J_C, and thus the best superconductor for high-field magnets [3].

ITER is a joint international research and development (R&D) project that aims to demonstrate the scientific and technical feasibilities of fusion power. As we all know, our present energy system relies heavily on fossil fuels, which supply 80% of the world energy demand. The energy demand of the world is growing due to the increase in world population, the increasing energy (especially electricity) use per capita and the fast deficiency of the irreproducible energy source. In order to curb the well known problems related to the present energy system, such as climate change and security of supply, it is urgently necessary to move to a sustainable energy mix. Fusion process utilizes two nuclei, deuterium and tritium, to fuse together, forming helium, a neutron and a large amount of energy, which is the energy source of the sun and the stars. Only one gram of the substances can develop 93,000 KW of huge energy. The basic fusion fuels, deuterium and lithium (from which tritium can be produced), are almost limitless on the Earth. Furthermore, fusion power energy also has some other features, such as safe, no polluting and radioactive waste, and no emission of greenhouse gases. For the purpose of this very important power energy, a few hundreds of scientists and engineers from the world have been organized for the R&D, design and construction of the ITER project since 1985. The ITER will be constructed in Europe, at Cadarache in the south

of France, with a power output of 1500 MW.

The magnetic confinement facility of the ITER fusion system needs large high-field magnets made with Nb_3Sn superconducting wire. For many years the R&D of this kind of Nb_3Sn superconductors have attracted much consideration around the globe. Since the target of ITER project is the production of AC power, a special requirement is made for the Nb_3Sn wire: modest critical current density J_C but rather lower hysteretic loss, due to the rapid pulsed feature of a tokamak. Comparatively, high Cu composite design, Restack Rod Process (RRP) internal-Sn method and smaller number of sub-elements with non-reaction diffusion barrier are usually the best choice for the wire manufacturing [4]. In our research work such designed and processed wires were made by the Magnets and Superconductors of Alstom Company (MSA/ALSTOM) in France and the Northwest Institute for Non-ferrous Metal Research (NIN)/ West Superconducting Technology (WST) in China.

Until now, a number of investigations have been made on ITER type Nb_3Sn wires [5,6], but with rarely systematic research. MSA/ALSTOM, NIN /WST and CNRS had an international cooperation program to carry out systematically the research on internal-Sn Nb_3Sn wires. Our main purpose is to optimize the superconducting properties and performances from two key factors, wire composite design and heat treatment (HT) process. At the same time, microstructure, microchemistry and especially, the dynamics of phase formations are investigated in order to find some general rules for internal-Sn Nb_3Sn superconductors.

1.2 Superconductivity Principle and Flux Pinning of Type-Ⅱ Superconductors

Kamerlingh Onnes discovered the “zero-resistivity” or “ideal conductivity” of superconductors in 1911, from which three important critical superconducting properties, critical temperature (T_C), critical field (H_C) and critical current (I_C) had been revealed since then. In 1933, Meissner and Ochsenfield made another major discovery that materials in superconducting state exclude magnetic field from their interior. This was known as “perfect diamagnetism”. Superconductors would be in Meissner state under critical temperature and

critical field, but in normal state above these conditions.

A superconductor is able to exclude magnetic field by developing surface shielding currents which flow in a direction of creating an opposite magnetic field that cancels the applied field and remains no net flux density (B=0) within the superconductor. However, these shielding currents are not confined entirely to the surface, otherwise the resulting current density would be infinite. The surface layer depth is defined as the penetration depth (λ) which has a relation with temperature as the following equation:

$$\lambda(T)= \frac{\lambda_0}{\sqrt{1-(T/T_c)^4}} \qquad (1\text{-}1)$$

The λ_0 in (1-1) is the penetration depth at 0K, which is a material characteristic. The shielding currents increase to maintain perfect diamagnetism as the applied field is increased, up to a limit known as the depairing current density (J_d), at which the energy imparted to the supercurrent equals the energy gap of the superconducting state.

The ideal conductivity of a superconductor resultes from electron-phonon interactions which pair electrons into Cooper pairs. It is this paring property that allows for the resistanceless flow of electricity. The dimension between the paired electrons is called the coherence length (ξ), which is also a function of temperature.

The ratio of λ to ξ is named Ginzburg-Landau (GL) parameter κ, that is

$$\kappa=\lambda/\xi \qquad (1\text{-}2)$$

Within a superconductor, the free energy per unit volume in the normal region is always higher than that in the superconducting region. There exists a surface energy (Es) between the normal and superconducting regions, approximately defined as

$$Es=(1/2)\mu_0 H_C^2(\xi-\lambda) \qquad (1\text{-}3)$$

where ξ is effectively the thickness of the boundary dividing the two regions. From (1-3), surface energy Es can be positive or negative, depending upon the relative magnitudes of λ and ξ. When GL parameter $\kappa<1/\sqrt{2}$, the Es is positive, making it thermodynamically unfavorable to allow normal regions within superconducting regions up to H_C, due to the resulting increase of free energy. This is called type-Ⅰ superconductivity and is associated with nearly all elemental superconductors. On the other hand, if $\kappa>1/\sqrt{2}$, the

normal-superconductor interfacial energy is negative and it is thermodynamically advantageous to have as much interfacial area as possible. In this situation, it becomes favorable for normal regions to develop within superconducting regions when the increase in free energy of the bulk normal region is over-weighted by the decrease in free energy of the surface region. The superconductor of existing normal regions within superconducting regions is said to be in the mixed state which occurs at an applied field above H_{c1} but below H_{c2}.This is called type-Ⅱ superconductivity and is associated with superconducting oxides and alloys, such as Nb-Ti and Nb_3Sn. Schematic diagrams of H-T phase space for type-Ⅰ and type-Ⅱ superconductors are shown in Fig.1-1.

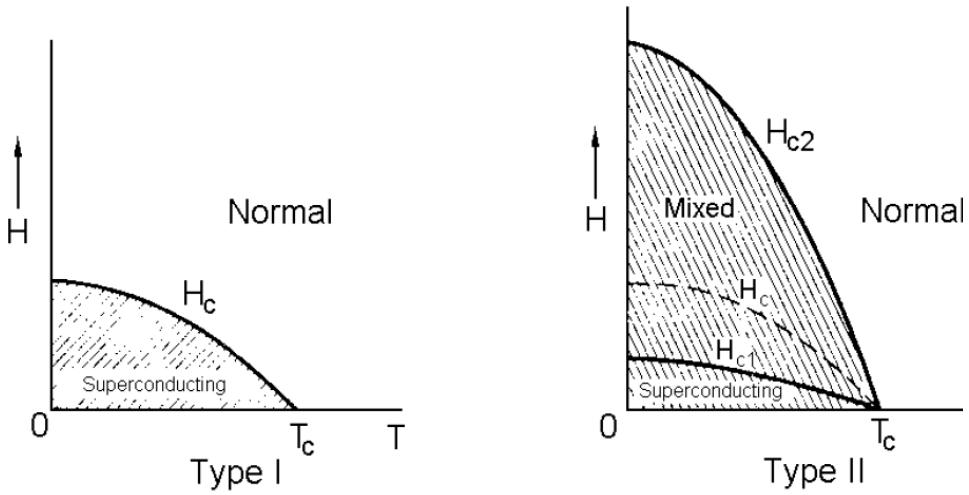

Fig.1-1 Schematic H-T phase diagrams of type-Ⅰ and type-Ⅱ superconductors. The mixed-state superconductivity occurs between H_{c1} and H_{c2} in the type-Ⅱ superconductor. H_c is also shown in the type-Ⅱ superconductor as the dashed line [7].

The critical current density J_C in type-Ⅰ superconductor is limited because supercurrent only flows along the surface. H_C and T_C are also low with maximum values of ~0.1mT and ~5K respectively. Such low values preclude type-Ⅰ superconductor from technological utilization. However, the supercurrent flows throughout the bulk in type-Ⅱ superconductor, which allows much higher J_C values. In addition, type-Ⅱ superconductors generally have higher critical fields and critical temperatures than type-Ⅰ superconductors. Therefore, it is indeed that nearly all technologically useful superconductors are of type-Ⅱ.

As mentioned above, when the applied field exceeds H_{C1}, a type-Ⅱ superconductor is then in a mixed-state and normal cores are allowed to be in the superconducting phase.

Fig.1-2 shows the mixed-state superconductivity.

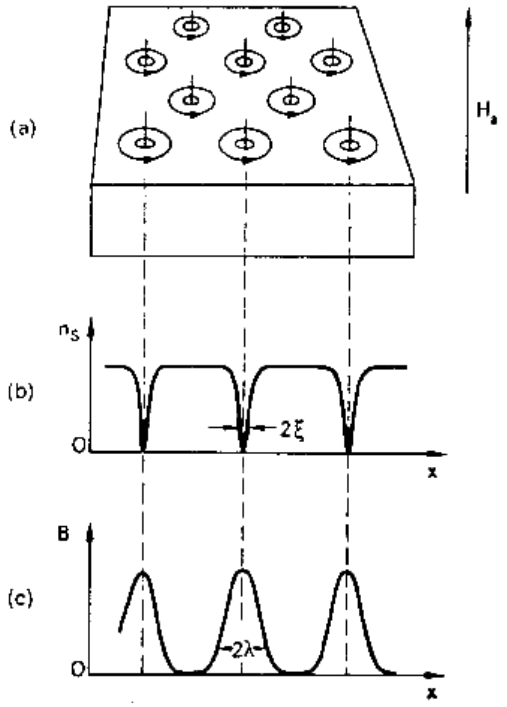

Fig.1-2 Mixed-state superconductivity in field strength just above H_{c1}, (a) lattice of cores and vortices, (b) variation with position of superelectrons concentration, (c) variation of flux density [8]

Normal cores of radius ξ exist within the superconducting region. Each core is penetrated by a quantum of magnetic flux, known as a fluxon, which has the same direction as that of the applied field and a magnitude of ϕ_0=he/2e~2.07 x 10^{-5}Wb. The fluxon is generated and maintained by a vortex of supercurrent of radius λ. The fluxons repel mutually and arrange themselves in a close-packed hexagonal form called a flux line lattice. Furthermore, a surface circulating current opposes the applied field and maintains the bulk diamagnetism. As shown in (b) and (c) of Fig.1-2 the superelectron concentration n_s and the flux density B in the mixed state vary with position in a periodic manner. Towards the centre of each vortex the concentration n_s falls to zero, so along the centre of each vortex is a very thin core with the dips about two coherence-lengths wide. The flux density reaches maximum in the normal cores and falls to a small value over a distance about λ away from the cores.

When magnetic field is closed to H_{C1} (=H_C/κ) in the mixed state, the fluxons are in low concentration with a lattice spacing a_0>λ(T). As B increases the fluxons move closer together, resulting in a decrease of the lattice spacing, ξ(T)<a_0<λ(T). Until H_{C2} (=ϕ_0/2πξ), the fluxon

normal cores overlap and superconductivity is extinguished. At fields approaching H_{C2}, B can be considered equal to the applied field.

When a transport current is introduced into a type-Ⅱ superconductor, a Lorentz force ($F_L=J_C \times B$), perpendicular to the applied field and current, acts on the fluxons. When a fluxon is forced to move, electrons may across their normal core, dissipate energy and even loose superconductivity. In order to prevent the energy loss and keep the supercurrent, the fluxons must be held "pinned". For an ideal type-Ⅱ superconductor, the fluxons are easy to move because there is no pinning site to hold the fluxons, such that the ideal type-Ⅱ superconductor will not possess any current-carrying capability. However, practical superconductors really exist with imperfections, such as dislocations, normal phases, grain boundaries and voids, which serve as pinning centers. It is these pinning centers that develop a volume flux pinning force F_P with a direction opposite to the Lorentz force F_L and retard the fluxon motion, as depicted in Fig.1-3.

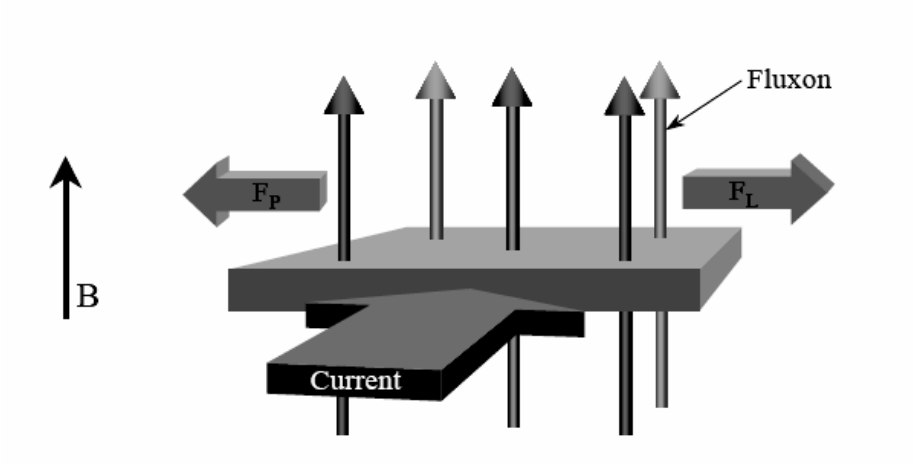

Fig.1-3 The forces acting on fluxons when an electric current is applied. The Lorentz force (F_L) on the fluxons is countered by the pinning force (F_P).

From Fig.1-3 it is seen that the fluxon motion is effectively prohibited only when F_L does not exceed F_P and a transport current can be resistancelessly carried only in this situation. If $F_L>F_P$, the fluxons move and energy is dissipated. Therefore, the critical current density (J_C) is defined by the condition $F_L=F_P$, where the fluxons become depinned and move across the volume, generating a voltage and energy loss. The field at which $F_P=0$ is named as irreversibility field H* and no bulk supercurrent can flow above this field. Thus, H* value at

F_P=0 is the technologically applicable maximum magnetic field.

The three critical superconducting properties of the type-Ⅱ superconductor, critical temperature (T_C), upper critical field (H_{C2}) and critical current density (J_C), create a three-dimensional space as shown in Fig.1-4. Within the critical boundary supercurrents can flow without energy loss and above the boundary the superconductor will be in normal state.

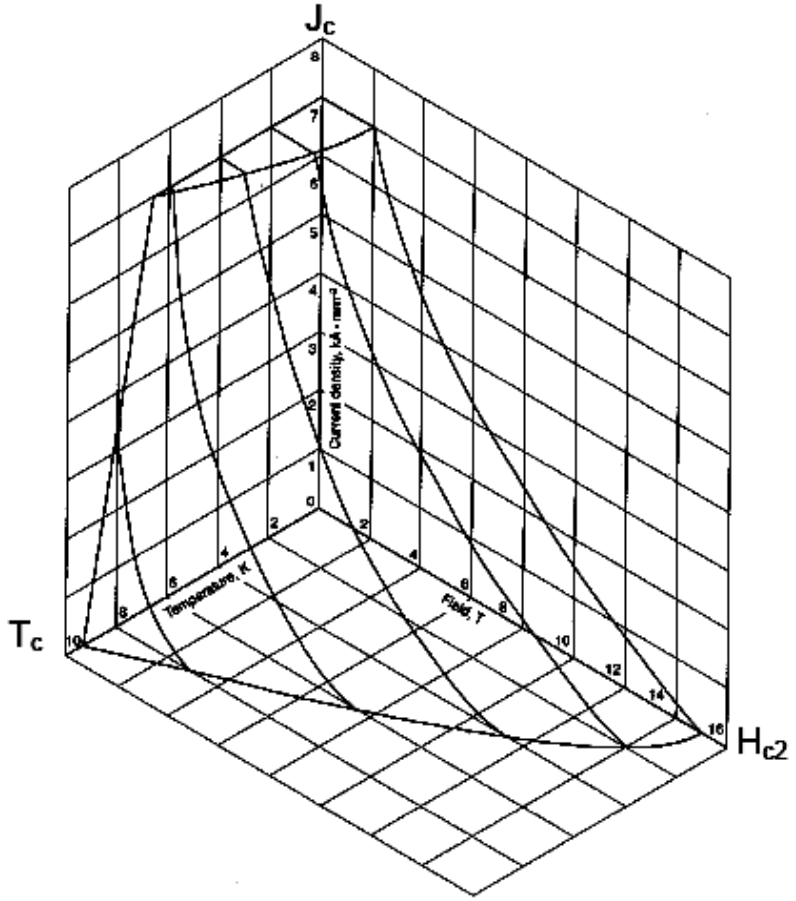

Fig.1-4 Three-dimensional space diagram of the superconducting current density (J) – magnetic field (B)- temperature (T) [9].

The magnetization behavior of the type-Ⅱ superconductor is also different from that of type-Ⅰ superconductor. It is well known that the magnetization curve of any superconductors is generally described as the function:

$$B=\mu_0(H+M) \quad (1\text{-}4)$$

or $$-M=H-B/\mu_0 \quad (1\text{-}5)$$

where M is the magnetization and is dependant on the applied field H and flux density B.

When H is below H_{C1}, the type-Ⅱ superconductor is in Meissner state and totally

excludes flux from penetrating. Then the magnetization curve is exactly identical to that of type-Ⅰ superconductor, M=-H. For field H >H_{C1}, fluxons penetrate the superconductor and magnetization decreases until becoming zero at H_{C2}, at which point the sample is fully penetrated by flux. Ideal magnetization curves are completely reversible and represent the characteristics of ideal type-Ⅱ superconductors, as seen in Fig.1-5.

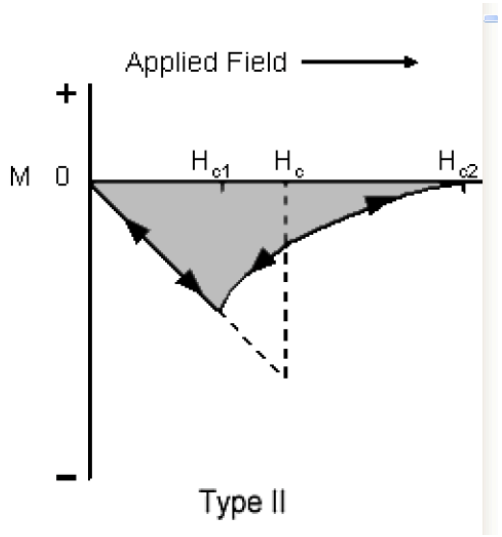

Fig.1-5 Ideal magnetization curves of type-Ⅱ superconductor at a constant temperature below T_C. The curve is completely reversible. The dashed line shows the ideal curve of the type-I superconductor.

Material imperfections found in all "real" superconductors do not allow for ideally exhibited superconducting behavior. A significant portion of the magnetization curve is irreversible, as illustrated in Fig.1-6. In other words, there exists a hysteresis for practical type-Ⅱ superconductors. This phenomenon is attributed to the fact that the fluxons are "pinned" to imperfections in the material and prevented from moving freely. Consequently, as the applied field is increased above H_{C1}, the entry of fluxons into the interior is hindered. Similarly, as the applied field is decreased from a value greater than H_{C2}, the escaping of fluxons from the superconductor is also inhibited. Therefore, in the irreversible regime the number of fluxons at a given field while the magnetic field is being increased is smaller than the number of fluxons at the same field when the field is being decreased and there is a residue magnetic moment when the field is being back to zero. This gives the irreversible magnetic curve shown in Fig.1-6. The difference in magnetization for increasing and decreasing applied fields is directly associated with the flux pinning properties of the

superconductor. Obviously, the stronger the flux pinning effect, the stronger is the retarding force for fluxons from movement, so that the larger is the irreversible performance. Also shown in Fig.1-6 is the irreversibility field H*, which marks the transition point between reversible and irreversible behavior. At a field over H*, a technological superconductor does not allow any lossless currents to flow through.

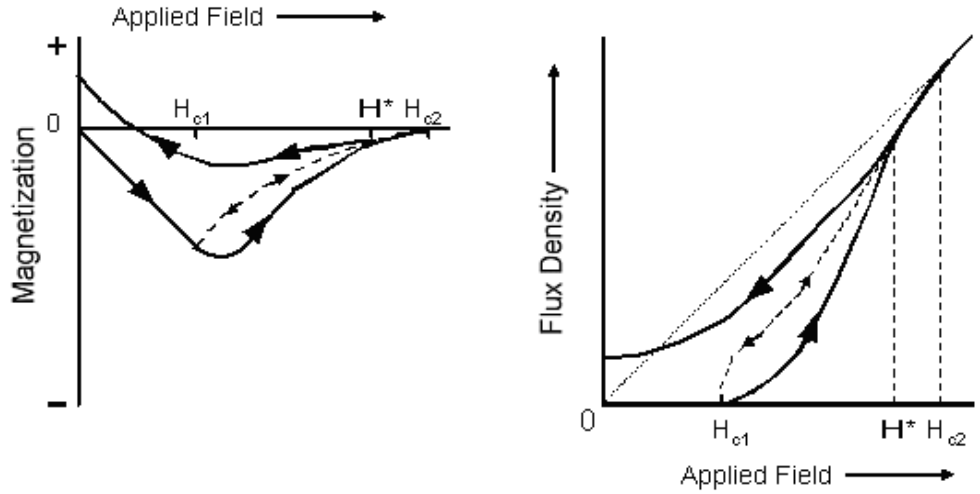

Fig.1-6 Irreversible magnetization curves of type-Ⅱ superconductor. The dashed lines illustrate reversible magnetization. H* marks the transition between reversible and irreversible behavior [7].

The hysteretic or irreversible property of the technological superconductor also varies with temperature. Generally, the magnetization behavior is becoming weak and its curve is shrinking as the temperature elevates, as shown in Fig.1-7. The reason is that the increase of temperature weakens the bulk flux pinning force and makes the fluxons easy to move.

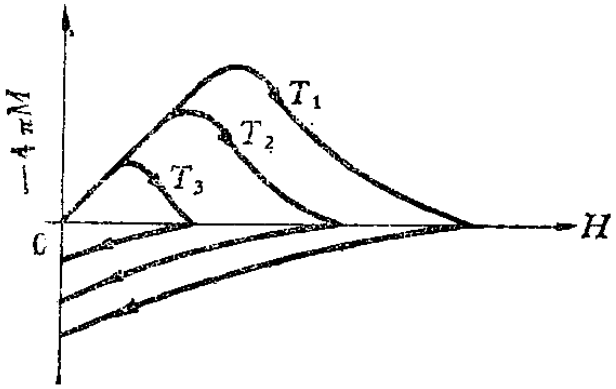

Fig.1-7 Schematic hysteresis curves at different temperatures where $T_3 > T_2 > T_1$ [10]

An entire hysteretic loop of the type-Ⅱ superconductors is origin symmetric, as shown

in Fig.1-8 and any magnetization curve is definite or a part of the loop, no matter how the magnetic field changes. As an example, Fig.1-8 also depicts the magnetization curve variation with the applied field from A_1 to A_4 and back to A_1.

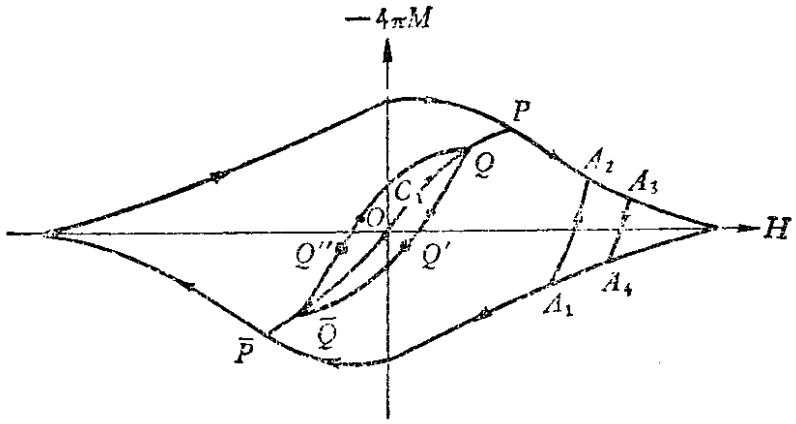

Fig.1-8 Schematic hysteresis loop of type-Ⅱ superconductor and its symmetry, in which a magnetization curve from A_1 to A_4 and back to A_1 is also shown [10].

According to this property, if some necessary magnetization curves are measured, the entire hysteretic loop will be obtained by the origin symmetric manner.

1.3 Nb_3Sn Properties and Phase Diagram

Nb_3Sn is a type-Ⅱ superconductor with the A15 crystal structure. For the generic A15 compounds A_3B, the crystal configuration is formed by a body-centered cubic lattice of B atoms with two A atoms centered at each face. The A atoms lie on three orthogonal chains which are often closer (10%~15%) to each other than pure A (Fig.1-9). it is then clear that in the crystal structure of Nb_3Sn, Sn atoms form a body centered cubic lattice with three orthogonal Nb chains arranged at every face. These Nb chains are closer than pure Nb, which not only increases the structural density, but also creates a higher d-band density of states and in turn enhances the superconducting properties. For instance, the Nb_3Sn and pure Nb lattice spacings are 2.645Å and 2.940Å respectively and the T_C values of Nb_3Sn and pure Nb are 18.3K and 9.1K respectively.

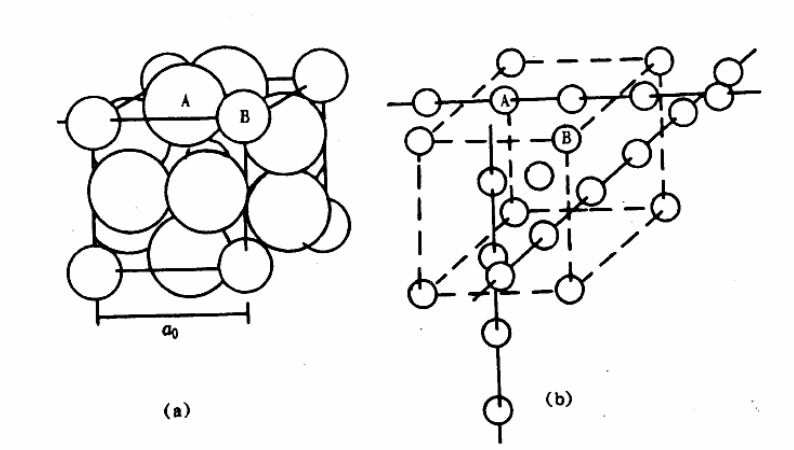

Fig.1-9 Atomic arrangement of the A15 Nb_3Sn compound where A atom is Nb and B atom is Sn [11].

The Nb-Sn phase diagram is shown in Fig.1-10. There are three intermediate phases in the Nb-Sn system, $NbSn_2$, Nb_6Sn_5 and Nb_3Sn, where Nb_3Sn is the lone superconducting phase. Unlike $NbSn_2$ and Nb_6Sn_5, Nb_3Sn is not a line compound but exists as a solid solution with composition ranging from 18~25at%. Any solution composition of this range has the A15 crystal structure.

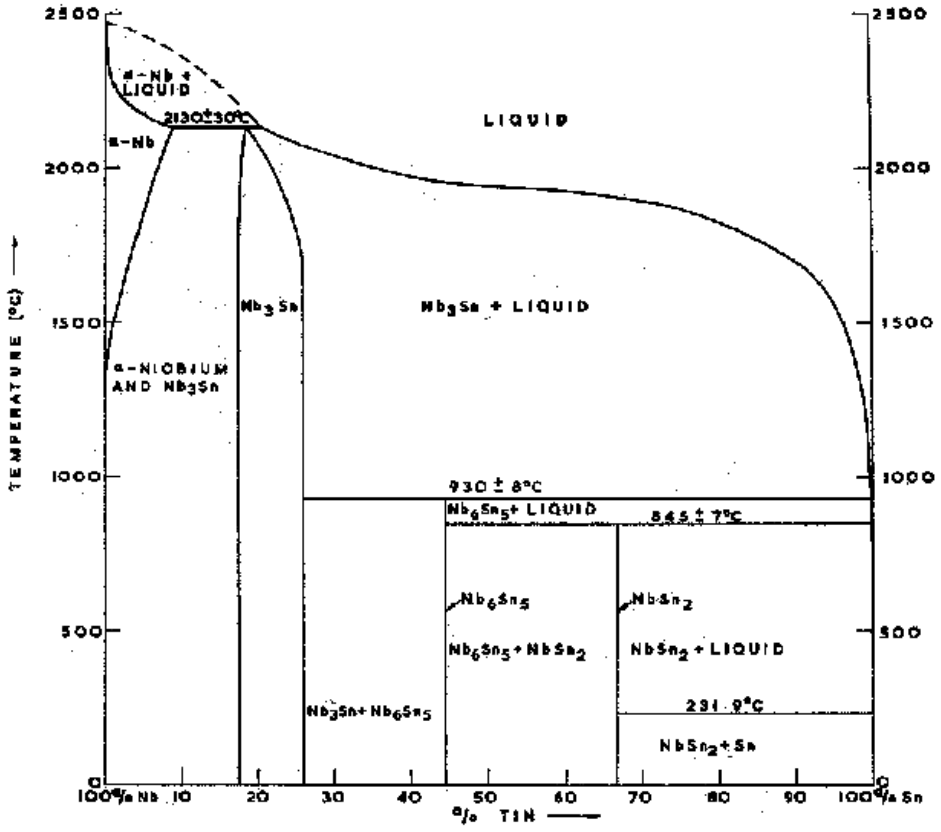

Fig.1-10 The Nb-Sn binary phase diagram. The Nb_3Sn phase exists from 18~25at%Sn [12].

All Nb-Sn A15 compounds are superconducting, but their superconductivities vary with Sn content. Usually, T_C and H_{C2} increase with increasing Sn concentration up to just below stoichiometry, but it is rarely achieved in practice due to the small Sn diffusion coefficients. As an example, Nb_3Sn has a T_C of 18.3K, whereas T_C diminishes with decreasing Sn concentration, to a value of 6K at the Sn-poor side of the Nb_3Sn phase (Fig.1-11). However, T_C abruptly drops by ~0.5K above Nb-24.5at%Sn owing to the decrease in the density of states caused by the cubic to tetragonal phase transformation [13].

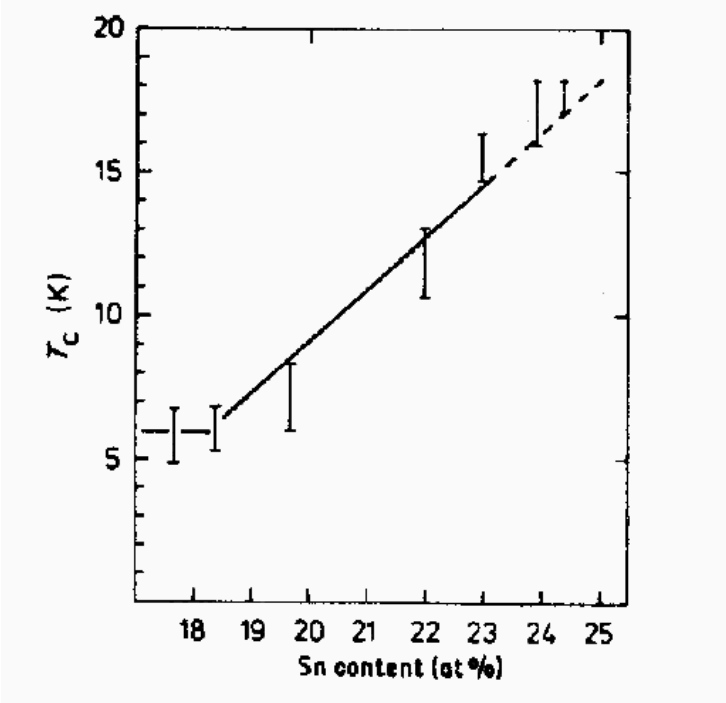

Fig.1-11 T_C variation with Sn content in A15 Nb_3Sn [13]

Nb_3Sn is a typically brittle intermetallic compound, which needs the processing of wires with niobium and tin metals prior to the formation of the brittle Nb_3Sn phase. This presents significant challenges in manufacturing the conductor, especially for long wire used in large magnets. Further more, the formation of Nb_3Sn through Nb and Sn or through Nb and Nb-Sn intermediate phase requires much higher reaction temperature. The fabrication of Nb-Sn intermetallic powder over 900ºC is an example. For this reason, Nb-Sn-Cu ternary system is actually used for the conductor manufacturing, i.e., bronze process and internal-Sn process. It was observed that the Nb_3Sn could not form under 700ºC without Cu, while there was the Nb_3Sn formation with as little as 5at%Cu even at 450 ºC [14]. The reason is that the presence

of Cu causes the intermediate phases, $NbSn_2$ and Nb_6Sn_5, unstable and promotes the reaction of them with Nb at rather lower temperature.

Fig.1-12 shows the Nb-Sn-Cu ternary diagram at 675 ºC isotherm. It is seen from this phase diagram that there are no any compounds in the Cu-Nb binary system and no any Nb-Sn-Cu ternary compounds in the A15 range either. That is to say the Cu does not enter into the A15 phase composition, such that its presence has little effect on the primary superconducting properties. Practically, Cu has a very low solubility in Nb_3Sn (about 0.3at.%) [16] and the majority of Cu is found localized at voids and grain boundaries[17]. The main purpose of Cu addition is to lower the A15 phase reaction temperature and to facilitate Nb_3Sn formation.

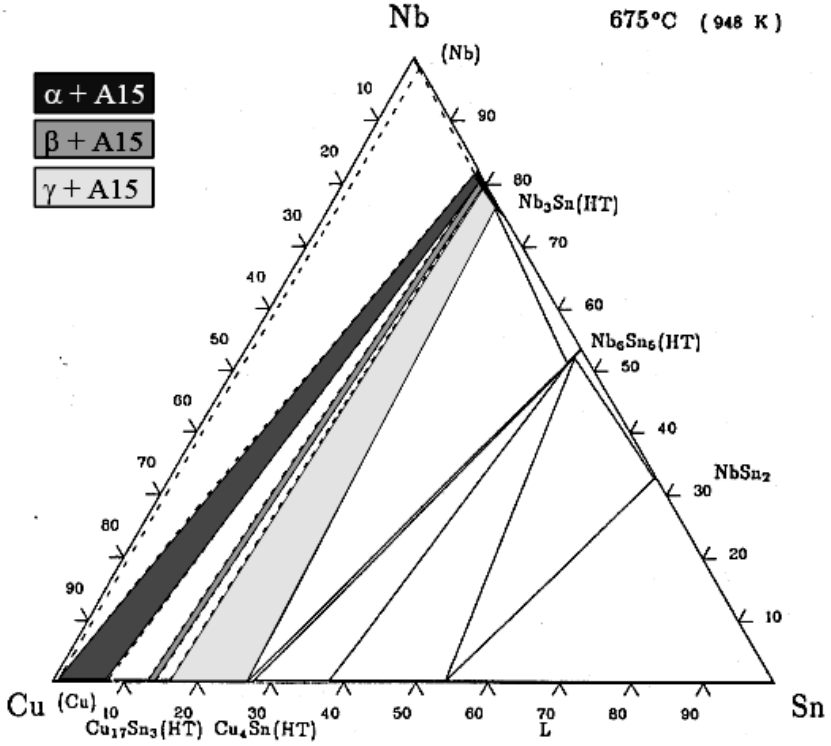

Fig.1-12 The Nb-Sn-Cu ternary phase diagram at the 675 ºC isotherm [15]

In the Nb-Sn-Cu phase diagram, three A15 solid solution ribbons widen continuously from Nb-Sn binary side to Sn-Cu binary side. This means that the three Sn-Cu alloyed phases, α, β and γ, are each in equilibrium with A15 compositions and the equilibrium range enlarges with the increase of Cu content.

According to this phase diagram the A15 phase formation progress is then clear during the heat treatment of practical wires. For bronze process, Nb filaments locate inside the bronze alloy and Nb is uniformly reacted with Sn in the Cu-Sn binary composition to form A15 phase. However, for internal tin process, Nb filaments locate among Cu matrix and Sn alloys with Cu prior to the Nb-Sn reaction, which results in the contact and reaction of Nb filaments with different Cu-Sn phases. It seems that this Cu-Sn inhomogeneity would affect the Sn composition in the A15 filaments and thus the superconducting properties. Actually, this is not the case. It was confirmed that the composition-related superconducting properties of the Nb_3Sn wire, T_C and H_{C2}, were not finally affected no matter what starting Cu-Sn phases were contacted with Nb filaments [23]. This is because Sn has a much larger diffusion coefficient than Cu and Nb, which makes the original inhomogeneity in Cu-Sn composition ineffective to affect the final A15 phase composition.

1.4 Development of Nb_3Sn Superconductors

In 1961, Kunzler et al [18] found that Nb_3Sn superconductor could produce over 1000 A/mm^2 of critical current density J_C even at the field of 8.8T. Since then, Nb_3Sn superconducting materials have entered technological application and many of A15 wire fabrication methods have been developed [19]. Among them the primary multifilamentary processes currently utilized in industry include the bronze, internal-Sn and powder-in-tube processes. The main difference of the three methods is in their Sn source, which has important repercussion for the overall wire design. The similarities, however, are that all designs use solid state diffusion to transport Sn from the source to the Nb filaments and all requires a diffusion barrier and a surrounding stabilizing Cu.

The development of the wire manufacturing methods is in accordance with its practical application. For Nb_3Sn wires there have been two primary requirements in practice. One focuses on increasing J_C values as high as possible for the ever-increasing field of high-field magnets and the other centralizes on decreasing the hysteretic loss, especially for AC use. Firstly, it is necessary to discuss the critical current density (J_C). J_C is defined by a normalization of the critical current (I_C) to a defined area. If the normalized I_C is divided by

the entire cross-section areas of the wire, a so called engineering critical current density (J_E) is obtained. The J_E values of different wires can not be compared because various wires have different fraction area of stabilizing Cu area, which does not carry current while the wire is superconducting. If the normalized I_C is divided by the A15 layer area, the obtained value is then the A15 layer critical current density ($J_{C,layer}$) which possibly reflects the current-carrying capacity of the superconducting phase. The complication is that the A15 layer area for a multifilamentary wire is difficult and usually resource-limited to be measured. The majority of the J_C value is practically the "non-Cu J_C" or "package J_C", which is the result of normalized I_C divided by the cross-section area excluding that of stabilizing Cu. Non-Cu J_C is more indicative of the actual superconducting properties and can thus be used for comparison of different conductors.

The first multifilamentary Nb_3Sn wire manufacturing method was the bronze process [20]. The schematic of the resulting wire is depicted in Fig.1-13(a). In this process, Nb rods are inserted into a α-bronze matrix, extruded and drawn to a final wire size, where the wire is then heat treated to form Nb_3Sn. A drawback of this process is that the bronze work-hardens so quickly that the wires must be annealed after every three drawing passes or ~50% area reduction. This makes the process labor-intensive and runs the risk of premature Nb_3Sn formation during the bronze anneals at ~450ºC, hampering further wire reduction. Another difficulty is that the maximum amount of Sn available is limited by the maximum solubility of Sn in α-bronze (15.8 wt %). Furthermore, to avoid formation of the hard δ phase, which is strongly detrimental to the cold procedure of bronze, the Sn content was limited to about 13wt% for many years, which obviously hinders the increase of J_C. However, the bronze process is really the most developed multifilamentary Nb_3Sn wire fabrication method and still accounts for much of the Nb_3Sn strands, especially for NMR spectroscopy magnets and scientific research magnets. Recently, fine powder spray casting methods have been developed to increase the Sn content to ~15wt%, close to the solubility limit [21]. With this high Sn content bronze, the bronze process can be used to fabricate Nb_3Sn wires even for ITER project [22].

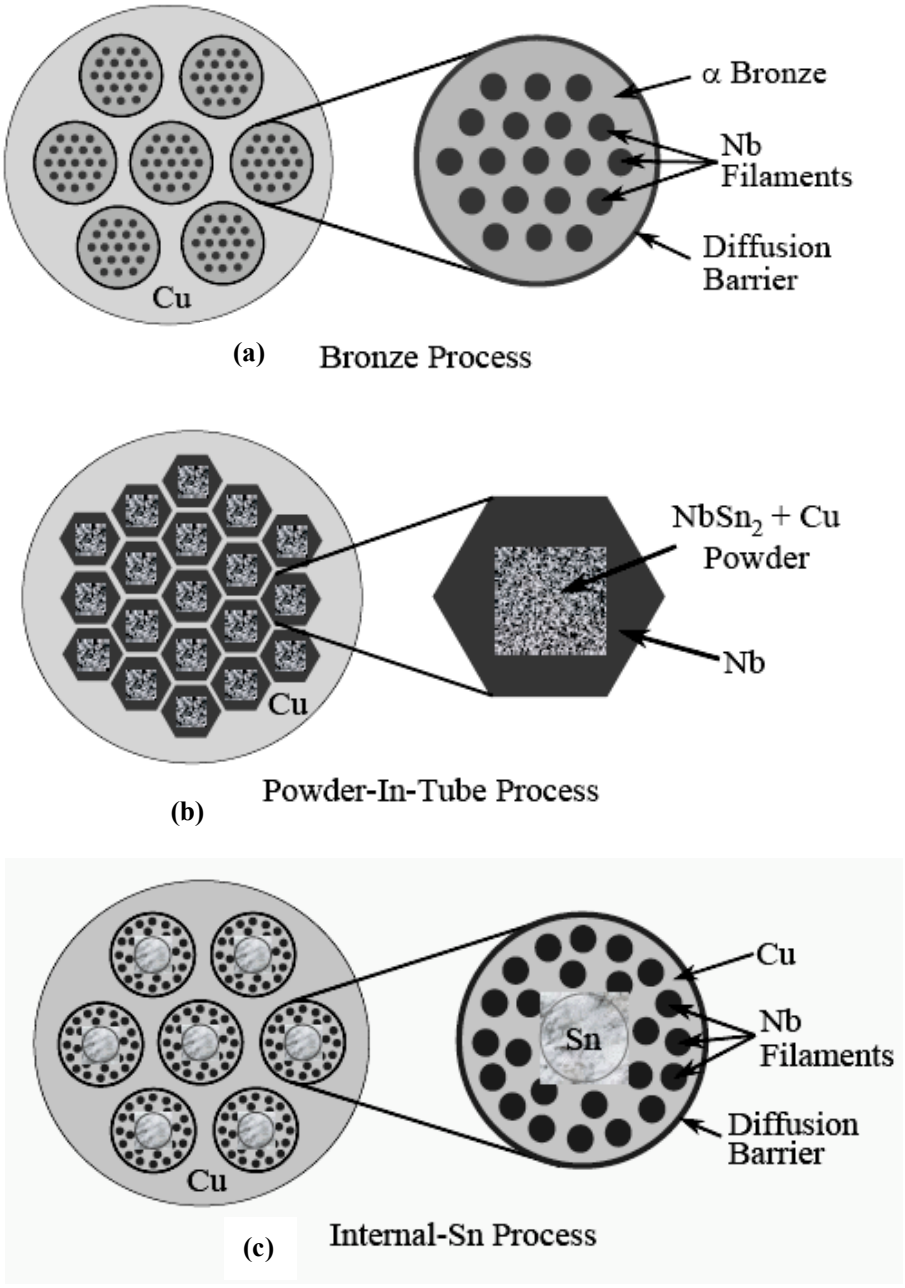

Fig.1-13 Schematics of three main Nb_3Sn wire fabrication techniques (a) bronze process, (b) powder-in-tube process, (c) internal-Sn process [23].

Another wire fabrication method that has drawn much attention in recent years is the powder-in-tube (PIT) process [24], as shown in Fig.1-13(b). In this process, $NbSn_2$, Sn and Cu powders are encapsulated and compacted into Nb tube, extruded, drawn down to final size and then heat-treated to form Nb_3Sn. The unreacted portion of the Nb tube serves as a natural diffusion barrier. There are several benefits to this wire design. The high Sn content source in the PIT conductor is capable of producing large areas of Nb_3Sn with compositions close to

stoichiometry over the majority of A15 layer, which promotes the wire J_C. The best PIT wires have achieved a non-Cu J_C (4.2K, 12T) of 2150 A/mm^2 [25]. The PIT wire also suffers less pre-compression than other designs as the Nb tube deforms more uniformly with the inside powders, so that it exhibits excellent strain resistance [26]. In addition, the PIT wire has rather small effective filament diameters (D_{eff}), close to the tube diameters (<50μm), resulting in very low hysteretic loss [24]. One of the disadvantages of the process is that the tubing and special powders are expensive, making the cost greater than other routes.

Presently, the most common manufacturing method for high J_C superconductors is the internal-Sn process (also the focus of this thesis), which was firstly developed in 1970's [27]. A schematic of a multifilament internal-Sn conductor is illustrated in Fig.1-13 (c). In this process, a high Sn source is surrounded by Cu-clad, Nb rods in a pure Cu matrix, which is all surrounded by a diffusion barrier, and the packages can be cold drawn to final size and heat-treated to form Nb_3Sn at the site of Nb rods. The internal-Sn process is advantageous compared with the bronze process as it allows their processing to proceed to final size without intermediate anneals. Also, the abundant Sn source (higher Sn/Cu ratio than in bronze) and the relatively high percentage of Nb content increase the A15 cross-section area and thus the non-Cu J_C. The primary advantage of this method over PIT is the lower cost of the basic components.

The most beneficial feature of the internal-Sn process is its wire-design flexibility of adjusting the Nb, Sn and Cu fraction within the superconducting sub-elements and the non-Cu fraction of the composite, which allows the creation of strands having a wide range of properties, depending on the application requirement [4]. Over the last decade, the internal-Sn process has also tended to two requirements, increasing the non-Cu J_C and decreasing the hysteretic loss. As for the increase of non-Cu J_C, a specific technique called the Modified Jellyroll (MJR) process may be the most achievable [28]. In the MJR process, a Sn core is wrapped with a double layer of Cu and expanded Nb metal, surrounding by a diffusion barrier of Nb or Nb-Ta alloy, and is drawn to a bundle or subelement. A number of the subelements are stacked and drawn to a final size, with the expanded Nb becoming Nb filaments. Oxford Instruments has used 50 such subelements to manufacture a multifilamentary strand and achieved over 3000 A/mm^2 of non-Cu J_C (4.2K, 12T) [29], the highest value of present wires.

Despite the high non-Cu J_C, the MJR process has inherent disadvantages. Hysteretic loss in these conductors is high due to the large D_{eff}, resulting from the unavoidable bridging of the Nb filaments. Nevertheless, this process is one of the most suitable techniques for DC magnets and still plays an important role in the region of high energy physics (HEP).

For further improvement of J_C, a distributed tin (DT) process, a variation of internal-Sn, has been developed [30], as schemed in Fig.1-14. In the DT process, a number of Nb/Cu composites are extruded and drawn to an Nb module and the Cu-clad Sn core is also formed to a tin module. The hexagonal Nb modules and Sn modules are uniformly arranged and drawn to a final size.

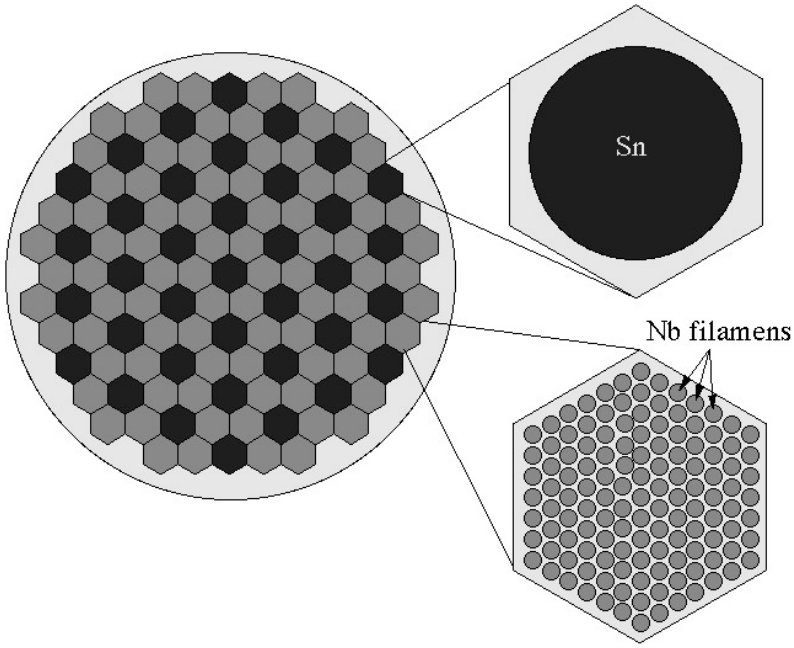

Fig.1-14 Schematics of distributed tin (DT) process [30]

Perhaps the most popular internal-Sn process is the Restack-Rod-Process (RRP), which is the one used by Alstom and NIN for the fabrication of our ITER-type multifilament wires. A schematic of the technological procedure will be shown in section 2.2.1. In the RRP process, a lot of Cu-clad Nb rods are surrounding a Sn core, forming a subelement. A number of the subelements are restacked inside the outer diffusion barrier and stabilizing Cu and then drawn to final size. It is much easier to change the component configuration with this design, for the purpose of suiting different utilization. More subelements and lower Cu ratio are often

designed for improving wire J_C. On the other hand, a smaller number of subelements plus high Cu ratio are usually the best way for decreasing hysteretic loss because the Nb filaments in this design are lonely distributed and are not easily to develop coupling, resulting in an effective decrease of D_{eff} in this case. Obviously, this high-Cu design is very suitable for ITER high-field magnets [4] and thus has been adapted by most wire suppliers, including MSA/ALSTOM and NIN.

A problem with using a pure Sn core in internal-Sn method is that the wire can be difficult to be processed to the final size as the Sn is softer than the other components. To remedy that, the Sn is often hardened by alloying a second element, such as Mg, Ti. Another difficulty of using nearly pure Sn is its low melting point which prevents extrusion. Thus the wire must be manufactured by cold drawing, leading to larger drawing losses than in better bonded, extruded billets. To overcome that, salt (NaCl) is used in place of the Sn during extrusion and is subsequently dissolved, while molten Sn is poured into the openings and the wire is then drawn to final size [31].

In practice, there appeared other ways to reduce the D_{eff} and thus the hysteretic loss in an internal-Sn design. One example is the use of internal fins as barriers to separate the Nb filaments [32]. Another is a distributed barrier configuration in which each subelement is cladded with a diffusion barrier, avoiding any capable bridging between the bundles [33].

In recent years, one modified internal-Sn method has been developed, so called "Rod-In-Tube (RIT)" process [34] or "Internal-Tin-Tube (ITT)" process [35]. In this process, a Cu-clad Sn rod inside Nb tube is composed and drawn to a subelement and a number of the subelements are stacked together to form a composite and then drawn to final size. Similarly, it is capable of easily adjusting the Nb/Sn/Cu ratio or alloying dopants into Sn and/or Nb. This process simplifies the strand fabrication procedure and thus reduces the wire processing cost. In this thesis, several mono-element internal-tin (MEIT) wires were prepared, each of which is actually one subelement of the RIT or ITT wire.

1.5 Research Progress on Nb_3Sn Superconducting Materials

Since a great current-carrying performance of Nb_3Sn at high field was found in the early

1960's, more and more research work has been made on this special superconductor material [18]. A concurrently proceeded conductor, Nb-Ti alloy, had been exceeded over Nb_3Sn in a period of years because of its low cost, reproducible critical current densities, long piece lengths and ductility [36]. However, Nb-Ti ceases to have any current carrying ability at 4.2K and 10.5T [37]. So, it becomes apparent that the high performance, high field Nb_3Sn conductors possess an incomparable value with the progress of ever-increasing high field magnets and the R&D on Nb_3Sn conductor materials have also made a great achievement, especially over the last decade.

The R&D of Nb_3Sn superconductors can be described in two respects. In the first place, much research work has focused on basic investigation. B.T. Matthias et al [38] first found that the β-W structure (e.g. A15 structure) of Nb_3Sn compound had a critical temperature T_C of 18.05K±0.1K. R.L. Cooper [39] made further measurements in which the T_C of stoichiometric Nb_3Sn crystals was known as 18.3K and its upper critical field H_{C2} was determined as ~25T. P.R. Bosomworth et al [40] measured the energy gap of superconducting Nb_3Sn and also showed several characteristics of Nb_3Sn superconductors, such as T_C of stoichiometric Nb_3Sn 18.3K, transition width 0.22K, crystal lattice constant 5.291±0.0005Å, coherence length ξ ~100Å and penetration depth λ ~2500Å. The Nb-Sn phase diagram was determined by J.P. Charleworth et al [12] in 1970. Later on in 1981, H. Devantay et al [41] obtained the detailed structure parameters and some superconducting properties of A15 Nb_3Sn conductors. It was notable that the lattice constant a_0 decreases nearly linearly with the composition from 5.290Å for Nb-25at%Sn to 5.280Å for Nb-18at%Sn and there is an abrupt drop by ~0.5K above Nb-24.5at%Sn due to the decrease in the density states caused by the cubic-to-tetragonal transformation. In the past few years, V. Guritanu et al [42] further studied the specific heat of concentrated Nb_3Sn crystals and made clear that Nb_3Sn is a special superconductor with two stages of energy gap. The main energy gap has a value of $2\Delta_L(0) \sim 4.9K_BT_C$ and a small secondary energy gap with a value of $2\Delta_S(0) \sim 0.8K_BT_C$ which will disappear at the field above ~7T. All the above fundamental researches have been playing valuable roles in the technological applications of Nb_3Sn superconductors.

Compared with basic studies, even more R&D has been centralized on the properties and performances of applicable Nb_3Sn wires. Before 1990's, the majority of early studies were on

the bronze-processed Nb_3Sn wires. As a meaningful example, J.D. Livingstone [43] gave a comprehensive review of earlier studies on bronze-processed wire composites from the aspects of phase diagram, reaction dynamics, alloying effect, structure-property relations etc. With the development of high-J_C internal-Sn method, significant research work has gathered on internal-Sn processed wires, although PIT wires have also garnered much attention [44,45]. Various researches on practical wires can be described as the follows.

The intrinsic properties, T_C and H_{C2}, are the first to be dealt with in all superconductor wires. It is known that A15 Nb_3Sn is not a lone compound, but a solid solution of a range of Sn content and the T_C value increases with the increase of Sn concentration in the solid solution [13]. The fact is that the T_C of a practical wire is rare to achieve 18.3K of stoichiometric Nb_3Sn. The reason is that the A15 phase in the real wires is formed by Sn diffusion and solid reaction and the Sn diffuses very slowly, especially across the A15 product layer.

Another cause of the lower T_C is the high strain sensitivity of the Nb_3Sn wire. D.C. Welch [46] reported the strain dependence of T_C for bronze-processed conductors (Fig.1-15), showing a T_C decrease with the increment of strain. Because of the difference of thermal contraction coefficients between different components and the metallurgical processing, the wire strain is then not avoidable, leading to the decrease of the T_C value. The real T_C range is usually at 17.2~17.8K due to the non-stoichiometry and the strain effect.

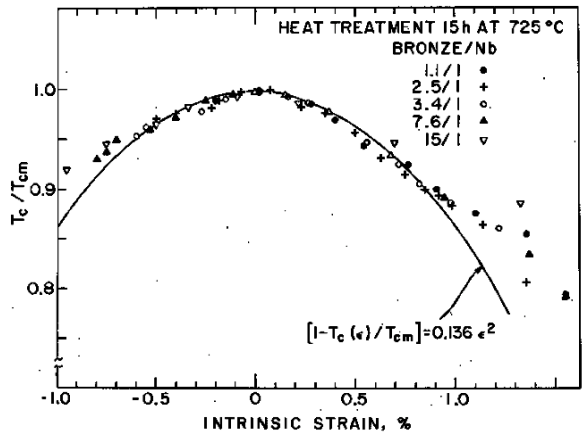

Fig.1-15 Strain dependence of T_C for bronze-processed monofilament Nb_3Sn conductors

The A15 H_{C2} values reported in the literature are much more varied than T_C, with the

$H_{C2}(0)$ ranging from 21.6T to 28T [47,48,49] and a more recent report of 31.4T [50]. The wide discrepancy in H_{C2} may be due to atomic order, true Sn concentration, strain states, apart from different measurement techniques and measurement criteria.

Orlando et al. [48] found that H_{C2} decreases with increasing atomic order because of the decrease of the resulted resistivity (ρ_n). There have been some investigations of the variation of H_{C2} as a function of Sn concentration [41,51,52]. R. Flükiger et al.[51] showed, based on pure, clean samples, that H_{C2} increases with increasing Sn content up to ~24.5at%Sn, where it falls off precipitously. The H_{C2} and T_C behavior can be understood with an equation derived by Kim et al. [53]

$$H_{C2}(0)=3.11\times10^3\rho_n\gamma T_C \qquad \text{(Tesla)} \qquad (1\text{-}6)$$

where γ is the electronic specific heat coefficient in $J/m^3\cdot k^2$, ρ_n is in Ω-m and T_C is in Kelvin. It is seen from (1-6) that the increase in atomic order reduces the ρ_n and thus the H_{C2} value. Both T_C and γ increase with increasing Sn, thus increasing H_{C2}. It is also seen that the sharp drop in T_C at the composition of Nb-24.5at%Sn caused by the cubic-to-tetragonal transition diminishes H_{C2}.

The strain sensitivity of Nb_3Sn wire also has an effect on H_{C2} values. J. Ekin [54] reported the strain dependence of the upper critical field for various A15 compounds, showing the strongest strain effect of Nb_3Sn conductors, as seen in Fig.1-16. That means a rather large decrease of H_{C2} resulted from a small strain increase.

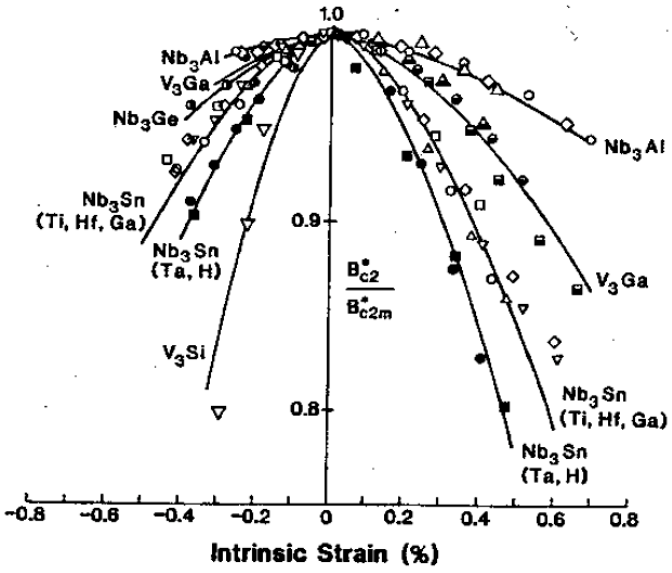

Fig.1-16 Strain dependence of the upper critical field for various A15 compounds [54]

As there are big differences in various wire-handling processes, it is not strange that different wires have different residual strain situations and thus explain the variation of H_{C2}. Practically, much effort has been made to enhance the H_{C2} by means of reinforcement with other materials or applying pre-compressions in the conductors, which are beneficial in increasing the wire fracture tolerance. For example, more recently, L.D. Cooly et al. [55] made great efforts to promote the flux pinning force and H_{C2} using a powder ball-milling process.

Another reason for the difference of H_{C2} values is that much of what was reported as H_{C2} is actually the irreversibility field H*, the field at which the J_C=0. The upper critical field was often determined by an extrapolation of F_P, J_C or a Kramer function ($J_C^{1/2}\cdot B^{1/4}$ versus field) [56] to zero. Clearly, these extrapolations have been shown to give H*, not H_{C2} [57]. Although H_{C2} and H* are very different, awareness of the existence of H* did not come about until the discovery of high temperature superconductors in the late of 1980's [37]. Up to today, however, many people are still mix-using the two different concepts.

H-T phase diagram is the upper critical field H_{C2} as a function of temperature $H_{C2}(T)$ or critical temperature T_C versus applied field $T_C(B)$. There have been few studies on the H-T phase diagram of Nb_3Sn conductors [42,58], possibly due to the great variation of H_{C2} values through different measurements. The authors [42] determined H_{C2}-T phase diagram of concentrated Nb_3Sn crystals by specific heat measurements. M.G. Adesso et al. [58] depicted the different H(T) characteristics of bulk superconductors, single crystal and multifilament Nb_3Sn wires through 1st and 3rd harmonics of the AC magnetic susceptibility measurements. In this thesis, magnetization measurements were used to determine the $T_C(B)$ values of our two ITER-type multifilament wires, obtaining a series of their H-T phase diagrams.

Irreversibility properties of a superconductor include irreversibility field H* and irreversibility temperature T*. Most investigations of Nb_3Sn wires have been made on the H* property, although many of them were still called H_{C2} or B_{C2}. The H* values can be determined by two ways. For most technological wires, the transport critical current measurement is usually used to determine the H* which is defined as the maximum field at J_C=0. Apparently, this value reflects the current-carrying ability of the Nb_3Sn wires. The other way is by magnetization measurement in which the magnetic hysteresis derived from the flux

pinning situation of the sample as a function of applied field is used to obtain the H* value. This kind of H* is defined as the maximum field of F_P=0. M.T. Naus et al. [23] obtained the Kramer irreversibility field property (H^*_{kramer}) of Modified Jelly Roll (MJR) internal-Sn superconductor wires by the magnetization measurement with a vibrating sample magnetometer (VSM) and found an almost linear relation of H* values with the sample T_C data. C. M. Fischer et al.[61] also obtained the H^*_{Kramer} values of some PIT Nb_3Sn wires by the same method and showed the H* results fitting quite well with the magnetization data. In this study, the two ways of magnetization measurements were adopted to get H*.

K.R. Marken et al [62] reported that in high fields the pinning force (and hence J_C) are less sensitive to the microstructure and the upper critical field H_{C2} (actually, the irreversibility field H*) is important in determining J_C. Since Nb_3Sn superconductors are usually utilized in high-field magnets, it is much necessary to enhance H* for the purpose of promoting the high-field performance. Small amounts of third element additions in Nb filaments are often beneficial to H* due to an increase in ρ_n through impurity scattering [63]. The optimization of heat treatment process also has a useful effect on H* enhancement [64].

M. Suenaga et al. [65] were the first to study the irreversibility temperature property of a multifilament Nb_3Sn wire. They found that there exists a surprisingly large temperature region for the Nb_3Sn wire below the upper critical field line $H_{C2}(T)$ (or critical temperature line $T_C(H)$) where the magnetization is reversible during a warming and cooling cycle. The lower boundary of the temperature region was called the irreversibility temperature T*(H). A SQUID magnetometer was used for the measurement and T*(H) was taken as the point of onset of reversible magnetization at an applied magnetic field. Moreover, the authors pointed out that the irreversibility temperature can also be measured by cycling the magnetic field at a constant temperature and by determining the value of field B at which the hysteresis width ΔM (B) vanishes. Clearly, this is the value of irreversibility field H*(T) and that means an equivalence of T*(B) with H*(T). Therefore, the investigation of irreversibility temperature actually reflects the situation of irreversibility field, which is also very valuable for the performance promotion of the superconducting wires. According to this point, much of our research work had been made on the irreversibility temperature variation with the applied field T*(B) and the optimization of heat treatment from the T*(B) examination results

[66,67].

The studies of technological Nb_3Sn wires have also been progressing in two directions, increase of J_C and reduction of hysteretic loss. The J_C enhancement is mainly for the utilization in HEP, such as large accelerator, and the AC loss reduction is mainly focused on the AC magnets, such as the ITER's. Whereas, most works are the combination of increasing J_C and diminishing hysteretic loss as much as possible at the same time [68,69]. In wire design, higher ratio of Nb/Sn/Cu can produce higher fraction of non-Cu A15 area, which can substantially elevate J_C. During wire processing and heat-treating, it is very significant for promoting current-carrying capability that the A15 composition, grain profile and strain state should be optimized [70]. The effective way of diminishing hysteretic loss is to lower the filament coupling or bridging and then the D_{eff} [71-74]. For the practical development of Nb_3Sn wire, OST [75] has made two achievements. The highest non-Cu J_C of up-to-date wires has reached over 3000A/mm^2 (4.2K, 12T) for high J_C use in HEP and their ITER-type internal-Sn wire has obtained the non-Cu J_C of ~1200 A/mm^2 (4.2K, 12T) with the hysteresis loss as low as ~400KJ/m^3. IGC [76] also developed an ITER-type wire with non-Cu J_C over 900 A/mm^2 (4.2K, 12T) and a much lower hysteresis loss of below 200KJ/m^3.

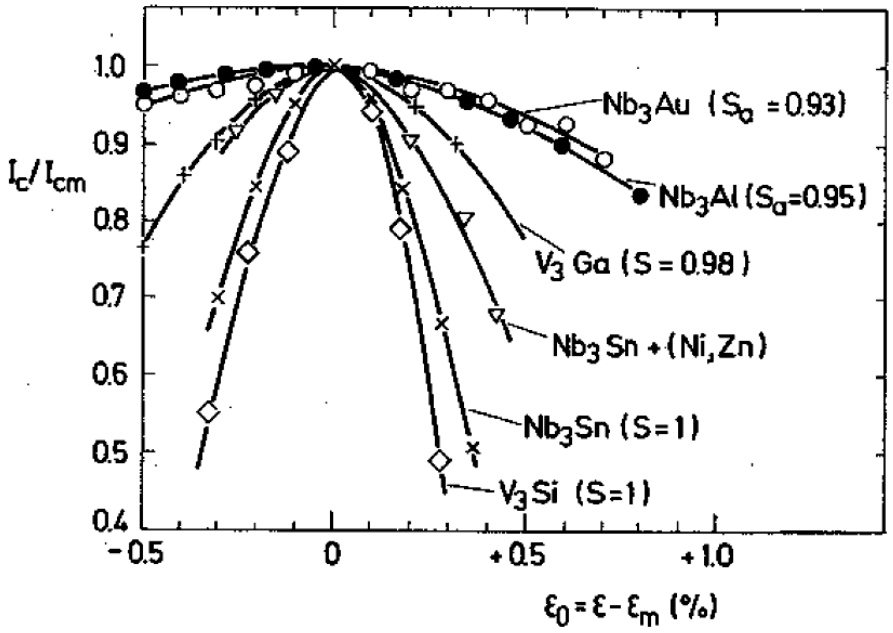

Fig.1-17 Strain dependence of critical current for various A15 compounds [78]

One of the main influences of wire J_C is also the strain sensitivity. As shown in F.g.1-17

[78], the variation of Nb_3Sn J_C with strain is the biggest among A15 compounds apart from V_3Si. This high degree of strain sensitivity not only introduces metallurgical handling concerns, but residual strains (typically compressive) can be retained in the wire upon heat treatment processing [77]. For many years, in order to increase J_C, a lot of development work has been afforded to reduce various unnecessary strain [79,80] or to reinforce the Nb_3Sn conductors for benefiting their strain tolerance [81].

Another key factor reflecting current-carrying ability J_C is the flux pinning properties. It is well established that the most important magnetic flux pinning centers in Nb_3Sn compounds are the grain boundaries [82,83,84]. It is to say that the grain size and crystalline morphology determine the flux pinning situation in the conductor. In their early studies, R.M. Scanlan et al. [82] illustrated the flux pinning force F_P dependence on grain size, reaction temperature and time. Pinning force F_P evaluated at its maximum is generally ~5T at 4.2K and has an inverse relation with grain size, seen in Fig.1-18. F_P is proportional to 1/d at large grain size, which corresponds to being directly proportional to grain boundary area per unit volume, while at smaller grain size, F_P is slowly increased with the grain boundary density, exhibiting parabolic variation.

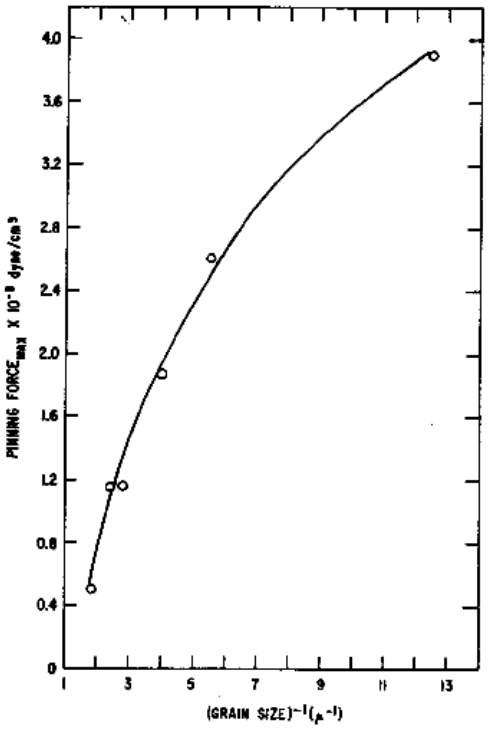

Fig.1-18 Flux pinning force versus inverse grain size for MF Nb_3Sn [82]

Grain size versus reaction temperature at different reaction times for multifilament Nb_3Sn was depicted in Fig.1-19 [82] from which a substantial increase of grain size is seen with the increase of temperature, especially at higher temperatures. According to their analysis, the grain size was required to be kept approximately less than 200nm in order to maximize the flux pinning force F_P and thus the critical current density J_C. That is to say, the F_P and J_C will increase with the coarsening of grain size up to ~200nm and then decrease afterwards.

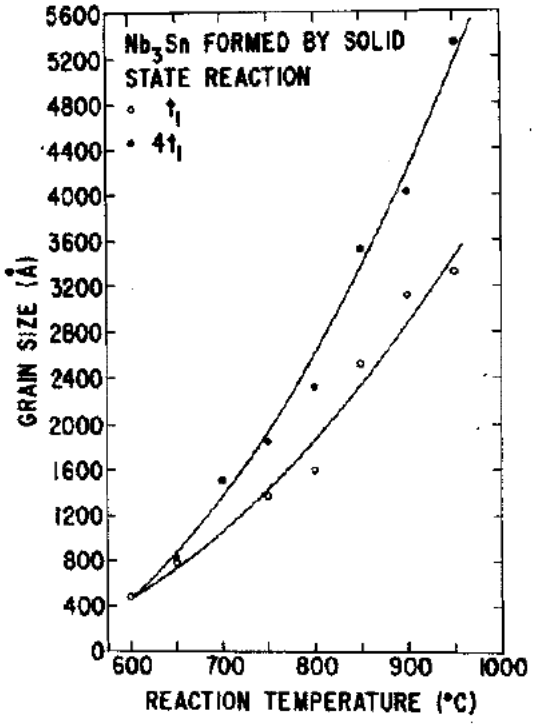

Fig.1-19 Grain size versus reaction temperature for MF Nb_3Sn [82]

To optimize the flux pinning property and other superconducting performances, the most significant factor is heat treatments for phase formation. The heat treatments are often designed to perform two functions: (1) alloying the Cu and Sn, and (2) form the Nb-Sn A15 phase. For the Cu-Sn mixing heat treatment, M.T. Naus [23,85] had carried out a systematic investigation with two MJR internal-Sn wires. Based on the Cu-Sn binary phase diagram (seen in Fig.1-20), the author chose ten different temperatures from 210ºC to 600ºC. At each temperature, 24hrs and 150hrs of holding time were adopted for the transformation and

development of various Cu-Sn phases. The seven Cu-Sn phases, from start to end at different temperature and time period, were examined by light microscopy (LM), backscattered scanning electron microscope (SEM-BSE) imaging and energy dispersive spectroscopy (EDS). For further studies of the Cu-Sn alloying progress, we used in-situ neutron diffraction measurement, combined with SEM analysis, to detect the Cu-Sn phase variation of our two ITER-type internal-Sn wires and obtained valuable results [86,87].

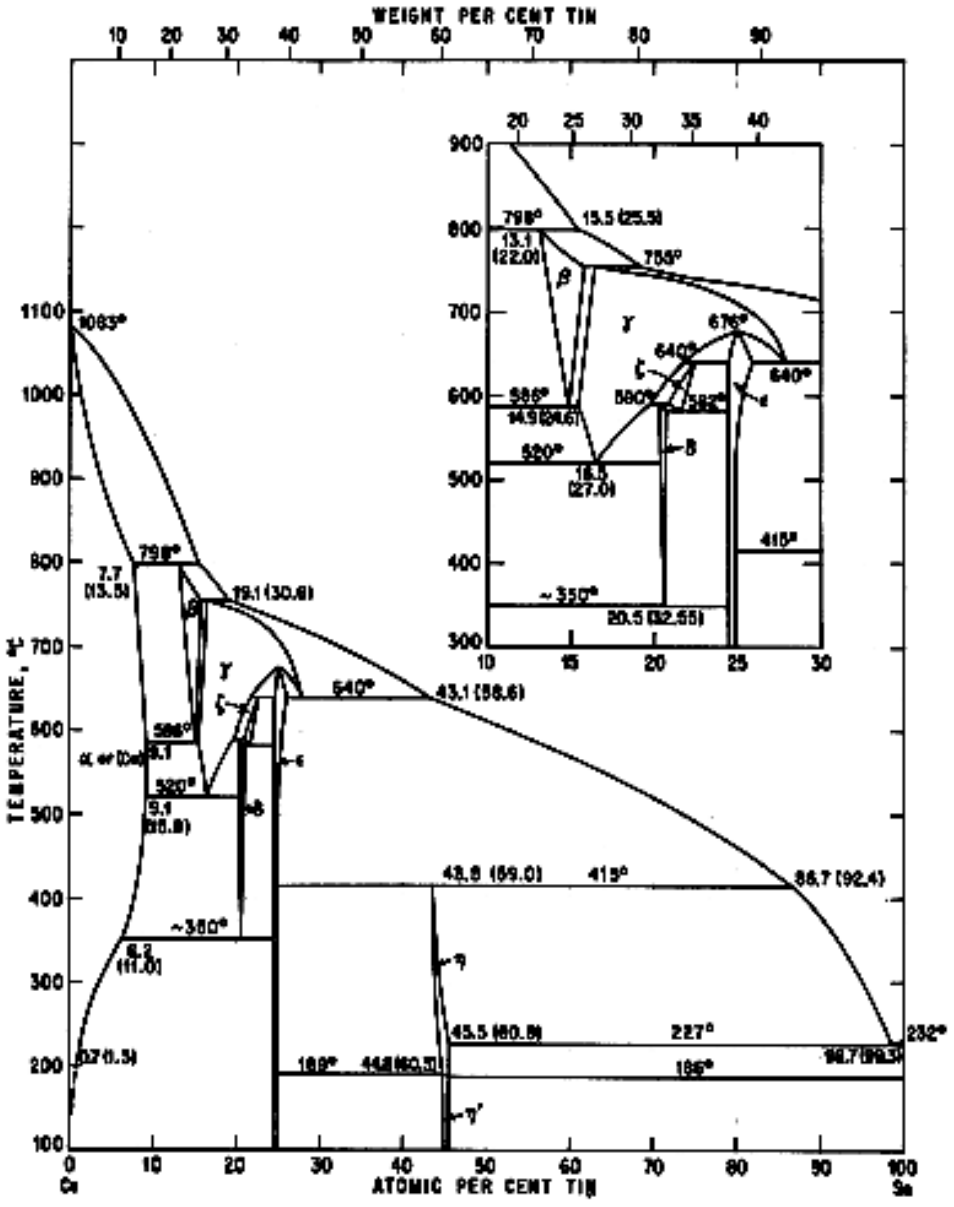

Fig.1-20 The Cu-Sn binary phase diagram [88]

It was concluded [23] that complete mixing of the Cu and Sn is highly unlikely and no

heat treatments generated a homogenous Cu-Sn microstructure in commercial wires. There were many concerns that Cu-Sn phase inhomogeneity might have an effect on the composition of the initial Nb-Sn A15 phase to form and thus affects the final superconducting properties. No evidences, however, were found [89,90,91] that the various Cu-Sn alloying steps influence the superconducting properties (including T_C, H*, H_{C2} or J_C) in fully reacted wire, even for the heat treatment without any Cu-Sn alloying steps [92,93]. In practice, some Cu-Sn alloying procedures are designed only to allow low melting point phases to transform into higher melting temperature phase(s) before the A15 reaction treatments at temperatures in excess of 650ºC.

For the heat treatment of Nb-Sn A15 phase formation, M.T. Naus [23] had also made much investigations with the two MJR wires, in which the author chose three treatment temperatures, 650ºC, 700ºC and 750ºC, to react the samples for various time intervals. T_C and H* values of all samples were determined through magnetization measurement. It was found that T_C values had nearly a linear relationship with H* data, no matter how the samples were heat-treated. Apart from this, some researchers evaluated the A15 reaction heat treatment effect on microstructure and superconducting properties [95], and others investigated the heat treatment optimization of some internal-Sn wires [92]. As for A15 heat treatment of PIT processed wires, C.M. Fischer [61,94] had made much work, in which not only the T_C, H* and H_{C2} properties were measured by means of the VSM magnetization method, the inductive J_C and flux pinning force F_P were also calculated as a function of reaction temperature and time. A. Godeke et al. [64] had also focused their work on PIT wires, in which the authors measured the sample upper critical field and T_C transition variation at different heat treatment conditions. In our study, a systematic measurement and analysis were made with the two ITER-type RRP internal-Sn wires. Four reaction temperatures, 650ºC, 675ºC, 700ºC and 725ºC, and various enduring times were arranged. The samples were measured for T_C, H* and flux pinning properties, from which we have optimized the heat treatment processes [96,97].

The purpose of optimizing heat treatment is to realize the maximum J_C in a specific wire. It is known that lower reaction temperatures produce smaller grain size which has a higher grain boundary density and is thus beneficial to elevate J_C, whereas, the Sn diffusion and thus the A15 formation rate are lowered because of the lower treating temperature, resulting in a

lowered quality of A15 phase. This is detrimental to J_C. The literature [82] observed that it took 500hrs at 600ºC to form an A15 layer just 1μm thick. Industrial applications require much shorter processing times, so typical processing temperatures are usually on the order of 650ºC. On the other hand, although higher temperature accelerates the A15 formation rate, the grain size coarsening is inevitable, which leads to decrease of grain boundary density and then to the reduction of flux pinning density. It is also detrimental to J_C when the grain size is beyond ~200nm. Growing large, stoichiometric Nb_3Sn layers and at the same time maintaining a fine grain size has been an inherent challenge in processing Nb_3Sn superconductors. A suitable solution is to introduce artificial pinning centers or dopants to retard the grain growth and thus reinforce the flux pinning force F_P [98]. Besides the grain size, the crystalline morphology also has a strong effect on flux pinning situation and superconducting performance. D.R. Dietderich et al. [99] reported that columnar crystals have a very strong orientation for flux pinning and may weaken the wire J_C, since the columnar crystals are not distributed in the same direction in the heat-treated wire. In comparison, equiaxed crystals have the same flux pinning performance in any direction and then can strengthen the superconducting properties, especially at high field. Generally, although the grain size is smaller at lower reaction temperature, there exist much more columnar crystals. On a contrary, the main crystalline profile is in equiaxed crystal state at higher temperature, even though the grain dimensions are coarser. From this viewpoint, the key target of heat-treating process is to find the equilibrium between increasing the amount of equiaxed crystals and reducing grain size, and thus enhance the superconducting performance J_C.

Microstructure and microchemistry analysis are often used to study the heat-treated wires. P.J. Lee et al. [100-103] have made much research on this respect. With the aids of SEM, FESEM, STEM and EDS, the authors analyzed the phase profiles and compositions of bronze, internal-Sn and PIT wires, and even specifically discussed the ITER-type wires [104]. One of the valuable results was that the crystalline morphology of A15 phase is inhomogenous not only at the cross section, but also along the length of the wire, which is the main reason for superconductivity reduction of long length wire.

In their early studies, H. Oikawa et al. [105] observed that Kirkendall voids appeared during heat treatment since Sn has a larger diffusion coefficient than Cu. Also, the atomic

volumes of the Cu-Sn phases decrease with decreasing Sn content. Therefore, voids can develop within a bundle as higher Sn content Cu-Sn phases transform to α-phase during A15 formation. The voids slow diffusion when agglomerated and are believed to cause stress concentrations when in contact with Nb_3Sn filaments. The effect of such voids, however, is still unclear. Although Easton et al. [106] showed large cracks near voids than elsewhere along an A15 filament, others have not been able to decisively correlate cracks with void locations [107].

Some third element additions can substantially influence the superconducting properties of Nb_3Sn conductors. In the early years, extensive studies of the alloyed dopping were focused on bronze-processed wires [108]. Around the last ten years, most third-element alloying researches have been dedicated to internal-Sn wires, besides some of the PIT wire dopping [109]. The addition of third element may include alloying Nb, Sn or both [75]. A primary function of alloying Nb is to promote the H* (or H_{C2}) and T_C and then to enhance the technological application at high fields [63]. The Sn alloying with third element has two effects. One is to harden the Sn core, reducing the drawing-loss and Sn leak during wire processing. The other is to increase the Sn diffusion rate and to lower the heat-treating temperature.

About the alloyed elements, Suenage et al. [108] had more detailed examination in bronze-processed wires. They showed that additions of 1 to 2at% of Ti or Ta increase T_C by ~0.3K, whereas V, Zr and Mo decrease T_C. Also, 2 to 4at% of Ti, Ta, V or Mo increase H_{C2} (4.2K) by up to 3.5T, with the largest increases due to Ti and Ta addition. R. Akihama et al [110] reported that non-transition metal additions also increase H_{C2} (4.2K) to up to ~30T. The increase in H_{C2} with small amounts of solute is likely owing to an increase in ρ_n through impurity scattering. One more, in the presence of solute atoms or atomic disorder, the cubic-to-tetragonal transition is suppressed and thus no fall-off of H_{C2} (or T_C) is expected at high Sn concentrations. Although there are still concerns, in recent years, about dopping in bronze-processed wires [111], the internal-Sn wires are more commonly alloyed with a third element, preferably Ti [112] or Ta [113]. More recently, alloying Zr in Nb_3Sn wires has attracted rather big attention [114,115]. In our study, we have also prepared mono-element wires, of which one was alloyed with 1at%Zr in Nb for microstructure and superconductivity

comparison [116].

Three of the most influential alloying elements may be Ti, Ta and Mg. It has been observed that these three elements can inhibit grain growth [117,118,119], and Ti and Mg can also enhance the Sn diffusion to Nb filament and increase Nb_3Sn layer growth rate [117,119,120]. As a result, all three elements have been shown to improve J_C properties. More over, a very important observation was that Ti addition can also increase the irreversibility field H* and decrease the J_C at lower field, resulting in the decrease of hysteretic loss [121]. Comparatively, Ti and Ta received more consideration though there are still some discussions about Mg addition nowadays [112]. Almost all commercially available Nb_3Sn conductors are alloyed with Ti or Ta. In our research work, Alstom MF wire was alloyed with 7.5at% Ta in Nb and NIN MF wire was alloyed with 2wt%Ti in Sn. Besides, all the prepared mono-element wires had 2wt%Ti alloyed Sn cores.

Understanding the most important factors involved in phase formation and growth kinetics of Nb_3Sn wire will contribute to the improvement of superconducting properties allowing better choices for the heat treatment parameters. The purpose of the formation kinetics study of various phases is to find the phase growth variation rule as a function of HT temperature and time, and thus to determine the diffusion and reaction coefficients and even the activation energy. However, little information is available on the phase formation kinetics, especially on A15 layer growth kinetics, in modern wire composite, although the superconducting properties of Nb_3Sn composites have been extensively studied. The reason may be the complexities of wire configuration and phase formation progress of the multifilament wires, in which the filament dimensions are usually 2~5μm and in most filaments exist deformation after metallurgical processing. So it is difficult to examine the phase variation during heat treatment. In addition, there are the problems of filament bridging and filament reaction difference between different locations, which make phase growth measurement of MF wire rather hard. Another important factor is the Sn ratio in the wire composite. It is known that the three primary processes—bronze, powder-in-tube and internal-Sn, differ in their Sn source, but they all use solid state diffusion to transport Sn from the source to the Nb filaments. The Sn ratio difference affects the Sn diffusion rate and then the A15 phase formation rate, which results in the kinetics study usually suitable only for a

specific MF wire. In this case, mono-element wires or wires with larger Nb thickness are possibly the best choice for kinetics analysis.

The phase growth progress of Nb_3Sn wire includes Cu-Sn alloying and A15 phase formation. There has been substantial work on the Cu-Sn alloying kinetics. M. Onishi et al. [122] and K. Hoshino et al. [123] analyzed reaction-diffusion in Cu-Sn alloys in their early reports. J.D. Verhoeven et al. [124,125] discussed the Sn diffusion and void formation in external-tin Nb_3Sn wires. Recently, S. Mattaffirri et al. [126] and J.M. Rey et al.[127] more finely surveyed the phase growth kinetics in the Cu-Sn system with their specially fabricated wire. A general common conclusion is that the intermetallic growth model of various Cu-Sn phases is in accordance with parabolic growth law:

$$Y^2=K(T)\cdot t \qquad (1\text{-}7)$$

where Y is the intermetallic layer thickness, t and T are duration and temperature of the HT, and K is the growth rate of the intermetallic layer. Specifically, the authors [126] also calculated the diffusion factor (k_0) and activation energy (E) of η、ε and δ Cu-Sn phases, using the Fick's first law.

Only a few researches have been reported to concern the Nb_3Sn phase growth kinetics. In 1980's, X.D. Tang et al. [128] investigated the Nb_3Sn phase formation rate as a function of HT temperature and time with a bronze-processed wire. According to $Y \propto t^n$, the authors plotted Log(Y) with Log(t) and obtained the exponent n values from linear fits. The more significant work was E. Barzi et al.'s recent report [129]. With mono-element internal-Sn and PIT strands, the authors measured various A15 layer thicknesses of different heat-treated samples and used the following model equation to fit:

$$Y^n=K(T)t \qquad (1\text{-}8)$$

where Y is the A15 layer thickness, K is the growth rate of A15 phase, t and T are also the duration and temperature, and n is the exponent of A15 growth. Their results were well in accordance with the n power relation (1-8). From the data refinement, the authors also obtained the Nb_3Sn growth rate k and the exponent n value of the two strands at each HT temperature. It is notable that the n value of Nb_3Sn growth, unlike the Cu-Sn phase formation, is dependent on reaction temperature. Besides, the Nb_3Sn A15 phase is not a compound but a solid solution of various compositions, and each composition should have its own reaction

parameters. Therefore, there has not appeared any report which deals with the activation energy of Nb_3Sn A15 phase until now, probably due to this reason. In this thesis, several mono-element internal-Sn wires will be used to further study the A15 phase formation kinetics.

1.6 Thesis Arrangement

This thesis focuses the following aspects of internal-Sn Nb_3Sn superconducting wires:

(1) The HT optimization of internal-Sn wire, especially the ITER-type multifilament wires.

(2) The variation relationship of primary superconducting properties, J_C, T_C, H_{C2}, H*(or T*) and flux pinning performance, as a function of magnetic field and HT temperature and time.

(3) The observation and analysis of phase formation, microstructure and composition.

(4) The effect of third-element alloying on primary superconductivities.

(5) The phase formation kinetics of internal-Sn Nb_3Sn superconductors.

For these purposes, two ITER-type MF wires were typically chosen, one supplied by MSA/ALSTOM with Ta alloyed in Nb filaments, the other supplied by NIN with Ti dopant alloyed in Sn source. Four mono-element internal-Sn wires with different Sn ratio and different dopping elements were prepared, for the need of investigating unique factor influence on phase formation and superconductivity, and especially for the study of A15 layer growth.

This thesis is then organized into six chapters. Chapter 1 gives out a brief introduction to the whole research work, including research motivation and target, and the R&D progress of Nb_3Sn superconducting materials and wires.

In chapter 2, Nb_3Sn wire design, fabrication and primary wire characteristics are described. There are two sections in this chapter, one mainly focusing on multifilamentary wires and the other dealing with mono-element wires. For MF wires, it includes the metallurgical process of the RRP internal-Sn wire and the characteristic comparison of the two ITER-type wires. As for mono-element (ME) wires, the wire composite design, fabrication and the main characteristics are exhibited.

Chapter 3 mainly describes the examination methods and techniques used in this thesis, including neutron diffraction, SQUID magnetization, transport critical current, and microstructure and microchemistry analysis.

Chapter 4 contains a global investigation of the two ITER-type MF internal-Sn wires. The two wires were firstly applied various heat treatments for phase formation, four different reaction temperatures and 6~8 duration time intervals. A two-step reaction procedure was also arranged as a comparison with other samples. In the second section, the heat-treated holder coil samples and short specimens were examined for transport critical current, from which the non-Cu critical current density J_C was determined. The third section mainly describes the SQUID magnetization measurement results, including T_C (B), T_C transition, irreversibility temperature T*(B), hysteresis loops, hysteretic width ΔM and irreversibility field H*. The fourth section gives a detailed description about the Cu-Sn alloying and 24hr A15 phase development by means of in-situ neutron diffraction examination, from which a dynamic variation of the phases can be determined. In the last section, SEM, FESEM and EDS were used to observe and analyze the microstructure, grain profile and phase composition of the heat-treated samples, aiming at finding the relationship among composition, microstructure and superconductivity.

Chapter 5 primarily focuses on a detailed investigation of the four monoelement internal-Sn wires. The wire samples were held a variety of heat treatments with four different temperatures and four duration times. On a number of selected samples, the SQUID magnetization measurements were made, the same as that for MF wires, but with a special emphasizing on the influences of Sn content ratio and third element addition on superconductivities. In the neutron diffraction examination all the heat-treated ME samples were carried out off-situ measurement, apart from the in-situ measurement of one ME wire. On the selected ME samples the element distributions were examined in cross section by EDS, aiming at detecting compositional variation with HT process. All heat-treated samples were determined the A15 layer thickness through SEM analysis for the purpose of phase formation kinetics study.

Chapter 6 is the summary of this thesis.

2. INTERNAL-Sn WIRE DESIGN, FABRICATION AND MAIN CHARACTERIZATION

2.1 Multifilament Wire Fabrication and Characterization Description

2.1.1 RRP Internal-Sn Process

The RRP Internal-Sn approach can be divided into two parts: sub-element (bundle) composite processing and multi-subelement composite wire processing. The former involves several procedures. In the first place, Nb rod and Cu clad are composed together, extruded and processed into a hexagonal Cu-Nb composite rod. Then, a number of the first composites and some Cu inserts are stacked between two Cu tubes, which is extruded and processed into a secondary multi-filamentary Nb-Cu composite. Furthermore, a Sn rod is encased in the inner Cu tube of the secondary composites to form a mono Sn core subelement composite which is then drawn into a suitable size. In the later part of the RRP approach, a diffusion barrier tube is firstly assembled into an outer stabilizing Cu tube, and then a few of the subelement composite rods are restacked into the diffusion barrier tube. Lastly, the restacked multifilament composite is drawn into the final wire size.

This technology can be schematically shown in Fig.2-1.

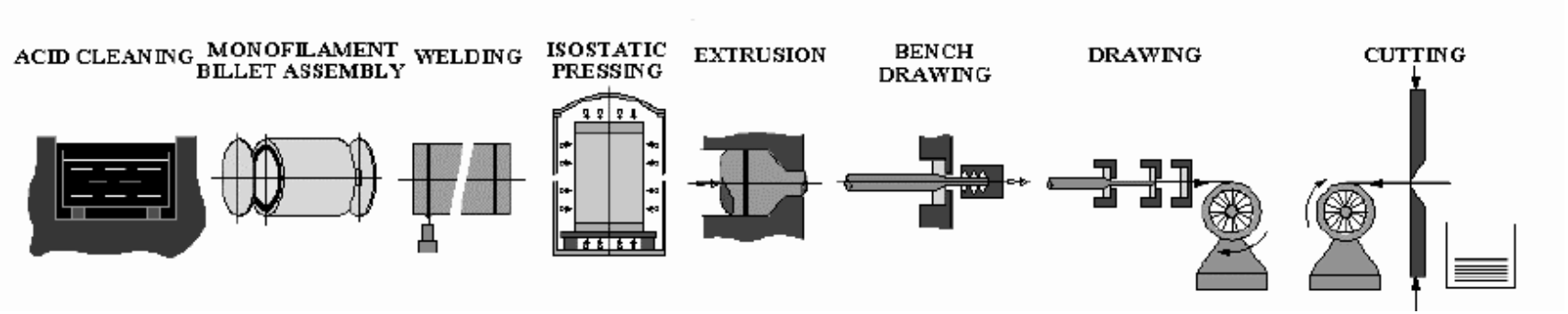

(a) Monofillament billet processing

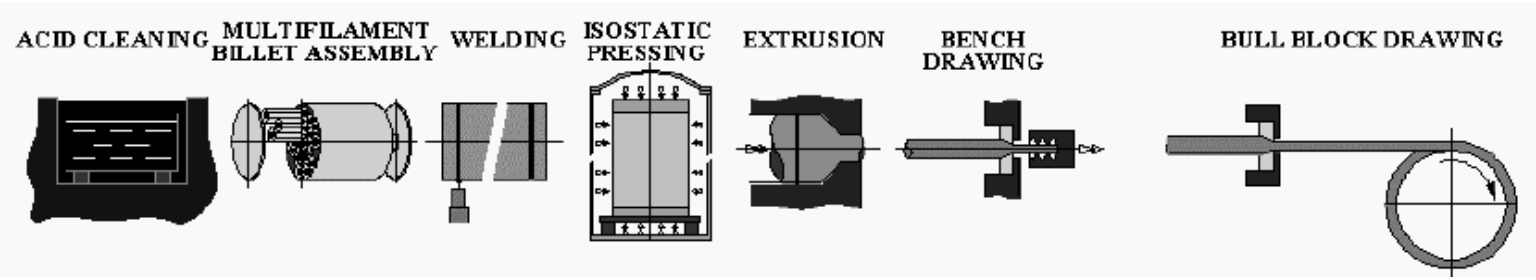

(b) Multifilament billet processing

Fig.2-1 Schematics of the RRP Internal-Sn process for the fabrication of multifilament Nb_3Sn wires, curtsey by Alstom/MSA

2.1.2 ITER-type Multifilament Wires and Their Characteristics Comparison

Two kinds of ITER-type internal-Sn Nb_3Sn superconducting wires supplied by NIN/WST and Alstom/MSA were manufactured with the Restack Rod Process (RRP) method through extrusion and drawing procedure. The former is named NIN wire and the later AST wire. Fig.2-2 shows the cross section photographs of the two wires.

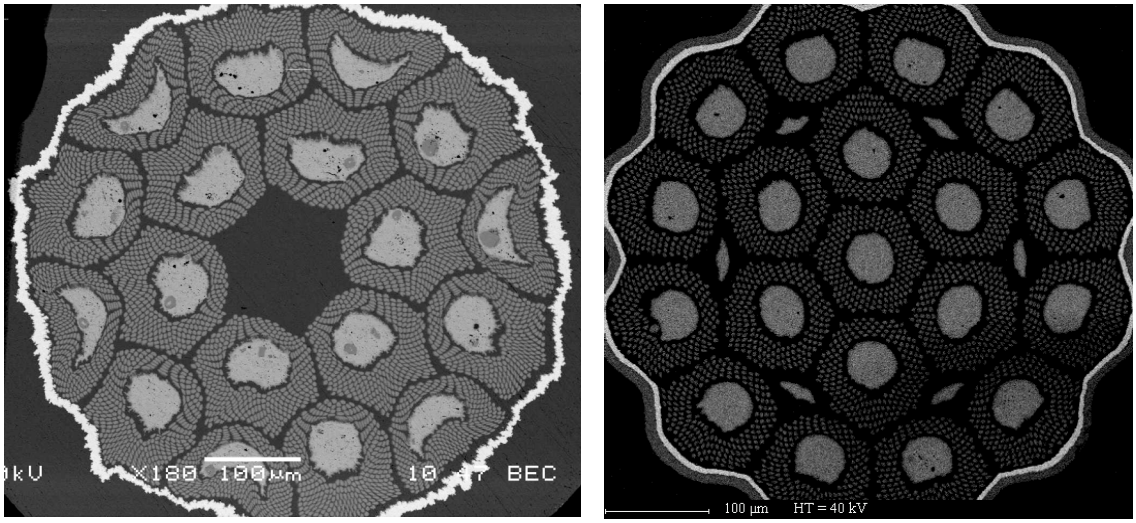

(a) NIN wire (b) AST wire

Fig.2-2 SEM photographs of the two superconductor wires. (a) NIN wire, (b) AST wire

The primary characteristics of the two wires are included in Table 2-1.

Table 2-1 Characteristic data of the two wires

wire	Outer diameter(mm)	Sn core composition	Filament composition	Diffusion barrier	Cu/non-Cu	Filament size(µm)
NIN	0.79	Sn-2wt%Ti	Nb	Ta	1:1	3~5
AST	0.825	Sn	Nb-7.5wt%Ta	Ta+Nb	1.4:1	3~5

From Fig.2-2 and Table 2-1 it can be seen that the main designs and characteristics of the two wires are nearly identical while the following differences can be found: (1) NIN wire has 18 subelements (bundles) within the outer diffusion barrier, but AST wire has 19 subelements together with six distributed tin inserts among the subelements. (2) NIN wire has just one layer of outer Ta diffusion barrier, but for AST wire, two layers of Ta and the outside Nb. (3)

The Sn core has 2wt% Ti alloyed in the composition for NIN wire, but just pure tin for AST wire. (4) The Nb filaments in NIN wire are nearly pure niobium, but AST wire has 7.5wt%Ta alloyed in its composition. (5) The AST wire is more regular in shape than the NIN wire in which a little deformation appeared.

2.2 Mono-element Wires Design, Fabrication and Their Characterization

2.2.1 Internal-Sn Mono-element Wire Design

The design of mono-element wire can be generally described as that a Sn-core, Cu-clad composite rod is embodied in a Nb (or Nb alloy) tube, with a stabilizing Cu tube at the outside. The cross section areas of the Sn rod and inner Cu tube can be adjusted to obtain a necessary Sn/Cu ratio. The Nb (or Nb alloy) tube is designed to have enough thickness to form A15 phase and to serve as diffusion barrier as well.

For comparison of the effect of different Sn/Cu ratio, three composites have been designed with pure Nb tube and different Sn/Cu ratio: (1) Cu-15(wt)%Sn, Sn/Cu =0.176(wt.) =0.095(at.); (2) Cu-20(wt)%Sn, Sn/Cu=0.25(wt.)=0.134(at.); (3) Cu-25(wt)%Sn, Sn/Cu =0.333(wt.) =0.178(at.). For the investigation of third element addition, a 1(at)%Zr alloyed Nb tube is designed to assembled with the Cu-20(wt)%Sn rod, apart from every Sn core alloyed with 2(wt)%Ti.

So, there are four monoelement wire designs with their name and components as the followings:

SF1: ($Sn_{(Ti2\%)}$15wt%-Cu85%)-Nb

SF2: ($Sn_{(Ti2\%)}$20wt%-Cu80%)-Nb

SF3: ($Sn_{(Ti2\%)}$25wt%-Cu75%)-Nb

SF4: ($Sn_{(Ti2\%)}$20wt%-Cu80%)-Nb(1at%Zr)

2.2.2 Wire Fabrication and Their Characterization Description

The four monoelement internal-Sn wires were prepared in NIN via metallurgical drawing and processing. They have the following final dimensions:

(1) All wires have the same outer diameter (OD) of 0.895mm;

(2) SF1: The outer stabilizing Cu thickness: 0.164mm;

The Nb tube thickness: 70μm;

The inner Cu tube thickness: 0.124mm;

The Sn(Ti) core diameter: 0.180mm;

(3) SF2: The outer stabilizing Cu thickness: 0.164mm;

The Nb tube thickness: 70μm;

The inner Cu tube thickness: 0.110mm;

The Sn(Ti) core diameter: 0.208mm;

(4) SF3: The outer stabilizing Cu thickness: 0.164mm;

The Nb tube thickness: 70μm;

The inner Cu tube thickness: 0.099mm;

The Sn(Ti) core diameter: 0.230mm;

(5) SF4: The outer stabilizing Cu thickness: 0.198mm;

The Nb(Zr) tube thickness: 36.5μm;

The inner Cu tube thickness: 0.110mm;

The Sn(Ti) core diameter: 0.207mm;

Fig.2-3 shows the cross section of the four monoelement internal-Sn wires.

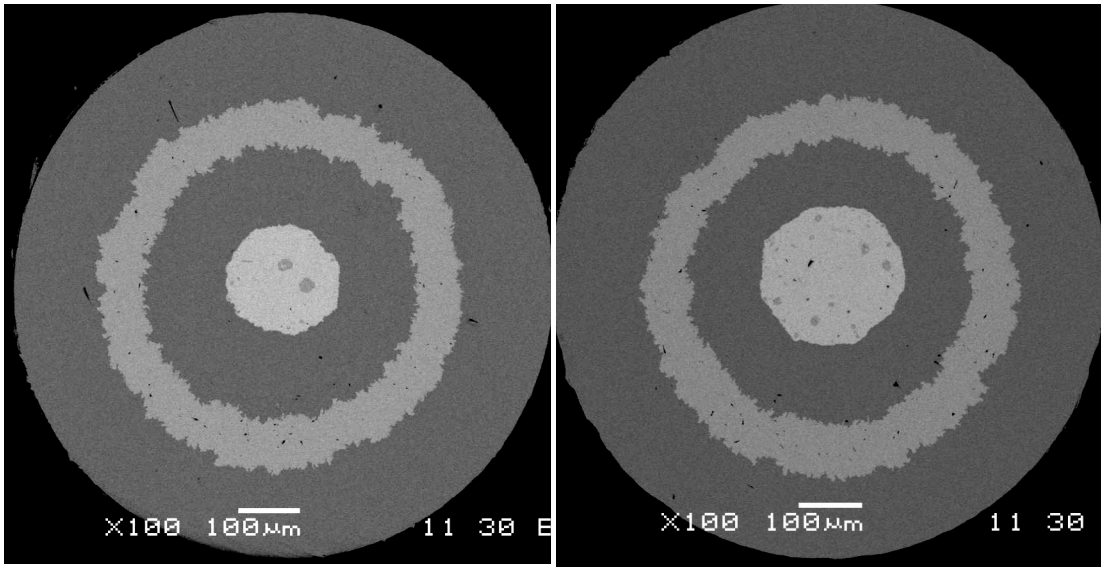

(a) SF1 (b) SF2

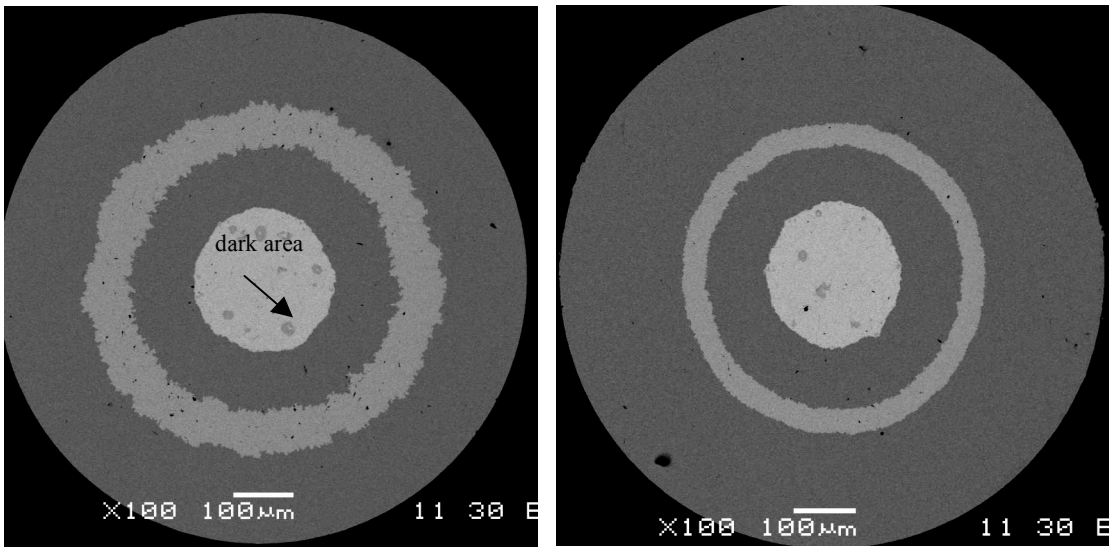

(c) SF3 (d) SF4

Fig.2-3 Cross section photographs of monoelement wires (a) SF1, (b) SF2, (c) SF3, (d) SF4

From Fig.2-3 one can also find some dark areas inside the Sn cores, which are Ti-enriched. By EDS analysis, the composition of the dark area is detected as 39.74at%Sn and 60.26at%Ti.

3. MAIN MEASUREMENT TECHNIQUES OF Nb_3Sn SUPERCONDUCTING WIRES

3.1 Neutron Diffraction Measurement Techniques

Neutron diffraction is a crystallography technique that uses neutrons to determine the atomic structure of a material.

Neutrons are particles found in the atomic nucleus. In a neutron reactor, neutrons can be set free when nuclei decay (fission, radioactivity). All quantum particles can exhibit wave phenomena we typically associate with light or sound. Diffusion is one of these phenomena; it occurs when waves encounter obstacles whose size is comparable with the wavelength. If the wavelength of a quantum particle is short enough, atoms or their nuclei can serve as diffusion obstacles. When neutrons from a reactor are slowed down and selected properly, their wavelength lies near one angstrom (0.1nanometer), the typical separation between atoms in a solid material.

Since neutrons are not charged, they do not interact with the neutron cloud surrounding the atom (unlike X-ray and electron diffraction; X-rays although not charged but do interact with electron cloud). The neutron nucleus will only interact with the nucleus of the atom. Thus neutron diffraction reveals the atomic structure, and not charge distribution around the atom. However, neutrons have a spin whose interaction with electron spins contribute to magnetic scattering. The structural details of a target material are measured by recording the way in which neutrons are deflected.

A neutron diffraction measurement requires a neutron source (e.g. a nuclear reactor or spallation source), a target (the material to be studied), and a detector. Other components may be needed to select the desired neutron wavelength. Some parts of the setup may also be movable. Fig.3-1 shows a schematic of the D1B diffractometer setup.

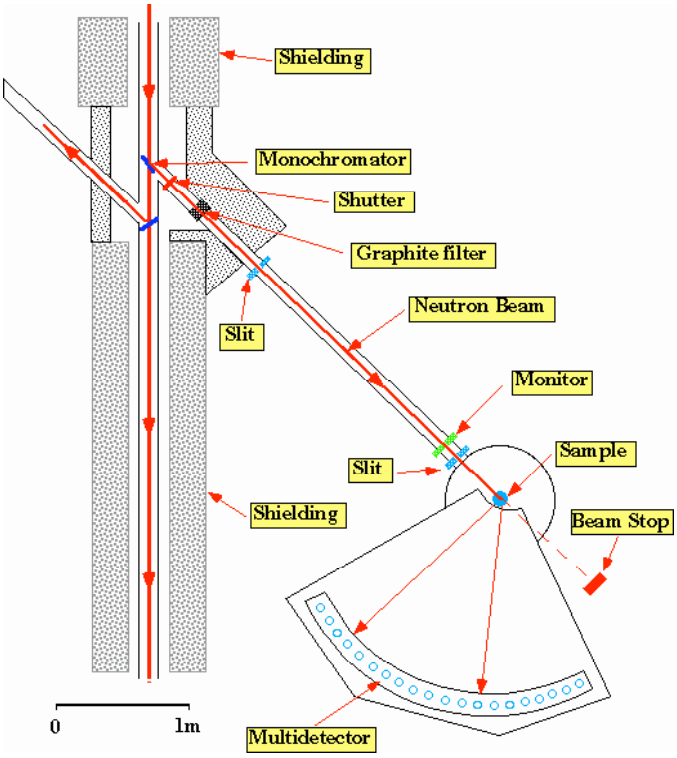

Fig.3-1 Schematic setup of the D1B diffractometer at Institut Laue-Langevin, Grenoble

As the selected neutrons can continuously interact with the target material, this setup can be used to record in-situ the reaction progress of the material. Fig.3-2 shows the in-situ measurement facility.

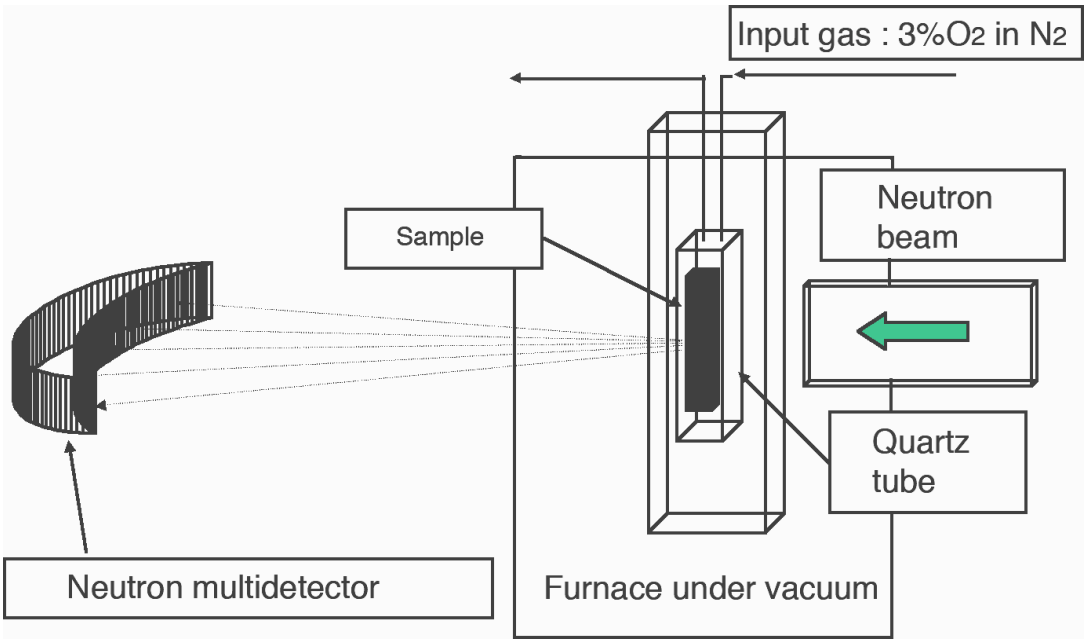

Fig.3-2 Schematic of the neutron diffraction in-situ system

There is a special furnace in the figure which can run heat-treating programs and the neutron detection at the same time. The furnace is under secondary vacuum in order to protect the heating elements. The sample is put into a quartz tube with a selected atmosphere as a function of the chosen process.

The neutron diffraction technique can also be applied to do off-situ measurements. In this situation, there is no such a special furnace, but heat-treated samples are fixed in the diffraction position for neutron detection.

3.2 Introduction to SQUID Magnetization Measurement

Magnetization is a conventional approach for measuring the superconducting properties of a material.

The principle of this SQUID magnetometer consists of measuring the change of the magnetic flux in a pick-up coil when the magnetized sample is moved throughout it [130]. The sample is mounted on the end of a sliding rod and a steady magnetic field of the required magnitude is applied by means of a superconducting coil in the liquid helium bath. The pick-up coil is configured as a second-order gradiometer (Fig.3-3(a)) and the magnetic flux versus the position of the sample is represented in Fig.3-3(b). This design minimizes background noises of the superconducting coil and the environment.

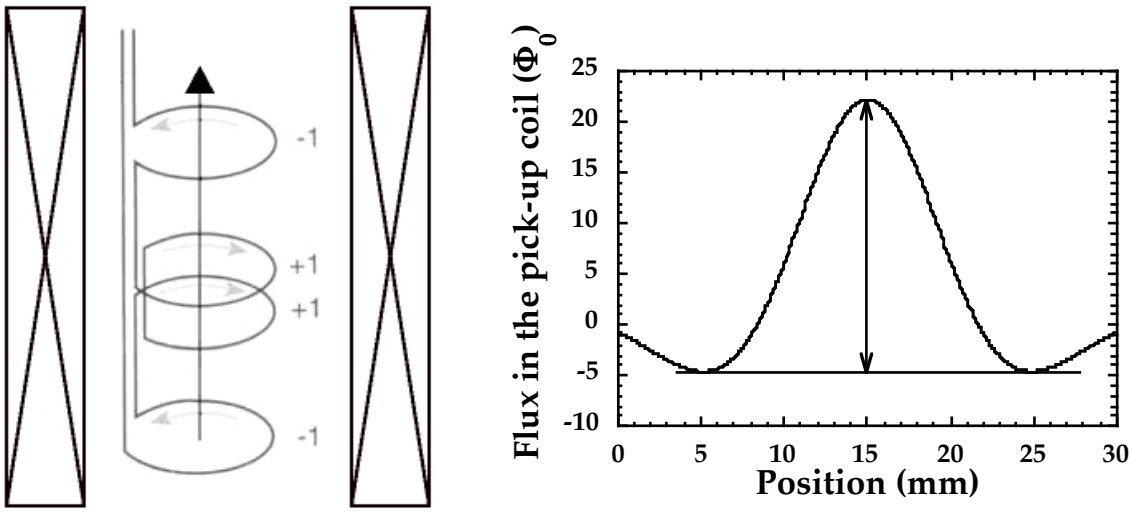

Fig 3-3 (a) Design of the pick-up coil with the superconducting coil and (b) magnetic flux in the coil versus the position of the sample.

The magnetic moment of the sample is proportional to the amplitude of the flux change, represented by the double arrow on figure 3-3(b). The pick-up coil is in a closed superconducting circuit constituting a flux transformer, which conveys the magnetic signal to a rf-SQUID connected to a control electronic and an integrator. The output voltage of this system is an image of the change of magnetic flux in the coil.

The sample moves in a tube (not represented here) with a helium gas flow whose temperature could vary between 1.7 K and 320 K. The applied magnetic field varies between 0 and 7.5 T. The sensitivity in magnetic moment is around 10^{-7} uem (10^{-10} SI) in low field and better than 10^{-5} uem (10^{-8} SI) in high field.

3.3 Description of Transport Critical Current Density Measurement

As a magnetic field is applied to a practical type-Ⅱ superconductor in mixed-state, there exist fluxons penetrating the superconductor. If a transport current, perpendicular to the field, flows through at the same time, a repulsive force (Lorentz force) F_L will act on the fluxons. The pinning centers formed by the defects in the superconductor will produce a pinning force F_P which has a orientation opposite to F_L. When the transport current is below a critical value, there is always a relation: $F_L \equiv F_P$, at which situation the conductor maintains resistanceless superconducting. While the transport current is above the critical one, the repulsive Lorentz force will be exceeded the flux pinning force, $F_L > F_P$. At this time the fluxons will be repulsed to move, leading to electric resistance appeared in the conductor and the loss of superconductivity. This critical value is called transport critical current (I_C).

The transport critical current I_C is usually measured through the standard 4-probe technique in a liquid helium bath, in which the I-V variation is recorded, as shown in Fig.3-4. The current value at which a definite electric field E_0 develops in the sample measurement is defined as I_C. The voltage between the two voltage leads is then expressed as $V_0 = LE_0$, in which L is the dimension of the two leads. V_0 and E_0 are usually named the voltage criterion and the electric field criterion respectively.

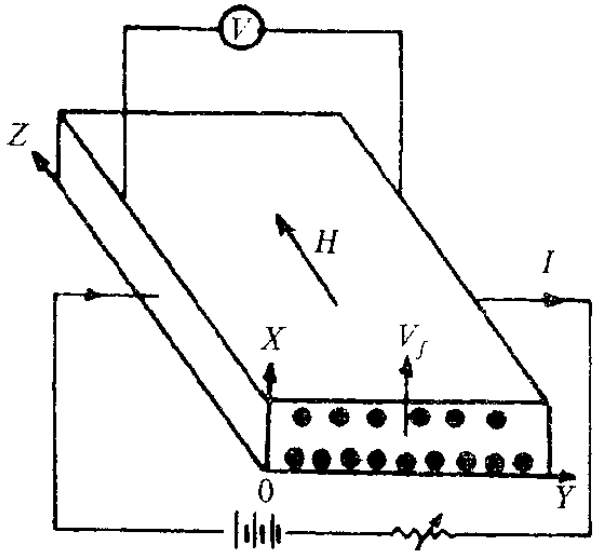

Fig.3-4 Schematic principle for the measurement of transport critical current

All I_C measurements in this study were carried out in LCMI/CNRS. The measurement facility can be schematically described in Fig.3-5.

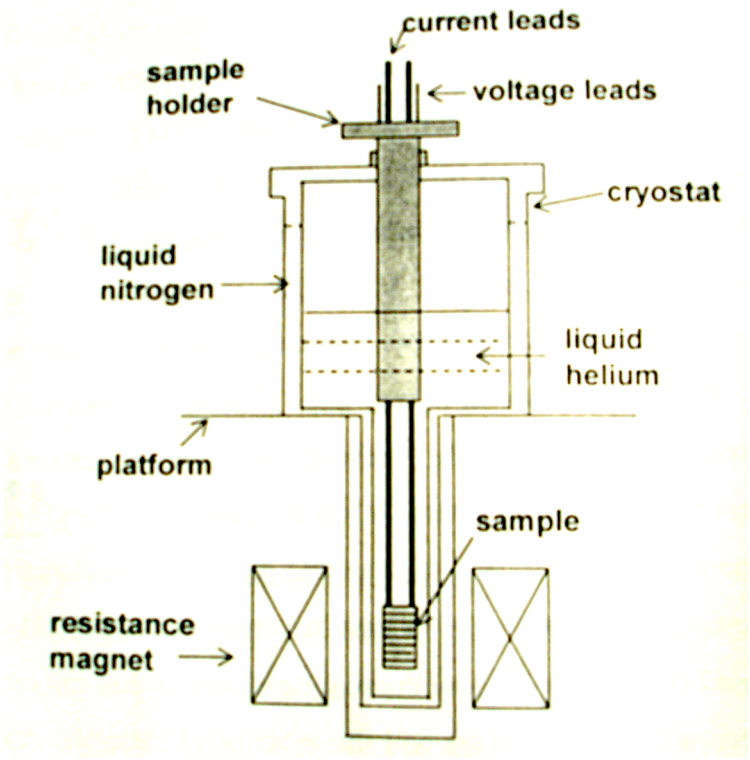

Fig.3-5 Illustration of the facility for transport critical current measurement

This facility can be divided into two systems: one includes the cryostat and magnet, the

other is the measurement device. The cryostat includes two parts, inside liquid helium and outside liquid nitrogen. There is enough liquid helium filled in the helium room for the sample to be immersed in, keeping 4.2K of testing temperature. The liquid nitrogen is used for helium protection. The magnet used is made of conventional resistance solenoid with the maximum field of 22T. The measurement system includes sample and its holder, 4-probe current leads and voltage leads, and the testing signal control system.

The sample is fixed on the sample holder with current leads and voltage leads soldered on it and then put inside the cryostat and fully immersed in the liquid helium. The current leads are connected to power supply system and the voltage leads to the signal control system. The capacity of the power supply is 1200A. During examination current ramping and cutting off are controlled with a computer and the voltage-current (V-I) curves are recorded automatically.

3.4 Microstructure Observation and Analysis Method

Microstructure examination is very necessary for property analysis of a superconducting wire. In this study all SEM observation and EDS analysis were carried out with two electronic microscopes, one is the model JEOL A840 in Crystallographe/CNRS, and the other is the model JSM 6460 in NIN. The SEM system has four imaging modes. Conventional secondary electron (SE2) is most sensitive to topography; in-lens secondary electron (SEI) has the highest resolution and sensitive to both topography and atomic number; backscattered electron image (BEI) is most sensitive to atomic number, and spectral imaging (SI) uses energy dispersive X-ray to produce compositional mapping.

In this study the LEO-1530 Field Emission Scanning Electronic Microscope (FESEM) in NIN was also used for grain size and crystalline morphology analysis. This FESEM has very high spatial resolution, capable of ~4nm, and is good enough for more detailed crystalline microstructure observation.

4. SUPERCONDUCTIVITY OPTIMIZATION, MICRO-STRUCTURE ANALYSIS AND PHASE FORMATION KINETICS OF INTERNAL-Sn MULTIFILAMENT WIRES

4.1 Heat Treatment for MF wires

Except for the samples used for transport critical current measurement of long length wires which will be specifically dealt within section 4.2.2, the two ITER-type MF wires of Alstom (AST) and NIN were cut into ~7cm length pieces, whose ends were crimped over 3mm to avoid Sn leakage. Each of the pieces was sealed in an evacuated quartz tube with ~4Pa of Ar. All samples underwent a 210°C/50hr + 340°C/25hr thermal treatment in horizontal tubular furnaces for Cu-Sn alloying prior to the A15 phase formation heat treatment. The ramp rate was 60 ºC/hr. Experiments at 650ºC, 675ºC, 700ºC and 725ºC were chosen to study the temperature influence on Nb-Sn A15 phase formation, and various durations at every temperature were used to show the effect of HT time. All the HT programs have been carried out in CRETA /CNRS and the detailed HT conditions were the followings:

$$210°C/50hr + 340°C/25hr \rightarrow \begin{cases} 650°C, 2hr, 8hr, 32hr, 74hr, 128hr, 200hr; \\ 675°C, 2hr, 8hr, 32hr, 74hr, 98hr, 128hr, 200hr; \\ 700°C, 2hr, 8hr, 32hr, 74hr, 98hr, 128hr, 200hr; \\ 725°C, 2hr, 4hr, 8hr, 32hr, 74hr, 98hr, 128hr, 200hr. \end{cases}$$

As 600°C is considered to be the practical lower temperature bound for Nb-Sn formation [82], a two-step HT procedure was introduced in the sample preparation. The samples were specially organized to be held at 600°C for 202hrs and then followed by the HT procedure at 650°C. That is, (210°C/50hr + 340°C/25hr)→600°C/202hrs→(650°C, 2hr, 8hr, 32hr, 74hr, 128hr, 200hr). The two-step heat-treated samples were used to compare with the ones heat-treated only at 650°C (one-step), i.e. (210°C/50hr + 340°C/25hr)→(650°C, 2hr, 8hr, 32hr, 74hr, 128hr, 200hr).

Totally, 70 samples were prepared, half for AST and half for NIN.

4.2 Transport Critical Current Density Investigation

4.2.1 Introduction

Non-Cu critical current density J_C (non-Cu J_C or $J_{C\text{-non Cu}}$) is one of the most important properties for Nb_3Sn superconducting wire. Nb_3Sn researchers and wire suppliers are usually much concerned about the non-Cu J_C value, of which the ITER project has also given a strict standard for measurement [137]. The sample preparation and the J_C examination in this thesis are in accordance with the ITER's requirements.

The critical current of a MF wire is often measured through the transport current method whose principle has been schematically described in section 3.3. For Nb_3Sn superconductors one usually takes the critical current values as a function of the applied magnetic field at 4.2K (liquid helium temperature), of which the value at 4.2K, 12T is the most significant. The non-Cu J_C is defined by the normalization of the critical current (I_C) to the cross-section area excluding that of stabilizing Cu. The I_C values can be compared for the same kind of wires as they have the same non-Cu areas; for different wires the non-Cu J_C values are the only way for superconducting performance comparison.

In magnet fabrication, it is necessary to have the data for engineering critical current density J_E which is the normalized I_C divided by the entire cross-section area of the wire. J_E can be used to calculate the wire quantity needed in the engineering. The J_E values of the two ITER-type wires at 4.2K, 12T were also obtained in this chapter.

There are a few factors to affect the critical current density in wire design, fabrication and heat treatment. For wire design, the factors include Nb/Sn/Cu ratio, the non-Cu area and the third alloying element addition; for wire fabrication, long length homogeneity, strain state etc.; and for the HT of phase formation, the reaction temperature and time. Combining all these factors, the main purpose of our J_C measurements is to optimize the heat treatment and to find the best solution for wire design and manufacturing.

According to ITER's standard of J_C measurement, the sample preparation and heat treatment are rather strict and complicated. The wire should be wound on a specific alloy

holder and kept in a vacuum furnace to react for a long time. This is really very necessary for the J_C determination of commercial wires. However, if we need to investigate the phase formation progress of the wire, many samples should be prepared and examined. The samples should be taken out of the furnace from time to time. This is very difficult and time-and-labour consuming. Therefore, in this study several wind-on-holder coil samples were prepared for quantitatively investigating the J_C of the commercial wires, but the short length samples prepared in section 4.1 were used to study the I_C variation with the HT conditions. It should be pointed out that the I_C results of short samples can only be used for qualitative comparison because they are not the values determined by standard method.

4.2.2 Experimental Process

4.2.2.1 Sample Preparation

(1) Wind-on-holder coil sample preparation

In accordance with ITER's requirement, the standard sample holder consists of a threaded hollow cylinder of Ti6Al4V with two copper rings (~5mm height) attached for current contact. The material of the holder is selected because of the coefficient of thermal expansion matching the one of the Nb_3Sn strand, and because of the high resistivity at cryogenic temperature (~$1.4 \cdot 10^{-6}\Omega$m). The size of the Ti6Al4V hollow cylinder is: overall height, 35mm; outer diameter, 32m; inner diameter, 28mm; thread, 90º V-shape groove, 8 turns/inch, 1mm deep. A graphite coating is sprayed on the Ti6Al4V grooved surface before the holder is put inside of a vacuum furnace (~4Pa) and held at 700°C for 10hrs, aiming to prevent sticking of the strand to the sample holder. The wire is then wound on the graphite-coating groove surface prior to heat treatment in a tubular furnace.

The HT procedure in this thesis is the following. The coil sample was set inside the tubular furnace which was then empted to ~4Pa with a diffusion pump. A small amount of Ar was leaded through the furnace, keeping the pressure inside ~6Pa during the whole heat treatment. Each sample underwent a 210°C/50hr + 340°C/25hr thermal treatment for Cu-Sn alloying, which is the same as the ITER's recommendation, prior to the HT of A15 phase formation. The ramp rate for heating up was 60°C/hr. The reaction temperatures of 650ºC, 675ºC, 700ºC and 725ºC were chosen for AST wire samples, and 650ºC, 675ºC and 700ºC

were used for NIN ones. After 128hr duration the samples were cooled down at a rate of 100°C/hr.

(2) Short length sample preparation

All short length samples were prepared and heat-treated as the procedure in section 4.1.

4.2.2.2 Transport Critical Current Measurement

(1) Wind-on-holder coil sample measurement

The heat-treated coil sample was mounted on the testing support cane with its axis parallel to the applied field. The attached brass ends of the sample holder were soldered to the current leads of the support with the braided tapes. The voltage sensing wires on the testing sample support were soldered to the sample at the intervals of ~500mm (5 turns) and 100mm (1 turn). Two additional varnished Cu wires were also wound and soldered to the voltage taps with the winding direction identical to that of the helical superconducting wire in order to produce an inductive anti-wise electric field to reduce noise. The strand is eventually bounded to the sample holder by a thin layer of grease; in this way, the direction of the electromagnetic load during testing (tension or compression) plays no longer a role.

Afterwards, the coil sample was put inside the cryostat, immersing it in the liquid helium bath. The current leads and voltage leads were connected before testing. During transport current measurement, the voltage-current curves were recorded automatically and the applied field varied in the range of 6~17T. The criterion of 0.1μv/cm was used to determine the value of critical current I_C which was then divided by the non-Cu area of the wire cross section to obtain the non-Cu J_C. The non-Cu J_C was then depicted as a function of the applied field (B). The non-Cu area is calculated like this: evenly measuring 8 outer diameters (OD) and 8 non-Cu diameters of the wire from its magnified SEM photographs, averaging the data and then obtaining the magnified average OD (D_b) and average non-Cu diameter (D_{nb}). As the real wire OD (D_a) is known, the real wire non-Cu diameter (D_{na}) is then calculated:

$$D_{na}= D_{nb}\times D_a/ D_b \qquad (4\text{-}1)$$

From (4-1) the non-Cu area (A_n) of the real wire is obtained:

$$A_n=\pi(D_{na}/2)^2 \qquad (4\text{-}2)$$

According to the relation $F_P=J_C\times B$, the flux pinning force variation with the applied field

can also be depicted from the non-Cu J_C values. In addition, if we plot $J_C^{1/2} \times B^{1/4}$ versus B and use Krammer linear fit, extrapolating it to J_C=0, the irreversibility field H* of the sample can thus be determined. Fig.4-1 is an example of the Krammer extrapolation for AST sample heat-treated at 700ºC/128hr.

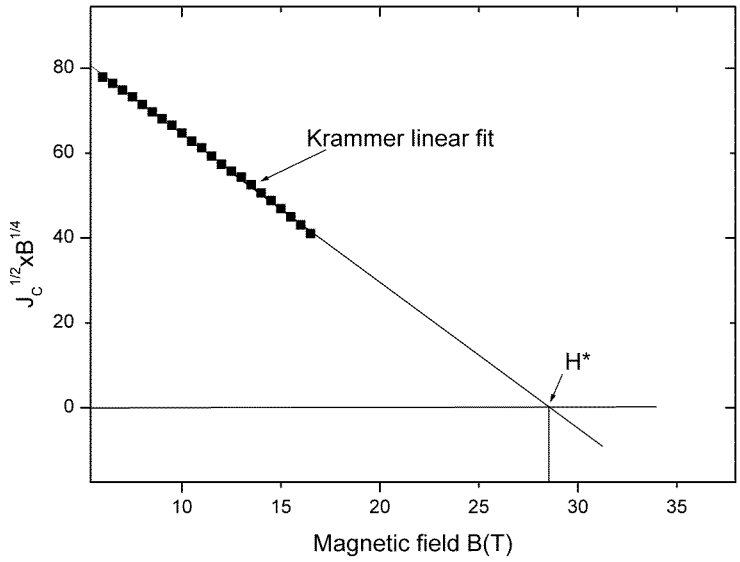

Fig.4-1 Irreversibility field H* derived from Krammer extrapolation for AST sample heat-treated at 700ºC/128hr.

(2) Short length sample measurement

The heat-treated short length sample was cut into a ~30mm piece in its middle part, ensuring the sample homogeneity. The piece sample was then mounted on the sample support cane with its axis perpendicular to the applied field. Solder the current leads and voltage leads, keeping the division between the two voltage leads 5mm long, and put the sample inside the cryostat full of liquid helium, afterwards.

The testing procedure for short sample is identical to that for coil sample. It should be pointed out that the obtained I_C values for short sample are eventually lower than those of normal measurement because of two reasons. One is that the interval between two voltage leads is too short and the voltage-current (V-I) curve may have a big noise interference. The other is that the short sample has not been fixed on the testing support as well as the wind-on-holder coil sample, so a possible sample movement and deformation may take place at higher current. However, the short sample measurements are enough to qualitatively show

the J_C variation with HT temperature and time. Therefore, in this experiment, a criterion of 1μv/cm was adopted to determine I_C values of short sample. The testing magnetic field was in the range of 2~20T.

4.2.3 Results and Analysis

4.2.3.1 Wind-on-holder coil samples

4.2.3.1.1 *Critical current density J_C*

(1) NIN wire

Three NIN coil samples heat-treated at three different conditions were measured for the critical current I_C at two voltage intervals (100mm and 500mm) respectively. Non-Cu J_C is obtained with the I_C value divided by the non-Cu area of NIN wire which is calculated as 0.251mm^2. The non-Cu J_C is depicted as a function of the applied field B, as shown in Fig.4-2.

From 4-2(a) figure it can be seen that NIN wire has reached a rather high non-Cu J_C at the reaction temperature of 650ºC; the non-Cu J_C-B curve moves upwards from 650ºC to 675ºC and reaches the highest position at 675ºC; at 700ºC, the curve lowers down largely.

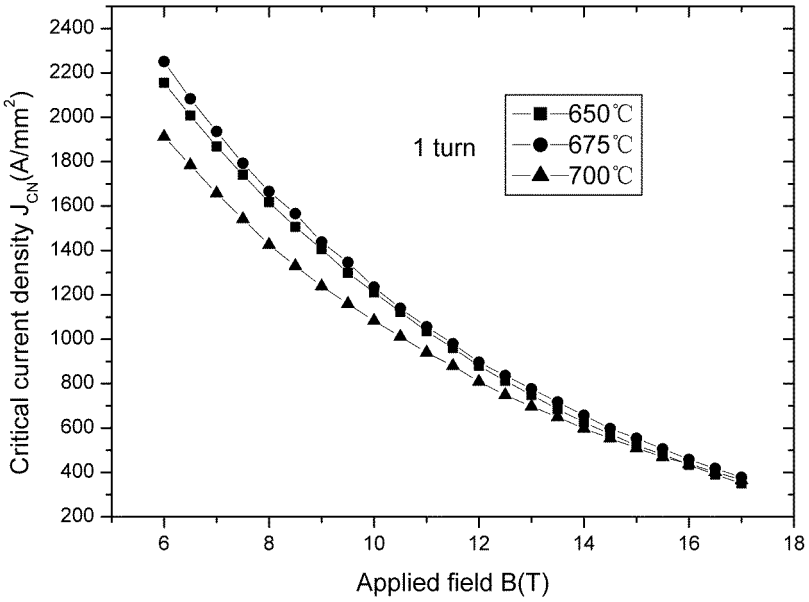

(a) 100mm voltage interval

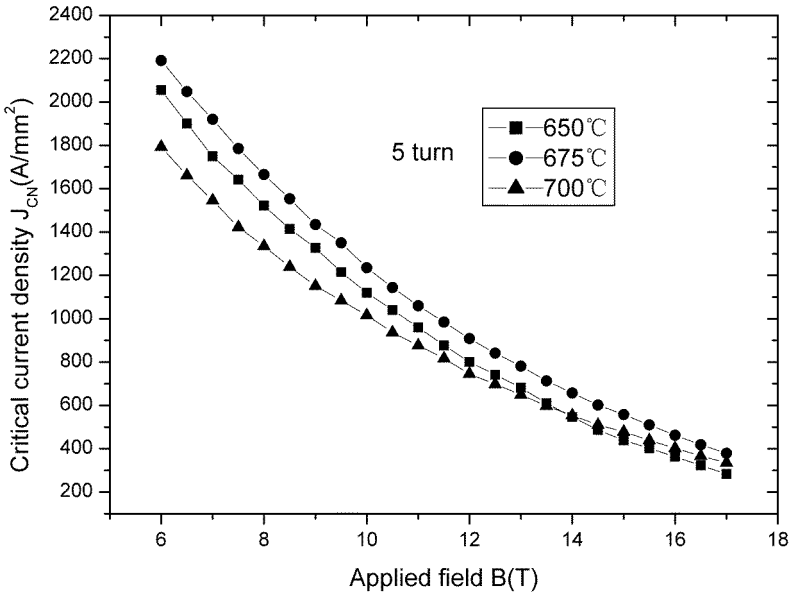

(b) 500mm voltage interval

Fig.4-2 Non-Cu J_C as a function of field B for NIN samples heat-treated at different temperatures

From 4-2(b) figure it is seen that the non-Cu J_C-B curves of 675ºC and 700ºC samples have very small difference between 500mm intervals and 100mm intervals, but the 650ºC curve has a clear shift-down. This can be clearly seen in Fig.4-3 in which the non-Cu J_C versus B at the two intervals are depicted.

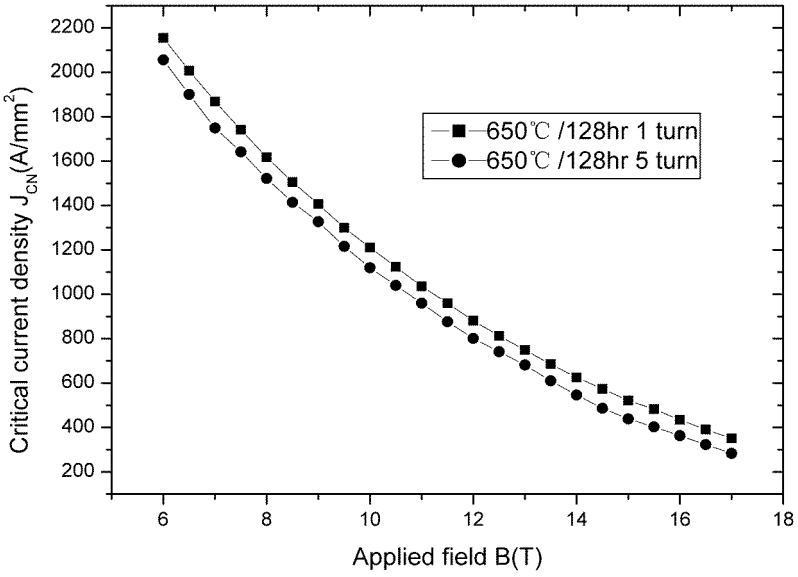

Fig.4-3 Non-Cu J_C curves at the two voltage intervals for NIN sample heat-treated at 650ºC/128hr

The results indicate that the 650ºC/128hr sample of NIN wire seems to have the A15

phase not uniformly distributed along the length of the wire, which leads to the decrease of the superconducting performance for long length wire.

(2) AST wire

Four AST coil samples heat-treated at four different conditions were measured for the critical current I_C at two voltage intervals (100mm and 500mm) respectively. Non-Cu J_C is obtained with the I_C value divided by the non-Cu area of AST wire which is calculated as 0.222 mm^2. The non-Cu J_C is depicted as a function of the applied field B, as shown in Fig.4-4.

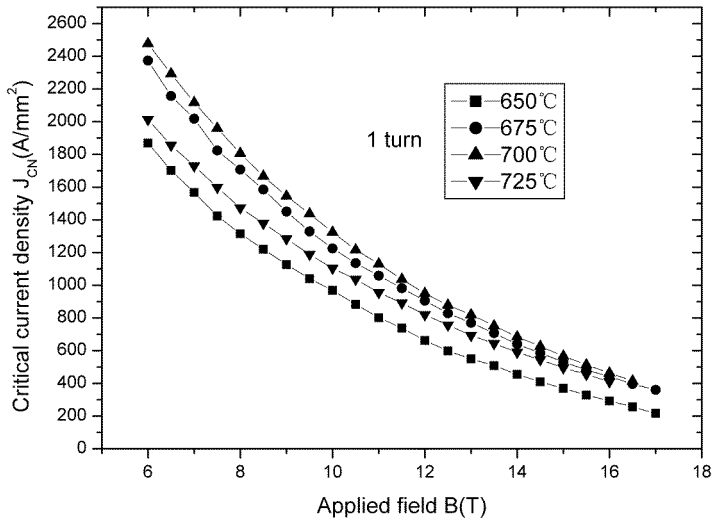

(a) 100mm voltage interval

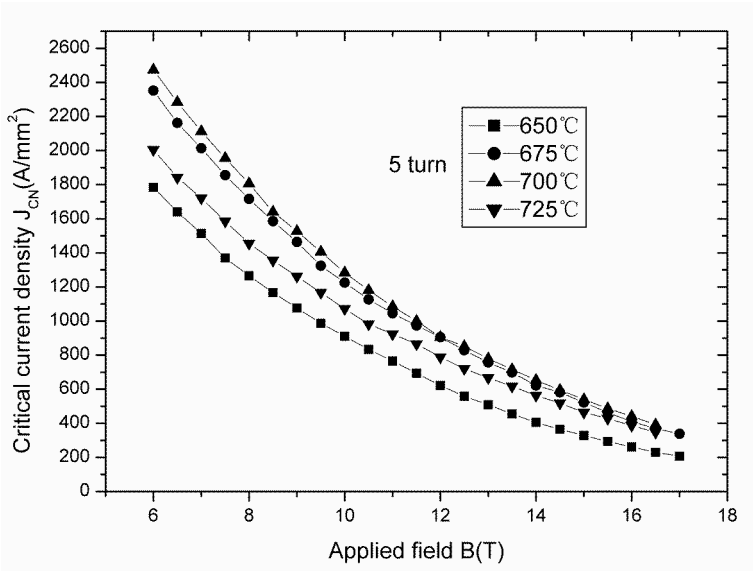

(b) 500mm voltage interval

Fig.4-4 Non-Cu J_C as a function of field B for AST samples heat-treated at different temperatures

From 4-4(a) and (b) figures it can be seen that AST wire has a rather lower non-Cu J_C at the reaction temperature of 650ºC; the non-Cu J_C-B curve moves largely upwards from 650ºC to 675ºC, and moves up a little, reaching the highest position at 700ºC; similarly, the curve lowers down largely at 725ºC.

Also from these figures it is noted that the non-Cu J_C-B curves of AST samples have little differences between the two voltage intervals, but a visible decrease can still be found with the 650ºC/128hr sample at 500mm intervals, as shown in Fig.4-5.

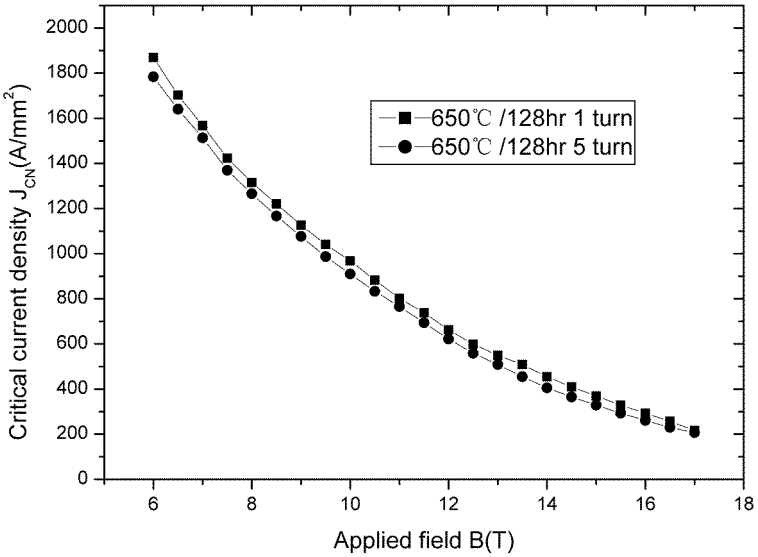

Fig.4-5 Non-Cu J_C curves at the two voltage intervals for AST sample heat-treated at 650ºC/128hr

This result also indicates a little inhomogeneity along the length of AST wire.

(3) Non-Cu J_C and J_E at 4.2K, 12T

The most significant values are those measured at 4.2K, 12T and with the criterion of 0.1μv/cm. For the special requirement, the non-Cu J_C and engineering critical current J_E have been obtained at the condition of 4.2K, 12T, 0.1μv/cm, as exhibited in table 4-1.

Table 4-1 Non-Cu J_C and J_E values (A/mm^2) for all coil samples measured at 4.2K, 12T, 0.1μv/cm

Sample	Heat treatment	100mm interval		500mm interval	
		non-Cu J_C	J_E	non-Cu J_C	J_E
NIN	650°C/128hr	880	451	801	410
	675°C/128hr	897	460	909	466
	700°C/128hr	809	415	746	382
AST	650°C/128hr	662	275	622	258
	675°C/128hr	937	389	924	384
	700°C/128hr	950	395	905	376
	725°C/128hr	809	336	789	328

From table 4-1 it is found that the non-Cu J_C (4.2K, 12T) of NIN wire has a very high value at 650ºC/128hr, and reaches the highest at 675ºC, but a big decrease happened at 700ºC. However, AST wire approaches very high non-Cu J_C at 675ºC/128hr and the highest at 700ºC, but an obvious decrease appeared at 725ºC. That is to say, the AST wire needs to react at higher temperature than that of the NIN wire. Comparing the non-Cu J_C and J_E of the two wires, it can be found that the highest non-Cu J_C value of AST wire is even larger than that of NIN wire, although the former has obtained the J_E values widely lower than those of the later. The reason is that the AST wire has a larger wire OD but a smaller non-Cu area. In other words, smaller non-Cu area enlarges the non-Cu J_C, but larger wire OD lowers the J_E.

4.2.3.1.2 *Flux pinning force*

(1) NIN wire

The values of flux pinning force F_P calculated from $J_C \times B$ are plotted as a function of the applied field. The results of three NIN coil samples are shown in Fig.4-6.

From 4-6(a) figure it can be seen that the NIN wire has achieved a rather high F_P-B curve at 650ºC; from 650ºC to 675ºC, the F_P-B curve shifts upwards a little; at 700ºC, the curve moves down largely at lower fields, but even elevates at higher fields. Figure 4-6(b) shows the F_P-B curves of 500 mm intervals similar to the curves of 100 mm intervals, but a little lower down for the 650ºC/128hr sample, indicating an inhomogenous flux pinning

situation along the wire.

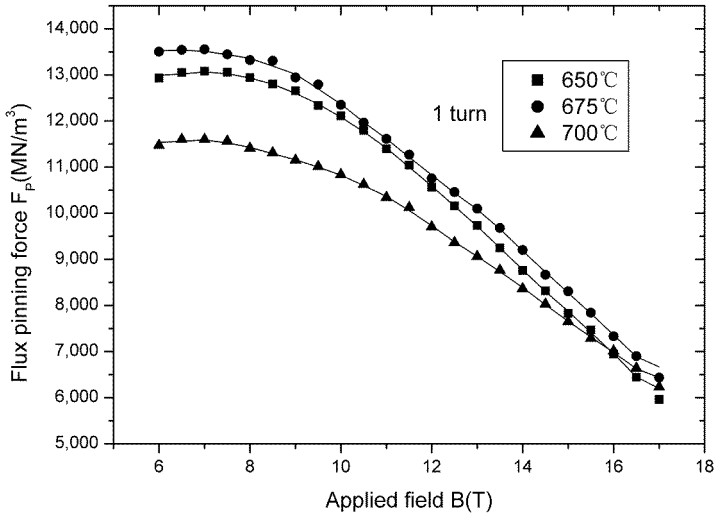

(a) 100mm interval

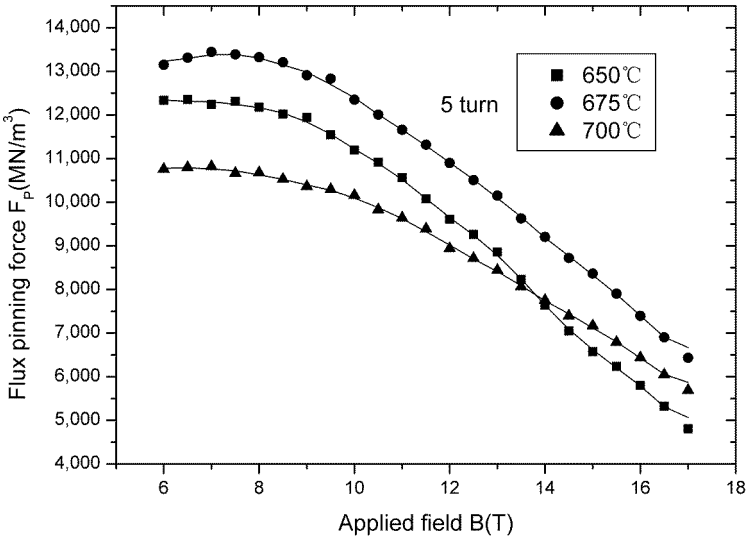

(b) 500mm interval

Fig.4-6 F_P-B curves of three NIN coil samples

Also from Fig.4-6 one can find the positions of the maximum flux pinning. It is obvious that the three coil samples achieve the maximum flux pinning at nearly the same field of 7T.

(2) AST wire

The F_P-B results of four AST coil samples are shown in Fig.4-7.

From Fig.4-7 (a) and (b) it can be found that the AST wire has a rather lower F_P-B curve at 650ºC; the F_P-B curve shifts upwards largely when the temperature increases to 675ºC and a little further upwards at 700C; similarly, at 725ºC the F_P-B curve lowers down largely at lower fields, but rather less at higher fields.

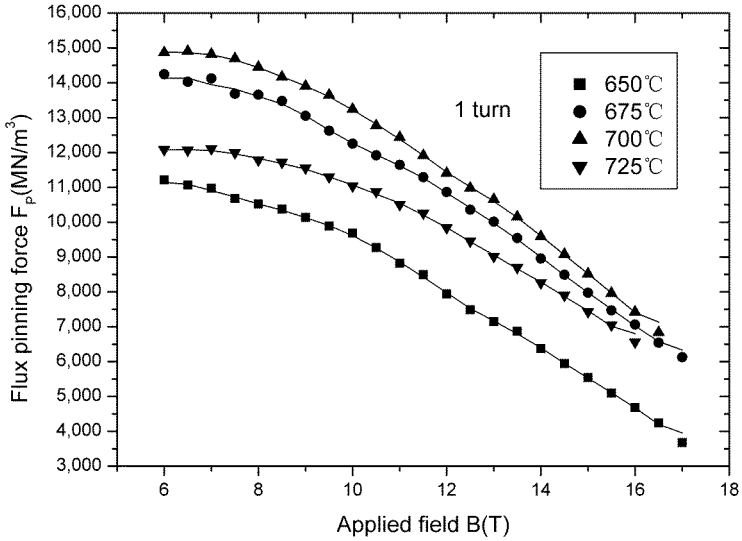

(a) 100mm interval

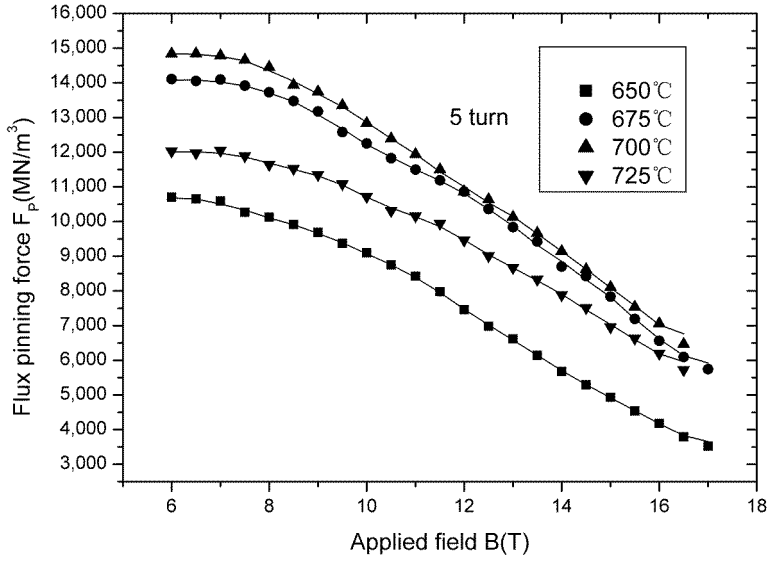

(b) 500mm interval

Fig.4-7 F_P-B curves of four AST coil samples

Also from Fig.4-7, it is obvious that the four AST coil samples achieve the maximum flux pinning at nearly the same field of 7T.

4.2.3.1.3 *Irreversibility field H**

By plotting $J_C^{1/2}\times B^{1/4}$ versus B and using Krammer linear fit, extrapolating it to J_C=0, we can determine the H* values of all AST and NIN coil samples measured at two voltage leads intervals. The obtained results are included in table 4-2.

Table 4-2 Irreversibility field H* (T) of all AST and NIN coil samples

Coil sample	Heat treatment	100mm interval	500mm interval
NIN	650ºC/128hr	28.6	27.6
	675ºC/128hr	28.9	28.8
	700ºC/128hr	29.9	29.8
AST	650ºC/128hr	26.1	25.5
	675ºC/128hr	27.7	28.0
	700ºC/128hr	28.3	27.3
	725ºC/128hr	29.1	28.7

From table 4-2 one can find that the two wires heat-treated at different conditions have very high irreversibility field H* and all the H* values have small differences, except of a little lower H* of the AST 650ºC/128hr sample. One can also find that the H* has a small increase when the HT temperature is increased, even though the non-Cu J_C may be lowered down.

4.2.3.2 Short length samples

The short length samples are primarily used to identify the HT time effect on the transport critical current versus magnetic field. For this purpose, the samples heat-treated at 675ºC and 700ºC for different durations were selected to do the examination. As it is only a qualitative analysis, the I_C-B, not non-Cu J_C-B, was used for the investigation.

(1) AST wire

The transport critical current I_C as a function of the applied field B (I_C-B) curves for AST samples heat-treated at 675ºC and 700ºC for different times were plotted in Fig.4-8 (a) and (b).

Fig.4-8 (a) and (b) show that the I_C-B plots of AST samples shift upwards with the reaction time elongation from 8hrs to 128hrs for both temperatures of 675ºC and 700ºC. Over reaction (200hrs) makes the I_C-B plots lowering down, more sharply at lower fields.

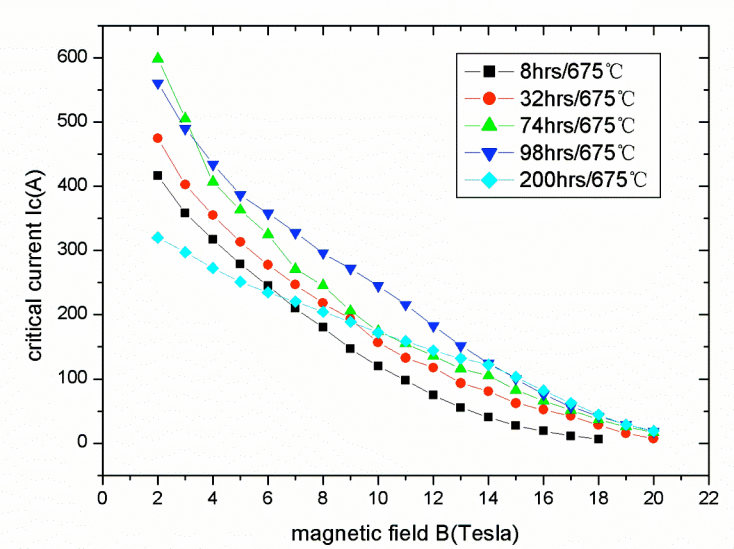

(a) 675ºC

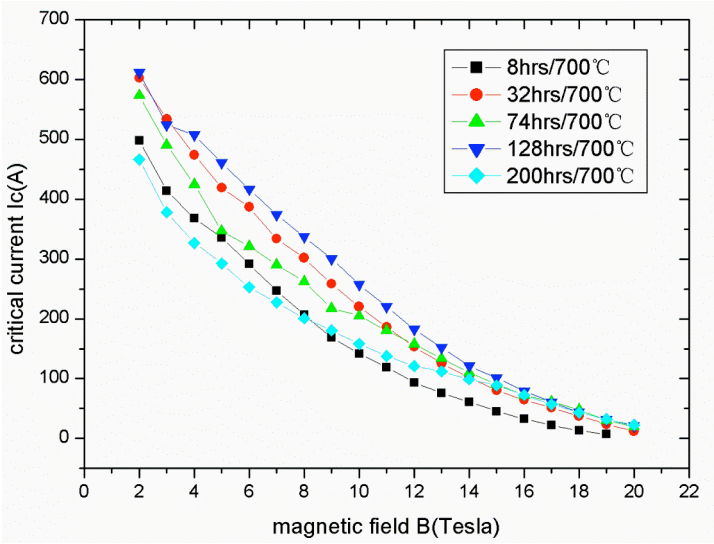

(b) 700ºC

Fig.4-8 I_C-B plots for AST short length samples

(2) NIN wire

The transport critical current I_C as a function of the applied field B (I_C-B) curves for NIN samples heat-treated at 675ºC and 700ºC for different durations were plotted in Fig.4-9 (a) and (b).

Fig.4-9 (a) and (b) also show that the I_C-B plots variation of NIN samples is similar to that of AST samples. That is, the I_C-B plots shift upwards with the reaction time increase from 8hrs to 128hrs for both temperatures of 675ºC and 700ºC. Over reaction (>128hrs) makes no benefit to I_C, especially at lower fields.

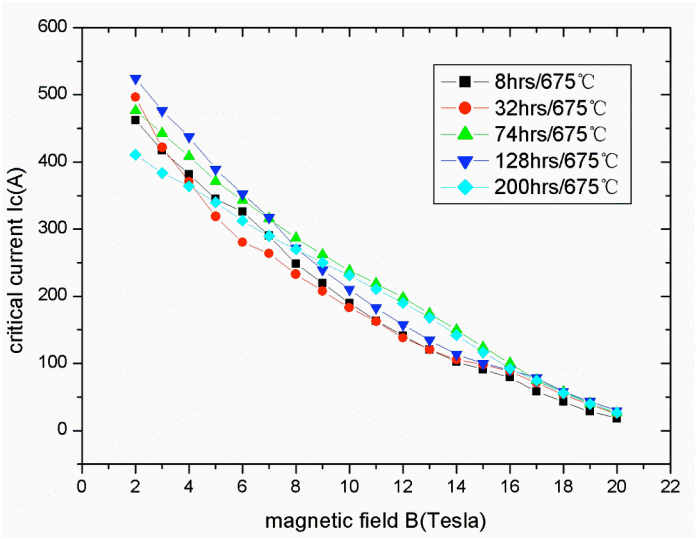

(a) 675ºC

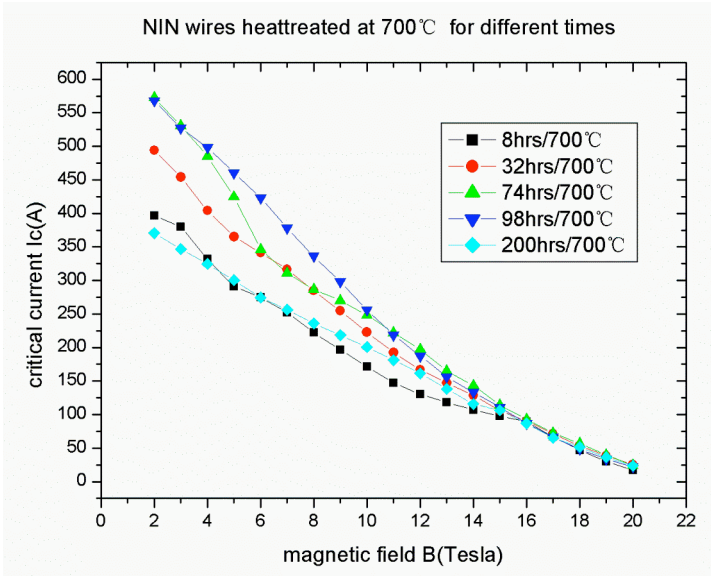

(b) 700ºC

Fig.4-9 I_C-B plots for NIN short length samples

4.2.4 Discussion

For a specifically designed Nb_3Sn wire, the primary factors affecting the critical current density are the heat treatment, including reaction temperature and time.

In the first place, the HT temperature is concerned. At lower reaction temperature the formed A15 phase has a small grain dimension and a large boundary area, resulting in a stronger flux pinning force, which is beneficial to the promotion of J_C. However, lower temperature retards the Sn diffusion and reaction rate, which not only elongates the reaction

progress but also makes the A15 layer hard to be homogenous. Obviously, this is detrimental to the increase of J_C, and even leads to J_C decrease. As an example, the AST coil sample of 650ºC/128hr treatment has a lower non-Cu J_C for the reason of lower reaction temperature. On the other hand, higher temperature accelerates the Sn diffusion and reaction rate and also promotes the compositional homogeneity of the A15 phase, which is beneficial to the increase of J_C. Whereas, higher temperature coarsens the grain size of the A15 phase and to some extent may decrease the flux pinning force and then may reduce the J_C. Also illustrated in J_C-B measurement, the NIN coil sample of 700ºC/128hr and the AST coil sample of 725ºC/128hr have a lower non-Cu J_C due to the higher reaction temperature. From the above analysis we can see that for maximizing the critical current density of Nb_3Sn wire one should choose the most suitable reaction temperature to balance the increase of reaction rate and the promotion of flux pinning force.

From the results of coil sample measurement it can be found that the component configuration of a wire is also very important for HT temperature selection. We know that NIN wire has 2wt%Ti alloyed in its Sn core, which has been already confirmed to increase the Sn diffusion rate, decrease the reaction temperature and thus promote the A15 phase formation. In this case, the NIN wire is suitable to be heat-treated at lower temperature. On the contrary, the AST wire needs to choose a relatively higher temperature for heat treatment because of no third-element Ti addition in Sn core. The coil sample measurements have confirmed (see Fig.4-2 to Fig.4-7) that the most favorable choice are the reaction temperature ranges of 650ºC-675ºC for NIN wire and 675ºC-700ºC for AST wire, which produce the best non-Cu J_C.

In the second place, the HT time is concerned. At the early stage of reaction progress, there develops an A15 layer on the filament outside of the wire, which has a gradient Sn distribution in its composition. Because the A15 layer is thin and has a smaller Sn concentration, the transport critical current I_C is certainly lowered. With the elongation of duration, the A15 layer becomes thicker and thicker, with its composition being gradually homogenous. So, the I_C will be increased. This is the situation of the two wire samples before 128hr heat treatment (see section 4.2.3.2). Until the filaments react through and the A15 composition becomes uniform, the I_C value will be mainly dependent on the flux pinning

situation in the A15 phase. Over duration makes grain size much coarser, which reduces the grain boundary area and then the flux pinning force, leading to the decrease of I_C. It is thus clear that the samples of the two wires heat-treated as long as 200hrs have lower I_C values.

Thirdly, the non-Cu J_C at 4.2K, 12T is discussed. From table 4-1 it is noted that the best non-Cu J_C (4.2K, 12T) for the two wires nearly has the same value. The only difference is that the AST wire gives better values at higher temperature than the NIN wire does. It seems that the magnitude of non-Cu J_C of Nb_3Sn wire is essentially dependent on the wire design, i.e. Nb/Sn/Cu ratio. In other words, if the Nb/Sn/Cu ratio of a wire is determined, its best non-Cu J_C can be estimated and achieved through a suitable heat treatment. Furthermore, the fact that the two wires have nearly the same value of non-Cu J_C also indicates that the third-element alloying only promotes the phase formation rate and progress, but has no effect on the best magnitude of non-Cu J_C.

Finally, the irreversibility field H* is discussed. From table 4-2 it can be found that the H* values of NIN 700ºC/128hr sample and AST 725ºC/128hr sample are increased although their non-Cu J_C is decreased. This is because the J_C-B curves of the two samples have a very large decrease at lower field, but very small and even no decrease at higher field, leading to the Krammer linear extrapolation having the increased values. From this view point it is certain that the non-Cu J_C of Nb_3Sn wire is mainly dependent on its flux pinning situation of A15 phase at lower field. If its flux pinning force F_P is high, the low-field non-Cu J_C will be increased. Contrarily, if F_P is weak the wire will have a decreased low-field non-Cu J_C. On the other hand, at higher field the non-Cu J_C should be primarily determined by the values of irreversibility field H*. In other words, if the wire H* is higher its high-field non-Cu J_C should have a higher value. Based on the above analysis, one should also consider the wire application ahead of heat treatment. If the wire is used at low-field, the flux pinning enhancement is important and if it is for high-field application, the H* promotion is more significant. For Nb_3Sn wire, the 12T field is in the middle position and one should balance the flux pinning and the irreversibility field.

It is known that the upper critical field H_{C2} of a superconductor is an intrinsic property and is dependent on its phase composition. The H_{C2} is defined by the last remnant of superconducting diamagnetism and reflects the strongest link of the wire. It means that the

H_{C2} may be the same even if the wire is not longitudinally uniform. However, the distinction between H* and H_{C2} is often ignored. $H^*_{Krammer}$ is defined by measurement of the highest field of long-range connectivity along the filament axis. If long-range compositional uniformity is lacking, dissipation first sets in at locations that can be considered the weakest links and $H^*_{Krammer}$ is actually the measure of such weak links. Therefore, the more uniform is along the wire length, the more beneficial to the increase of H*. The ideal situation is the H* having the same value as H_{C2}. In practice, however, the manufacturing and heat processing of Nb_3Sn wire make the H* never as high as the H_{C2}. The most favorable way is to improve these processes. For instance, the transport critical current measurements in section 4.2.3 have showed that elevating HT temperature or elongating the duration effectively strengthens the long-range compositional uniformity and elevates the H* although coarsening the grain size.

4.2.5 Conclusion

The non-Cu critical current density J_C is the property that can be used to compare the current-carrying capacity of different Nb_3Sn wires and the superconducting performances of the same wire at different HT conditions. The non-Cu J_C measurement can reflect the wire design characterization and can also be used to optimize the heat treatment.

For the same kind of wires, such as the ITER's, the best non-Cu J_C has nearly the same magnitude although a rather big difference of the engineering critical current density J_E. This indicates that the main factor affecting the non-Cu J_C of Nb_3Sn is the configuration design. If the Nb/Sn/Cu ratio is determined, the wire final non-Cu J_C will have an estimable magnitude.

The selection of HT conditions is one of the most important factors to maximizing non-Cu J_C, whereas, the HT choice is surely determined by the third-element alloying. The Ti alloyed in Sn can effectively lower the reaction temperature, and this kind of wire is suitable to be heat-treated at lower temperature or a relatively short time. On the contrary, the wire without Ti addition in Sn needs the HT of higher temperature or longer duration. From our examination, the NIN wire is favorable to be heat-treated in the range of 650ºC~675ºC, while for the AST wire, 675ºC to 700ºC may be the best choice.

The non-Cu J_C is mainly dependent on the flux pinning situation of A15 phase at lower field, but on the irreversibility field H* at higher field. Therefore, for low-field application of

the wire, the enhancement of flux pinning force is the principal purpose, but for high-field utilization, the promotion of H* should be chiefly considered. This investigation demonstrates that lower reaction temperature is beneficial to flux pinning enhancement, and elevated temperature or elongation of reaction time is propitious to promoting long-range compositional uniformity along the wire and then increasing the H* value.

4.3 SQUID Magnetization Study of Internal-Sn Multifilament Wires

4.3.1 Introduction

There have been a few techniques for measuring the superconducting properties of the wire, of which the SQUID method is one of the most precise, reliable and effective ones and has obtained a wide use in recent years [89, 94]. With a SQUID magnetometer one can make two kinds of measurements. One is the irreversibility temperature T*(H) and the critical transition temperature T_C(B) measurements, which are determined by a warming and cooling cycle at a fixed field. T_C(B) is actually the H_{C2}(T). If the measurement is under very weak field (i.e. 1mT, which is actually the minimum field required for inductive magnetization measurement), the so-called zero-field critical temperature T_C will be obtained. The transition line (M-T) was considered to reflect the quantity and quality (composition) variation of the A15 phase [64]. Accordingly, the T_C-related irreversibility temperature T*(B) also reflects the A15 phase change in composition. Therefore, the measurement of warming and cooling cycle at a fixed field is useful to optimize the HT process from the view point of A15 composition.

The other measurement is the way of cycling the magnetic field at a constant temperature, from which an entire hysteresis loop can be determined. With the aid of the magnetization curves, the magnetization difference or hysteresis width (ΔM), and the irreversibility field H*(T) or Krammer field $H^*_{Krammer}$ can be determined. As J_C is proportional to ΔM, the ΔM as a function of magnetic field B is the indication of J_C versus field B. Furthermore, because flux pinning force $F_P=J_C\times B$, the $\Delta M\times B$ variation with field B is thus the reflection of F_P versus field B. Therefore, the measurement of cycling the field at a constant temperature aims at evaluating the heat treatment from the respect of flux pinning situation.

M. Suenaga et al. [65] were the first to study the irreversibility temperature property of a multifilament Nb_3Sn wire. They found that there exists a surprisingly large temperature region for the Nb_3Sn wire below the upper critical field line $H_{C2}(T)$ (or critical temperature line $T_C(B)$) where the magnetization is reversible during a warming and cooling cycle. The lower boundary of the temperature region was called the irreversibility temperature T*(B). A SQUID magnetometer was used for the measurement and T*(B) was taken as the point of onset of reversible magnetization at an applied magnetic field.

Cycling magnetic field at a constant temperature with a SQUID magnetometer was adopted by the authors of Refs. [89] and [94]. Fischer et al. not only obtained the Kramer irreversibility field (H^*_{Kramer}) but also calculated the flux pinning force and even critical current density J_C for their PIT wire. However, owing to the complexity of MF wire configuration and fabrication it is not practical to calculate the non-Cu J_C from magnetization measurement for internal-Sn wire.

The SQUID magnetization measurements of both cycling temperature at a fixed field and cycling field at a constant temperature were used to investigate the two ITER-type internal-Sn Nb_3Sn superconducting wires in this study. Combining T*(B) and $T_C(B)$ values with hysteresis curves, the A15 phase formation and the flux pinning property were investigated for the purpose of the HT optimization.

4.3.2 Experimental Approach

4.3.2.1 Test Preparation

The experiments were carried out using a SQUID magnetometer with a maximum magnetic field of 7.5T. Each of the wire samples heat-treated in section 4.1 was cut into short (~6mm) segments. Three of the segments were weighed and mounted together for one measurement on a clear plastic straw with their axis perpendicular to the applied field (some samples parallel to the field for comparison).

4.3.2.2Critical Temperature $T_C(B)$ and Irreversibility Temperature T*(B) Measurements

$T_C(B)$ and T*(B) were measured through the following procedure. Specimens were

zero-field cooled to 10K and then a fixed magnetic field was applied. The magnetic moments were measured upon warming up to 20K and then cooling back to 10K in steps of 0.25K. For temperatures far from the onset of reversible magnetization, steps of 0.5~1K were adopted for measurement. The magnetization moment (M) was recorded two times at each temperature point to reduce noise. So, an entire magnetization curve (M-T) was obtained during a warming and cooling cycle. All the moments were normalized to the sample mass. The measurement magnetic field was in the range of 0.1 to 5T.

T_C was measured with the procedure identical to the T_C(B) and T*(B) measurement, but with a starting temperature of 2K. The sample was zero-field cooled to 2K and then a field of 1mT was applied. The moment was taken upon warming up to 20K in 0.25K step near the transition region and 0.5~1K step far from the region. That is a 2K→20K→2K cycle.

From the magnetization as a function of temperature (M-T) going up and down, the irreversibility temperature T*(B) can be obtained as the onset value of the irreversibility. Fig.4-10 shows a typical normalized M-T curve and the corresponding onset point. The T*(B) value was taken as the temperature at which the moment difference (ΔM) upon warming and cooling tends to zero, as plotted in Fig.4-11. The T*(B) values were all determined with this criterion.

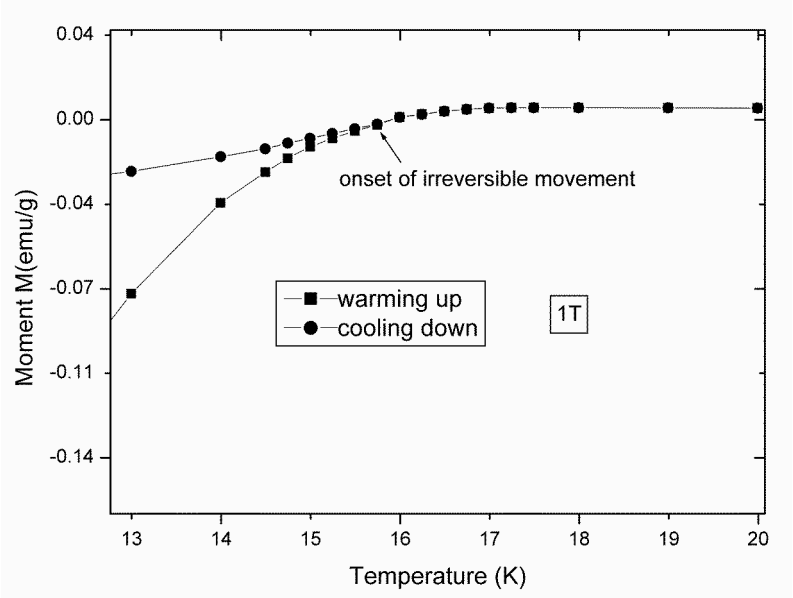

Fig.4-10 A typical normalized M-T curve and the onset point. This is a portion of the curve of a warming and cooling cycle of the AST wire sample heat-treated at 675°C/128hrs

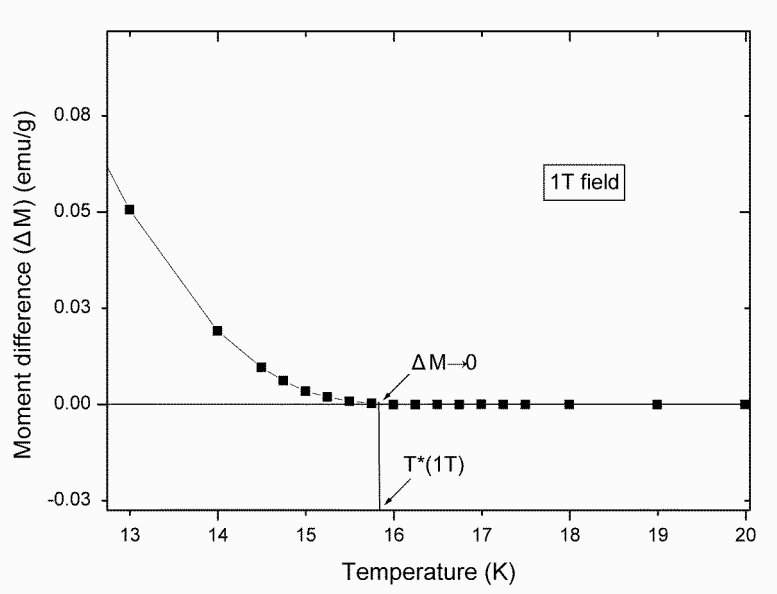

Fig.4-11 The irreversibility temperature is defined as the point where ΔM tends to zero. The curve plotted for the same sample as shown in Fig.4-10 shows an irreversibility temperature of ~15.8K

The T_C and T_C(B) are usually determined by a few ways in which the midpoint manner is the most popular one. That is, the midpoint of the critical temperature transition (50% of the baseline value) is taken as the T_C or T_C(B), and 10% to 90% of the baseline temperatures were obtained to characterize the transition width. However, it was found in this study that the midpoint manner and even 90% transition point are not suitable to determine the T_C(B). This is because the T_C(B) value taken by this manner may be smaller than the T*(B) value of the same M-T curve, which is very unreasonable. Therefore, the T_C(B) and T_C in this study were obtained in the way of which the up-heating section (from 2K→20K) of the M-T curve was selected and the visible deviation temperature point from superconducting state to normal state was taken as the value of T_C or T_C(B), as illustrated in Fig.4-12. All T_C and T_C(B) measurements in this thesis were from this criterion.

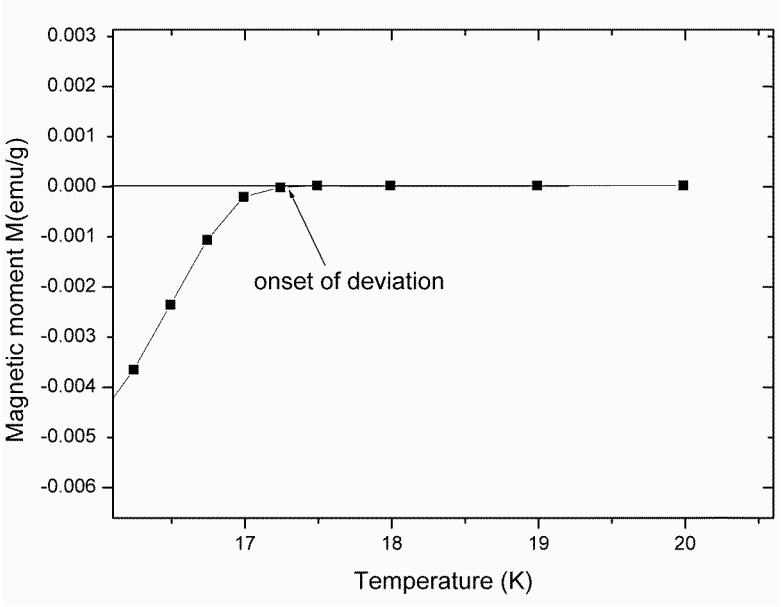

Fig.4-12 The visible deviation point of up-heating portion of the M-T curve is taken as T_C or $T_C(B)$

4.3.2.3 Hysteretic Loop (M-B), Irreversibility Field H* and Hysteresis Width (ΔM) Measurement

This experiment used the same SQUID magnetometer as that in the T_C (B) measurement. 12K and 14K were chosen as the constant temperatures. The sample was zero-field cooled to the fixed temperature and then a magnetic field was applied. The applied field was increased from zero to 7.5T, back to zero, and then decreased to -7.5T, back to zero again, in steps of 0.25T. In the range of ±1T the field was changed in steps of 0.05~0.1T for the sharp variation of magnetic moment. The magnetic moments were tested during the whole field cycle and were normalized to the sample mass. The moment M was recorded two times at each field point to reduce noise. An entire magnetization curve was obtained when the normalized moments were plotted as a function of field.

According to the origin-symmetry property of a hysteresis loop, the magnetization curve section of the second quadrant can be origin-symmetrically allocated in the fourth quadrant. The magnetization difference (hysteresis width ΔM) is then determined by the magnetization curves of the second and the fourth quadrants. Fig. 4-13 shows the magnetization curves and the hysteresis width (ΔM) of a typical sample.

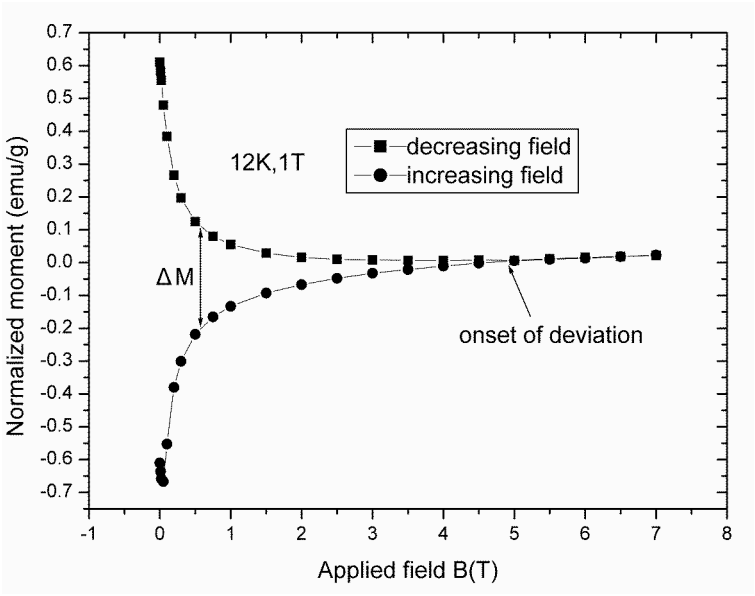

Fig. 4-13 Magnetization curves and hysteresis width (ΔM) of the AST 675ºC/128h sample tested at 12K and 1T.

The irreversibility field (H*) is defined as the field where J_C=0, and can be identified as the field at which hysteretic loop closure occurs. Fig.4-13 shows the closure point. The H* value can be determined by two ways; one is the point of hysteresis width (ΔM) versus field (B) curves when the ΔM tends to be zero; the other is the Krammer linear fit extrapolation of $\Delta M^{1/2}B^{1/4}$ versus B to B=0. The later is useful when hysteretic loop closure is too high to be measured. Fig.4-14 demonstrates the two ways of determining H* value. In this study, the Krammer extrapolation was adopted for the samples whose values of H* are exceeded 6T and the ΔM-B curves was used in the case of H* value lower than 6T.

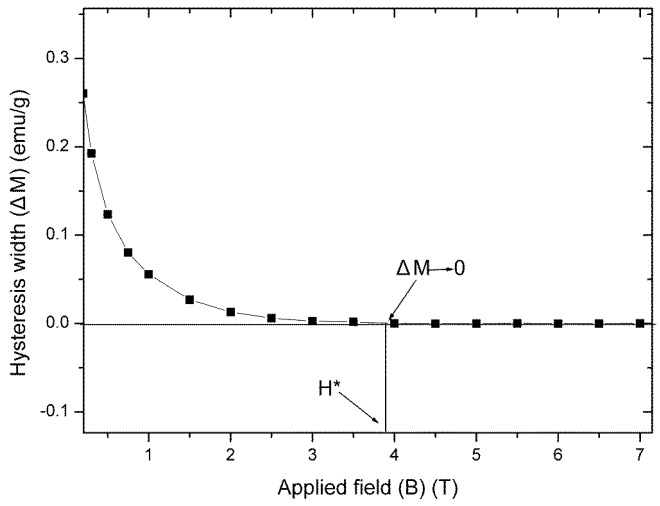

(a) ΔM→0

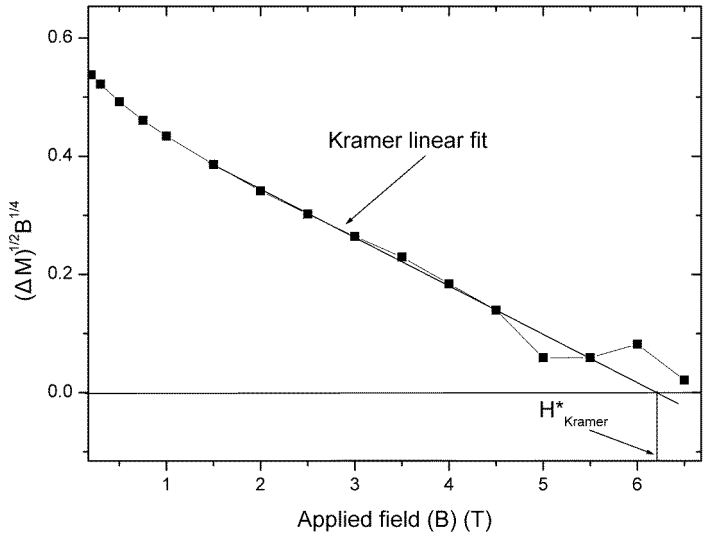

(b) Krammer extrapolation

Fig.4-14 The ways of H* value determination

As ΔM as a function of magnetic field B is the indication of J_C versus field B and the ΔM×B variation with field B is the reflection of F_P versus field B, the ΔM-B curves and the ΔM×B-B curves can be used to interpret the J_C and flux pinning variations of various samples and thus used to optimize the HT conditions.

4.3.3 Results and Analysis

4.3.3.1 Magnetic Field versus Temperature (H-T) Lines

The T_C versus field T_C (B) is identical to the H_{C2} versus temperature H_{C2} (T). So, if the T_C (B) values are plotted as a function of applied field, we can also obtain the field-temperature line (H-T) of the Nb_3Sn superconductor. The M-T lines of NIN and AST wire samples were measured in the SQUID magnetometer over the field range of 0.1~6T. The results are described as following.

(1) The HT time influence

The wire samples heat-treated at 675ºC for 8~200hrs were measured for the T_C (B) values which were then plotted with the variation of field, as shown in Figs.4-15 and 4-16.

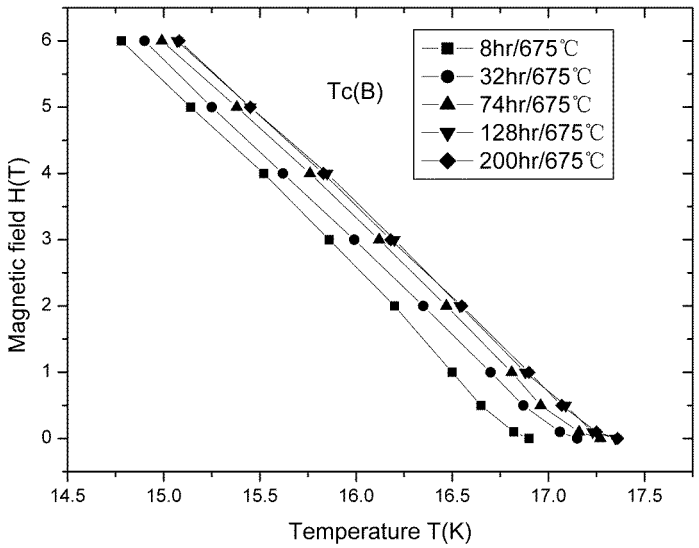

Fig.4-15 The H-T lines of NIN wire samples heat-treated at 675ºC for different durations

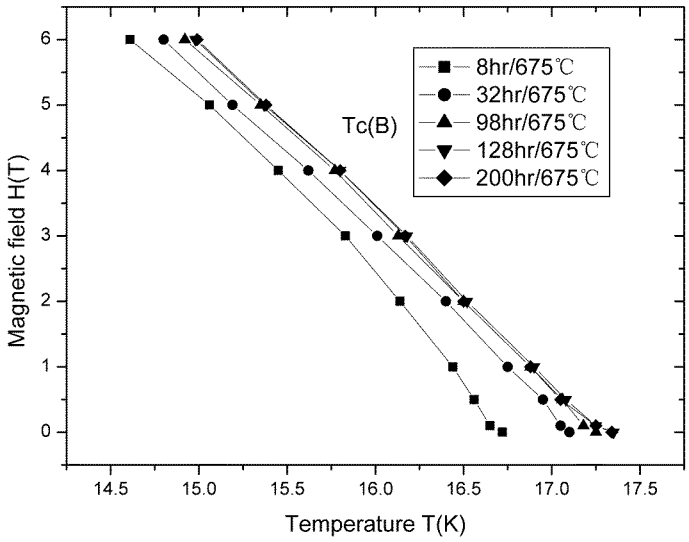

Fig.4-16 The H-T lines of AST wire samples heat-treated at 675ºC for different durations

From Figs.4-15 and 4-16, it is seen that the NIN wire and AST wire have nearly the same variations: the samples of 8hr heat treatment have the lowest H-T line. As the reaction time increases from 8hrs to 200hrs, the H-T line shifts upward and stays nearly in the same position after 128hr reaction.

(2) The HT temperature influence

The wire samples heat-treated at four different temperatures for 128hrs were measured for the T_C (B) values which were also plotted with the variation of field, as shown in Figs.4-17 and 4-18.

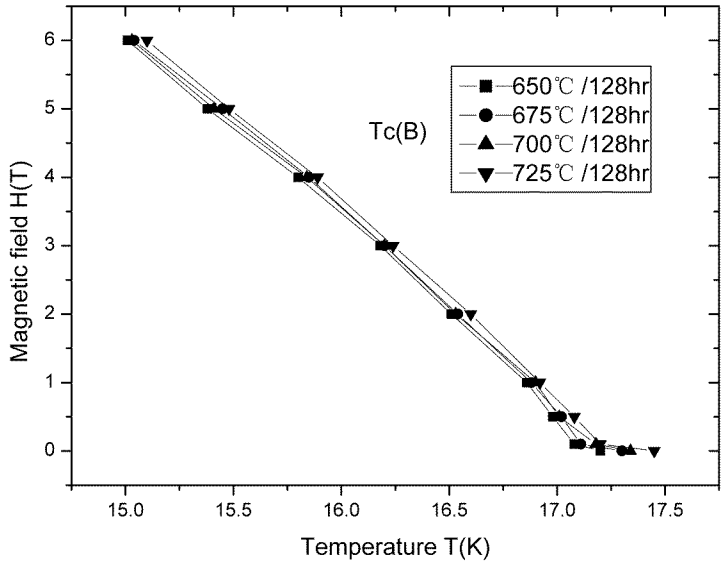

Fig.4-17 The H-T lines of NIN wire samples heat-treated at four different temperatures for 128hrs

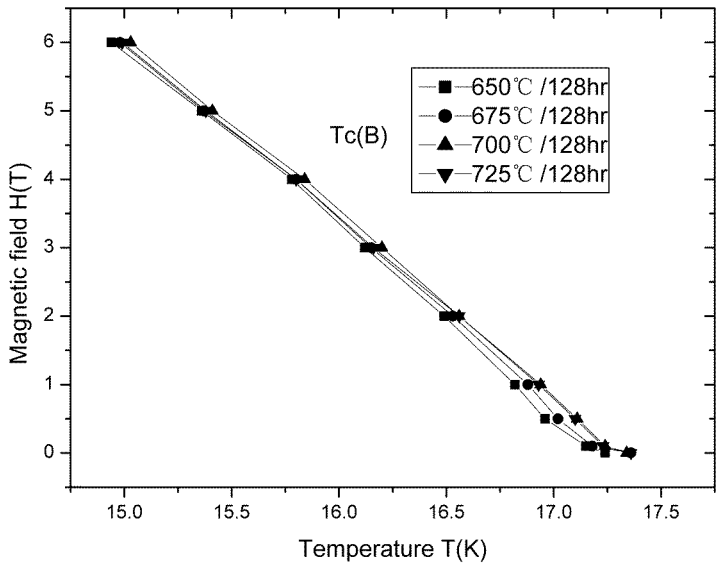

Fig.4-18 The H-T lines of AST wire samples heat-treated at four different temperatures for 128hrs

From Figs.4-17 and 4-18 it can be seen that the NIN wire and AST wire also have nearly the same variations: the H-T lines of all the samples heat-treated at different temperatures for 128hrs have very little variation and nearly overlapped; the largest difference is not exceeded 0.3K.

4.3.3.2 T*(B) Values Comparison and Analysis

The T*(B) values as a function of applied field for the NIN and AST wire samples were measured in the SQUID magnetometer over the field range of 0.1~6T. The results are

described as following.

(1) The HT time influence

The wire samples heat-treated at 675ºC for 8~200hrs were measured for the T*(B) values which were then plotted with the variation of field, as shown in Figs.4-19 and 4-20.

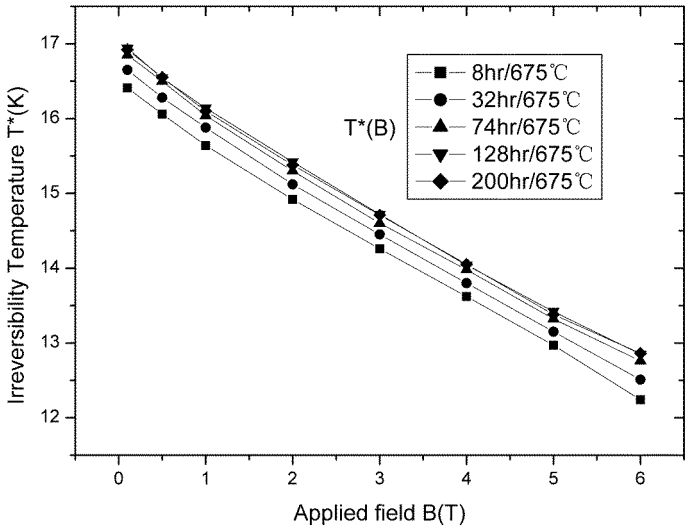

Fig.4-19 The T*(B) values as a function of field for NIN wire samples heat-treated at 675ºC for different durations

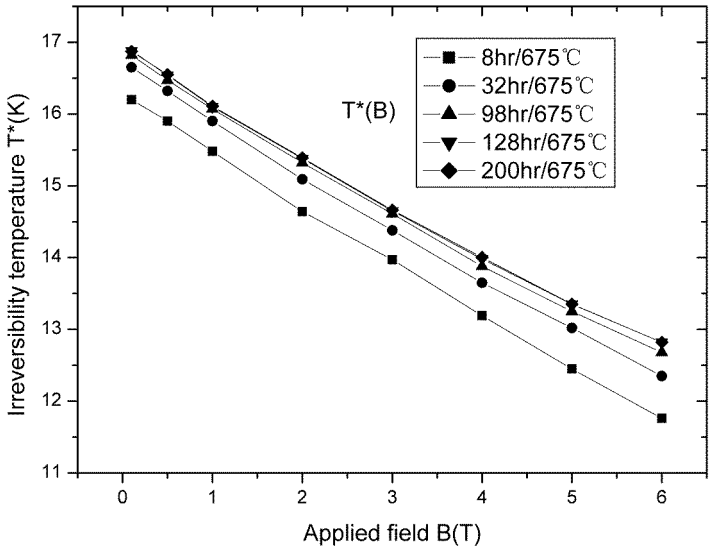

Fig.4-20 The T*(B) values as a function of field for AST wire samples heat-treated at 675ºC for different durations

From Figs.4-19 and 4-20, it can be seen that the T*(B) decreases with the increment of applied magnetic field for each heat-treated wire. As the thermal reaction time increases the

T*(B)-B curve also shifts upward and stays nearly in the same position after the 128hr heat treatment. The 128hr line and the 200hr line are nearly overlapping.

This is more clearly demonstrated in Figs.4-21 and 4-22, in which the T*(B) values as a function of heat treatment time are plotted for the three fields of 1T, 2T and 3T. The three curves have nearly the same variation in that as the heat-treating time increases from 8hrs to around 128hrs, the T*(B) first shows a continuous increase and then remains approximately as a plateau after the 128hr thermal treatment for each tested field.

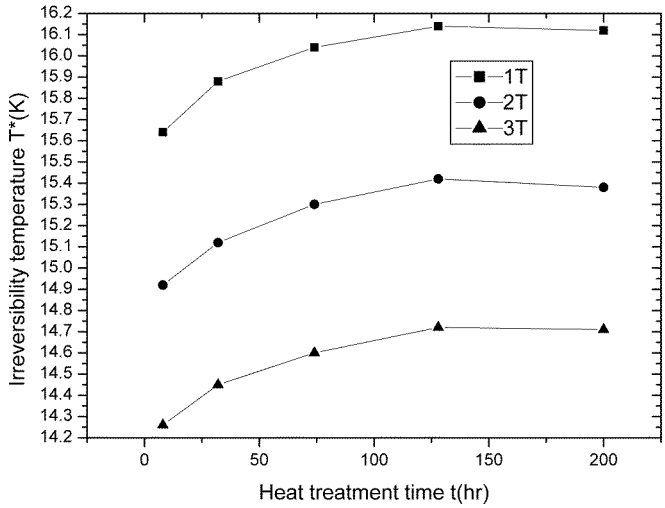

Fig.4-21 The T*(B) values as a function of heat treatment time at1T, 2T and 3T tested fields for NIN wire

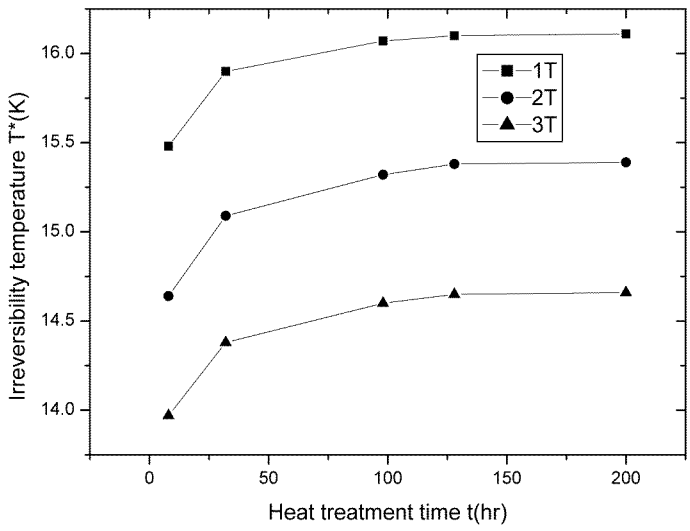

Fig.4-22 The T*(B) values as a function of heat treatment time at1T, 2T and 3T tested fields for AST wire

(2) The HT temperature influence

For the reaction temperature effect on the T*(B), wire samples heat-treated for a 128hr "full time reaction" at four temperatures of 650ºC, 675ºC, 700ºC and 725ºC were used for measurement. The T*(B) results obtained are included in Tables 4-3 and 4-4.

Table 4-3 Influence of reaction temperature on T*(B) at various field for NIN wire

NIN sample	**T*(B)（K）**							
	0.1T	**0.5T**	**1T**	**2T**	**3T**	**4T**	**5T**	**6T**
650°C/128hr	16.8	16.5	16.0	15.3	14.7	14.0	13.3	12.8
675°C/128hr	16.9	16.5	16.0	15.3	14.7	14.1	13.4	12.8
700°C/128hr	16.9	16.5	16.1	15.4	14.7	14.1	13.4	12.9
725°C/128hr	16.9	16.5	16.1	15.4	14.8	14.0	13.4	12.9

Table 4-4 Influence of reaction temperature on T*(B) at various field for AST wire

AST	**T*(B)（K）**							
sample	**0.1T**	**0.5T**	**1T**	**2T**	**3T**	**4T**	**5T**	**6T**
650°C/128hr	16.8	16.5	16.0	15.3	14.6	13.9	13.3	12.8
675°C/128hr	16.9	16.5	16.1	15.4	14.7	14.0	13.4	12.8
700°C/128hr	16.9	16.5	16.0	15.3	14.7	14.0	13.4	12.9
725°C/128hr	16.9	16.5	16.1	15.3	14.6	14.0	13.4	12.9

From Tables 4-3 and 4-4 it can be seen that the T*(B) values have nearly no change at the four temperatures for NIN wire, and for AST wire. This seems to identify the characteristic of reaction-temperature independence of T*(B) values for fully reacted samples.

4.3.3.3 Critical Temperature T_C and Transition Curves (M-T)

All the AST and NIN samples heat-treated at four temperatures for 128hrs and at 675ºC for 8~200hrs were measured the M-T transition curves from which the critical temperature T_C values were determined. The moments were all normalized to their sample mass. The results

are also described from HT temperature influence and time influence.

(1) The reaction temperature influence

The determined T_C values of the two wire samples heat-treated at different temperatures are included in Table 4-5.

Table 4-5 The T_C values for NIN and AST wire samples heat-treated at different temperatures

NIN sample	**T_C(K)**	**AST sample**	**T_C (K)**
600ºC/202hr- 650ºC/128hr	17.3	600ºC/202hr- 650ºC/128hr	17.3
650ºC/128hr	17.3	650ºC/128hr	17.2
675ºC/128hr	17.3	675ºC/128hr	17.3
700ºC/128hr	17.4	700ºC/128hr	17.3
725ºC/128hr	17.5	725ºC/128hr	17.4

It is seen from Table 4-5 that the NIN and AST wires have very small T_C difference between themselves and between each other for the fully-reacted samples of 128hrs at various temperatures. It seems that the T_C of fully-reacted Nb_3Sn wire is temperature-independent.

The normalized M-T transition curves of the different temperature samples are shown in Figs.4-23 and 4-24.

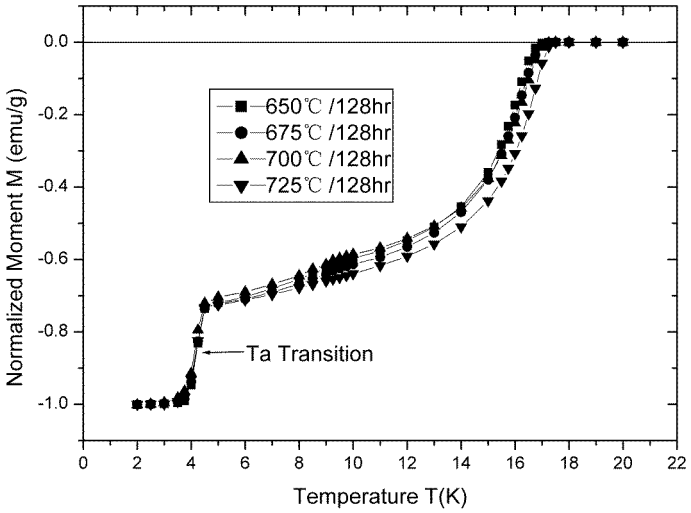

Fig. 4-23 The M-T transition curves for NIN samples heat-treated at different temperatures for 128hrs

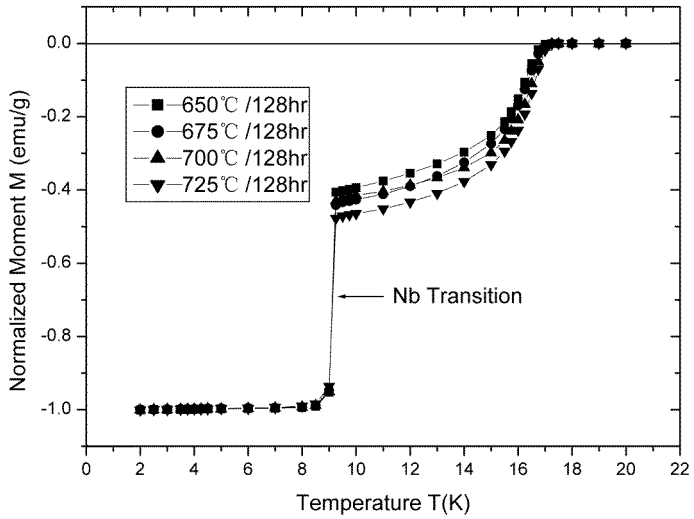

Fig. 4-24 The M-T transition curves for AST samples heat-treated at different temperatures for 128hrs

In Fig.4-23, the NIN samples have two moment transitions, of which the lower one is the transition of diffusion barrier Ta (around 5K), while the upper one is the A15 phase transition that we are mainly concerned. As Ta has a constant volume during heat treatment, all the M-T transition curves are also normalized to the Ta base transition line.

In Fig.4-24, the AST samples also have two moment transitions, but the lower one is the transition of wire outside diffusion barrier Nb (around 9K). The upper one is also the A15 phase transition curve. Because the diffusion barrier Ta is located inside the outer Nb barrier, the Ta transition has been screened by the Nb transition and does not appear in the measurement. Due to the invariable Nb barrier, all the M-T transition curves of AST samples are normalized to the Nb base transition line.

It was reported [64] that in the A15 phase transition curve the magnetization amplitude indicates the A15 phase quantity and the shift of the transition, combined with the transition width (the transition difference between 10% and 90%), reflects the Sn content (or A15 quality) or the deviation to stoichiometric Nb_3Sn.

From Figs.4-23 and 4-24, it is noted that for both NIN wire and AST wire, the A15 phase transition curves have nearly the same characteristics. After full reaction, the magnetization amplitude and the transition curve shift of A15 phase have just small variation, no matter what the reaction temperature was. The three transition curves of NIN samples from

650ºC to 700ºC are nearly overlapping, and the same for the curves of AST samples from 675ºC to 700ºC. The largest difference is not exceeding 0.5K. The results also mean that the A15 composition of Nb_3Sn wires is temperature-independent.

(2) The reaction time influence

Three sets of samples selected from NIN and AST respectively were measured for the T_C values. The results are included in Table 4-6.

Table 4-6 The T_C values for NIN and AST wire samples heat-treated for different times

NIN sample	**T_C(K)**	**AST sample**	**T_C (K)**
600°C/202hr- 650°C/8hr	16.9	600°C/202hr- 650°C/8hr	16.9
600°C/202hr- 650°C/32hr	17.2	600°C/202hr- 650°C/32hr	17.1
600°C/202hr- 650°C/74hr	17.3	600°C/202hr- 650°C/74hr	17.3
600°C/202hr- 650°C/128hr	17.3	600°C/202hr- 650°C/128hr	17.3
600°C/202hr- 650°C/200hr	17.3	600°C/202hr- 650°C/200hr	17.3
650°C/8hr	16.4	650°C/8hr	16.4
650°C/32hr	17.1	650°C/32hr	17.0
650°C/74hr	17.3	650°C/74hr	17.3
650°C/128hr	17.3	650°C/128hr	17.4
650°C/200hr	17.4	650°C/200hr	17.3
675°C/8hr	16.7	675°C/8hr	16.7
675°C/32hr	17.2	675°C/32hr	17.2
675°C/74hr	17.3	675°C/74hr	17.3
675°C/128hr	17.3	675°C/128hr	17.4
675°C/200hr	17.4	675°C/200hr	17.4

It can be seen from Table 4-6 that the T_C values are lower for the samples of shorter time reaction and are increased with the elongation of duration. After the sample is reacted through, the T_C is no longer changed. Comparing the T_C values of fully-reacted samples at different HT conditions, they nearly have the same magnitude.

The normalized M-T transition curves of the three sets of samples are shown in

Figs.4-25 and 4-26.

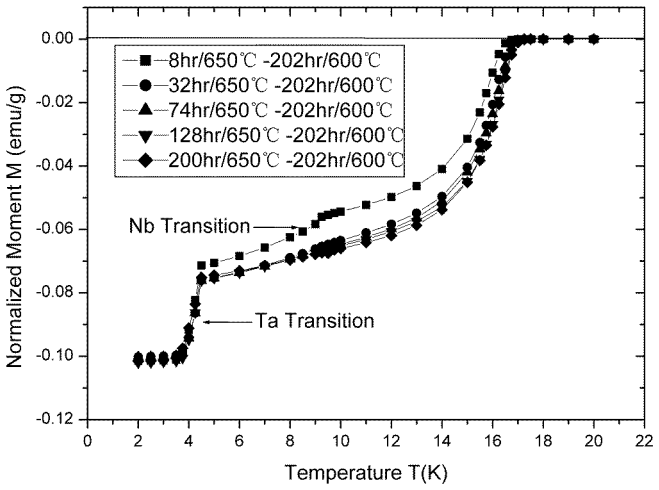

(a) 600ºC/202hr-650ºC

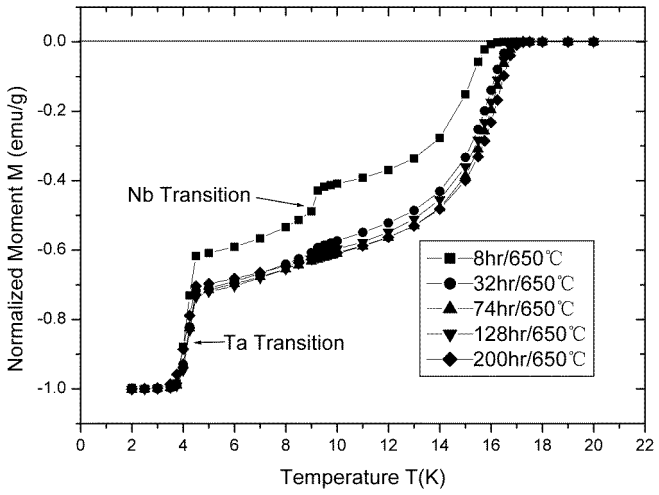

(b) 650ºC

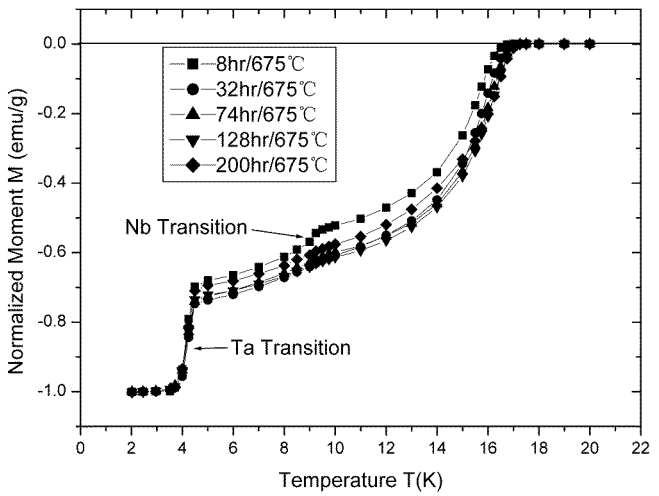

(c) 675ºC

Fig. 4-25 The M-T transition curves for three sets of NIN samples

In Fig.4-25, the samples of shorter time reaction (i.e. 8hr) have three moment transitions. The lowest one is the transition of diffusion barrier Ta (around 5K); the middle one is the transition of the unreacted Nb and the upper one is the A15 phase transition that we are much concerned. After a period of duration, the Nb filaments are reacted through and the M-T curves have only the two transitions of Ta and A15 phase. Here also the M-T transition curves of NIN samples are normalized to the Ta base transition line.

It can be found from Fig.4-25 that a large amount of Nb is remained for NIN sample heat-treated at 650ºC for 8hrs (see the Nb transition line of (b)). However, for the sample underwent a pre-reaction of 600ºC/202hr before 650ºC/8hrs, the remanent Nb becomes smaller (see the Nb transition line of (a)). The increase of temperature to 675ºC also reduces the amount of remanent Nb for the 8hr duration (see (c)) due to the acceleration of reaction rate. It can also be found from Fig.4-25 that after 74hr reaction the A15 phase transition curves of NIN wire samples heat-treated at any temperatures have very small variation. This means that the quantity and quality (Sn content) will be kept stable after an enough duration time.

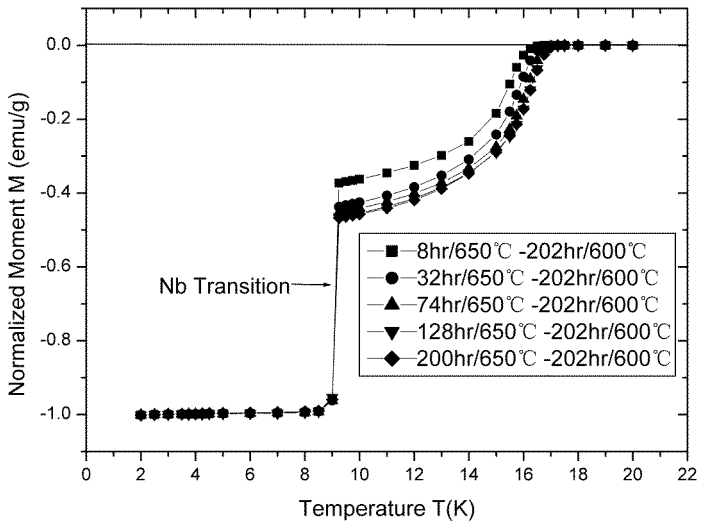

(a) 600ºC/202hr-650ºC

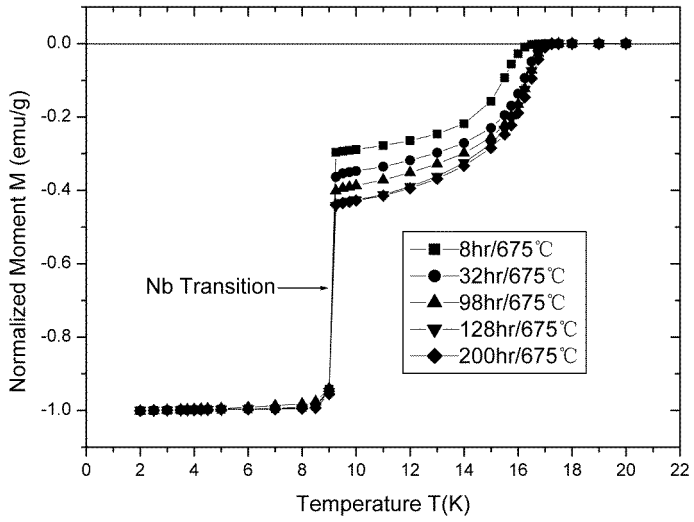

(b) 675ºC

Fig. 4-26 The M-T transition curves for two sets of AST samples

Fig.4-26 shows the AST sample results. Because the outer diffusion barrier Nb always shields the transition of inner diffusion barrier Ta and the unreacted Nb during measurement, the M-T curves of all AST samples only have two transitions: the lower is the transition of the outer barrier Nb and the upper is the A15 phase transition that we are mainly concerned. Similarly, all the M-T transition curves of AST samples are normalized to the Nb base transition line.

From Fig.4-26 we can find that the A15 transitions are gradually progressed from 8hr to 128hr duration, being reflected by the increase of magnetization moment M and the right-shift of the transition curve. This indicates that the amount of A15 phase and the Sn content in its composition become continually increased during the progress. In addition, the transition curves of 128hr and 200hr treatment for the three sets of samples are nearly overlapped, meaning the equilibrium of the A15 quantity and composition after full-time reaction.

(3) The transition curve comparison between two-step and one-step reaction

The transition curves of NIN and AST samples heat-treated with 600ºC/202hr-650ºC and the 650ºC procedures are compared respectively. The former is called two-step reaction and the later one-step reaction. Fig.4-27 shows the comparisons.

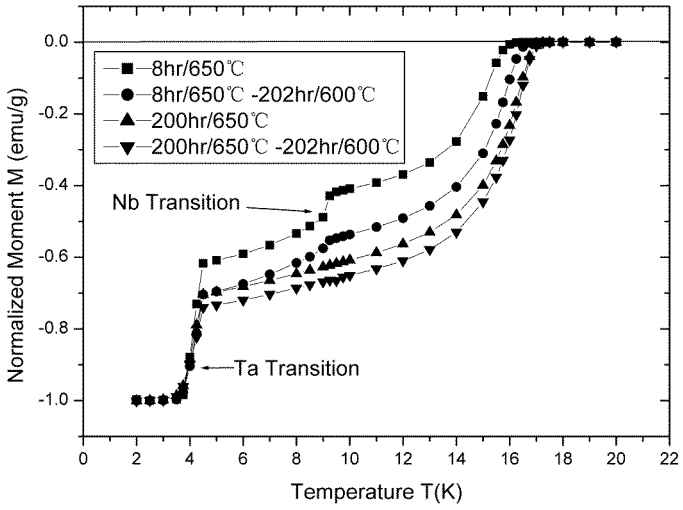

(a) NIN wire

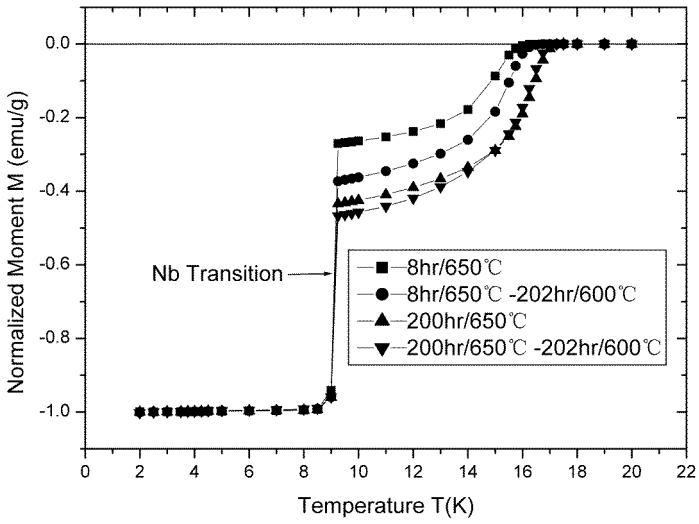

(b) AST wire

Fig.4-27 The transition curve comparisons between two-step and one-step reactions

From 4-27(a) figure it is noted that for NIN wire the 8hr transition curve of two-step reaction sample has a rather large right-shift and craggedness, indicating the increase of A15 quantity and quality. However, the 200hr transition curve has a very small shift. Figure (b) has more clearly demonstrated the variation for AST wire: very large shift of transition curve from two-step to one-step procedure for 8hr duration and nearly overlap of the curves for 200hr reaction.

The results obviously indicate that the two-step reaction only changes the HT progress and does not affect the final A15 phase formations. In other words, the A15 phase

composition is no longer varied after enough phase formation reaction, no matter what HT procedure is used.

4.3.3.4 ΔM-B result and Analysis

As the ΔM is proportional to J_C, the ΔM-B curve actually reveals the J_C variation with the applied field. In this experiment, the selected samples were measured for the hysteretic loops at 12K and 14K testing temperatures, from which the hysteresis widths are determined. The ΔM values were plotted as a function of field B and the results are shown as following.

(1) The reaction temperature influence

The NIN and AST wire samples heat-treated at four different temperatures for 128hrs have been plotted the ΔM-B curves, shown in Figs.4-28 and 4-29.

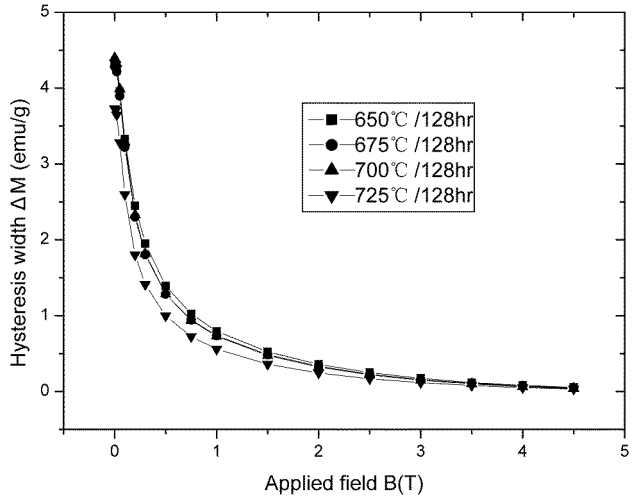

(a) 12K

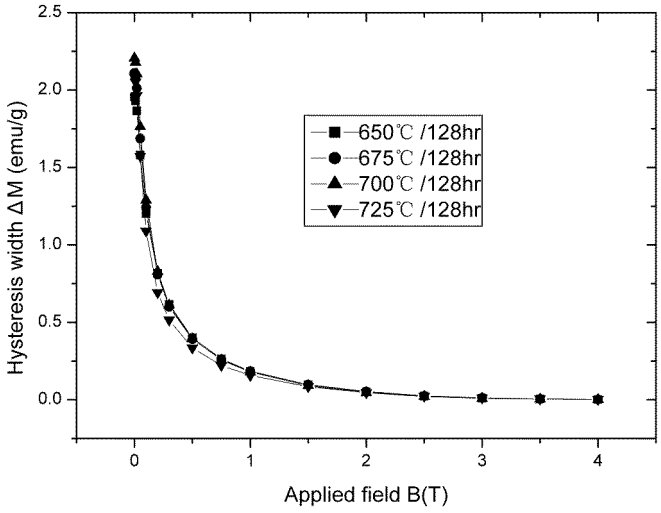

(b) 14K

Fig.4-28 The ΔM-B curves of NIN samples heat-treated at different temperatures

From Fig.4-28 (a) and (b), it can be seen that the ΔM-B curve of NIN 650ºC sample is at the highest position, meaning the strongest inductive J_C. With the reaction temperature increase from 675ºC to 700ºC, the ΔM-B curve has a small shift downwards and a large shift down at 725ºC, indicating the J_C decrease at higher HT temperature.

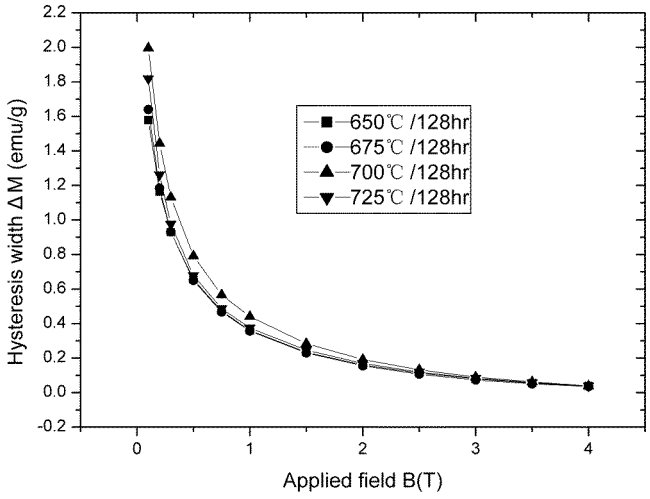

(a) 12K

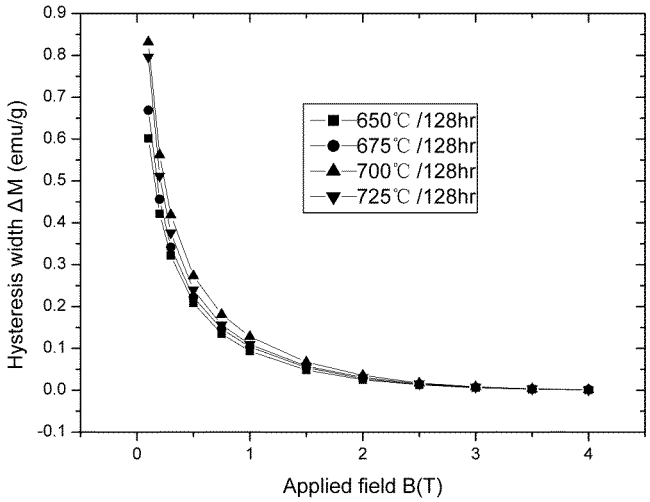

(b) 14K

Fig.4-29 The ΔM-B curves of AST samples heat-treated at different temperatures

From Fig.4-29 (a) and (b), it can be found that the ΔM-B curve of AST samples shifts upwards from 650ºC to 700ºC, and reaches the highest position at 700ºC. A large shift-down happens at 725ºC. These also mean that AST wire has a lower J_C at 650ºC and the highest J_C appears at 700ºC.

(2) The reaction time influence

The two sets of samples from NIN and AST respectively were plotted the ΔM-B curves at 12K of testing temperature for the purpose of evaluating reaction time influence. The results are shown in Figs.4-30 and 4-31.

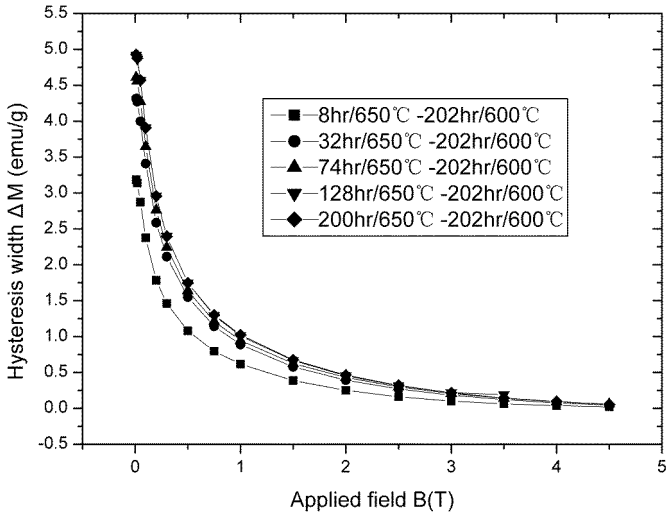

(a) 600ºC/202hr-650ºC, 12K

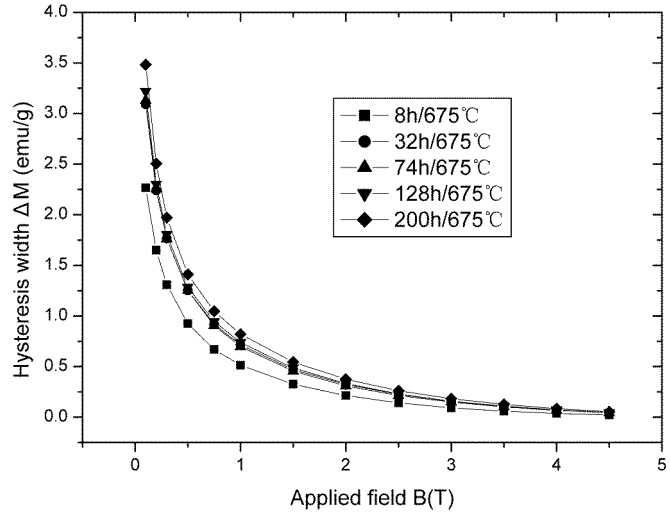

(b) 675ºC, 12K

Fig.4-30 The ΔM-B curves of NIN samples heat-treated for different durations

From Fig.4-30 (a) and (b), it can be seen that the ΔM-B curve of NIN wire shifts upwards gradually from 8hr to 128hr reaction when it approaches the highest position. After then, the ΔM-B curve keeps the position or has a small shift down. The ΔM-B variation also indicates the variation of inductive J_C which will increase from 8hr to 128hr and reach the

highest value at the 128hr reaction.

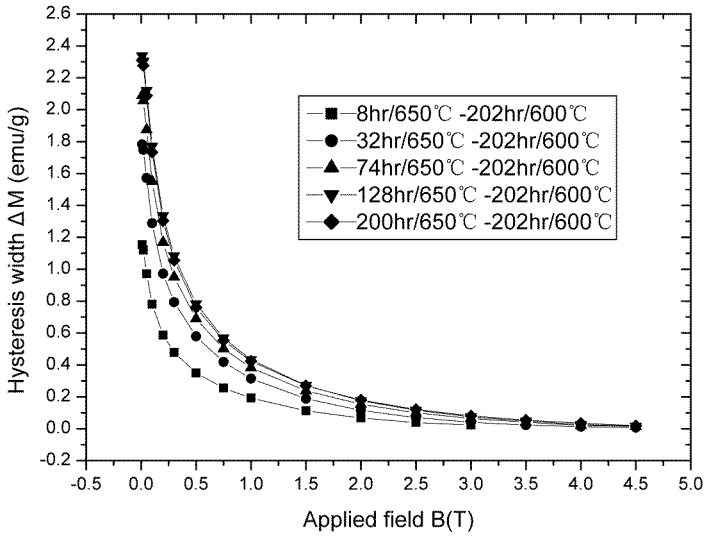

(a) 600ºC/202hr-650ºC, 12K

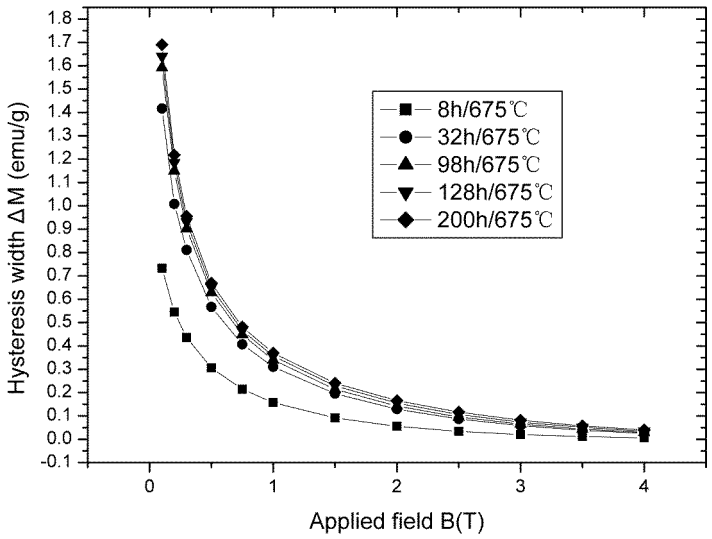

(b) 675ºC, 12K

Fig.4-31 The ΔM-B curves of AST samples heat-treated for different durations

Observing Fig.4-31 (a) and (b), it can be found that the AST samples have nearly the same variation rule of ΔM-B curves, which shift upwards from 8hr to 128hr and approach the highest position for the 128hr samples.

4.3.3.5 (ΔM×B)-B Curves

As ΔM×B is proportional to flux pinning force F_P, the ΔM×B versus field B actually reflects the F_P variation with the applied field. The same samples as in section 4.3.3.4 were

plotted the ΔM×B values as a function of field B. The results are also analyzed from HT temperature and time respectively.

(1) The reaction temperature influence

The NIN and AST wire samples heat-treated at four different temperatures for 128hrs have been plotted the (ΔM×B)-B curves, shown in Figs.4-32 and 4-33.

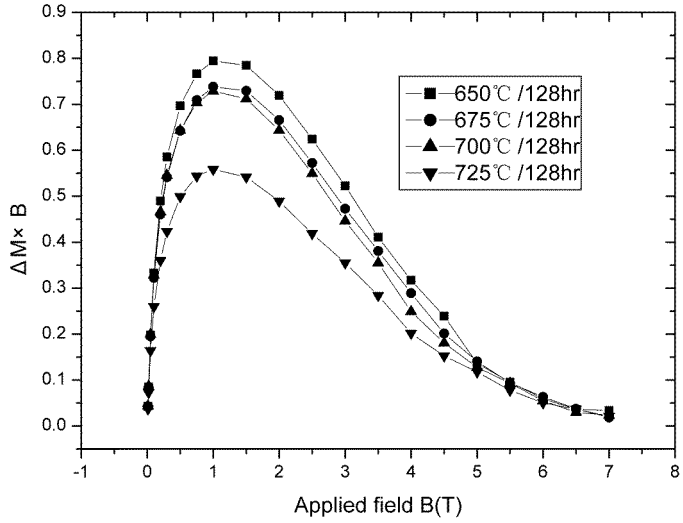

(a) 12K

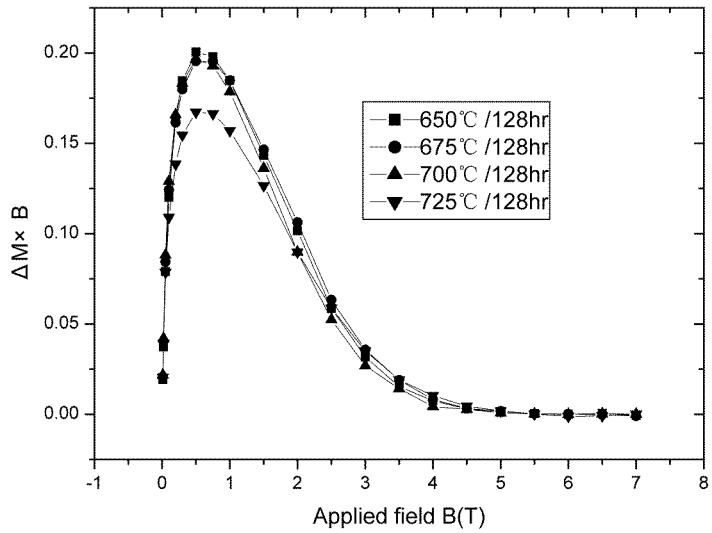

(b) 14K

Fig.4-32 The (ΔM×B)-B curves of NIN samples heat-treated at different temperatures

From Fig.4-32 (a) and (b), it can be seen that the (ΔM×B)-B curve of NIN 650ºC sample is at the highest position, meaning the strongest flux pinning force F_P. With the reaction temperature increase from 675ºC to 700ºC, the (ΔM×B)-B curve has a small shift downwards

and a large shift down at 725ºC, indicating the flux pinning situation weakened at higher HT temperature.

The field at the highest position in the (ΔM×B)-B curve is defined as the value of the position of maximum flux pinning force. Looking at the position in Fig.4-32, the maximum flux pinning force in every (ΔM×B)-B curve appears at 1T for 12K of testing temperature (see (a)), and at 0.5T for 14K (see (b)).

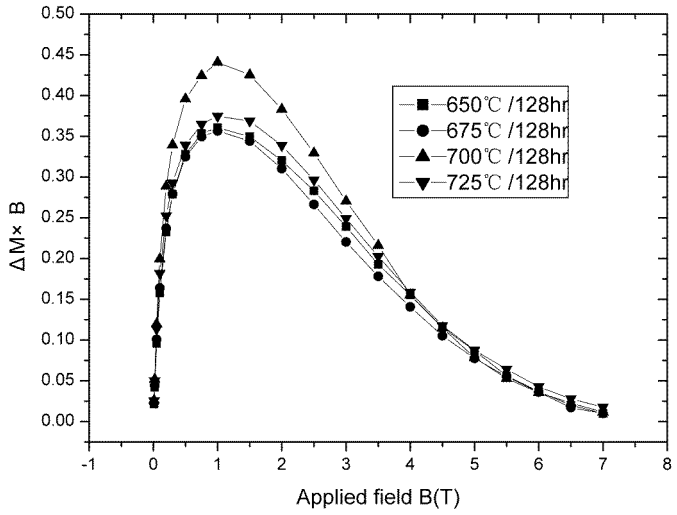

(a) 12K

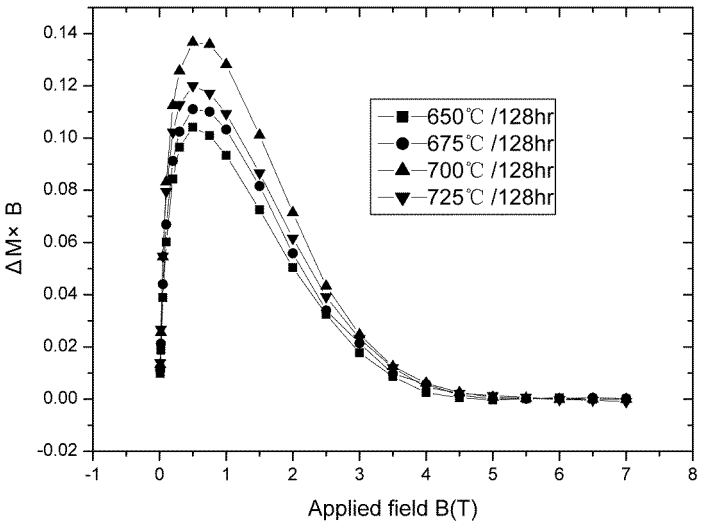

(b) 14K

Fig.4-33 The (ΔM×B)-B curves of AST samples heat-treated at different temperatures

From Fig.4-33 (a) and (b), it can be found that the (ΔM×B)-B curve of AST samples shifts upwards from 650ºC to 700ºC, and reaches the highest position at 700ºC. A large

shift-down happens at 725ºC. These also mean that AST wire has a weak flux pinning force at 650ºC and the strongest F_P appears at 700ºC.

Observing the position of the maximum flux pinning force, all samples in (a) figure appear at 1T, and in (b) figure, at 0.5T.

(2) The reaction time influence

The two sets of samples from NIN and AST respectively were plotted the (ΔM×B)-B curves at 12K of testing temperature for the purpose of evaluating reaction time influence. The results are shown in Figs.4-34 and 4-35.

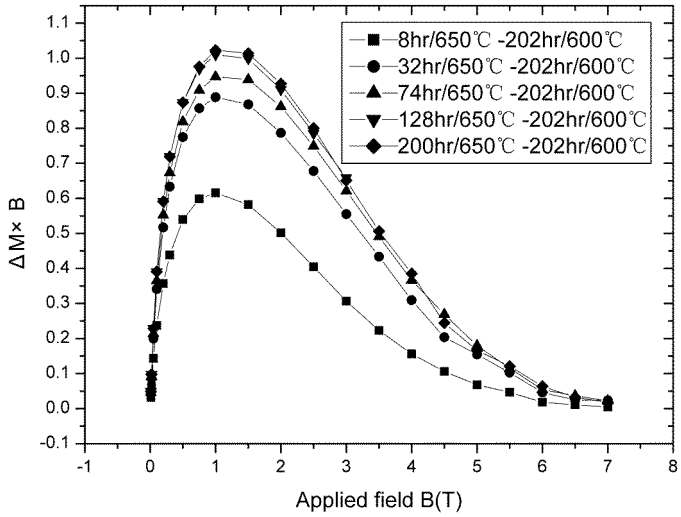

(a) 600ºC/202hr-650ºC, 12K

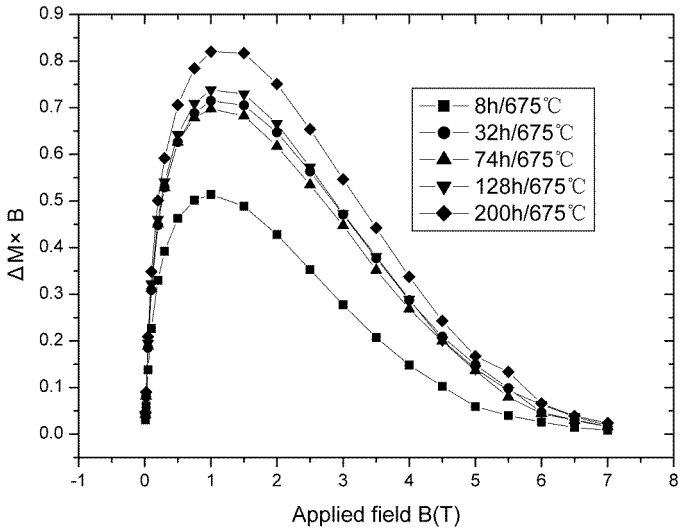

(b) 675ºC, 12K

Fig.4-34 The (ΔM×B)-B curves of NIN samples heat-treated for different durations

From Fig.4-34 (a) and (b) it can be seen that the (ΔM×B)-B curve of NIN wire shifts up-and-rightwards fast from 8hr to 32hr heat treatment. After then, it slows down and nearly has no any movement longer than 128hrs. That is to say, the flux pinning performance is strengthened very fast before 32hr, then slows down gradually and approaches the strongest value at 128hr reaction.

The positions of maximum F_P have a visible change. Observing the (a) and (b) figures, the fields of maximum F_P appear at 0.75T for 8hr samples and increase to 1T for 200hr samples.

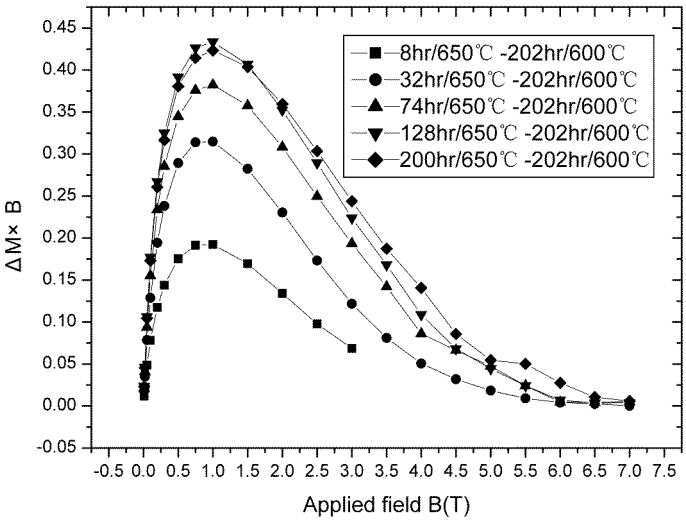

(a) 600ºC/202hr-650ºC, 12K

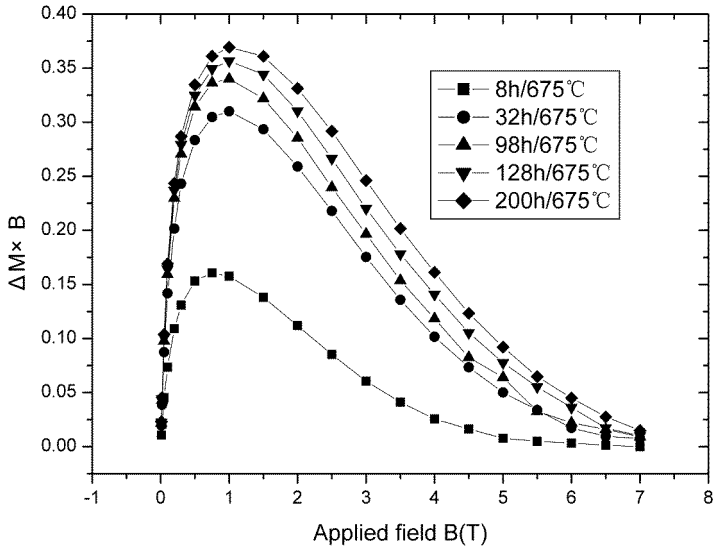

(b) 675ºC, 12K

Fig.4-35 The(ΔM×B)-B curves of AST samples heat-treated for different durations

From Fig.4-35 (a) and (b) it is found that the movement of (ΔM×B)-B curve of AST wire has the same variation as that of NIN wire: shifting up-and-right quickly before 32hr reaction, then slowing down and approaching the strongest value at 128hr heat treatment. The fields of maximum F_P also appear at 0.75T for 8hr samples and increase to 1T for 200hr samples.

(3) The (ΔM×B)-B curve comparison between two-step and one-step reaction

The two wires were plotted the (ΔM×B)-B curves of two-step and one-step reaction at 650ºC, respectively. Fig.4-36 shows the comparison.

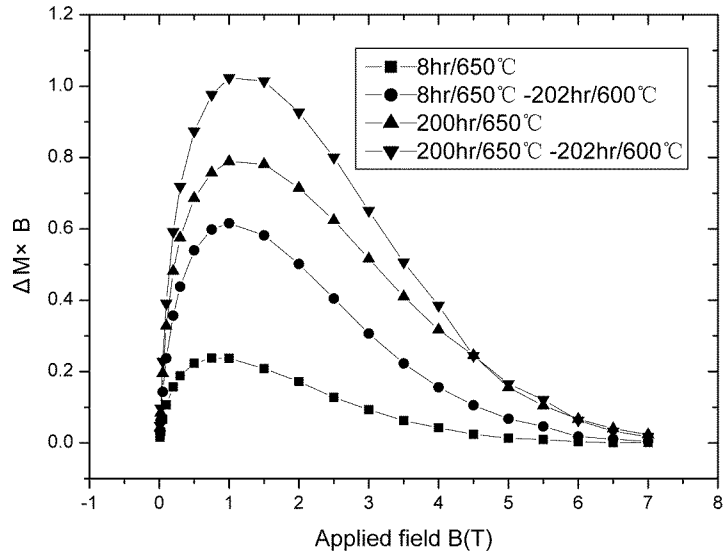

(a) NIN wire

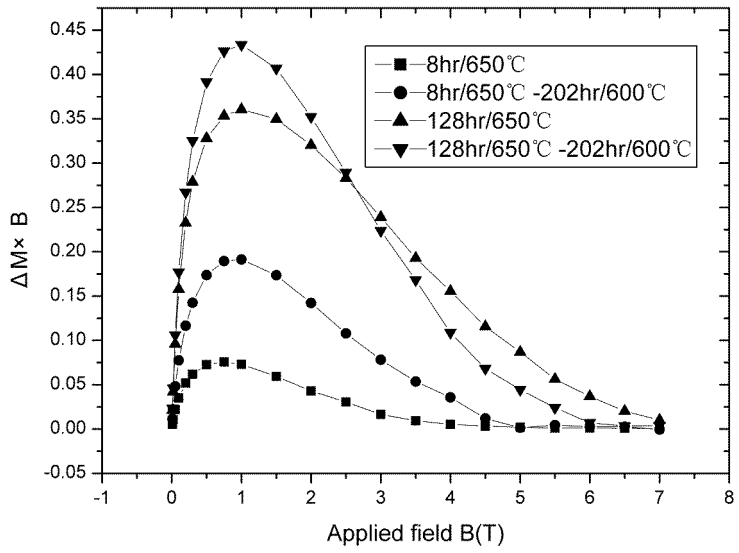

(b) AST wire

Fig.4-36 The (ΔM×B)-B curve comparisons between two-step and one-step reactions

From Fig.4-36 (a) and (b) it can be noted that the NIN wire and AST wire have the same variation in which the (ΔM×B)-B curve of 8hr sample has a large up-and-right shift from one-step to two-step reaction, indicating the enhancement of flux pinning force. The maximum F_P position also has a visible increase. However, the (ΔM×B)-B curve of 8hr sample of two-step reaction has a visible shift down at high-field section. This may be caused by too much grain coarsening of A15 phase. The results indicate that two-step reaction may accelerate the phase formation rate and strengthen the flux pinning force faster than one-step reaction, but for full-reaction situation it can not increase the high-field F_P.

4.3.3.6 Irreversibility Field H* Values

The selected NIN and AST wire samples were measured for the irreversibility field H* values by means of two ways: one is to use the ΔM-B curve when ΔM tends to be zero; the other is the Krammer extrapolation. The results are also divided into the reaction temperature influence and the reaction time influence.

(1) The reaction temperature influence

The two wire samples heat-treated at four different temperatures for 128hrs were measured for the H* values which are included in Table 4-7.

Table 4-7 The H* values for NIN and AST wire samples heat-treated at different temperatures

NIN sample	H* value (T)		AST sample	H* value (T)	
	12K	14K		12K	14K
600ºC /202hr- 650ºC /128hr	6.3	---	600ºC/202hr- 650ºC/128hr	5.9	---
650ºC/128hr	6.3	3.8	650ºC/128hr	6.2	3.8
675ºC/128hr	6.4	3.8	675ºC/128hr	6.3	3.9
700ºC/128hr	6.3	3.8	700ºC/128hr	6.4	3.8
725ºC/128hr	6.3	3.9	725ºC/128hr	6.3	3.8

From Table 4-7 it can be seen that the H* values for both NIN wire and AST wire heat-treated at different temperatures for full-time reaction have very small difference.

(2) The reaction time influence

The three sets of NIN and AST wire samples were obtained the H* values which are included in Table 4-8.

Table 4-8 The H* values for NIN and AST wire samples heat-treated for different times

NIN sample	H* value (T)		AST sample	H* value (T)	
	12K	14K		12K	14K
600°C/202hr- 650°C/8hr	5.4		600°C/202hr- 650°C/8hr	4.5	
600°C/202hr- 650°C/32hr	6.2		600°C/202hr- 650°C/32hr	5.2	
600°C/202hr- 650°C/74hr	6.3		600°C/202hr- 650°C/74hr	5.6	
600°C/202hr- 650°C/128hr	6.3		600°C/202hr- 650°C/128hr	5.8	
600°C/202hr- 650°C/200hr	6.3		600°C/202hr- 650°C/200hr	6.2	
650°C/8hr	4.7		650°C/8hr	4.3	
650°C/32hr	5.7		650°C/32hr	5.0	
650°C/74hr	6.3		650°C/74hr	6.2	
650°C/128hr	6.3		650°C/128hr	6.3	
650°C/200hr	6.3		650°C/200hr	6.3	
675°C/8hr	5.9	3.3	675°C/8hr	4.9	2.8
675°C/32hr	6.3	3.7	675°C/32hr	5.7	3.5
675°C/74hr	6.3	3.7	675°C/74hr	6.0	3.8
675°C/128hr	6.4	3.8	675°C/128hr	6.3	3.9
675°C/200hr	6.4	3.9	675°C/200hr	6.3	3.9

It can be seen from Table 4-8 that the H* values are lower for both wire samples of heat duration shorter than 32hrs. After then, the H* maintains the value with almost no variation. Comparing NIN and AST wire, it is noted that for shorter time treated samples, the H* values of AST wire are lower than those of NIN wire. We can also find that the full-reacted samples have nearly the same H* values (6.3~6.4T, 12K; 3.8~3.9T, 14K) for both wires, no matter what HT procedures they underwent.

4.3.3.7 Results Comparison between Perpendicular Field and Parallel Field

The above measurements were carried out with the sample axis perpendicular to the applied field (perpendicular field). In addition, some samples were selected to do the measurement with their axis parallel to the applied field (parallel field) in order to compare the effect of the sample orientation on the magnetization properties.

(1) Critical temperature T_C

Some of the NIN and AST wire samples were measured for the T_C values with the two sample orientations, as shown in Table 4-9.

Table 4-9 The T_C comparison between perpendicular field and parallel field

NIN sample	T_C (K)		AST sample	T_C (K)	
	perpendicular field	parallel field		perpendicular field	parallel field
650ºC/128hr	17.3	17.3	650ºC/128hr	17.2	17.2
675ºC/8hr	16.9	16.9	675ºC/8hr	16.7	16.7
675ºC/32hr	17.2	17.2	675ºC/32hr	17.1	17.1
675ºC/128hr	17.3	17.4	675ºC/128hr	17.4	17.4
700ºC/128hr	17.3	17.3	700ºC/128hr	17.3	17.3

From Table 4-9 it can be seen that the T_C values are nearly the same for both sample orientations. This means that the T_C value is independent to sample orientation and is only dependent on the composition of the superconducting phase.

(2) Irreversibility temperature T*(B)

The selected NIN and AST wire samples were also measured for the T*(B) values with the two sample orientations. The results are shown in Figs.4-37 and 4-38.

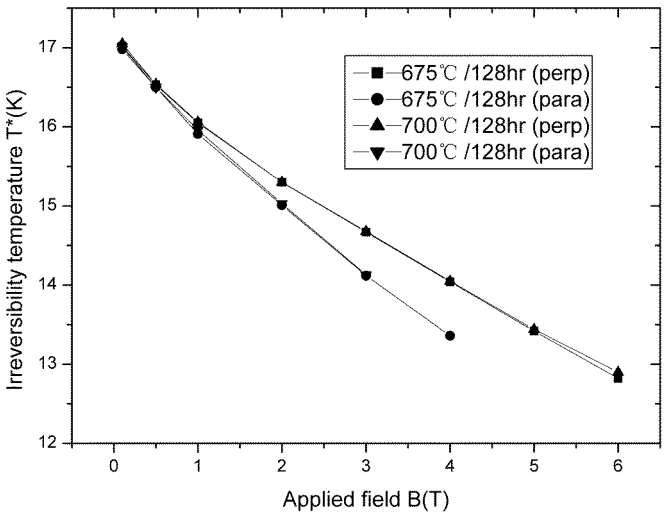

(a) NIN wire

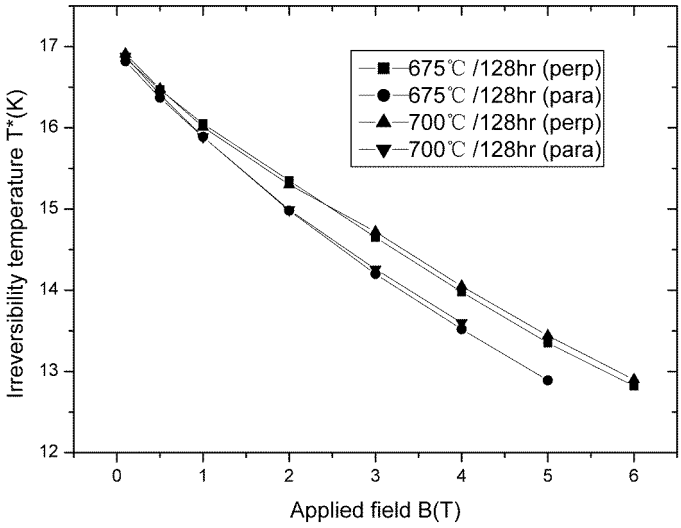

(b) AST wire

Fig.4-37 The T*(B) comparison between the two sample orientations for samples heat-treated at different temperatures

From Fig.4-37 (a) and (b) it can be found that the two wire samples of 675ºC/128hr and 700ºC/128hr have lower T*(B) values at parallel field than those at perpendicular field, and the T*(B) difference is enlarged with the increase of the applied field.

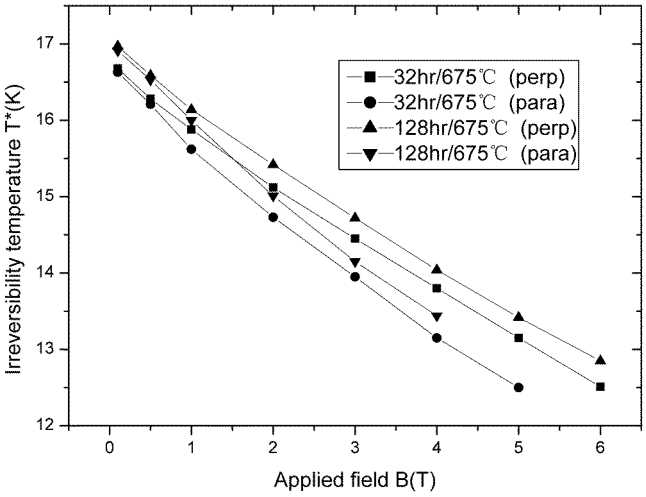

(a) NIN wire

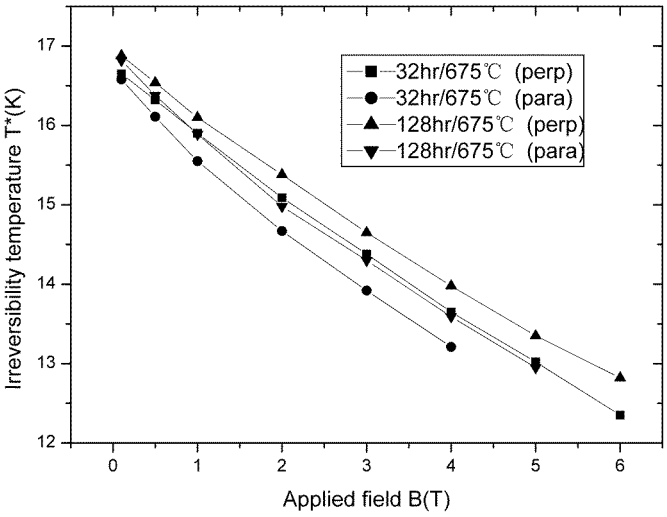

(b) AST wire

Fig.4-38 The T*(B) comparison between the two sample orientations for samples heat-treated for different times

From Fig.4-38 (a) and (b) we can find the same characters. The T*(B) lines at parallel field are all below those at perpendicular field for both wire samples heat-treated for different times. And again, the T*(B) difference is enlarged with the field increase. Therefore, the T*(B) values are affected by the sample orientations.

(3) ΔM-B curves

The selected NIN and AST wire samples were yet plotted the ΔM-B curves which are shown in Figs.4-39 and 4-40.

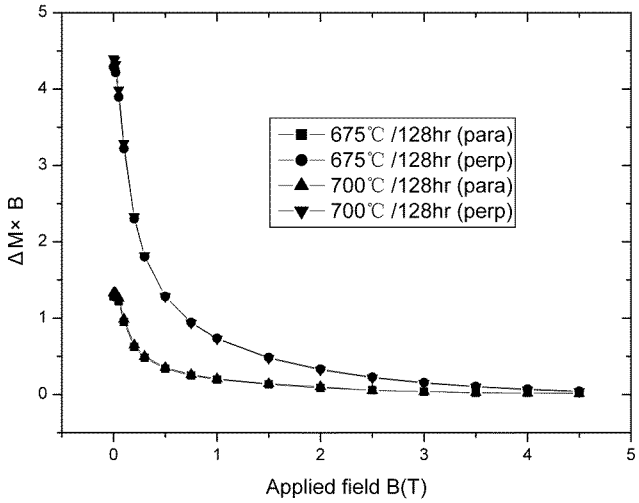

(a) NIN wire

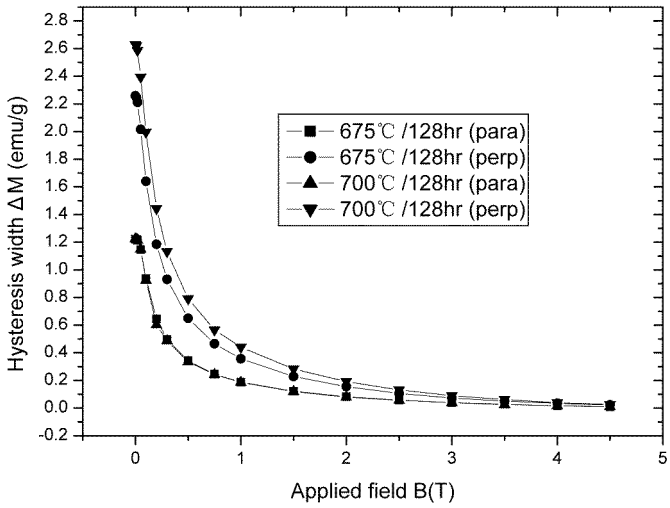

(b) AST wire

Fig.4-39 The ΔM-B comparison between the two sample orientations for samples heat-treated at different temperatures

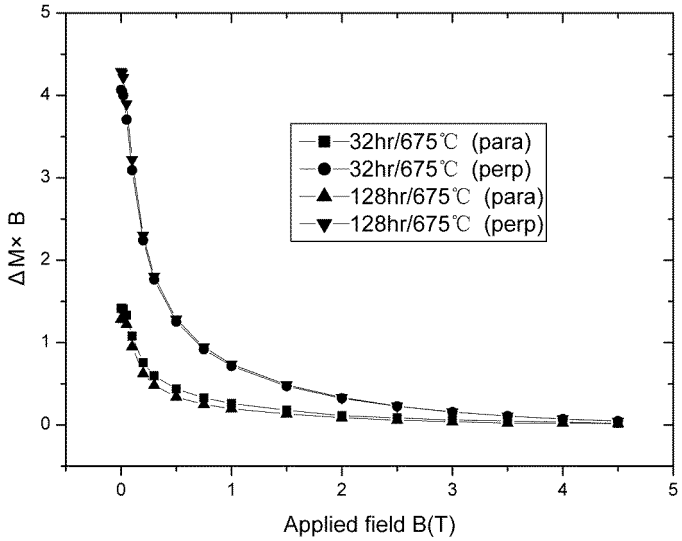

(a) NIN wire

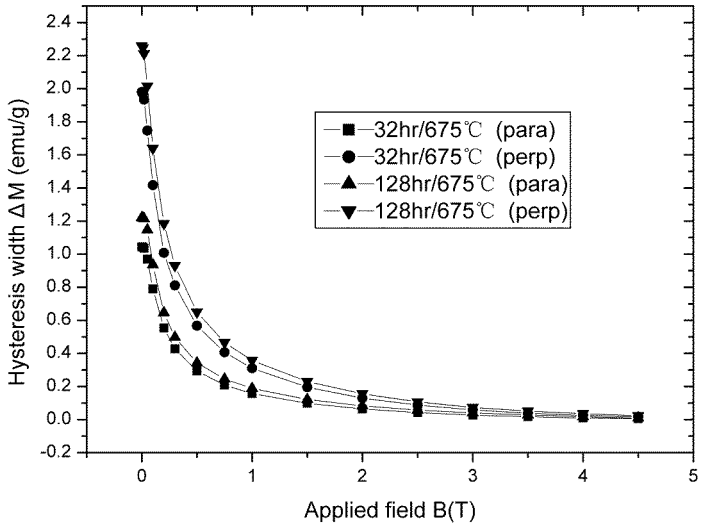

(b) AST wire

Fig.4-40 The ΔM-B comparison between the two sample orientations for samples heat-treated for different times

From Figs.4-39 and 4-40 it is clearly seen that the ΔM-B curves at perpendicular field are much higher than those at parallel field for both wires heat-treated at any conditions.

(4) (ΔM×B)-B curves

With the ΔM values of above samples, the (ΔM×B)-B curves were plotted in Figs.4-41 and 4-42.

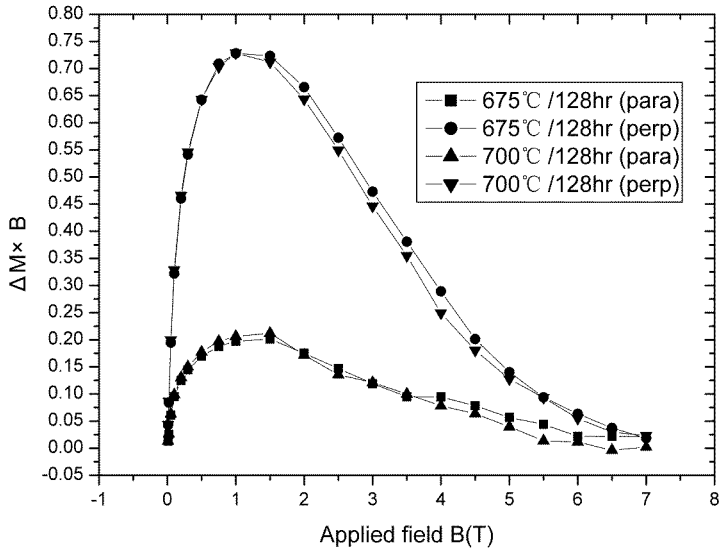

(a) NIN wire

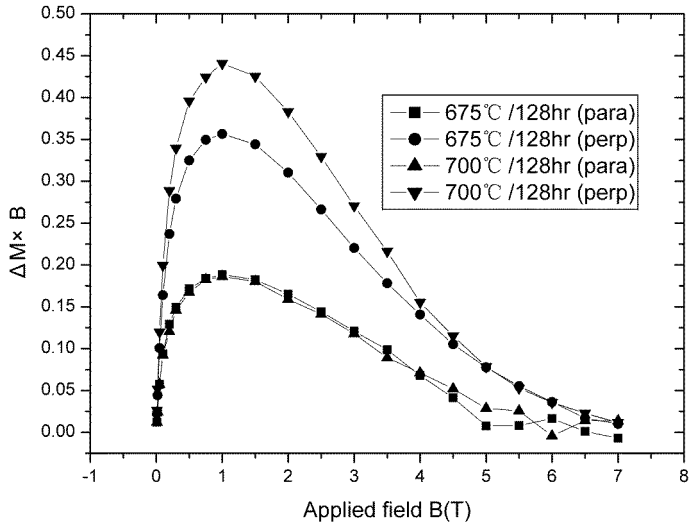

(b) AST wire

Fig.4-41 The (ΔM×B)-B comparison between the two sample orientations for samples heat-treated at different temperatures

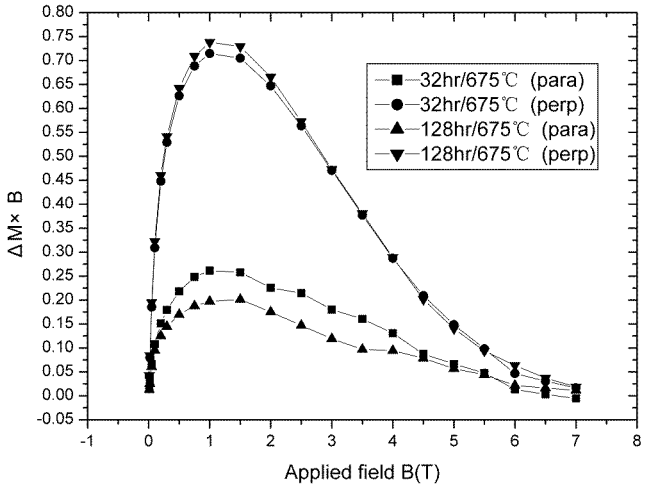

(a) NIN wire

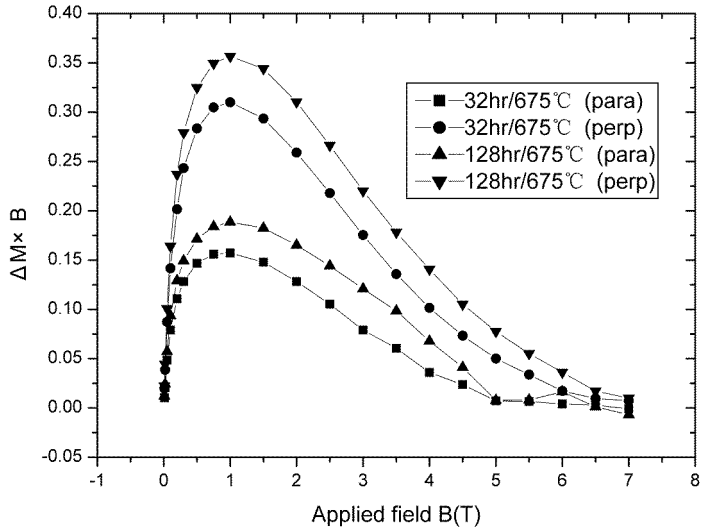

(b) AST wire

Fig.4-42 The (ΔM×B)-B comparison between the two sample orientations for samples heat-treated for different times

From Figs.4-41 and 4-42 it can also be clearly seen that the (ΔM×B)-B curves at perpendicular field are much higher than those at parallel field for both wires heat-treated at any conditions.

4.3.4 Discussion

4.3.4.1 Heat Treatment Optimization of MF wires

To optimize the heat treatment of the two MF wires through magnetization technique, it is necessary to describe the A15 phase formation progress of internal-Sn wire and the features of magnetization measurement.

It is well known that in the internal-Sn MF Nb_3Sn wire configuration, the Sn core is located within the center of a bundle of Nb filaments. After the Cu-Sn alloying process, all the Nb filaments are surrounded by various Cu-Sn binary phases. The A15 phase formation progress is like this: the Nb filament in the wire first develops a radial gradient layer of Nb-Sn A15 phase within which the Sn content is distributed with higher concentration at the outside of filament. This distribution character can be obviously seen with the SEM and EDS analysis in section 4.5.3.1. With the progress of heat reaction the A15 phase gradient layer formed is continuously to grow and the Sn concentration gets enriched. Until the filament reacts completely, the gradient layer will flatten gradually and its composition becomes more and more homogenous. We can also clearly find the phase formation progress in section 4.5.3.1.

Since the high Sn-content composition is located on the filament outside layer, it is indeed that only the outer layer of A15 phase is measured by magnetization method due to the shielding of the lower-Sn part by the high-Sn part. Meaningfully, this feature of magnetization measurement can be used to evaluate the development of A15 layer with the HT time variation. It can obviously indicate the reaction time effect for a fixed-temperature treatment. However, in order to reflect the reaction temperature influence, full-time treated samples with uniform phase composition across the filaments should be chosen. Measuring the filament outer part is the indication of measuring the whole filament. All the sample selection in magnetization measurement is in accordance with this criterion.

The optimization of heat treatment for NIN and AST wire is concerned hereafter. Firstly, the temperature optimization is considered. The selected samples are all heat-treated at different temperatures for 128hr complete reaction and their A15 phase compositions have homogenous distribution which will also be confirmed by the SEM and EDS analysis later.

From the results in sections 4.3.3.1 and 4.3.3.3, we have seen that NIN wire and AST wire have the same characters in which the T_C (B) and T*(B) values have very small

variations, and the M-T transition curves are nearly overlapped for the samples of different reaction temperatures. These T_C-related properties are chiefly determined by the amount (quantity) and composition (quality) of A15 phase. For the selected samples of temperature influence, all the filaments inside the wire were completely reacted and transformed to A15 phase, i.e., the A15 quantity is the same, then the A15 composition is the determined factor. From the fact that the T_C-related superconducting properties have no obvious change at different HT temperatures, it can be concluded that the A15 phase composition of Nb_3Sn wire is temperature-independent.

The reaction temperature optimization is thus reflected in F_P-related properties. From the results in sections 4.3.3.4 and 4.3.3.5 it is known that NIN wire has achieved the highest inductive J_C and the best flux pinning performance at HT temperature of 650ºC or a little higher, from which the NIN wire is suitable to be heat-treated at 650ºC-675ºC. AST wire, however, has obtained the highest values of flux pinning performance and inductive J_C at HT temperature from 675ºC to 700ºC, so the AST wire is favorable to do the heat treatment at this temperature range.

Secondly, the HT time optimization is discussed. From the results in sections 4.3.3.1 and 4.3.3.2 the same characters for both NIN wire and AST wire can be found that with the extension of HT time from 8hrs to 128hrs at 675ºC, the T_C(B) and T*(B) gradually increase to the highest values and then keep the same positions after 128hr reaction. The results in 4.3.3.3 also demonstrate that T_C values and M-T transition curves reach to the highest magnitude and keep almost no changes after complete reaction. These variations of T_C-related properties obviously reveal the progress of A15 phase formation and development, from which it is also probed that the A15 composition is uniformly distributed and does not vary after complete heat treatment.

The HT time can also be optimized from the measurements of F_P-related properties. From the results in sections 4.3.3.4 and 4.3.3.5 it is known that the inductive J_C and the flux pinning performance of the two wires were promoted to highest values with the extension of the reaction time to 128hrs when small decreases happened afterwards. It can be explained that the F_P-related performances are dependent on the A15 composition and crystalline grain size. If the composition no longer changes, the grain size is then the primary factor. Over

extension of reaction time coarsens the grain size as the Sn concentration in A15 composition did not change any more. Large grain dimension weakens flux pinning force and thus decreases critical current density J_C. Therefore, it is very reasonable for the two wires to be heat-treated no longer than 128hrs.

The above interpretation demonstrates clearly that the 650°C/128h of NIN wire and 675°C/128h of AST wire are the most favorable heat treatment processes for the two ITER-type internal-Sn Nb_3Sn superconductor wires due to the best A15 phase composition and flux pinning situation.

4.3.4.2 Effect of Heat Treatment on Wire Superconductivity

The heat treatment of Nb_3Sn superconducting wire includes two processes: (1) alloying the Cu and Sn, and (2) form the Nb-Sn A15 phase. The Cu-Sn mixing process has been substantially investigated and a common viewpoint is that the final primary superconducting properties (including T_C, H^*, H_{C2} or J_C) in fully reacted wire have not been affected no matter what reaction temperature, duration and up-heating rate during the Cu-Sn alloying are used [23]. In practice, some Cu-Sn alloying procedures are designed only for the technological needs, for example, allowing low melting phases to transform into higher melting temperature phases before the A15 reaction treatments. The Cu-Sn alloying process of 210°C/50hr+340°C/25hr was chosen in this study in accordance with ITER's requirement.

The significant effect on superconducting properties is the A15 phase reaction process, in which one of the most important factors is the HT temperature selection. Firstly, the configuration design of the wire composite should be seriously considered in choosing the temperature. For a bronze-processed wire, the temperature should be a little higher to promote the Sn diffusion as the Sn concentration in bronze is usually lower. The PIT-processed wire also needs a higher reaction temperature, because there is no Cu in the powder to reduce the Nb_3Sn formation temperature. Comparatively, the internal-Sn processed wire has not these disadvantages and is, therefore, suitable to be heat-treated at lower temperature.

Secondly, the component composition of the wire composite also should be paid much attention in consideration of the HT temperature, mainly focusing on the third-element addition, i.e., the alloyed element property and the amount added. Generally speaking,

alloying Sn core or alloying Nb filaments or alloying both is beneficial to some of the superconducting performances. Much research has been made in this respect. For example, adding Ti in Sn core has been proved to increase the Sn diffusion rate, decrease the reaction temperature and enhance the A15 phase formation. Therefore, the wire with Ti alloyed in Sn should choose lower reaction temperature, as in the case of NIN wire. On a contrary, the one without Ti addition needs higher phase formation temperature as in the case of AST wire. The results in this experiment have confirmed that NIN wire and AST wire are suitable to be heat-treated at 650°C and 675°C, respectively. Indeed, the AST wire has 7.5wt%Ta alloyed in Nb. The fact that the alloyed Ta did not obviously enhance the A15 formation may be due to two reasons. One is that the Ta dopant in Nb does not promote the Sn diffusion in Cu-Sn phases and lowers the phase formation temperature. The other is that small amount of Ta alloyed in Nb (i.e. less than 2wt%) may promote the H_{C2} and H*, but over addition may retard the performance enhancement.

Lastly, the most important factor in consideration of the HT temperature is the maximizing of critical current density J_C and flux pinning properties. It is well known that lower reaction temperature produces smaller grain size, resulting in the enlargement of boundary area and then the flux pinning force. However, lower reaction temperature not only reduces the dynamics of Sn diffusion and reaction, prolonging the reaction time, but also tends to make the grain crystalline profile inhomogenously distributed, which may lower the flux pinning force and even J_C. As an example, the AST sample heat-treated at 650°C has lower superconducting performance. On the other hand, although the increase of reaction temperature may accelerate the Sn diffusion and A15 formation rate, the grain size enlargement is inevitable, which, to some extent, will also weaken the flux pinning and reduce the J_C. The two samples of NIN and AST wires heat-treated at 725°C had rather poor superconducting performance due to this reason. From above discussion it can be seen that the optimization of HT temperature is actually to balance the increase of phase formation rate and the enhancement of flux pinning force.

Another key factor for A15 phase formation is the HT time. On the one hand, the heat duration should be long enough to ensure not only all Nb filaments reacted completely, but the formed A15 phase has a homogenous composition as well, as in the case of 128hr

duration in this study. On the other hand, over duration may coarsen the grain size too much, leading to the decrease of flux pinning force and even the J_C property, as in the case of 200hr duration in this study. As a whole, for the balance of increasing reaction rate and enhancing flux pinning situation, the Nb_3Sn MF superconducting wire is favorable to be heat-treated at higher temperature for shorter time and at lower temperature for longer duration.

The result comparisons between two-step and one-step reaction are concerned herewith. From the result analysis in sections 4.3.3.4 and 4.3.3.5 it can be found that so long duration of 600°C/202hr actually did not improve the final superconducting property of the wires. Combining the other researches described in section 1.5, we can conclude that any heat treatment procedures before A15 phase formation has no influence on the final superconducting properties of the internal-Sn Nb_3Sn wire.

4.3.4.3 About Sample Orientation in SQUID Magnetization Measurement

There are two sample orientations in SQUID magnetization measurements: perpendicular to the applied field and parallel to the field. M. Suenaga et al. [65] used the perpendicular field position, while the literatures [89] and [94] chose the parallel way to do their measurements. What is the difference between the two sample orientations? Which one is better? For this purpose, the two orientation ways were arranged in this study and the result comparisons were demonstrated in section 4.3.3.7.

From the section 4.3.3.7 it is known that the critical temperature T_C has no relationship with the sample orientation. This is because the T_C is composition-dependent. Since the A15 phase composition in the sample is the same for any orientations, the T_C values certainly have no difference. Except for T_C, other field-related properties were obviously affected by the sample positions. The irreversibility temperature T*(B) values at parallel field are always below those at perpendicular field, and the T*(B) difference is enlarged with the field increase. The ΔM-B curves and the (ΔM×B)-B curves are all much higher at perpendicular field than those at parallel field. These seem to say that all the differences of the superconducting performances are caused by the field direction applied to the sample. Actually, this is not the case.

Here the Bean model is introduced for analysis. In the Bean model formula, the relation

between the J_C and M depends on the shape and the size of the sample. For an infinite cylinder with the field parallel to its axis, the relationship is:

$$J_C=2(\Delta M/D) \qquad (4\text{-}3) \qquad \text{(in SI unit)}$$

where D is the diameter of the cylinder. When the shape is not in the parallel way, this formula has to be introduced some corrections, and the D should be the effective diameter.

For MF Nb_3Sn wires, the filament is like a cylinder. If the samples are positioned in the same orientation, such as the perpendicular way, the shape factor has the same effect, so that the obtained ΔM values can be used to compare the relative magnitude of J_C. However, if the samples are positioned in different ways, the shape factor should be considered seriously.

In the experiment of 4.3.3.7, we have known that the values of field-related properties, i.e. ΔM are always higher at perpendicular field than those at parallel field. On the other hand, the effective filament diameter is also higher at perpendicular field. Furthermore, the Nb_3Sn superconducting phase is formed through solid-state reaction, it is easy to infer that the phase configuration in the filament is not isotropic, such that the formula (4-3) should be added another correction. Therefore, the higher ΔM value does not mean higher J_C at different sample orientations. In other words, the ΔM values at different sample orientations cannot be used to compare the inductive J_C and F_P.

Comparing the two sample orientations in SQUID magnetization measurement, the perpendicular field is more advantageous. In magnets, wires are wound perpendicular to the field. The ITER project also requires the J_C measurement in perpendicular way. Furthermore, it is known that the inductive supercurrent circulates along the filament length when the sample is positioned in the perpendicular way, while the current will circulate around the filament if the sample is fixed in parallel way. From the way of the transport current flowing along the wire length, the perpendicular orientation reflects the real case. In addition, since the magnitude of the signal is stronger at perpendicular field, it is more convenient to obtain data in this way. Therefore, the results in perpendicular field are more practical and useful.

4.3.5 Conclusion

The magnetization measurements with a SQUID magnetometer are useful to optimize the HT process. The HT optimization is actually to search for the best reaction conditions in

which the A15 phase composition approaches the stoichiometric Nb_3Sn and, at the same time, the flux pinning property reaches the best situation. The former can be examined by a warming and cooling cycle at a fixed field and by maximizing the determined T_C and T* values. The later can be evaluated by cycling the magnetic field at a constant temperature and by analyzing the variation of hysteretic loops.

By means of optimizing the HT process, the two ITER-type internal-Sn MF Nb_3Sn wires have found the most favorable reaction conditions: 650°C/128hr for NIN wire and 675°C/128hr for AST wire, with which the two wires have achieved the best A15 phase composition and flux pinning situation.

The analysis of T_C and T* values has shown that the final A15 composition of Nb_3Sn superconductors is reaction-temperature independent. The temperature influence only changes the phase formation rate and grain crystalline configuration, but does not affect the final A15 composition. This conclusion is for the first time reported in this thesis.

The result comparisons between two-step and one-step reactions have proved that any heat treatment procedures before A15 phase formation have no influence on the final superconducting properties of Nb_3Sn wires.

In SQUID magnetization measurement, the sample orientation has nearly no influence on the composition-related superconductivities, such as T_C, and the field-related properties, such as inductive J_C and F_P. Compared with parallel way, the perpendicular field orientation is more practical and useful.

4.4 In-Situ Neutron Diffraction Analysis of Multifilament Wires

4.4.1 Introduction

Neutron diffraction technique utilizes the diffraction phenomena of neutrons to determine the atomic structure of a material. The diffraction occurs when the selected waves of quantum neutron particles encounter the atoms that serve as diffraction obstacles. If the obstacle substance is formed during a period of time, its reaction progress and phase variation can be recorded by this technique. For the Nb-Sn-Cu ternary system of Nb_3Sn composite wire, the Cu-Sn alloying process and the A15 phase formation process take a long time to react, usually a few hundreds hours required. Therefore, the neutron diffraction technique can be used to continuously examine the phase variation progress. This is called in-situ neutron diffraction measurement which is the main method for our ITER-type MF wire analysis in this thesis.

However, the reaction time of the Nb_3Sn composite wire is too slow that an entire heat treatment may take over ten days. Because the neutron source is very expensive, it is impossible to take so long time for the measurement. As the Cu-Sn alloying progress is complicated and that there are possibly seven Cu-Sn intermediate phases to develop or to be transformed, the whole Cu-Sn alloying progress has been examined with the in-situ neutron technique. For A15 phase formation only happens the quantity variation after the phase is formed. So, it is not necessary to examine the whole progress. It is enough for phase formation kinetics study if enough time is taken to examine the A15variation trend. In this experiment, we took approximately 24hrs for A15 phase measurement in-situ.

4.4.2 Sample Preparation and Experiment

The NIN and AST wires were cut into ~60mm length short pieces respectively and the ends of each piece have been crimped along about 3mm. Forty of the short pieces were introduced in one quartz tube of 12mm diameter. The quartz tube was then fixed in a special furnace which can run heating program and neutron examination at the same time. Argon atmosphere was put through the quartz tube with a bubbling apparatus during the whole experiment for sample protection.

The following heat treatment program was arranged, in which the sample was heated at 60°C/hr from RT to 460°C and then to 660°C in 40hrs, and kept in 660°C for 24hrs before rapidly cooling down.

Neutron diffraction patterns have been recorded every 5 minutes on the D1B diffractometer of the ILL-Grenoble, at a wavelength of 2.524 Å. Refinements have been done by the Rietveld technique using the Fullprof program. The structures of the phases observed have been refined with the following starting parameters. The Cu and α-Cu phases, space group (SG) Fm3m, *a*=3.610 Å and *a*=3.618 Å respectively, preferred orientation [100]. The Nb and Ta phases, SG=Im3m, *a*=3.300 Å, preferred orientation [100]. The γ-CuSn phase as Cu_3Sn, SG=Fm3m, *a*=3.669 Å. The δ-CuSn phase as $Cu_{41}Sn_{11}$, SG=F-43m, *a*=18.148 Å. The Nb_3Sn phase, SG=Pm3n, *a*=5.293 Å, preferred orientation [100]. For each phase, only the scale factor (SF), the cell parameter *a* (all phases being cubic) and the preferred orientation (PO) have been fitted with the instrument parameters known from calibration experiments. The diffractograms recorded by neutron diffraction reflect the whole volume sample contained in the quartz tube.

4.4.3 Results and Analysis

The samples of the two MF wires were carried out the in-situ neutron diffraction measurement with the diffraction patterns being recorded continuously. In order to observe the phase development and transformation, the results have been depicted in three-dimensional (3D) or two-dimensional (2D) patterns.

Figs.4-43 and 4-44 show the 3D patterns of the neutron diffraction of the two wires.

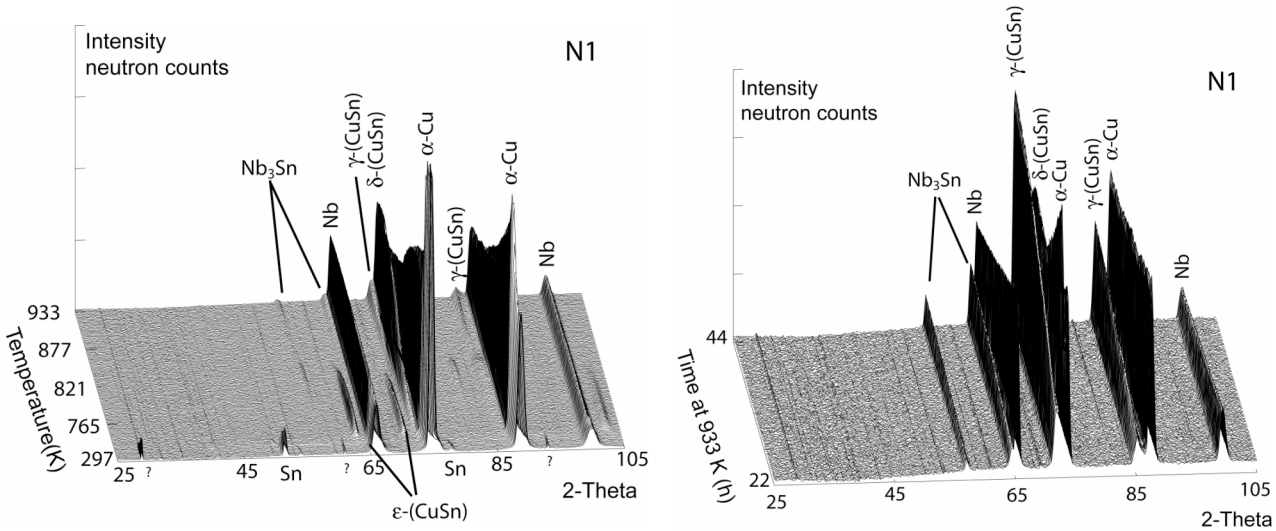

(a) from RT to 660°C (b) 24hr duration at 660°C

Fig.4-43 The neutron diffraction 3D patterns of NIN wire

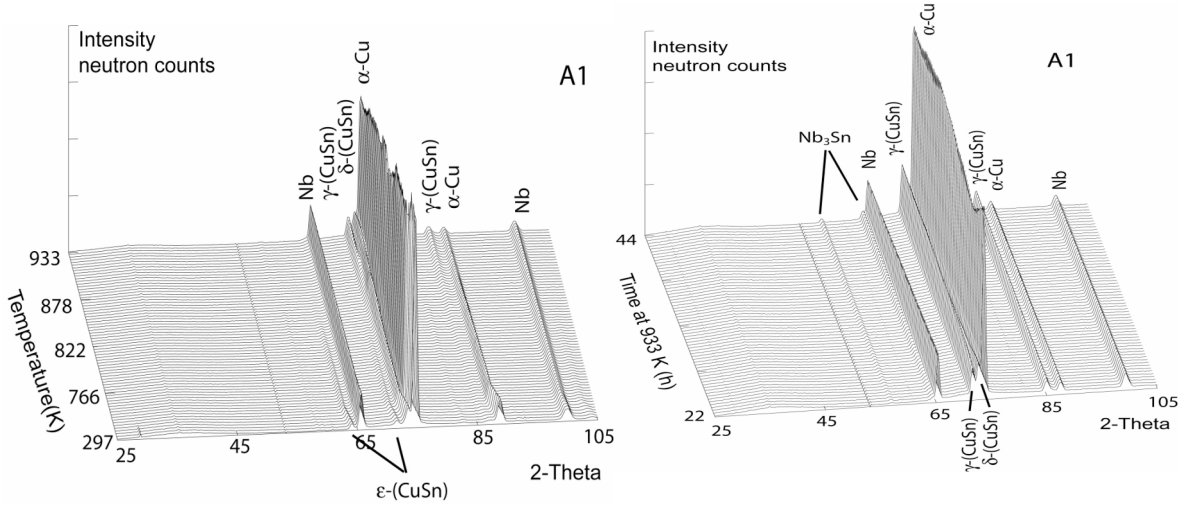

(a) from RT to 660°C (b) 24hr duration at 660°C

Fig.4-44 The neutron diffraction 3D patterns of AST wire

The (a) figures reflect the phase variation of Cu-Sn alloying progress, while (b) figures primarily exhibit the A15 phase formation progress.

For clearly demonstrating the continuous variation of the phases, the (a) figures and (b) figures are plotted together and shown in 2D patterns, seeing Figs.4-45 and 4-46.

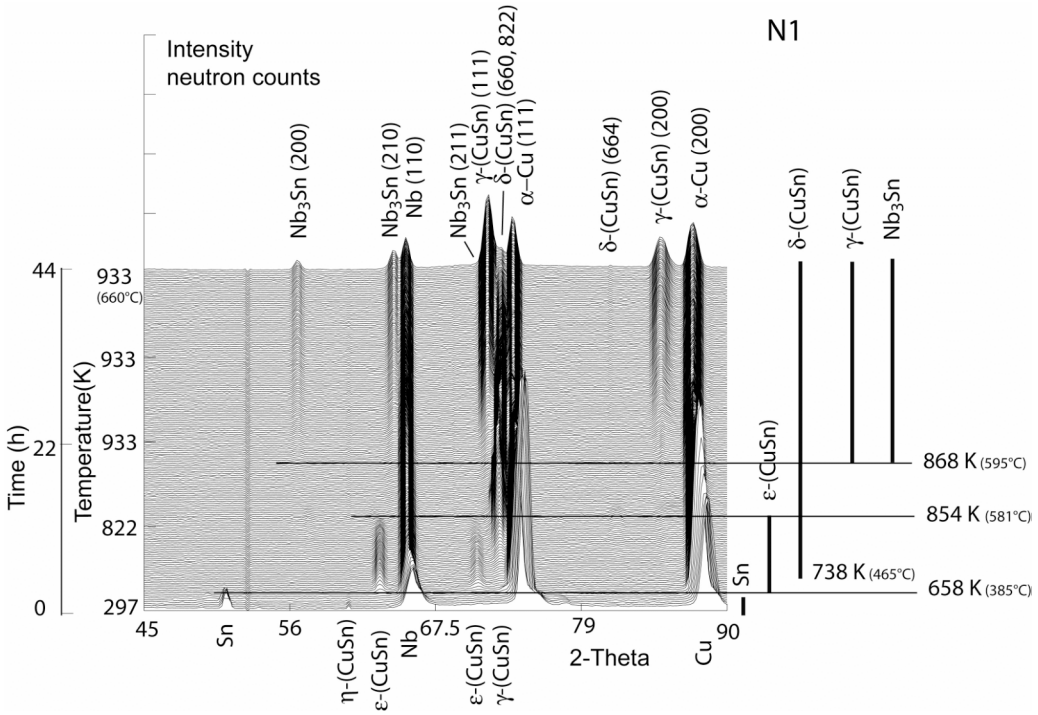

Fig.4-45 The neutron diffraction 2D pattern of NIN wire

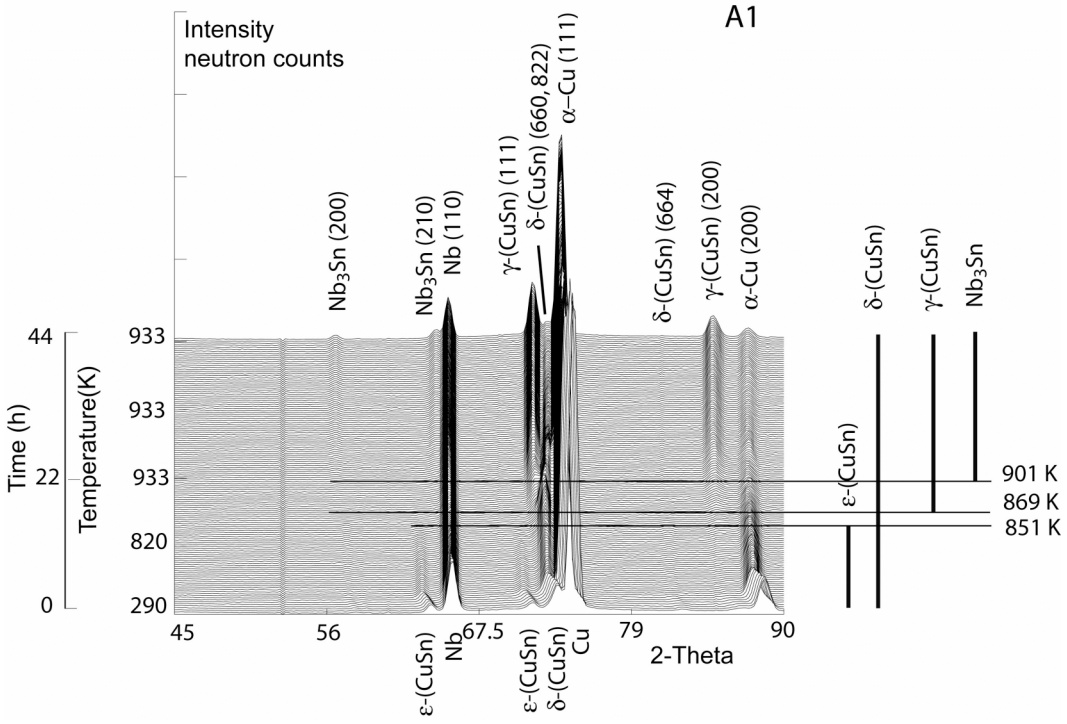

Fig.4-46 The neutron diffraction 2D pattern of AST wire

First, the Cu-Sn alloying progress is analyzed. From Figs.4-43(a) to 4-44(a) and Figs.4-45 to 4-46 one can see the following phase variation progress. The Cu, Sn and Nb (Ta)

are the initial phases observed. The η-CuSn phase develops under the temperature of 210°C and is transformed into ε-CuSn phase with the diffusion of Sn. The ε-CuSn phase is formed at about 385°C, keeping a long period of time, and disappears at around 580°C. The δ-CuSn phase appears at about 450°C and its amount keeps increasing during a long time period. With the elevation of reaction temperature, δ- CuSn phase gradually disappears and transforms into γ-CuSn phase and Nb_3Sn.

Observing the A15 Nb_3Sn phase formation progress, from Figs.4-43(b) to 4-44(b) and Figs.4-45 to 4-46 it can be found that the Nb_3Sn phase appears at about 600°C and keeps growing rapidly within the 24hr duration time, being reflected by the fast increase of neutron intensity.

Comparing the in-situ neutron diffraction patterns of NIN wire and AST wire, it is noticed that they have the same phase formation and transformation rule, but the NIN wire has much stronger neutron intensity than AST wire does, not only in Cu-Sn alloying procedure but also in the Nb_3Sn formation progress. That is to say, NIN wire has faster phase formation rate than AST wire in the same HT conditions.

4.4.4 Discussion

From the results of neutron diffraction measurement it can be found that both Cu-Sn alloying and Nb_3Sn phase formation have their own variation rules, from which we can search for the kinetics information of the variations. For instance, the neutron intensity variation of γ-CuSn phase of NIN wire is plotted as a function of reaction time. Fitting the plots, seeing Fig.4-47, we can find that the γ-CuSn phase varies in a parabolic manner, which is in accordance with other researches. Due to the short time interval analyzed in this study, the fit should be taken with caution, but the trend is in agreement with a logarithmic kinetics variation of phase formed as a function of time.

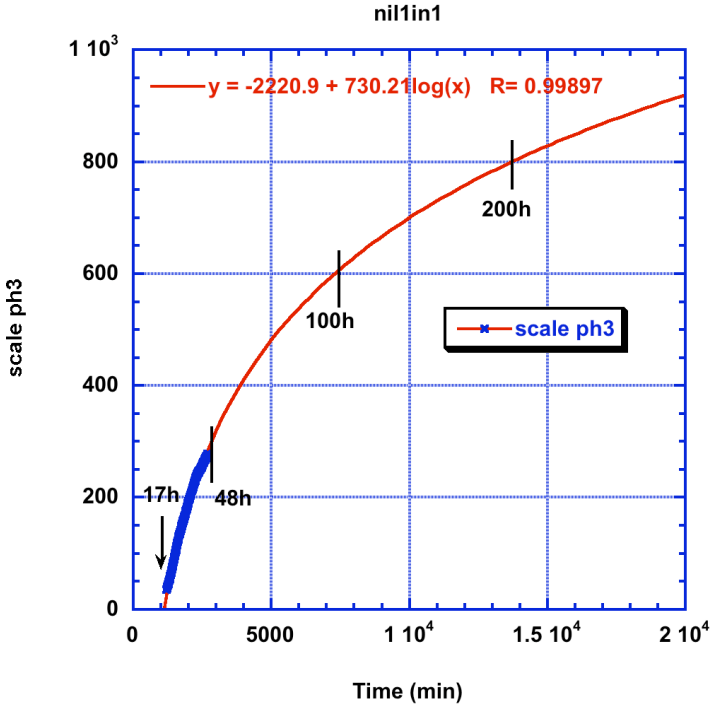

Fig.4-47 The neutron intensity fit line of γ-CuSn phase as a function of reaction time for NIN wire

In this experiment, we emphasize the kinetics of Nb_3Sn phase formation, for which the neutron diffraction intensities of the two wires were plotted with the variation of the reaction time, as shown in Fig.4-48. Fig.4-49 exhibits the fitted lines of the variations, with the same limitations as above.

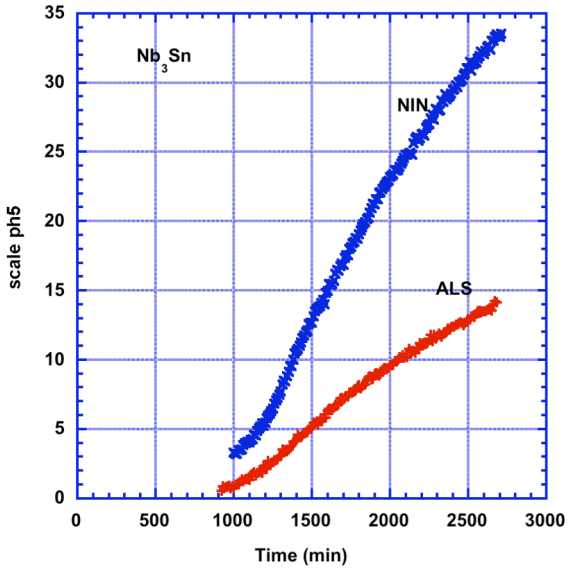

Fig.4-48 The neutron diffraction intensities of Nb_3Sn phase as a function of reaction time for NIN and AST wires

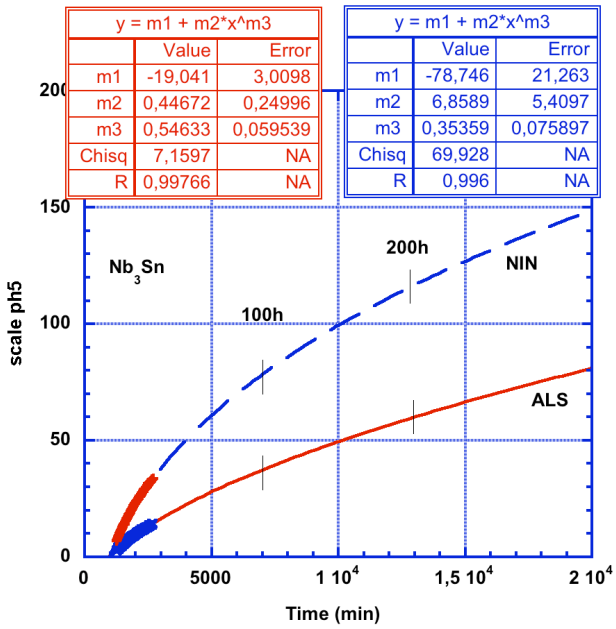

Fig.4-49 The fitted lines of the Nb_3Sn phase variation in Fig.4-48 for NIN and AST wires

From the above results of neutron diffraction measurement it is clearly seen that the phase formation rates of NIN wire are higher than those of AST wire for both Cu-Sn alloying and Nb_3Sn phase formation progresses.

In order to interpret these results, the third-element alloying is primarily considered. We know that the two wires both have third-element alloyed in the composites, but with different alloying manner. The AST wire has 7.5wt%Ta alloyed in Nb, but nearly pure Sn cores. On the contrary, the NIN wire has 2wt%Ti alloyed in Sn core, but nearly pure Nb filaments. Comparing the alloyed Ta in Nb filaments with the alloyed Ti in Sn core, the later seems to be more effective in promoting the phase formations. There was a report in which the Ta addition in Nb filaments can increase the upper critical field H_{C2}, but has no dynamic promotion to the Nb_3Sn phase formation [132]. On the other hand, the Ti addition in Sn core has two effects. One is to harden the Sn core, reducing the drawing-loss and Sn-leak during heat processing. The other, which is the most important we are concerned here, is to accelerate the Sn diffusion and reaction rate. The increase of Sn diffusion rate substantially improves the development and transformation of various Cu-Sn phases. This can be proved by the fact that the neutron diffraction intensities of the Cu-Sn phases of NIN wire increase

more rapidly than those of AST wire during the Cu-Sn alloying progress. Further more, the increase of Sn reaction rate also obviously promote the A15 phase formation rate, which can be confirmed by the fact that the neutron diffraction intensity of Nb_3Sn phase of NIN wire has a faster increase than that of AST wire.

4.4.5 Conclusion

In-situ neutron diffraction technique is an effective way to dynamically investigate the Cu-Sn alloying and Nb_3Sn phase formation progresses.

The Cu-Sn alloying procedure first develops η-CuSn phase which is then transformed into ε-CuSn phase. The δ-CuSn phase appears at about 450°C, increases for a long time and then gradually disappears, accompanying the formation of γ-CuSn phase. The Nb_3Sn phase develops at about 600°C and keeps growing with the increase of reaction temperature and time.

The third-element alloying is one of the main factors that affect the Cu-Sn alloying and Nb_3Sn phase formation progresses. Comparing the alloyed Ta in Nb with the alloyed Ti in Sn, the later is more effective. Small amount of Ti addition in Sn core not only promotes the development and the transformation of various Cu-Sn phases, but also increases the growth rate of Nb_3Sn phase.

4.5 Microstructure and Microchemistry Analysis of Wire Phase Formation

4.5.1 Introduction

The various phases in internal-Sn Nb_3Sn superconductors are formed by the Sn diffusion and reaction through Cu matrix and Nb filaments. The microstructure and phase formation kinetics of Cu-Sn alloying process has been sufficiently investigated [85,126,127]. In this study, the A15 Nb_3Sn phase formation is primarily concerned.

It is known that the A15 phase first develops at the interface between Nb filament and the surrounding Cu-Sn phases during the Nb_3Sn formation heat treatment. With the progress of reaction, A15 quantity (volume) and quality (Sn concentration and distribution) are

continuously growing, and the crystalline configuration, including grain size and morphology, is gradually improved. Until the filaments react completely, the A15 phase approaches a stable and equilibrium state. Different HT conditions develop different phase formation situations, which can be directly visualized with electronic microscope, and can be detected by the phase composition and Sn distribution with energy dispersion spectrum (EDS).

Much A15 phase microstructure and microchemistry analysis of internal-Sn Nb_3Sn superconductors have been studied before [104]. However, there have been few researches which substantially focus on composition and Sn distribution investigation, especially on the kinetics study of the phase formation. The main purpose of this study is to systematically investigate the phase formation progress and kinetics rule of the two ITER-type internal-Sn wires with the aid of scanning electronic microscope (SEM), field emission scanning electronic microscope (FESEM) and EDS.

4.5.2 Sample Preparation and Microscopic Measurement

The selected heat-treated samples were cut into small pieces and embedded in resin vertically before polishing. Most of the sample preparation was made in CRETA/CNRS.

The samples for FESEM observation were immersed in liquid nitrogen for a few minutes before bending, leaving the new surface for examination. This work was done in Analysis Center/NIN.

Most microstructure and microchemistry examination for MF wire samples were carried out in the Analysis Center/NIN. The phase profile, phase composition and Sn distribution were tested on a model JSM-6460 SEM, and the grain configuration was observed on a model LEO-1530 FESEM.

4.5.3 Results and Analysis

4.5.3.1 Variations of A15 Phase Formation and Sn Distribution

The incompletely-reacted samples were chosen for this measurement, aiming at observing the effect of HT temperature and time on the phase reaction progress. The two MF wires were analyzed individually.

4.5.3.1.1 *AST wire*

(1) The reaction time influence

Four samples heat-treated at 675°C for 2hr, 8hr, 32hr and 74hr were used for A15 phase observation and the cross-filament Sn distribution examination. The results are shown in Fig.4-50.

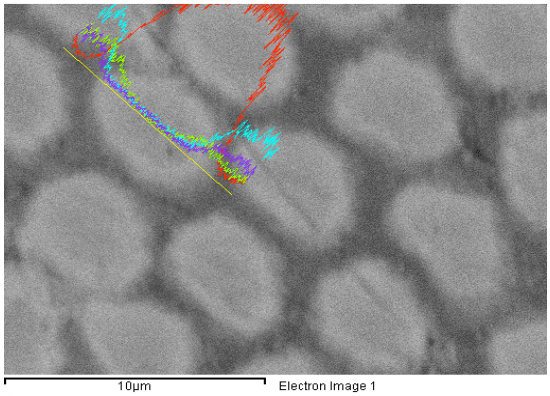

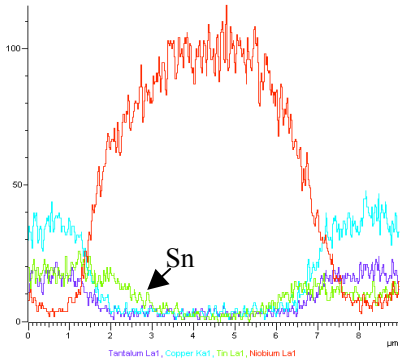

(a) 2hr/675°C

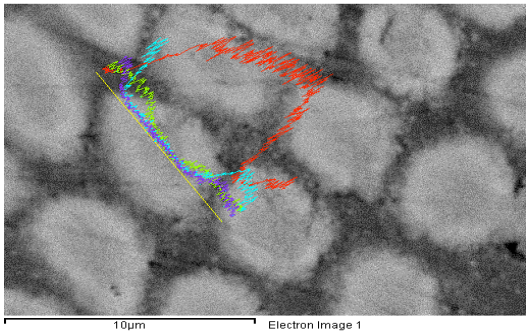

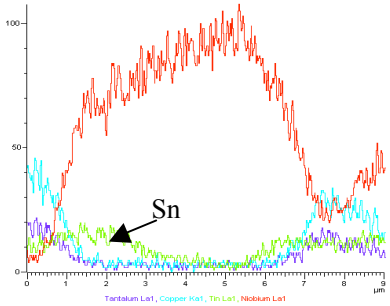

(b) 8hr/675°C

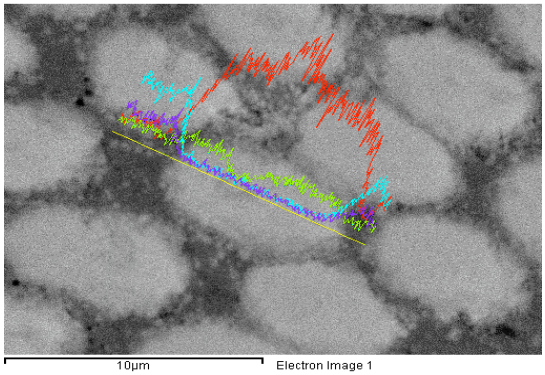

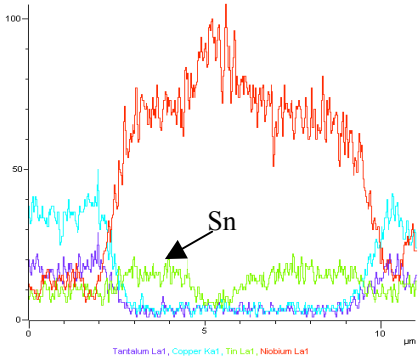

(c) 32hr/675°C

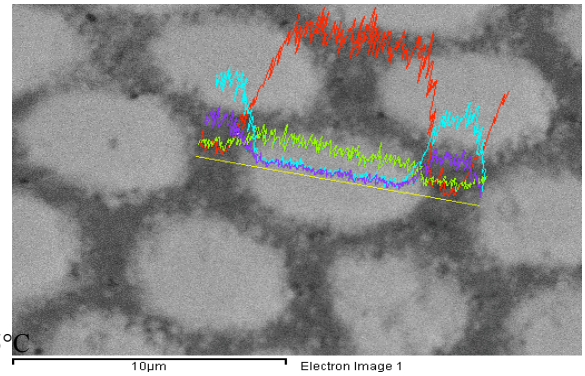

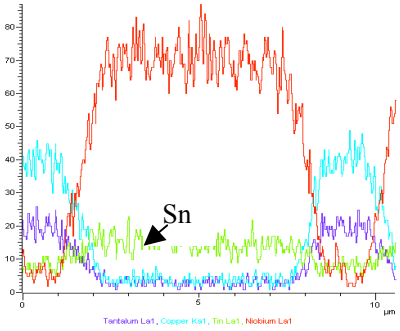

(d) 74hr/675°C

Fig.4-50 The filaments profile and elements distribution across a filament for AST samples of different reaction times

It can be directly observed from Fig.4-50 that the A15 phase layer formed on the filaments (outside light area) becomes thickening with the increase of reaction time. Most of the filaments have reacted at 32hr duration, besides a small dark area in the center of the filaments. Until 74hr reaction, all the filaments have transformed completely into A15 phase. From the element distribution lines depicted by the EDS analysis (see right figures), we can find that the filament first forms a gradient A15 layer with higher Sn concentration at the outside. The formed A15 layers are estimated as 0.7μm, 1.5μm and 2.4μm for 2hr, 8hr and 32hr reaction, respectively. For 74hr reaction the Sn distribution is nearly homogenous across the filament, with about 16at% Sn concentration.

(2) The reaction temperature influence

Four samples heat-treated at 650°C, 675°C, 700°C and 725°C for 32hrs were chosen for A15 phase observation and the cross-filament Sn distribution examination. The results are shown in Fig.4-51.

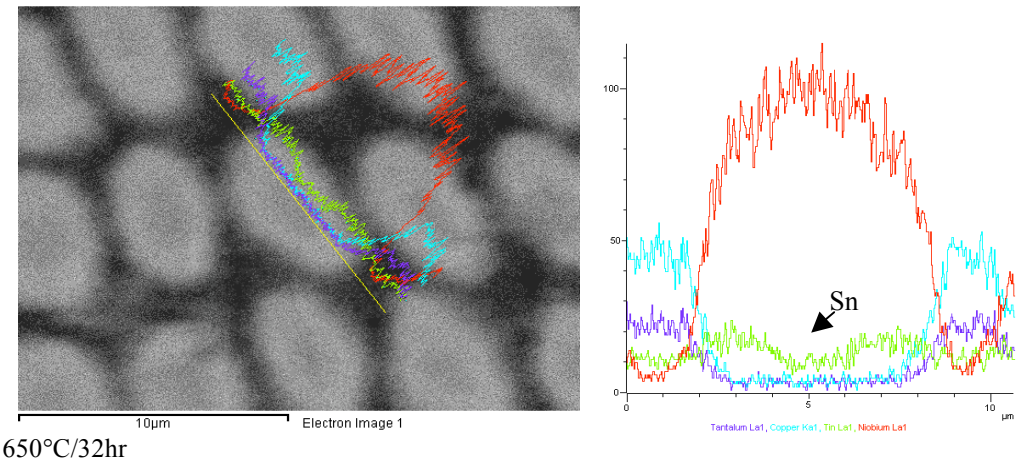

(a) 650°C/32hr

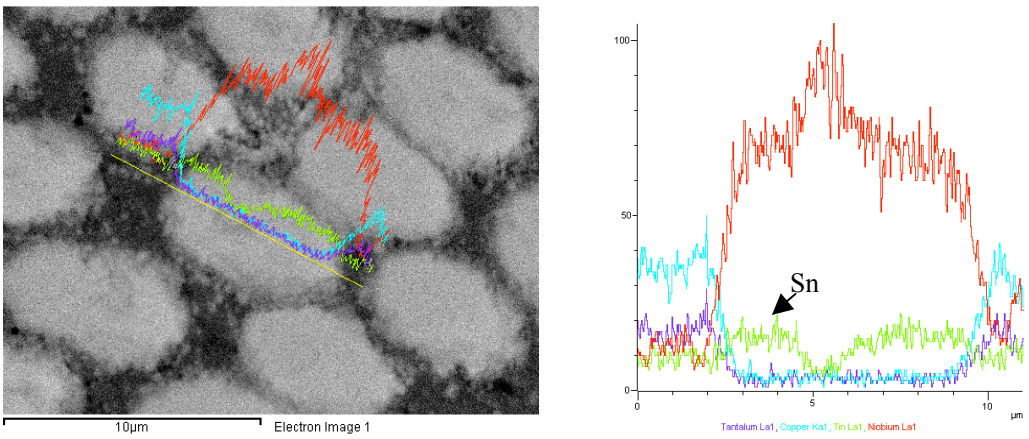

(b) 675°C/32hr

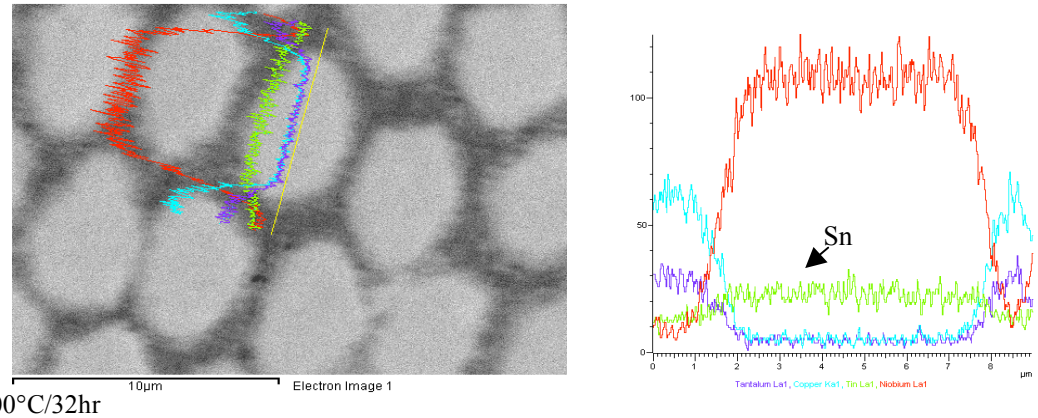

(c) 700°C/32hr

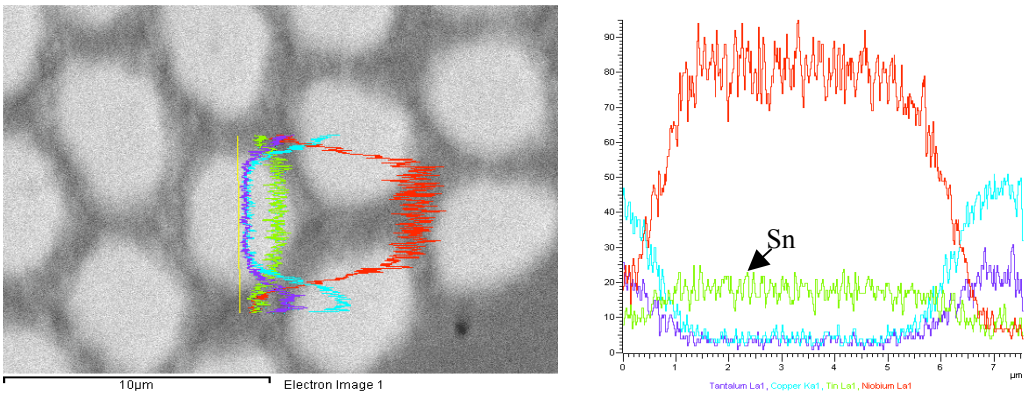

(d) 725°C/32hr

Fig.4-51 The filaments profile and elements distribution across a filament for AST samples of different reaction temperatures

It can be clearly seen from Fig.4-51 that about half of the filaments have formed the A15 phase layer for the 650°C /32hr sample; almost all of the filaments have reacted for the 675°C /32hr sample; and all filaments have transformed completely into A15 phase at temperatures of 700°C and 725°C for 32hr duration. From the element distribution lines depicted by the EDS analysis (right figures), we can estimate that the formed A15 layers are 2.0µm and

2.4μm for 650°C and 675°C reaction respectively, while for 700°C and 725°C reaction the Sn distributions are nearly homogenous across the filaments, with about 20at% Sn concentration.

4.5.3.1.2 *NIN wire*

(1) The reaction time influence

Similarly, four samples heat-treated at 675°C for 2hr, 8hr, 32hr and 74hr were chosen for A15 phase observation and the cross-filament Sn distribution examination. The results are shown in Fig.4-52.

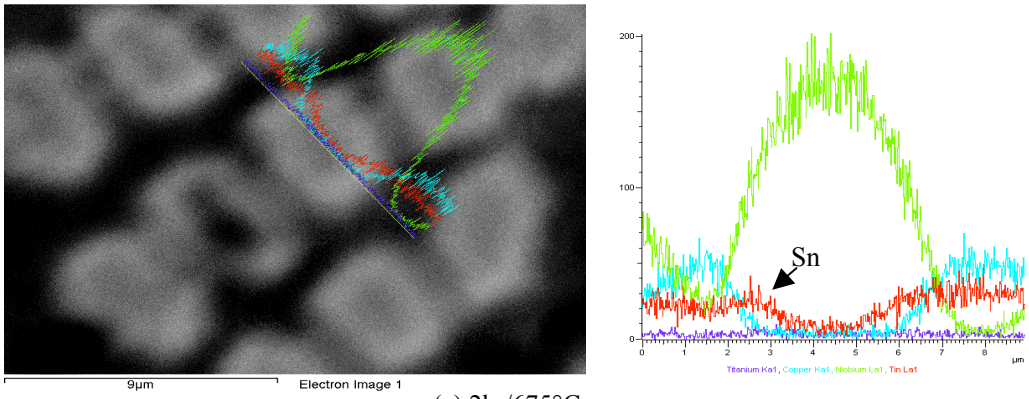

(a) 2hr/675°C

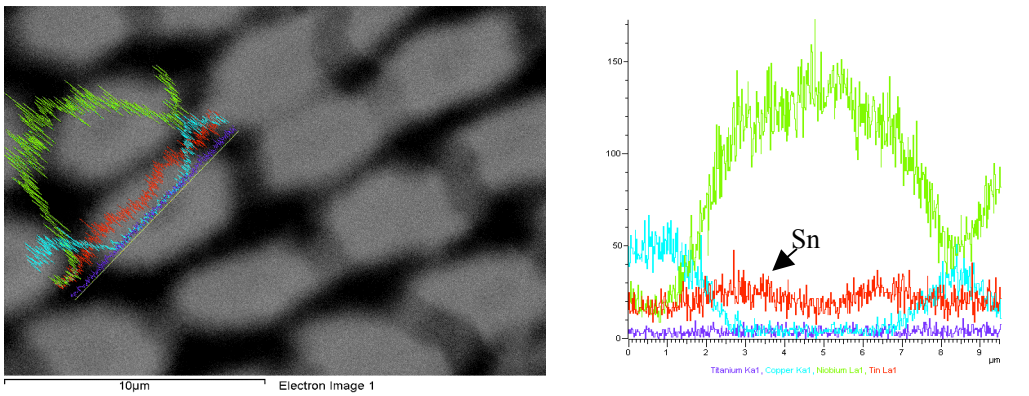

(b) 8hr/675°C

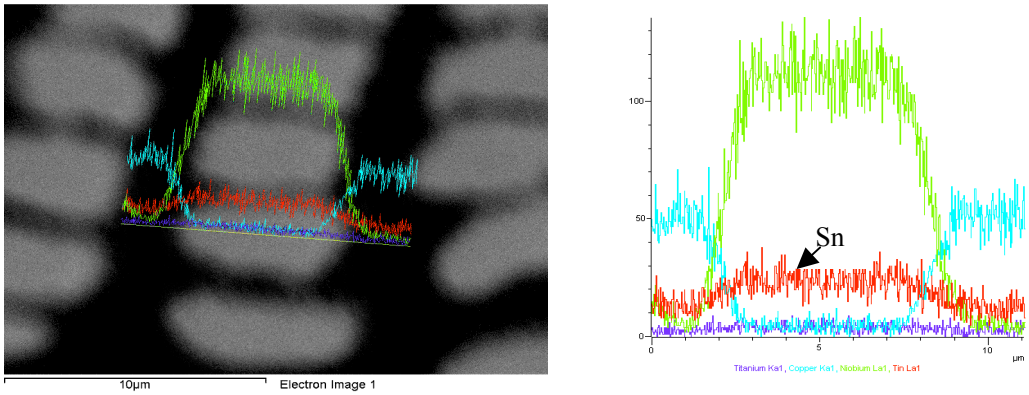

(c) 32hr/675°C

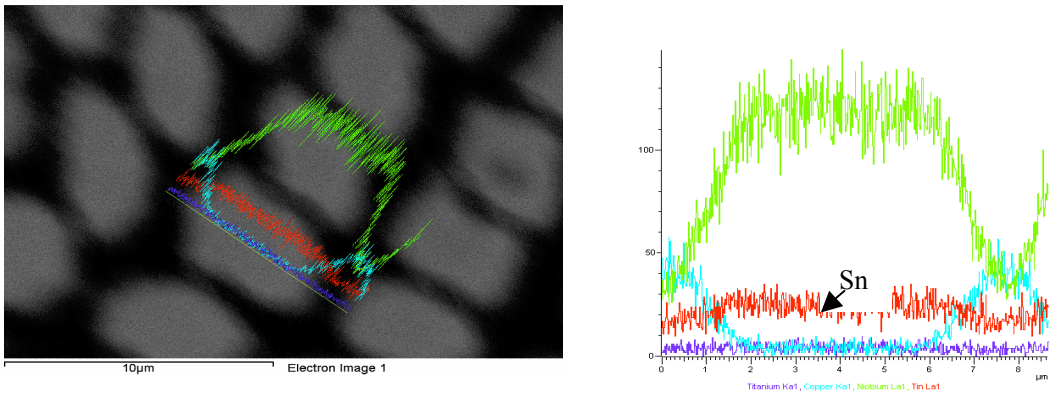

(d) 74hr/675°C

Fig.4-52 The filaments profile and elements distribution across a filament for NIN samples of different reaction times

From Fig.4-52 it can be found that nearly half of the filaments have reacted at 675°C for only 2hrs, with an A15 layer thickness of 1.5μm; most of the filaments have reacted at 8hr duration, apart from a lower Sn concentration in the center of the filaments; all the filaments have transformed completely into A15 phase after 32hr reaction, and the Sn distributions are nearly homogenous across the filaments, with about 21at% Sn concentration.

(2) The reaction temperature influence

The four samples heat-treated at 650°C, 675°C, 700°C and 725°C for 8hrs were chosen for A15 phase observation and the cross-filament Sn distribution examination. The results are shown in Fig.4-53.

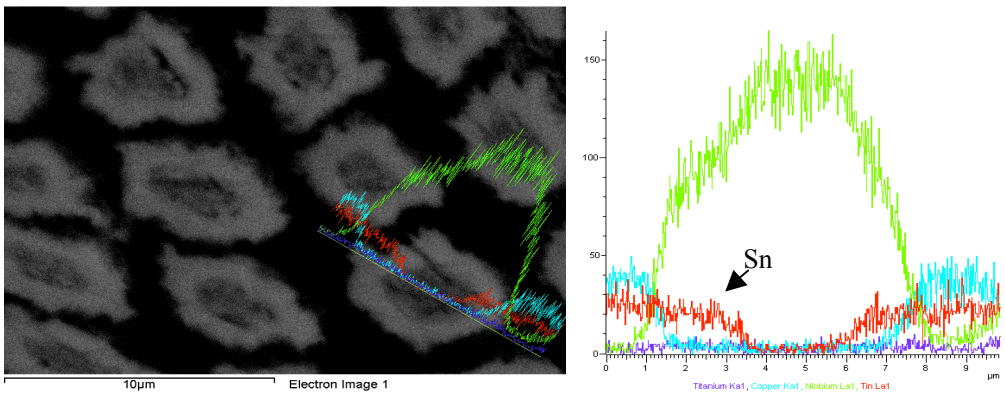

(a) 650°C/8hr

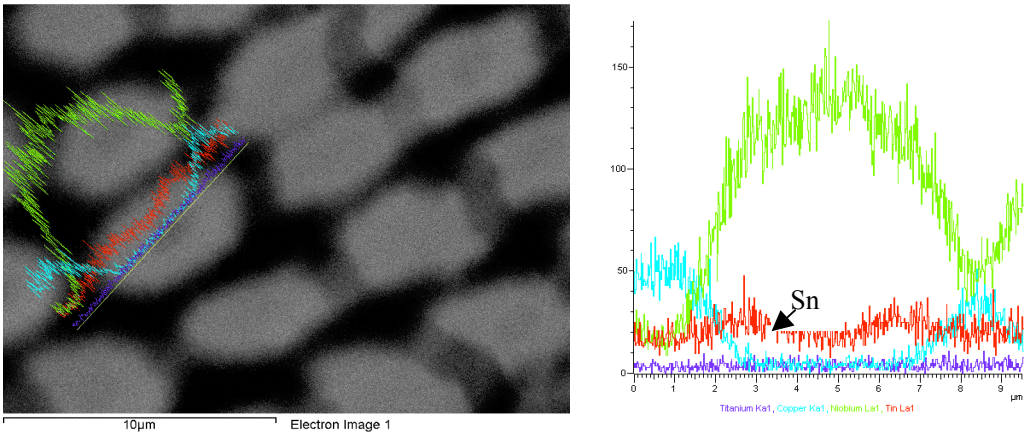

(b) 675°C/8hr

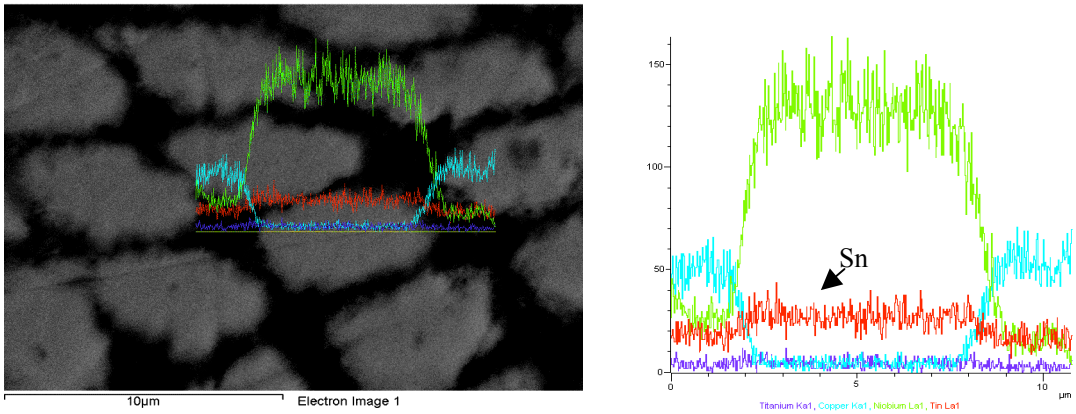

(c) 700°C/8hr

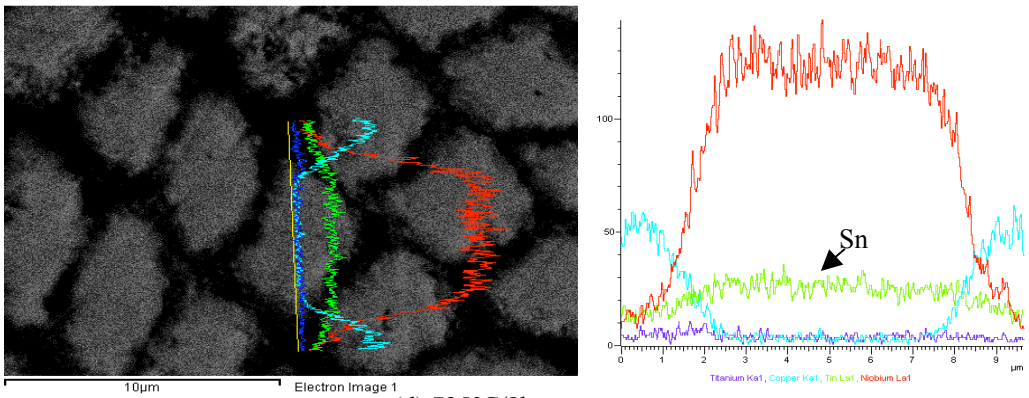

(d) 725°C/8hr

Fig.4-53 The filaments profile and elements distribution across a filament for NIN samples of different reaction temperatures

From Fig.4-53 it can be clearly seen that nearly half of the filaments have reacted at 650°C for only 8hrs, with an A15 layer thickness of 1.6µm; most of the filaments have reacted at 675°C for 8hrs, apart from a lower Sn concentration in the center of the filaments; all the filaments have transformed completely into A15 phase at 700°C and 725°C for 8hr duration, and the Sn distributions are nearly homogenous across the filaments, with about

23at% Sn concentration.

4.5.3.2 FESEM Observation for Nb_3Sn Grain Configuration

Five heat-treated samples from NIN and from AST respectively were selected for FESEM observations of grain size and crystalline configuration. The results are also analyzed individually.

4.5.3.2.1 *NIN wire*

(1) The reaction time influence

Three samples heat-treated at 675°C for 32hr, 128hr and 200hr were used to show the reaction time influence as in Fig.4-54.

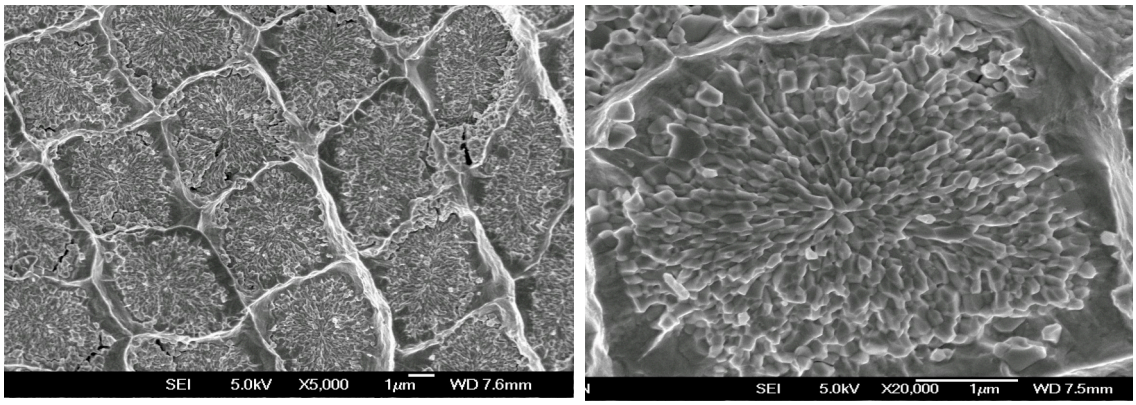

(a) 32hr

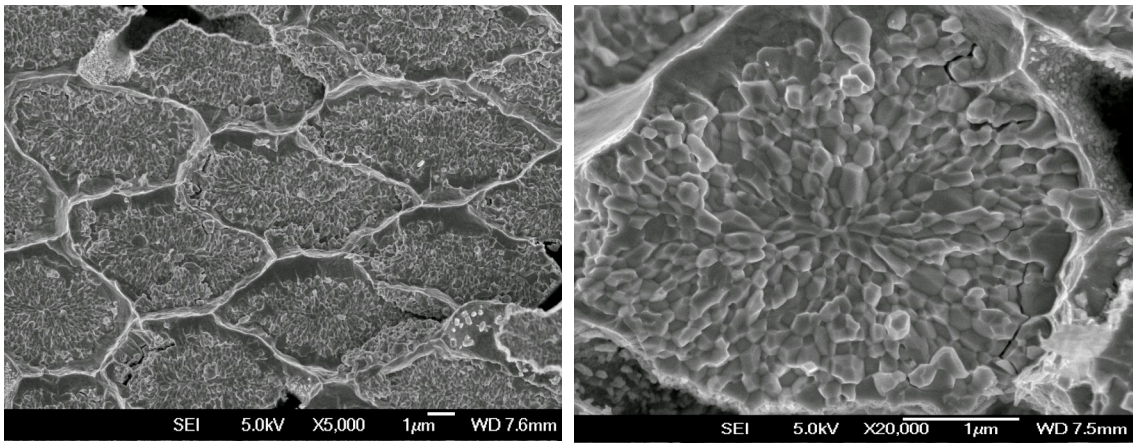

(b) 128hr

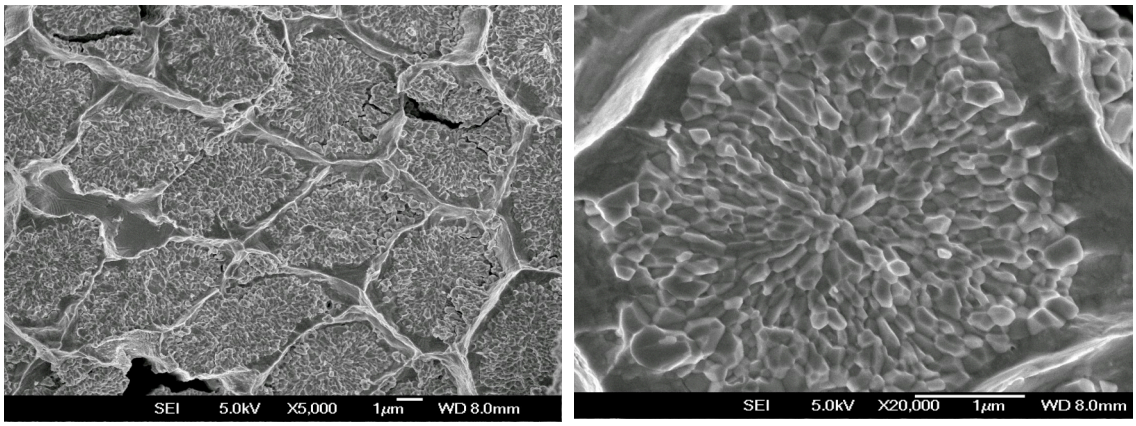

(c) 200hr

Fig.4-54 The FESEM photographs of NIN samples heat-treated at 675°C for different time

From Fig.4-54 (a) it can be found that the Nb filament of NIN sample has totally reacted at the HT of 675°C/32hr with the following characteristics. The formed A15 phase is radially and continuously distributed, with the coarser grain size locating at the filament outer layer and finer grain centralizing at the inner area. There are more columnar crystals in the middle part, while more equiaxed crystals gather on the outer layer. From (b) figure it is seen that after 128hr heat treatment, the grain size and crystalline morphology become more uniformly distributed and on the filament inner part appears more equiaxed crystals. After 200hr reaction (see (c) figure), the filament is enriched with equiaxed crystals, but the grain size becomes much coarser.

(2) The reaction temperature influence

Three samples heat-treated at 650°C, 675°C and 725°C for 128hrs were used to show the reaction temperature influence as seen in Fig.4-55.

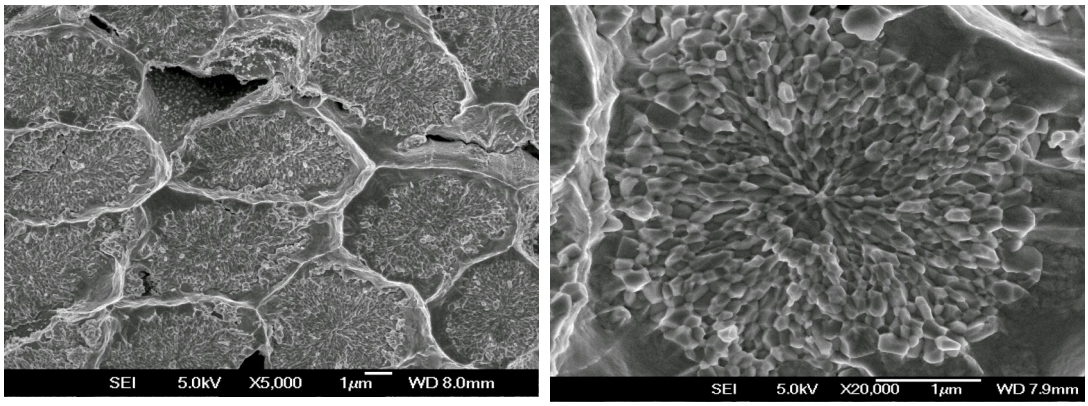

(a) 650°C

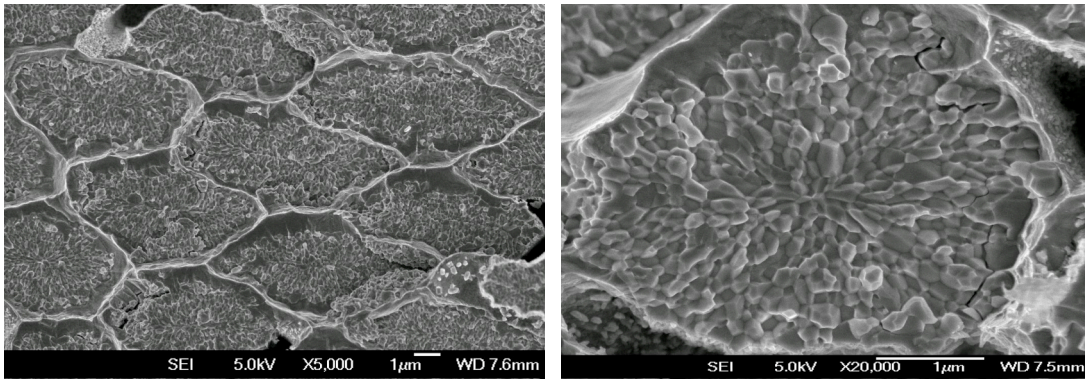

(b) 675°C

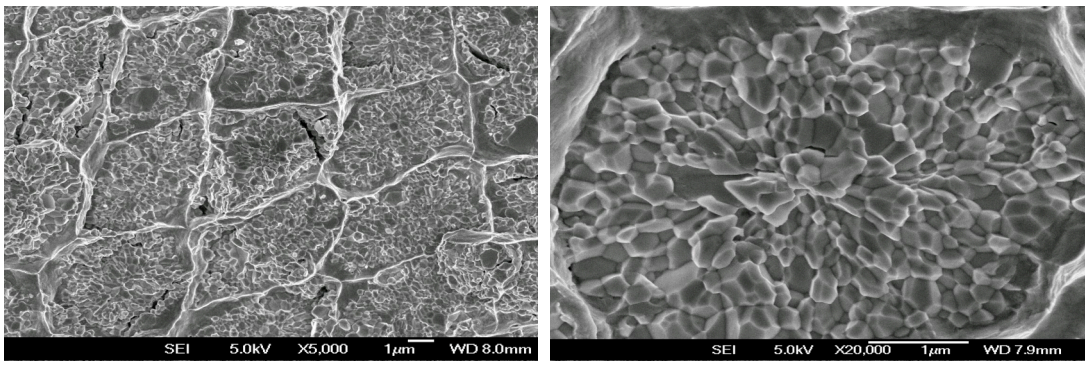

(c) 725°C

Fig.4-55 The FESEM photographs of NIN samples heat-treated at different temperature for 128hrs

From Fig.4-55 it is noticed that the Nb filament of NIN samples heat-treated at different temperatures for full-time (128hr) has completely reacted (left figures), with the following characteristics. Generally, the grain size and crystalline morphology are much more uniformly distributed with the equiaxed crystals as the main phase. Comparing the situations at different reaction temperatures, the 650°C/128hr sample has fine grain size and some visible columnar crystals in the middle of the filament; the elevated temperature increases the grain size and the amount of the equiaxed crystals as well; the 725°C/128hr sample seems to have too coarse grain size in the A15 phase, a few times larger than that of the 650°C/128hr sample.

4.5.3.2.2 *AST wire*

(1) The reaction time influence

Similarly, three samples heat-treated at 675°C for 32hr, 128hr and 200hr were used to show the reaction time influence as in Fig.4-56.

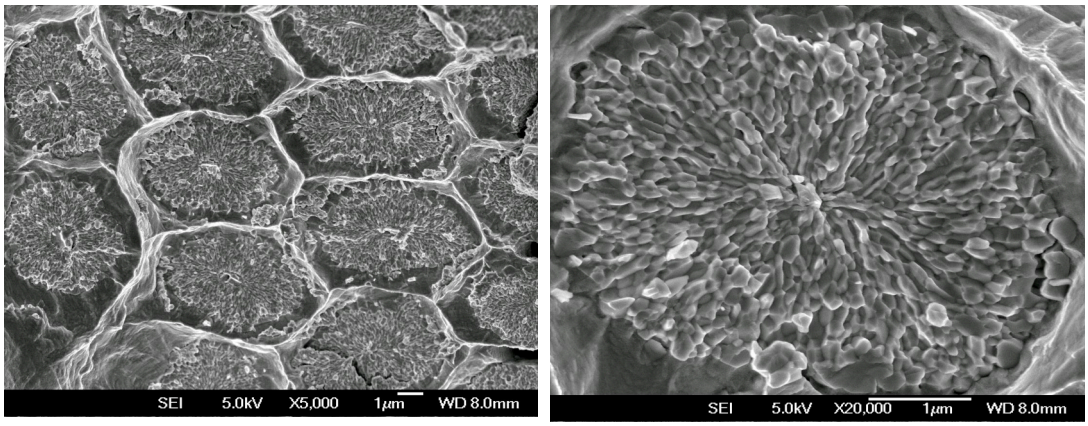

(a) 32hr

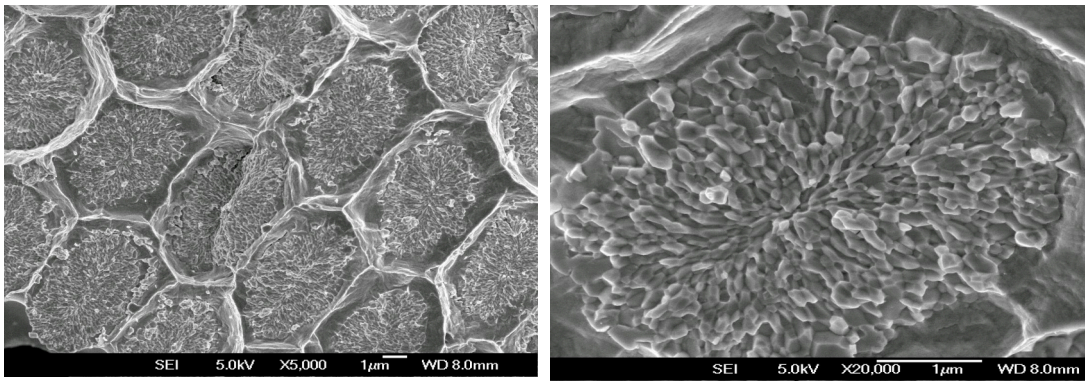

(b) 128hr

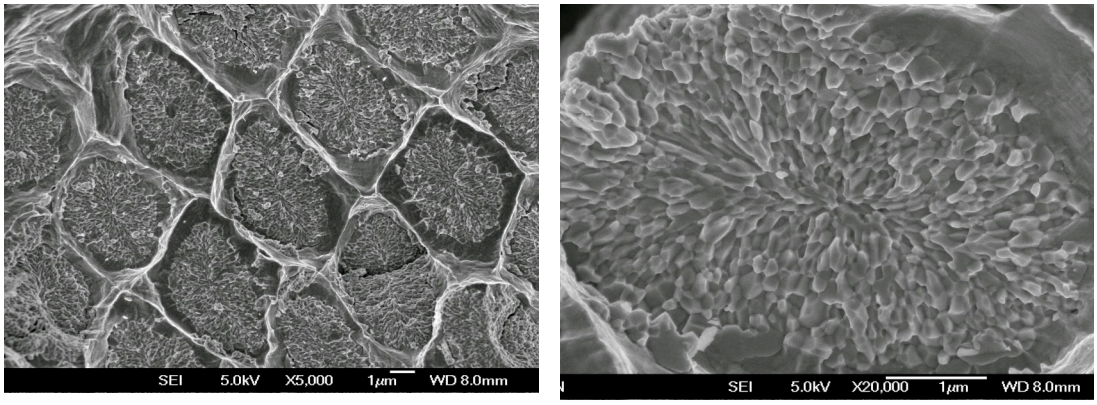

(c) 200hr

Fig.4-56 The FESEM photographs of AST samples heat-treated at 675°C for different time

From Fig.4-56 (a) it can be found that most filaments of AST samples have not completely reacted after 32hrs at 675°C; there exist small unreacted areas in the filament middle part (left figure, dark area). Chosen the nearly reacted-through filament (right figure), one can see that the formed A15 phase is also radially and continuously distributed, with the coarser grain size at the filament outer layer and finer grain at the inner area. Whereas, the grain is very fine and in middle area most grains are columnar crystals. From (b) figure it is

seen that the grain size and crystalline morphology become more uniformly distributed with more equiaxed crystals appearing in the filament inner part after 128hrs reaction. After 200hr reaction (see (c) figure), the filament is full of equiaxed-crystals, but the grain size becomes even coarser.

(2) The reaction temperature influence

Also, the three samples heat-treated at 650°C, 675°C and 725°C for 128hrs were used to show the reaction temperature influence as in Fig.4-57.

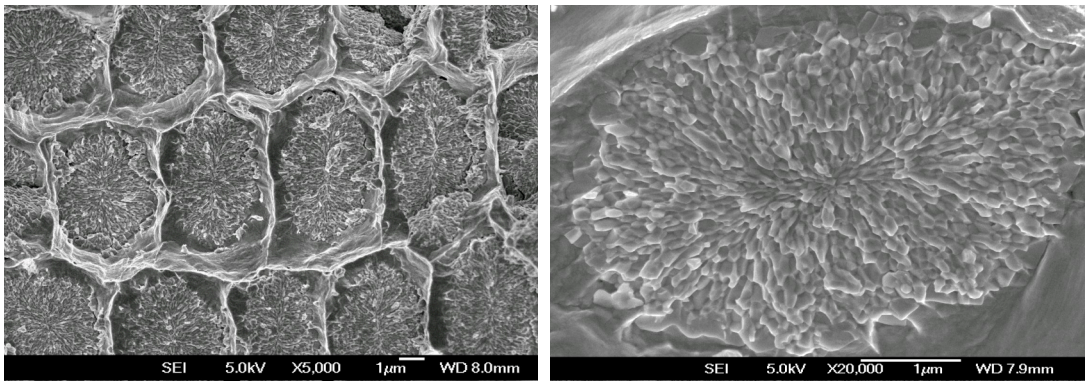

(a) 650°C

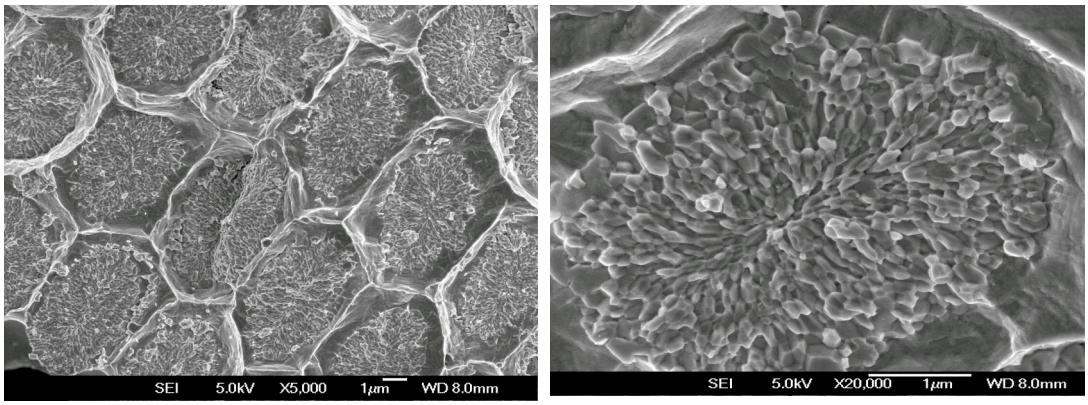

(b) 675°C

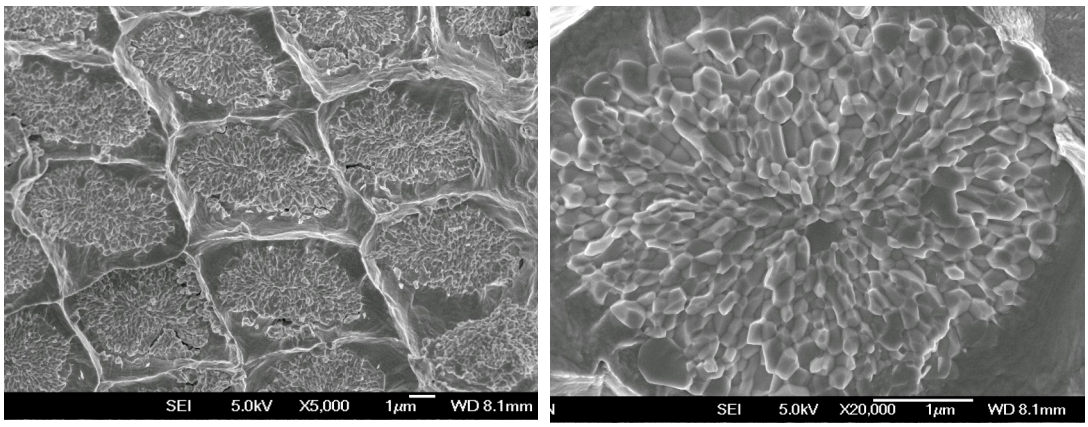

(c) 725°C

Fig.4-57 The FESEM photographs of AST samples heat-treated at different temperature for 128hrs

From Fig.4-57 it is found that the AST samples nearly have the same characteristics as NIN ones. All filaments of full-time (128hr) heat-treated samples have completely reacted. The grains are very fine at 650°C reaction and become coarser and coarser with the increase of reaction temperature to 675°C and 725°C. More columnar crystals appear in the filament inner part for the lower temperature sample (see (a) figure), but the equiaxed crystals are the main crystalline phase for the higher temperature samples (see (b) and (c) figures).

4.5.4 Discussion

The composite design of NIN superconducting wire is different from that of AST one. Comparatively, the later seems to be more beneficial to Sn diffusion and reaction, and thus should have faster A15 phase formation rate, because it has more uniformly distributed Sn, alloyed Ta in Nb and more regular shape. However, this is not the real case. NIN wire, on the contrary, exhibits higher phase formation rate, as observed from the microstructure and microchemistry examination.

The above results clearly show the differences. First, the phase formation is considered. The AST wire still has unreacted parts in the filaments after 32hr heat treatment at 675°C, and the 74hr/675°C sample only has 16at%Sn in its A15 phase although completely reacted (see Fig.4-43). However, NIN wire has developed almost the same amount of A15 layer only for 8hr reaction at 675°C, and the Sn concentration has achieved 21at% after 32hr reaction (see Fig.4-45). Observing the temperature influence, only 8hr reaction of NIN samples has developed the amount of A15 phase even more than that of the 32hr reaction of AST samples. Comparing completely-reacted samples, NIN wire has about 23at%Sn in the A15 composition, while AST wire, just 20at% or so (see Figs.4-44 and 4-46). All these results demonstrate that the phase formation dynamics of NIN wire is much higher than that of the AST wire.

Moreover, the grain configuration in A15 phase is considered. At the same reaction temperature, the grain size and crystalline morphology of AST wire change with reaction time more slowly than those of NIN wires (compare Fig.4-47 with Fig.4-49). At different reaction temperatures for 128hrs, the AST wire has smaller grain size and more columnar crystals in

A15 phase than NIN wire does, especially at 650°C (compare Fig.4-48 with Fig.4-50).

The above microstructure and microchemistry analysis seems to indicate that the Sn distribution in the original wire does not affect A15 phase formation, as Sn diffuses faster that Cu and Nb. In addition, Ti alloyed in Sn is much more effective than Ta alloyed in Nb for the promotion of A15 phase formation. Except for hardening Sn core, the Ti addition has two functions. One is the acceleration of Sn diffusion and reaction rate, which remarkably improves the A15 phase formation, resulting in fast growth of A15 layer. At the same time, high Sn diffusion rate is favorable to the development of equiaxed crystals, which is beneficial to the promotion of superconducting properties. The other function is the decrease of reaction temperature, which is propitious to the finer grain size formation, resulting in the enlargement of boundary area density and thus the enhancement of flux pinning force. From the two functions of Ti alloying, we are easy to conclude that the configuration design of a small amount of Ti alloyed in Sn is the more favorable choice from the respects of the promotion of phase formation and the decrease of reaction temperature.

As long as the phase formation kinetics of an internal-Sn MF wire is concerned, some investigations have been made in the section of neutron diffraction measurement. In this section, some work has been made on the Sn concentration variation with the HT conditions, which can be used to dynamically evaluate the phase formation progress. In general, however, it is very difficult to quantitatively investigate the phase variation of multifilamentary wires because of the following factors. Firstly, a multifilament wire is composed of hundreds of thousands of filaments which have very small dimensions of about a few micrometers. The phase formation progress succeeds radially from filament outside to inside, and will react through in much shorter time. It is not easy to estimate the A15 layer variation with the reaction time. Secondly, the filaments in different locations of the wire cross section have different reaction degrees. It is hard to determine which filament is the most suitable one. Lastly, the MF wire has experienced a few times of extrusion and drawing, leading to a large deformation of the filaments. The irregular filament shape increases the difficulty of evaluation. For these reasons, multifilament conductors are not favorable for quantitative study of the A15 phase formation kinetics.

4.5.5 Conclusion

The microstructure and microchemistry analysis has shown large phase formation differences between the NIN wire and AST wire. The phase formation progress of NIN wire is faster than that of AST wire with the increase of both reaction temperature and time. In the same heat treatment conditions NIN wire produces more equiaxed crystals in the A15 phase configuration, but AST wire, a large amount of columnar crystals, especially at lower temperature of 650°C. These differences are mainly caused by the Ti addition in Sn or not.

Except for hardening the Sn core, the Ti alloyed in Sn has two functions. One is the acceleration of Sn diffusion and reaction rate, which not only improves the A15 phase formation rate, but also benefits to the development of equiaxed crystals. The other is the decrease of reaction temperature, which is propitious to the smaller grain size formation and the flux pinning force enhancement.

5. SUPERCONDUCTIVITY COMPARISON, MICRO-STRUCTURE ANALYSIS AND PHASE FORMATION KINETICS OF MONO-ELEMENT WIRES

5.1 Heat Treatment for Mono-element Wire Samples

The four designed internal-Sn mono-element (ME) wires: SF1-Nb(Cu-15wt%Sn), SF2 -Nb(Cu-20wt%Sn), SF3-Nb(Cu-25wt%Sn) and SF4-Nb(1at%Zr)(Cu-20wt%Sn), were cut into ~60mm length pieces, whose ends were crimped over 3mm to prevent of Sn leakage. In accordance with off-situ neutron diffraction examination, 40 of the pieces were sealed in one evacuated quartz tube with ~4Pa of Ar atmosphere. Similarly, all mono-element samples underwent a 210°C/50hr + 340°C/25hr thermal treatment in horizontal tubular furnaces for Cu-Sn alloying prior to the A15 phase formation heat treatment. The ramp rate was 60 ºC/hr. At the end of the Cu-Sn alloying process, four samples (one from each wire) were taken out for the examination of Cu-Sn phases. The HT of A15 phase formation is somewhat different from that of MF wires. The four reaction temperatures of 650ºC, 675ºC, 700ºC and 725ºC were still chosen to study the temperature influence but with different durations. All the HT programs have been carried out in CRETA /CNRS and the detailed HT conditions were the followings:

$$210°C/50hr + 340°C/25hr \rightarrow \begin{cases} 650°C, 8hr, 32hr, 100hr, 200hr; \\ 675°C, 8hr, 32hr, 100hr, 200hr; \\ 700°C, 8hr, 32hr, 100hr, 200hr; \\ 725°C, 8hr, 32hr, 100hr, 200hr \end{cases}$$

Totally, 78 samples were prepared, including the 6 of Cu-Sn alloying process.

5.2 SQUID Magnetization Study of Internal-Sn Mono-element Wires

5.2.1 Sample Preparation and Experiment

The ME wire samples heat-treated according to section 5.1 were cut into short (~6mm) segments. Three of the segments were weighed and mounted together for one measurement

on a clear plastic straw with their axis perpendicular to the applied field. The SQUID measurement approaches are the same as those for MF wire measurement in section 4.3.2.

5.2.2 Results and Analysis

The selected ME wire samples were measured for the T_C (B), T*(B) and T_C transition lines by the warming-cooling approach, and were also tested for the hysteretic loops by cycling-field method for the purpose of investigating the effects of various factors on A15 phase formation.

ΔM value actually reflects the package critical current density (package J_C) of a wire. Similarly, ΔM×B value indicates the package flux pinning force (package F_P) of the wire. For the mono-element wire in this study the thickness of the formed A15 phase layer can be measures through microscopic technique. Therefore, it is possible to calculate both A15 layer critical current density (A15 layer J_C) with the obtained ΔM values, and A15 layer flux pinning force (A15 layer F_P) by ΔM×B values [133].

Based on Bean model, the calculation of 15 layer J_C can be described as the followings.

Assuming that a filament is in the Bean critical state, if it is positioned in a perpendicular way to the applied field, the critical current density can be expressed as:

$$J_C \text{ cylinder} = \frac{M}{2L + 2D} \qquad (5\text{-}1)$$

where M is the magnetization of the conductor , L and D are the length and diameter of the filament cylinder respectively. Since

$$M = \frac{\Delta M}{V} \qquad (5\text{-}2)$$

where ΔM is the hysteretic width, V is the volume of the filament, approximated as the volume of the superconducting cylinder of radius R. Considering 2L>>2D，2D can be negligible and the Eq.5-1 can thus be transformed into

$$J_C \text{ cylinder} = \alpha \times \frac{\Delta M}{L^2 R^2} \qquad (5\text{-}3)$$

where α is a coefficient of proportionality.

For the mono-element wire, the reacted Nb_3Sn is approximated as cylindrical shells. Thus,

$$\text{A15 layer } J_C = \beta \times \frac{\Delta M}{L^2(R_{out}^2 - R_{inner}^2)} \qquad (5\text{-}4)$$

where R_{out} is the outer radius of the cylindrical shell, that is, the effective radial distance from the wire core to the interface between the A15 layer and the Nb (or Nb(Zr)). R_{inner} is the inner radius of the cylindrical shell, i.e., the effective radial distance from the wire core to the interface between the Cu-Sn phase and A15 layer, β is also a coefficient of proportionality, and L is actually the length of the sample.

According to Eq.5-4, if we plotted $\frac{\Delta M}{L^2(R_{out}^2 - R_{inner}^2)}$ as a function of the field B, the variation of A15 layer J_C of the samples can thus be compared. From the relation of $F_P = J_C \times B$, we can also compare the relative magnitude of the A15 layer F_P of the ME wire samples.

5.2.2.1 The Reaction Temperature Influence

The SF2, SF3 and SF4 wire samples heat-treated at different temperatures for 200hrs were selected to compare the reaction temperature influence. The results are the followings.

(1) H-T lines

The three wire samples of 700°C and 725°C reaction for 200hrs were measured for the T_C (B) values which were then plotted with the variation of field, as shown in Fig.5-1.

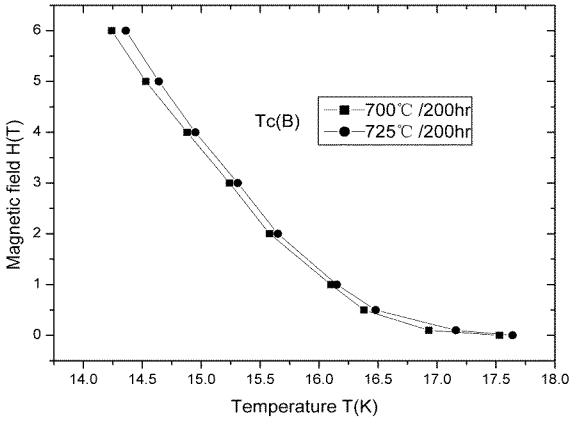

(a) SF2

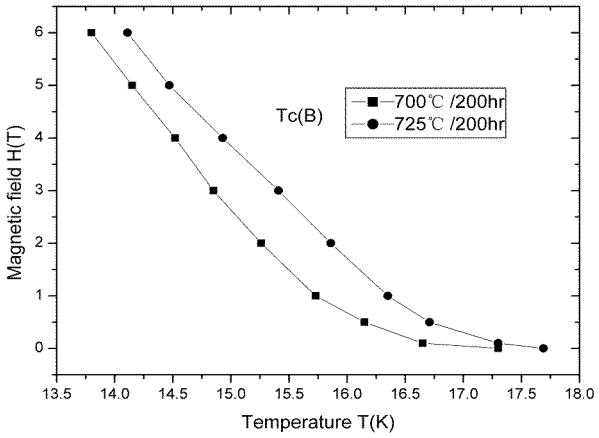

(b) SF3

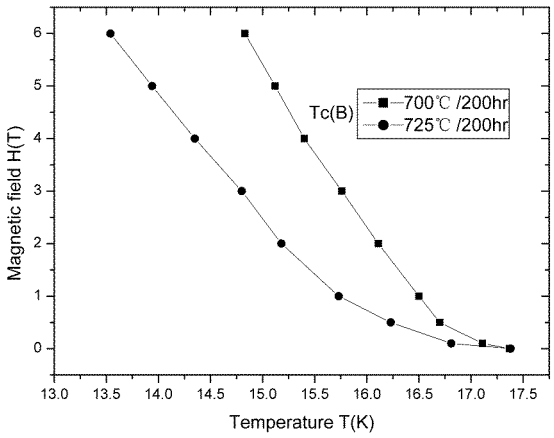

(c) SF4

Fig.5-1 H-T lines of the samples heat-treated at 700°C and 725°C for 200hrs

The 5-1(a) figure shows that from 700°C to 725°C the H-T line of SF2 wire had a small shift upwards, while 5-1(b) figure showed a large up-shift for the SF3 wire. On a contrary, for the SF4 wire appeared an obvious shift-down.

Comparing the H-T lines of MF wire in the section 4.3.3.1, it is noticed that the ME wire seems to be affected by reaction temperature more liable than the MF wire does. That is, the T_C (B) value of ME wire is temperature-dependent. Actually, this is caused by the different configuration designs between ME wire and MF wire. The A15 reaction of MF wire was radially from the filament outside to inside. After reaction through, the filament of MF wire became uniformly distributed in the A15 phase composition. On the other hand, the ME wire reacted from the inside of the Nb tube to its outside and there was nearly always remained Nb even undergoing 200hr reaction, because the Nb tube has a very thick design. Furthermore, the formed A15 phase layer in ME wire always had a gradient compositional distribution with high Sn concentration at the layer outside, due to the progressive reaction. It is the gradient composition of A15 layer that results in the T_C (B) differences at different reaction temperatures.

The large H-T shift-down of 725°C/200hr sample in (c) figure is caused by the Sn leakage into the stabilizing Cu (see section 5.4.2.1). Both the very high temperature of 725°C and the Zr addition in Nb substantially accelerated the A15 phase formation rate and made the Nb(Zr) tube react completely before 200hr duration.

(2) T*(B) lines

The three wire samples of 700°C and 725°C reaction for 200hrs were measured for the T*(B) values which were then plotted with the variation of field, as shown in Fig.5-2.

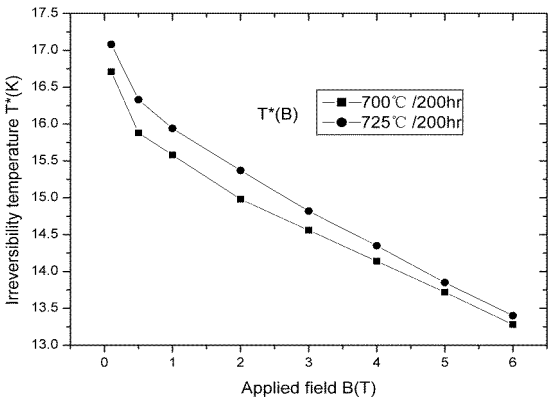

(a) SF2

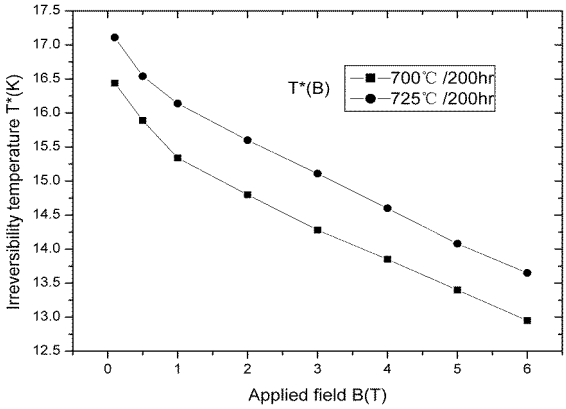

(b) SF3

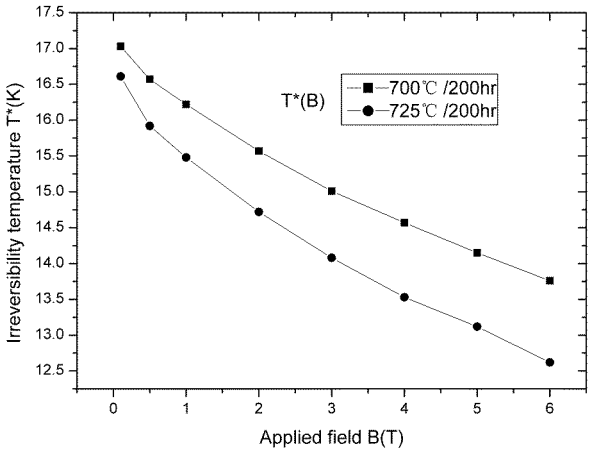

(c) SF4

Fig.5-2 T*(B) lines of the samples heat-treated at 700°C and 725°C for 200hrs

From 5-2 (a) and (b) figures it can be found that the T*(B) lines of SF2 and SF3 samples showed large up-shifts from 700°C to 725°C, with the 725°C sample even larger. That is also to say, the T*(B) values of ME wire is increased with the elevation of reaction temperature, the same consequence as that for T_C (B) measurement, which can also be explained from the different configuration designs and different reaction progresses between MF wire and ME wire. The (c) figure showed a shift-down of the T*(B) line. This is also the reason of Sn leakage from filament tube into the stabilizing Cu.

(3) M-T transition curves

The three ME wire samples were measured for the M-T transition curves, as shown in

Fig.5-3.

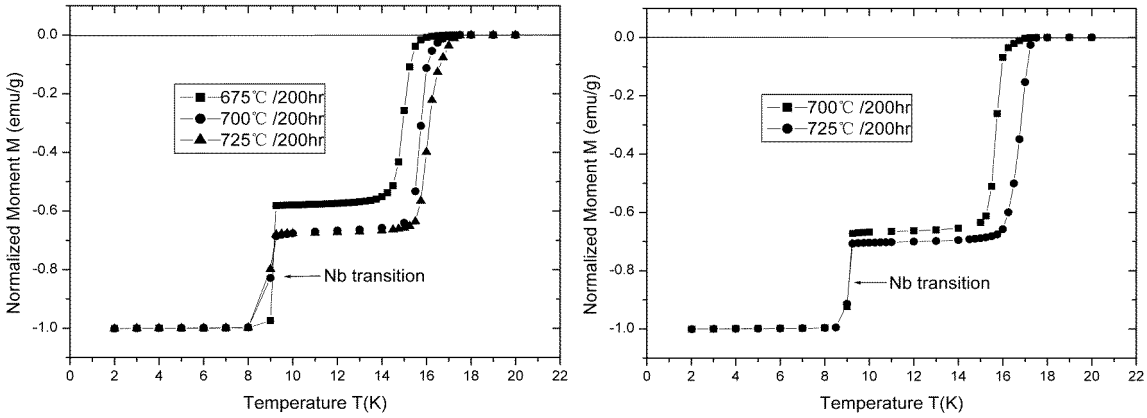

(a) SF2 (b) SF3;

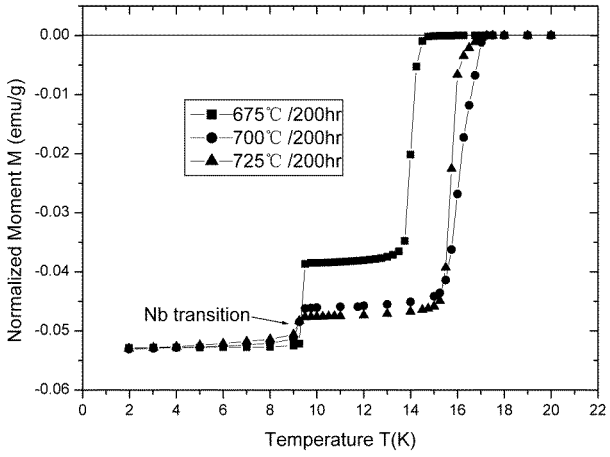

(c) SF4

Fig.5-3 M-T transition curves of the samples heat-treated at different temperatures for 200hrs

In Fig.5-3, the ME wire samples have two moment transitions, of which the lower one is the transition of the unreacted Nb (serving as diffusion barrier), while the upper one is the A15 phase transition. All the M-T transition curves are normalized to the unreacted Nb base line.

From Fig.5-3 (a), (b) and (c), it can be seen that the A15 transition curves of the three ME wires have shifted right-and-down wards but with nearly no variation of the curve craggedness, with the increase of reaction temperature. Comparing the results of the three reaction temperatures, it also can be seen that the A15 transition curves shifted much sharply from 675°C to 700°C, whereas a small shift was observed from 700°C to 725°C.

The shift-down of the A15 transition curves indicates the increase of the formed A15

quantity (A15 layer thickness) with the increase of reaction temperature. The amount of A15 layer grows faster from 675°C to 700°C, because of the acceleration of reaction rate in this temperature region. In addition, the right-shift of the A15 transition curves implies the enhancement of the formed A15 layer quality (Sn concentration distribution) with the elevation of reaction temperature, especially from 675°C to 700°C. As for the transition decrease of the 725°C/200hr sample of SF4 wire (see (c) figure), it is due to the decrease of A15 quality caused by the Sn leakage.

(4) ΔM-B curves and A15 layer J_C-B

The three ME wire samples were measured for the hysteretic loops at 12K of testing temperature, from which the hysteresis width ΔM were determined. The ΔM values were plotted as a function of the field B, as shown in Fig.5-4.

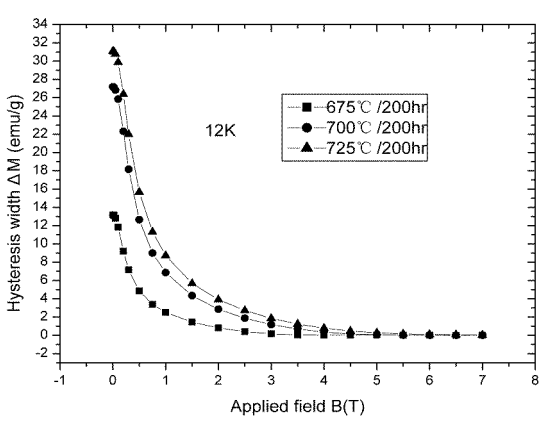

(a) SF2

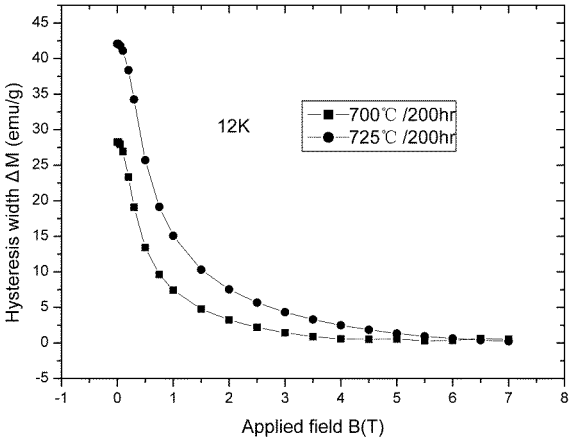

(b) SF3

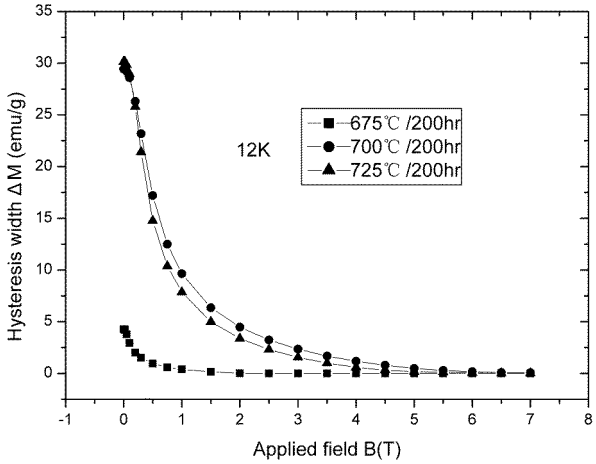

(c) SF4

Fig.5-4 The ΔM-B curves of the ME samples heat-treated at different temperatures for 200hrs

From Fig.5-4 (a), (b) and (c) it can be found that the ΔM-B curves of the three ME wires shifted upwards largely with the increase of reaction temperature, especially from 675°C to 700°C, except for a small shift-down of the 725°C/200hr sample in (c) figure. This result reveals the increase of package J_C with the reaction temperature elevation.

The calculated A15 layer J_C as a function of field B was depicted in Fig.5-5.

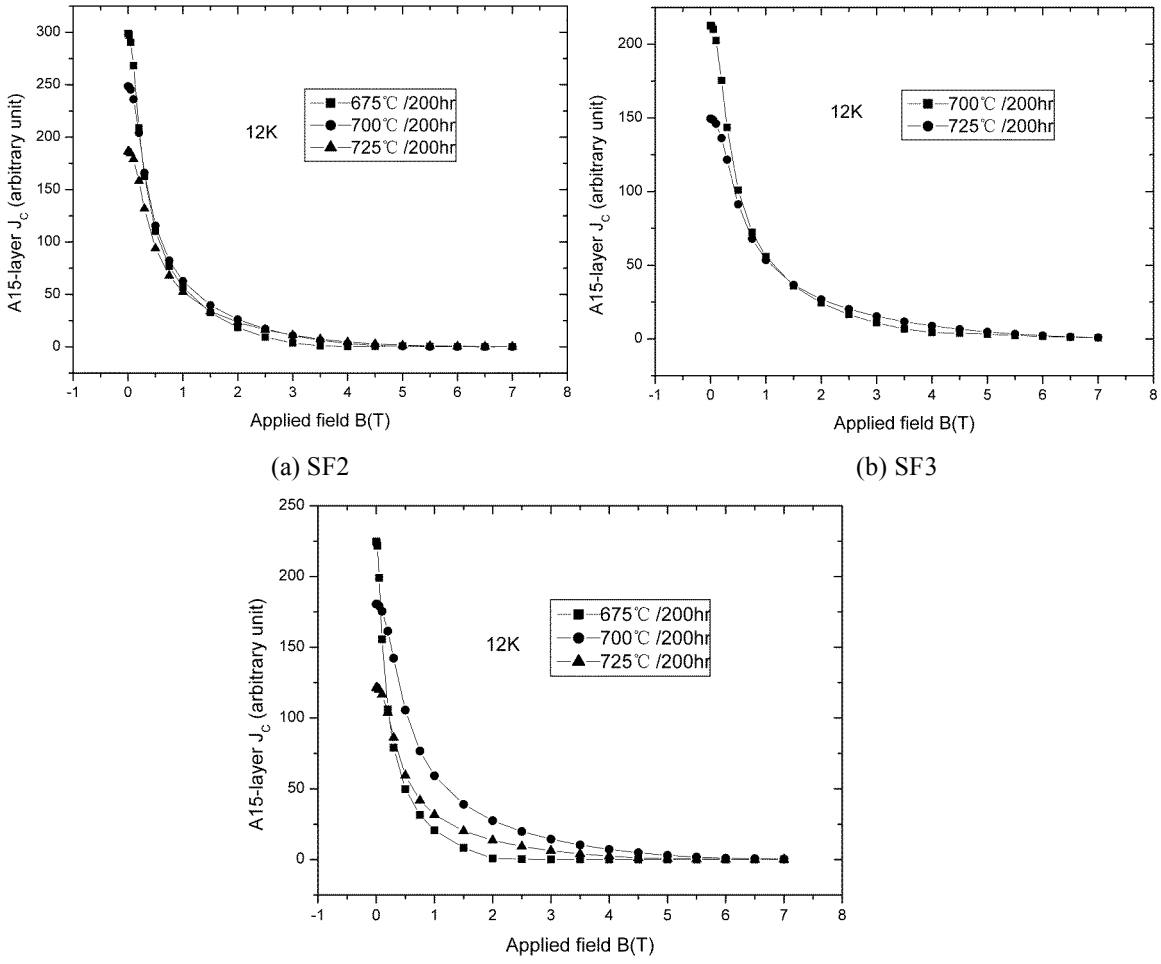

(a) SF2

(b) SF3

(c) SF4

Fig.5-5 The A15 layer J_C-B curves of the ME samples heat-treated at different temperatures for 200hrs

In Fig.5-5, different characteristics can be found. The (a), (b) and (c) figures showed small variations of A15 layer J_C-B with the reaction temperature, but a shift-down of the curve can be seen for the 725°C/200hr sample in (c) figure. This result indicates that the A15 layer J_C changes very little with the increase of reaction temperature. That is to say, the current-carrying capacity per unit A15 area maintains constant although the higher

temperature may accelerate the reaction rate and increase the A15 layer thickness.

Another characteristic can be seen from Fig.5-5 (a), (b) and (c) that the samples heat-treated at lower temperatures had rather high A15 layer J_C at low field, but quick decrease of the A15 layer J_C at high field, especially for the 675°C/200hr sample in (c) figure. This result demonstrates that lower reaction temperature is liable to increase the current-carrying capacity of low field, but decrease that of high field.

(5) ($\Delta M \times B$)-B curves and A15 layer F_P-B

The three ME wire samples were also plotted for the $\Delta M \times B$ values as a function of the field B, as shown in Fig.5-6.

From Fig.5-6 (a), (b) and (c) it can be found that the ($\Delta M \times B$)-B curves for the three ME wires had large up-and-right shifts with the increase of reaction temperature, especially from 675°C to 700°C (see (c) figure). This result indicates that the package F_P of the ME wires increases with the increment of reaction temperature. In the range of 675°C to 700°C, the A15 phase layer increases very quickly, leading to the large increase of package F_P.

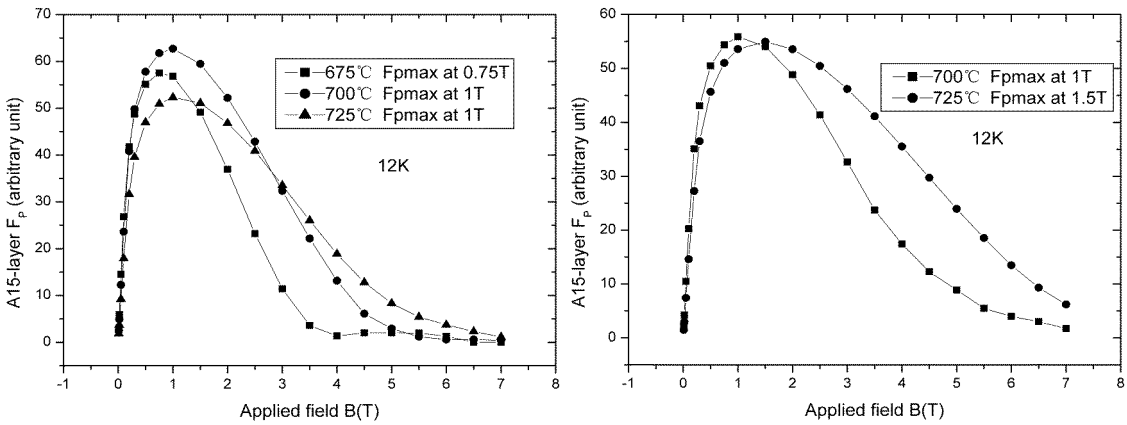

(a) SF2

(b) SF3

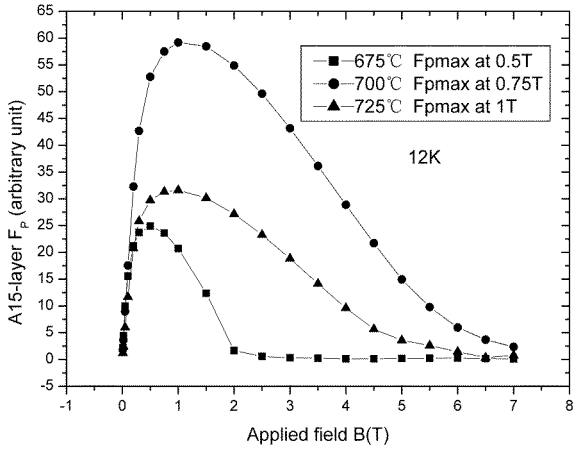

(c) SF4

Fig.5-6 The (ΔM × B)-B curves of the ME samples heat-treated at different temperatures for 200hrs

The calculated A15 layer F_P as a function of field B was depicted in Fig.5-7.

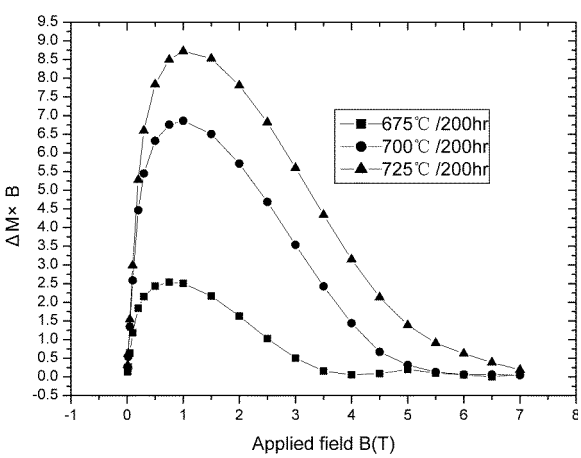

(a) SF2

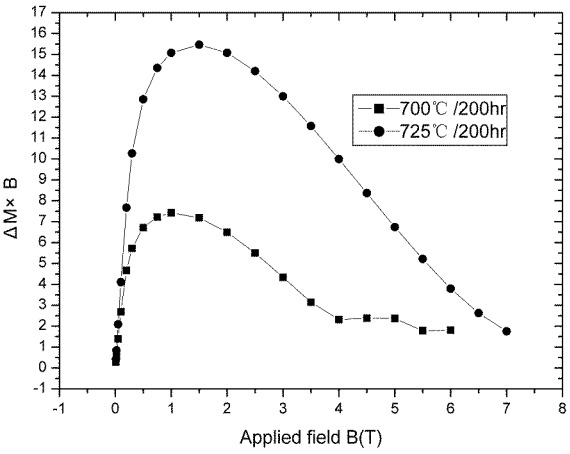

(b) SF3

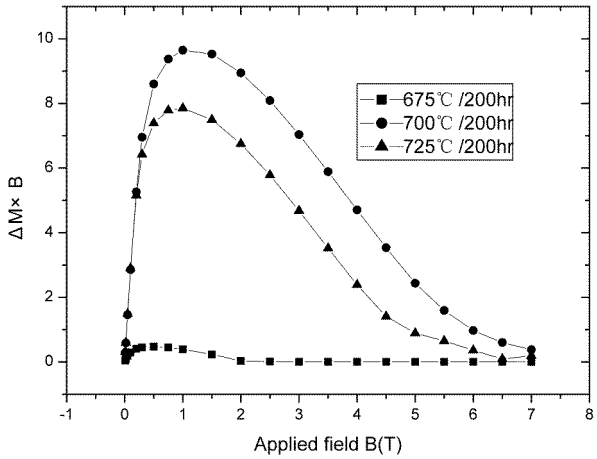

(c) SF4

Fig.5-7 The A15 layer F_P-B curves of the ME samples heat-treated at different temperatures for 200hrs

Compared with Fig.5-6, the A15 layer F_P-B curves of the three ME wire samples in Fig.5-7 showed very small variations with the reaction temperature. Observing the (a) and (b) figures, the curves before peaks are almost overlapped. However, after the maximum values the A15 layer F_P-B curves of the samples heat-treated at high temperature shifted downwards more slowly than those reacted at low temperature, except for the 725°C/200hr sample in (c) figure whose A15 layer F_P-B curve had a large shift-down due to the Sn leakage. These results exhibit that A15 layer F_P at high field is strengthened more substantially than that at low field with the increase of reaction temperature.

From Fig.5-7, it can also be seen that the maximum flux pinning force of SF2 sample in (a) figure appeared from 0.75T at 675°C to 1T at 725°C; SF3 sample in (b) figure, from 1T at

700°C to 1.5T at 725°C, and SF4 sample in (c) figure, from 0.5T at 675°C to 1T at 725°C. These results show that the maximum flux pinning force moves towards high-field direction with the increase of reaction temperature.

5.2.2.2 The Reaction Time Influence

The SF2 and SF4 wire (the same Sn ratio in the composite composition) samples heat-treated at 700°C for different times were selected to compare the reaction time influence. The results are as the followings.

(1) M-T lines

The two wire samples heat-treated at 700°C for 8hr, 32hr, 100hr and 200hrs were measured the T_C (B) values which were then plotted with the variation of field, as shown in Fig.5-8.

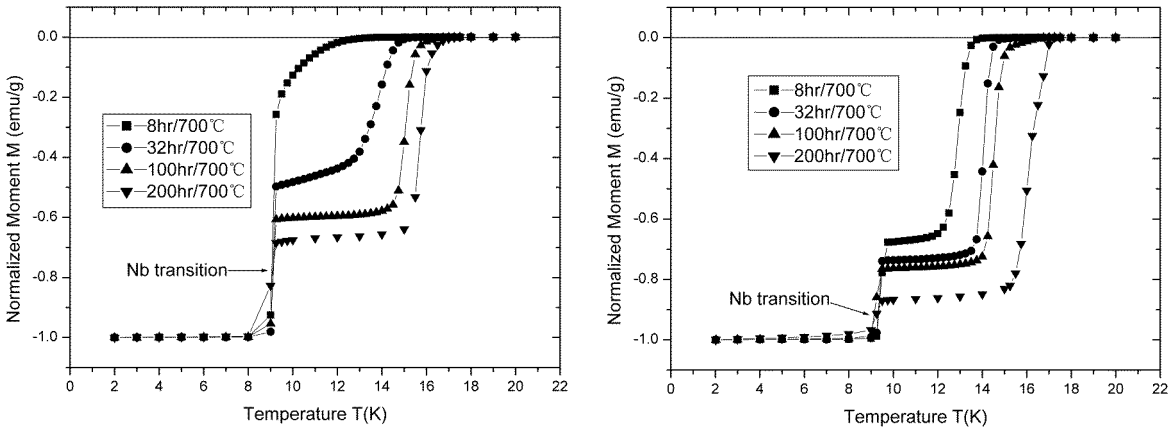

(a) SF2 (b) SF4

Fig.5-8 M-T lines of the samples heat-treated at 700°C for different times

The (a) figure shows that the M-T line of SF2 wire gradually shifted right-and-down wards with the reaction time elongation from 8hrs to 200hrs and the transition width became narrowed. The (b) figure had the same trend, but with much substantial variation. The 700°C/200hr sample had a very small Nb transition, meaning very thin remained Nb layer. This result indicates that both the A15 quantity (layer thickness) and quality (Sn content distribution) are improved with the prolongation of reaction duration.

(2) ΔM-B curves and A15 layer J_C-B

The two wire samples heat-treated at 700°C for four duration times were measured for

the hysteretic loops at 12K of testing temperature, from which the hysteresis widths were determined. The ΔM values were plotted as a function of the field B, as shown in Fig.5-9.

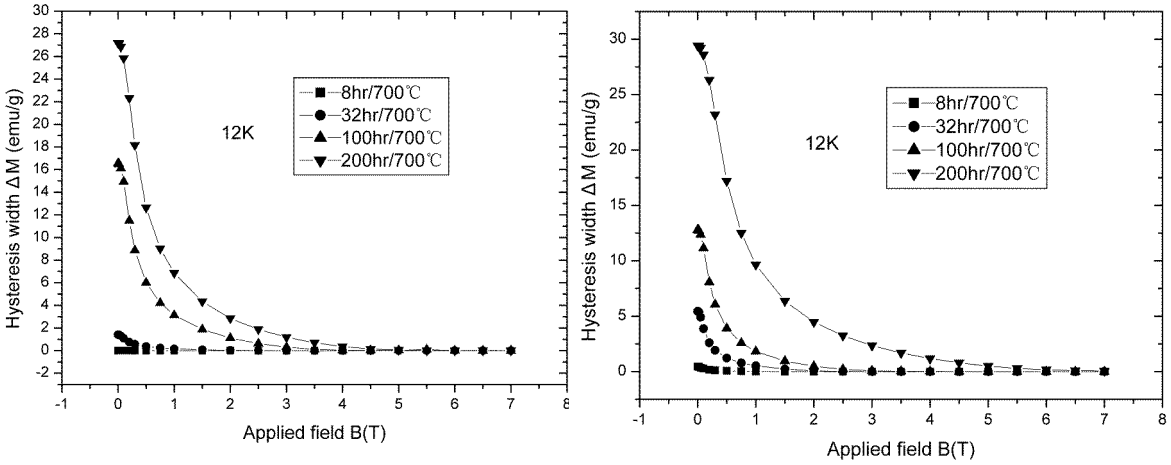

(a) SF2 (b) SF4

Fig.5-9 The ΔM-B curves of the ME samples heat-treated at 700°C for different times

From Fig.5-9 (a) and (b) it can be found that the ΔM-B curves of the two ME wires shifted upwards with the increase of reaction time from 8hrs to 200hrs, more substantially for SF4 wire in (b) figure. This result reveals the increase of package J_C with the reaction time elongation.

The calculated A15 layer J_C as a function of field B was depicted in Fig.5-10.

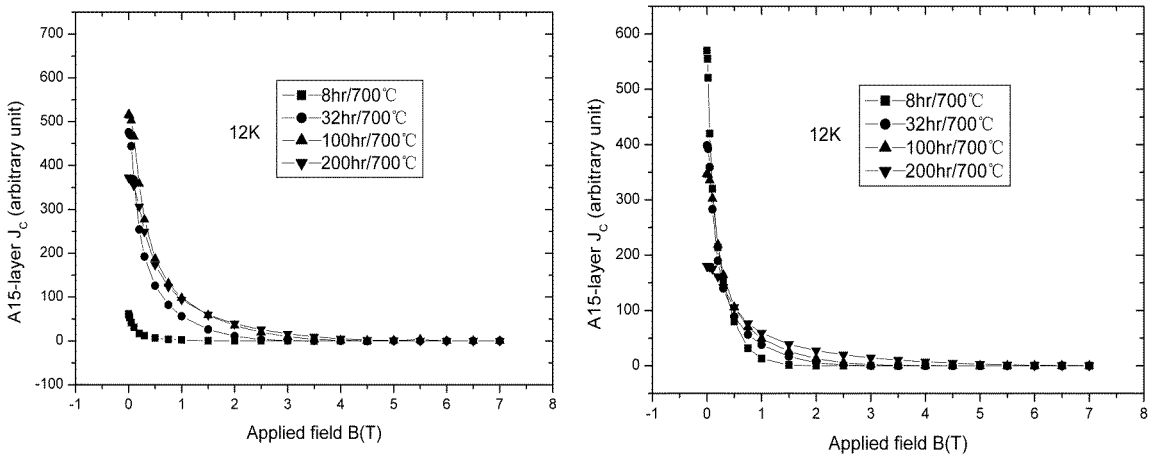

(a) SF2 (b) SF4

Fig.5-10 The A15 layer J_C-B curves of the ME samples heat-treated at 700°C for different times

In Fig.5-10, two characteristics can be found. The first is that the (a) and (b) figures

showed very small variations of A15 layer J_C-B with the reaction time, except for the lower curve of the 8hr /700°C sample in (a) figure. This result indicates that the A15 layer J_C changes very few with the increase of reaction time. That is to say, the current-carrying capacity per unit A15 area maintains no change although the elongation duration may increase the A15 layer thickness.

The other characteristic is that the samples heat-treated for short times had rather high A15 layer J_C at low field, but quick decrease happened with the increase of the field, whereas the long duration samples had a slow shift-down at high field, especially for the SF4 wire in (b) figure. This result demonstrates that long reaction time is liable to increase the current-carrying capacity of high field.

(3) (ΔM × B)-B curves and A15 layer F_P-B

The two wire samples heat-treated at 700°C for four duration times were also plotted for the (ΔM × B) values as a function of field B, as shown in Fig.5-11.

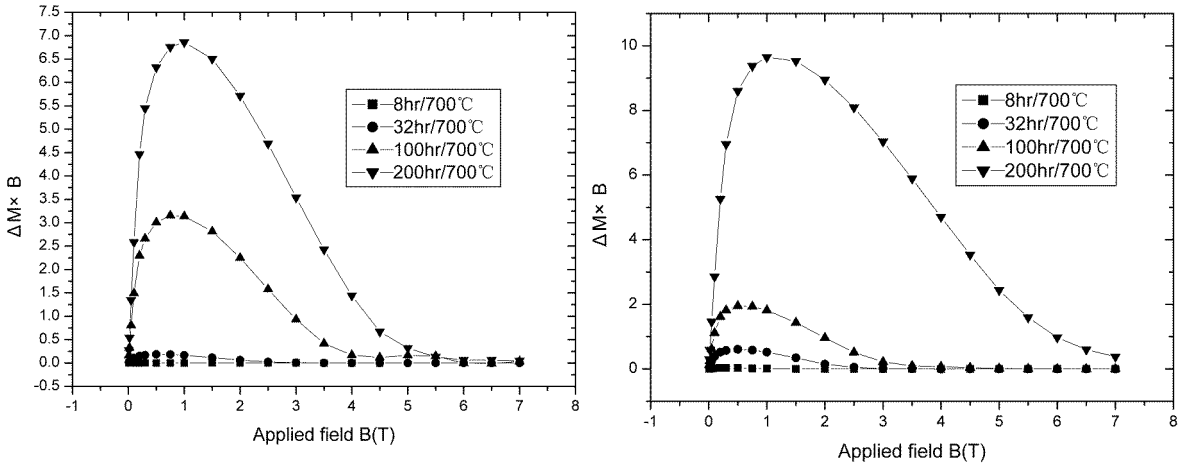

(a) SF2 (b) SF4

Fig.5-11 The (ΔM × B)-B curves of the ME samples heat-treated at 700°C for different times

From Fig.5-11 (a) and (b) it can be found that the (ΔM × B)-B curves of the two ME wires shifted upwards with the increase of reaction time from 8hrs to 200hrs, more substantially after 32hr reaction for SF2 wire in (a) figure. This result reflects the increase of the package F_P of the ME wires with the reaction time elongation. Before 32hr reaction time, the amount of the developed A15 layer is very thin, causing the weak package F_P; after that, the flux pinning situation is improved obviously because of the growing thickness of the A15

layer.

The calculated A15 layer F_P versus field B was depicted in Fig.5-12.

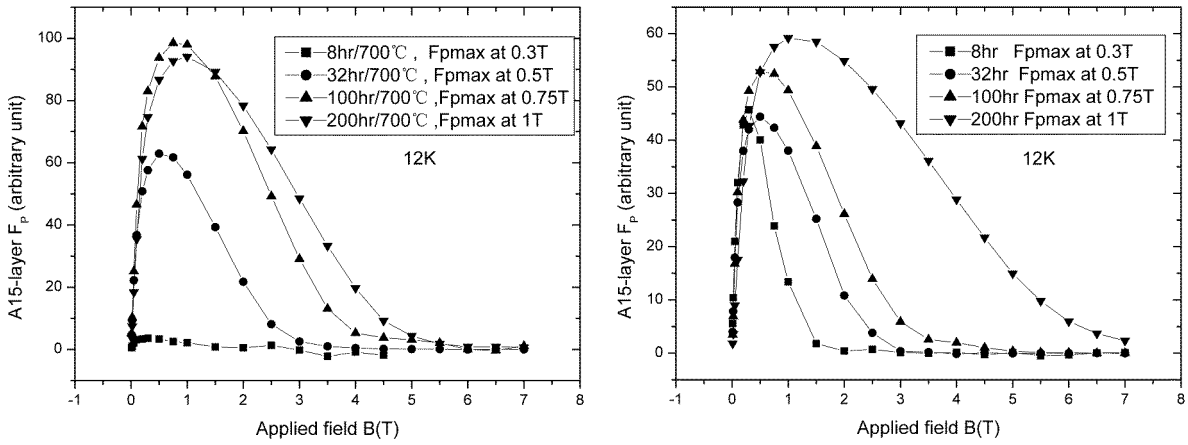

(a) SF2 (b) SF4

Fig.5-12 The A15 layer F_P-B curves of the ME samples heat-treated at 700°C for different times

In Fig.5-12, also two characteristics can be found. The one is that the (a) and (b) figures showed very small variations of A15 layer F_P-B before the peaks with the reaction time increase, except for the lower curve of the 8hr /700°C sample in (a) figure. This result indicates that the A15 layer F_P and then the current-carrying capacity per unit A15 area changes very little with the increase of reaction time, although the elongation duration may increase the A15 layer thickness.

The other characteristic is that the A15 layer F_P-B curves are expanded to high field direction with the elongation of reaction time and are shifted down slowly for long duration samples with the increase of testing field. This result demonstrates that long reaction time is liable to increase the A15 layer F_P, especially at high field.

Observing the positions of maximum flux pinning force in Fig.5-12, the two wires both showed 0.3T at 8hr to 0.5T at 32hr, and to 1T at 200hr reaction duration. These results exhibit that the maximum flux pinning force moves towards high-field direction with the increase of reaction time. That is to say, the extension of reaction time may not only increase the grain boundary area, but also improve the homogeneity of grain configuration.

5.2.2.3 Wire Sn Ratio Effect

The SF1, SF2 and SF3 wire samples (different Sn ratios in the composite composition) heat-treated at the same temperature for the same duration were selected to compare the Sn ratio influence. The results are as the followings.

(1) H-T lines and T*(B) lines

The three wire samples heat-treated at 725°C for 200hrs were measured for the H-T lines and T*(B) lines, as depicted in Figs.5-13 and 5-14 respectively.

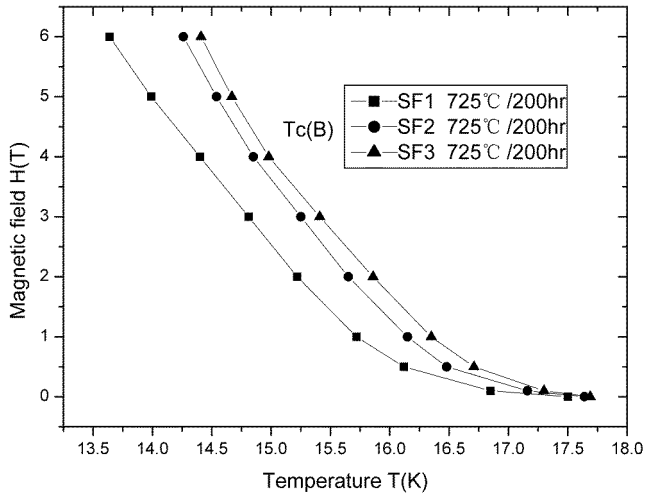

Fig.5-13 H-T lines of the three wire samples heat-treated at 725°C for 200hrs

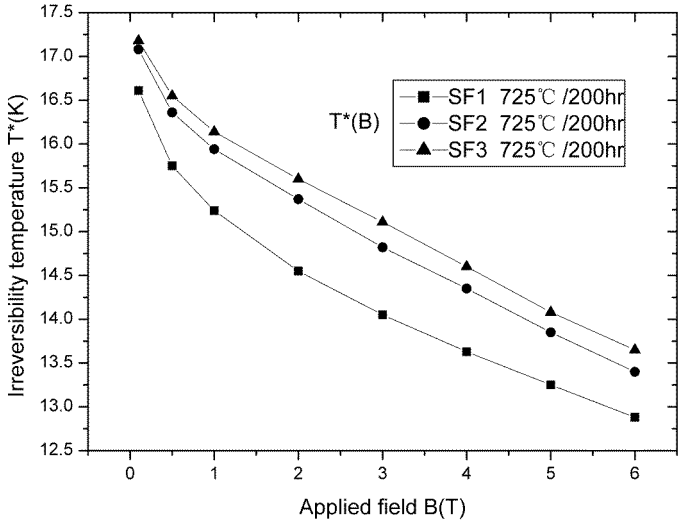

Fig.5-14 T*(B) lines of the three wire samples heat-treated at 725°C for 200hrs

From Fig.5-13 it is found that the H-T lines showed large up-shifts from SF1 to SF3 samples, with even larger variation from 15wt%Sn ratio of SF1 wire to 20wt%Sn of SF2 wire. That is to say, the T_C (B) value is increased with the increase of Sn ratio in the composite

wire.

From Fig.5-14 it is seen that T*(B) lines also had the same variation trend as the H-T lines, meaning that T*(B) value is also increased with the increment of Sn ratio in the composite wire.

(2) M-T transition curves

The three wire samples heat-treated at 700°C and 725°C for 200hrs were also measured for the M-T transition curves, as shown in Fig.5-15.

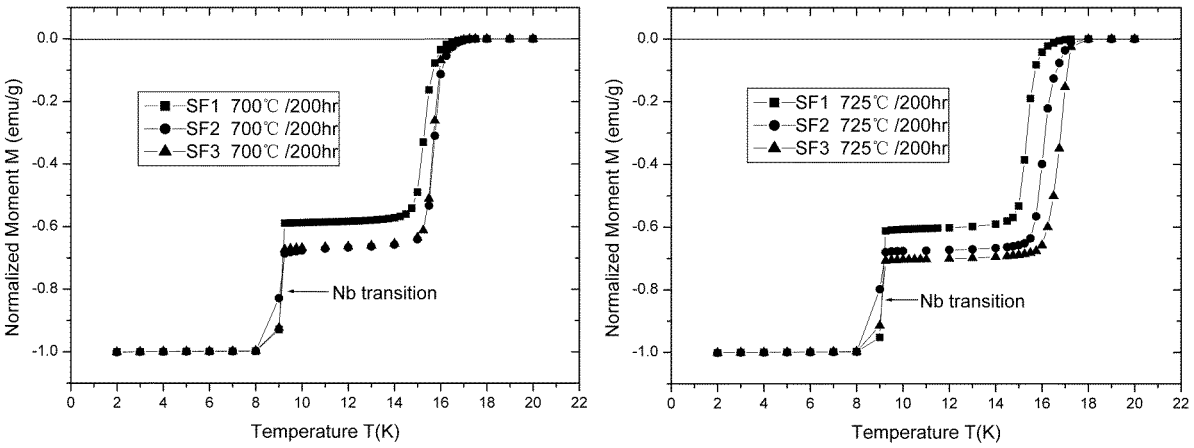

(a) 700°C/200hr (b) 725°C/200hr

Fig.5-15 M-T transition curve comparison of the samples heat-treated at the same conditions

From Fig.5-15 (a) and (b), it can be seen that the A15 transition curves of the three ME wires have shifted right-and-down wards with the increase of the Sn ratio, in which more obvious variation appearing from 15wt% to 20wt%. This result indicates that the increase of Sn ratio in the composite wire not only increases the amount of A15 layer but also improves the A15 phase quality, with the Sn ratio range of 15wt% to 20wt% more substantially.

(3) ΔM-B curves and A15 layer J_C-B

The three wire samples heat-treated at 700°C and 725°C for 200hrs were measured for the hysteresis width ΔM values which were plotted as a function of the field B, as shown in Fig.5-16.

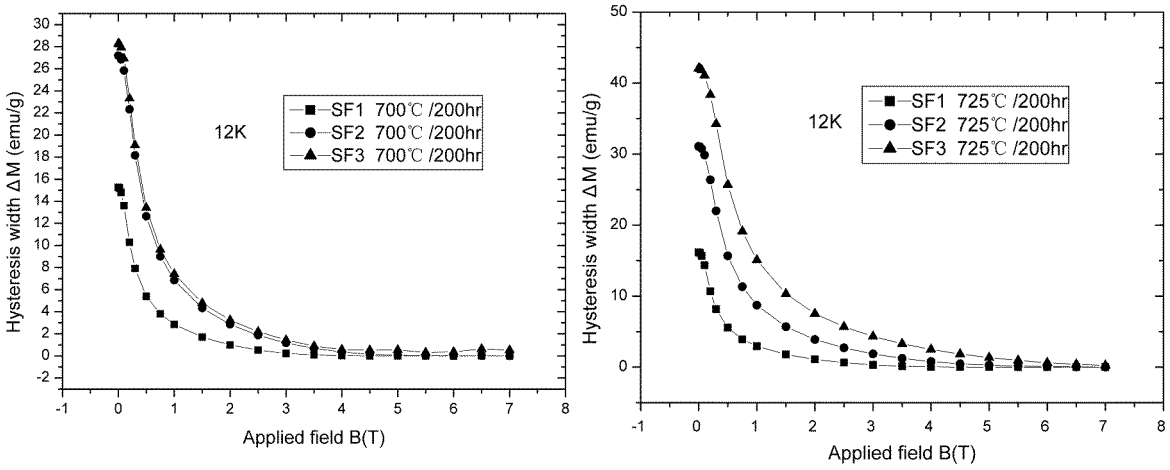

(a) 700°C/200hr (b) 725°C/200hr

Fig.5-16 ΔM-B curve comparison of the samples heat-treated at the same conditions

From Fig.5-16 (a) and (b), it can be seen that the ΔM-B curves of the three ME wires have shifted upwards with the increase of the Sn ratio, with more obvious variation appearing from 15wt% to 20wt% (see (a) figure). This result indicates that the package J_C is promoted with the Sn ratio increase.

The calculated A15 layer J_C as a function of field B was depicted in Fig.5-17.

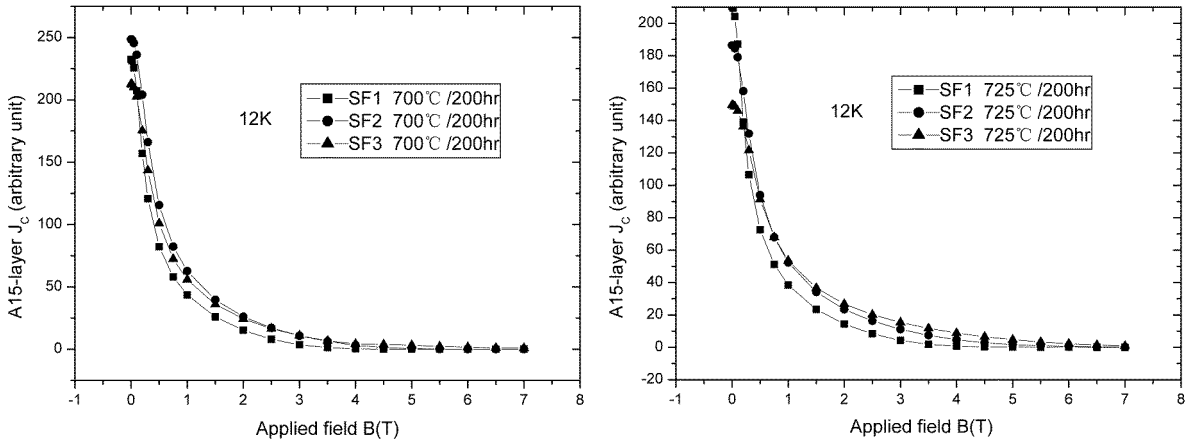

(a) 700°C/200hr (b) 725°C/200hr

Fig.5-17 A15 layer J_C-B curve comparison of the samples heat-treated at the same conditions

Different characteristics can be found in Fig.5-17 (a) and (b), where the A15 layer J_C-B curves had nearly no variation, besides a small lower position of the SF1 wire. This result demonstrates that the A15 layer J_C values of the three ME wires have no obvious variation with the Sn ratio, although large differences in the package J_C values.

(4) (ΔM × B)-B curves and A15 layer F_P-B

The three wire samples heat-treated at 700°C and 725°C for 200hrs were also plotted for

the (ΔM × B) values as a function of field B, shown in Fig.5-18.

From Fig.5-18 (a) and (b) it can be found that the (ΔM × B)-B curves of the three ME wires shifted upwards largely with the increase of the Sn ratio, more substantially from 15wt% to 20wt% (see (a) figure). This result indicates that the increase of the Sn ratio promotes the A15 phase formation, enlarging the grain boundary area and thus enhancing the package F_P.

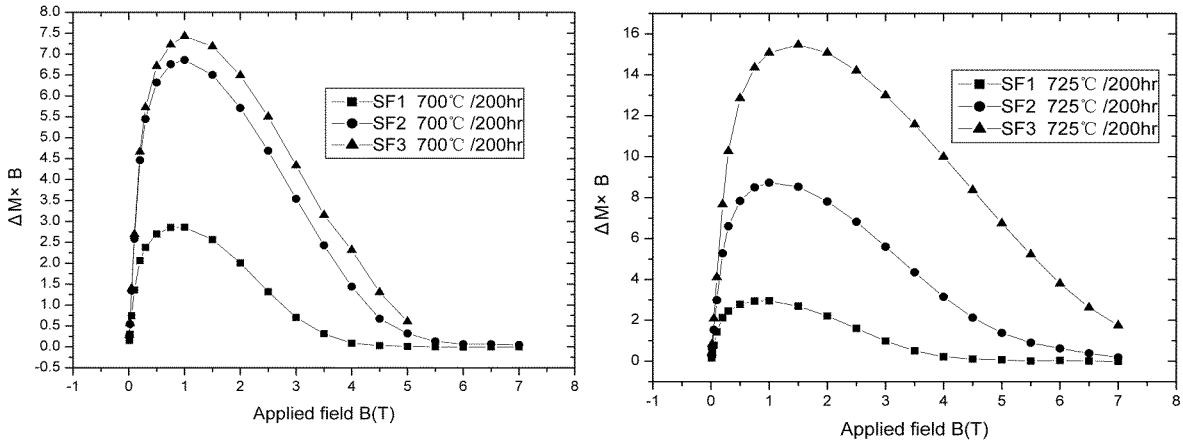

(a) 700°C/200hr (b) 725°C/200hr

Fig.5-18 The (ΔM × B)-B curve comparison of the samples heat-treated at the same conditions

The calculated A15 layer F_P versus field B was depicted in Fig.5-19.

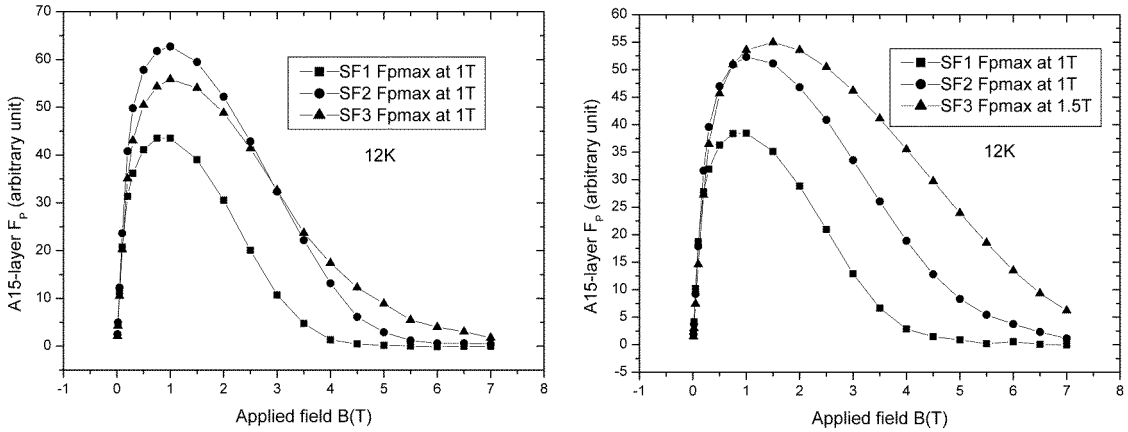

(a) 700°C/200hr (b) 725°C/200hr

Fig.5-19 The A15 layer F_P-B curve comparison of the samples heat-treated at the same conditions

Different characteristics can also be found in Fig.5-19 (a) and (b), where the A15 layer F_P-B curves had nearly no difference before the curve peaks, but expanded to high field direction with the increase of the Sn ratio. This result exhibits that the A15 layer F_P is

strengthened with the Sn ratio increase, more obviously at high field.

Observing the positions of maximum flux pinning force in Fig.5-19, it is seen that the three samples at 700°C/200hr reaction in (a) figure all showed the maximum F_P at 1T, but the samples at 725°C/200hr in (a) figure showed a small shift rightwards from 1T for SF1 and SF2 wires to 1.5T for SF3 wire. This result indicates that the maximum flux pinning force moves a little towards high-field direction with the increase of Sn ratio, meaning that the increase of Sn ratio in the composite wire improves the homogeneity of A15 configuration to some extent.

5.2.2.4 Alloyed Dopant Effect

The SF2 and SF4 wire samples (the same Sn ratio of 20wt% in the composite composition) heat-treated at the same temperature for the same duration were selected to compare the influence of third element alloying. The results are as the followings.

(1) H-T lines and T*(B) lines

The two wire samples heat-treated at 700°C for 200hrs were determined for the H-T lines and T*(B) lines, as depicted in Figs.5-20 and 5-21 respectively.

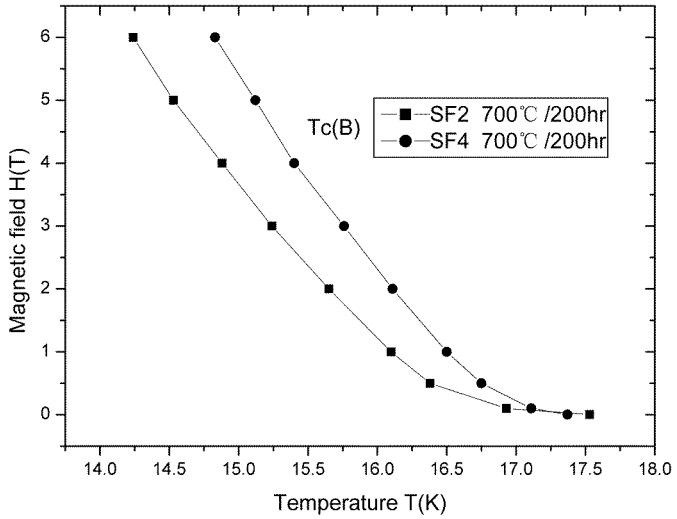

Fig.5-20 H-T lines of the two wire samples heat-treated at 700°C for 200hrs

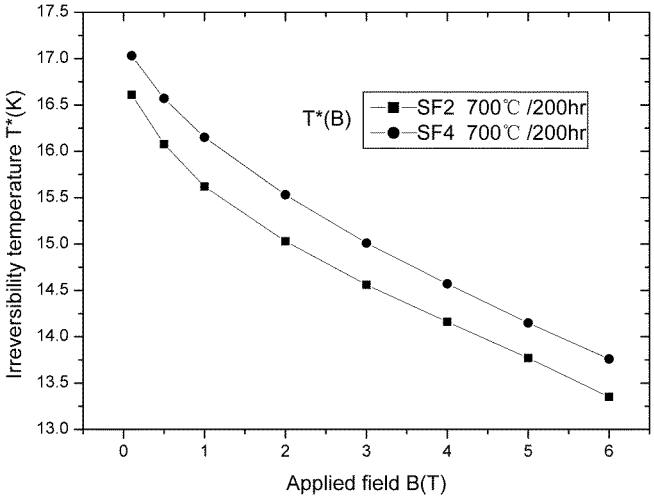

Fig.5-21 T*(B) lines of the two wire samples heat-treated at 700°C for 200hrs

From Figs.5-20 and 5-21 it is seen that the H-T and T*(B) lines of SF4 sample located at the higher position than those of SF2 sample. That is to say, the Zr alloying largely increases the T_C (B) value and T*(B) value.

(2) M-T transition curves

The two wire samples heat-treated at 700°C and 725°C for 200hrs were measured for the M-T transition curves, as shown in Fig.5-22.

The samples at 700°C/200hrs in Fig.5-22 (a) show that the M-T transition curves of the SF4 wire with 1at%Zr addition in Nb shifted right-and-down wards largely, compared with the SF2 wire without Zr alloying. The samples at 725°C/200hrs in Fig.5-22 (b) shows that the M-T transition curves of the SF4 wire had an even larger shift-down, but a small left shift, due to Sn leakage into stabilizing Cu.

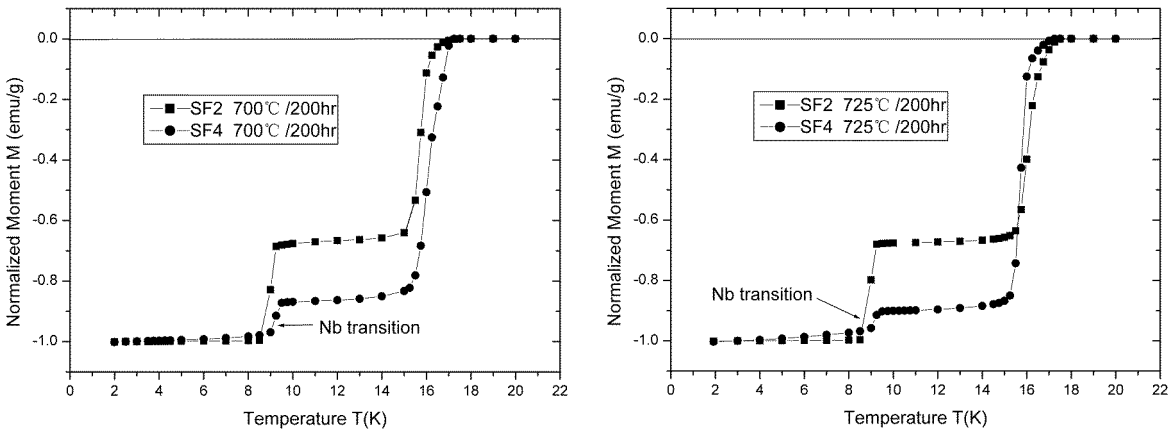

(a) 700°C/200hr (b) 725°C/200hr

Fig.5-22 M-T transition curve comparison of the samples heat-treated at the same conditions

These results indicate that the Zr alloying substantially accelerates the A15 phase formation (large increase of A15 layer thickness) and improves A15 phase quality (Sn content distribution) either.

(3) ΔM-B curves and A15 layer J_C-B

The two wire samples heat-treated at 700°C and 725°C for 200hrs were determined for the hysteresis width ΔM values which were plotted as a function of the field B, as shown in Fig.5-23.

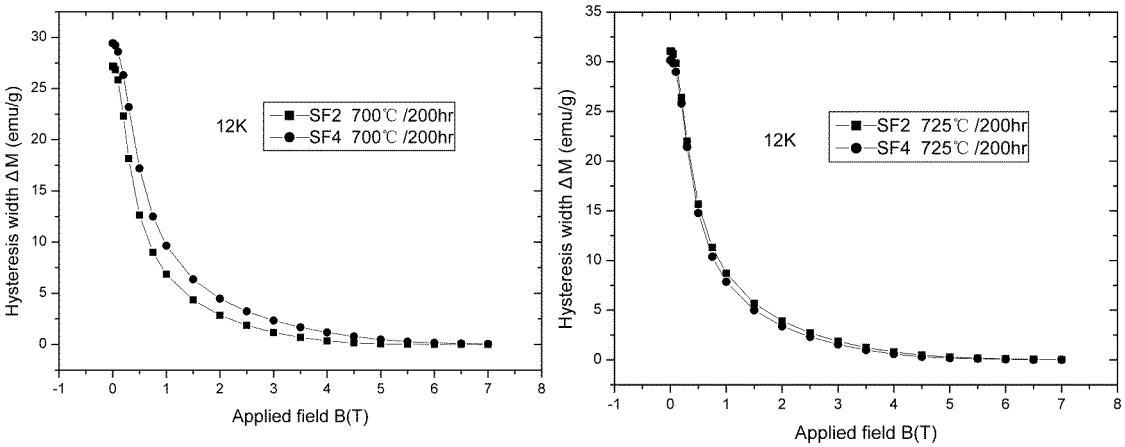

(a) 700°C/200hr (b) 725°C/200hr

Fig.5-23 ΔM-B curve comparison of the two wire samples heat-treated at the same conditions

From Fig.5-23 (a) it can be seen that the ΔM-B curves of the Zr alloyed SF4 wire shifted upwards largely, compared with the SF2 wire without Zr addition. The shift-down of the ΔM-B curve of SF4 725°C/200hrs sample in (b) figure was also caused by the Sn leakage. This result indicates that the package J_C is promoted substantially with the Zr addition.

The calculated A15 layer J_C versus field B was depicted in Fig.5-24.

Different characteristics can be found in Fig.5-24, where the A15 layer J_C-B curves had nearly no variation, besides a small decrease of the SF4 725°C/200hrs sample in (b) figure due to the Sn leakage. This result demonstrates that the A15 layer J_C has not been improved with the Zr addition, although large difference appeared with the package J_C values.

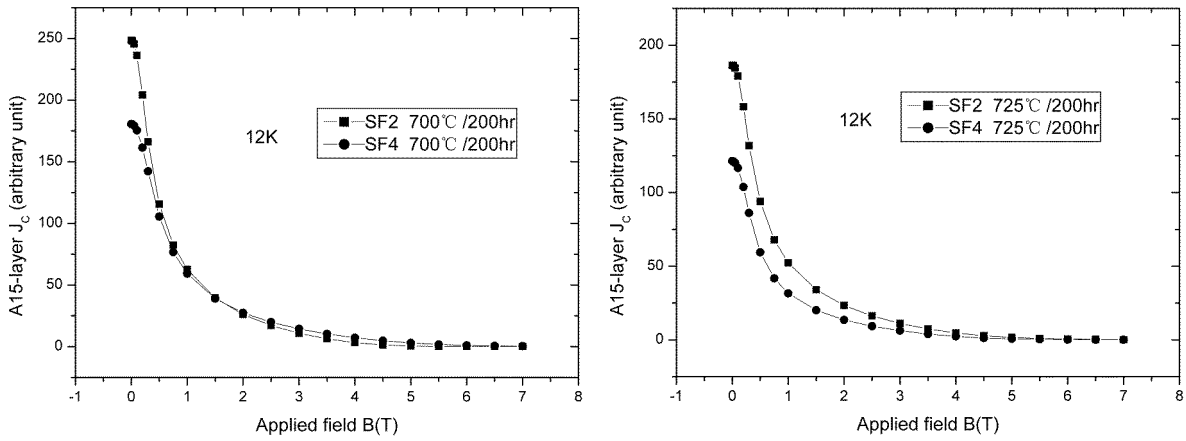

(a) 700°C/200hr (b) 725°C/200hr

Fig.5-24 A15 layer J_C-B curve comparison of the two wire samples heat-treated at the same conditions

(4) (ΔM × B)-B curves and A15 layer F_P-B

The two wire samples were also plotted for the (ΔM × B) values as a function of field B, shown in Fig.5-25.

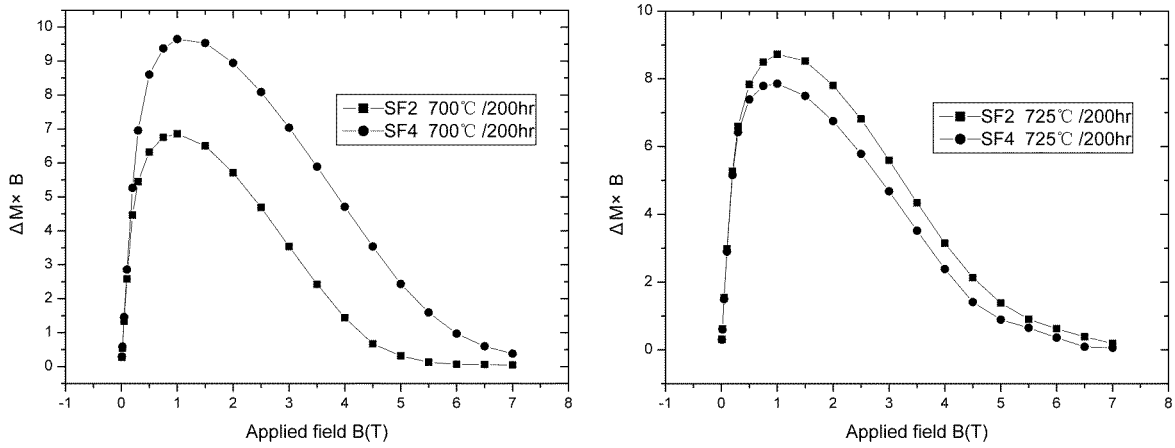

(a) 700°C/200hr (b) 725°C/200hr

Fig.5-25 The (ΔM × B)-B curve comparison of the samples heat-treated at the same conditions

From Fig.5-25 (a) it can be found that the (ΔM × B)-B curves of the Zr alloyed SF4 wire shifted upwards largely, compared with the SF2 wire without Zr addition. The shift-down of the ΔM-B curve of the SF4 725°C/200hr sample in (b) figure was also due to the Sn leakage. This result indicates that the addition of Zr in the composite wire substantially accelerates the A15 phase

The calculated A15 layer F_P versus field B was depicted in Fig.5-26.

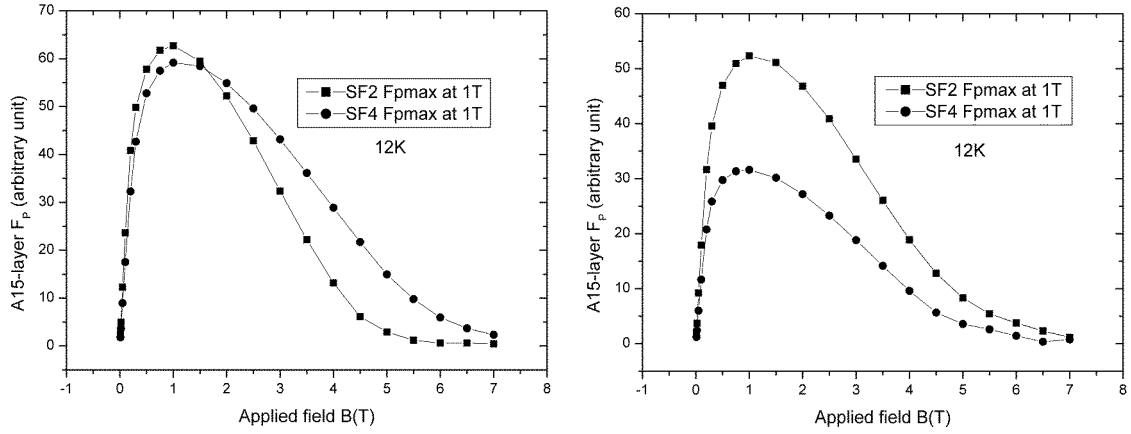

(a) 700°C/200hr (b) 725°C/200hr

Fig.5-26 The A15 layer F_P-B curve comparison of the samples heat-treated at the same conditions

Different characteristics can also be found in Fig.5-26, where the A15 layer F_P-B curves had nearly no difference before the curve peaks, but expanded to high field direction with the Zr addition, indicating the enhancement of A15 layer F_P at high field. The shift-down of the A15 layer F_P-B curve of the SF4 725°C/200hr sample in (b) figure was also caused by the Sn leakage.

Observing the positions of maximum flux pinning force in Fig.5-26 (a) and (b), the two wire samples all showed the maximum F_P at 1T, meaning no improvement of the maximum F_P with the Zr alloying.

5.2.2.5 T_C and H* Values

The selected ME wire samples were measured for the M-T transition curves from which the critical temperature T_C values were determined and were also obtained the irreversibility field H* values at 12K were also obtained with their hysteretic loops. The results are included in Table 5-1.

Table 5-1 exhibits the following characteristics:

The 675°C/200hr samples of SF2 and SF4 wires had a rather low T_C, and the T_C values were increased and achieved the values of MF wires when the reaction temperature was increased to 700°C and 725°C. The irreversibility field H* at 12K testing temperature was increased with the elevation of reaction temperature, except for the decrease of the 725°C/200hr sample of SF4 wire due to the Sn leakage. The HT time influences are like these: (1) the T_C values at 700°C were increased from 8hr to 100hr reaction and extended to the

same values as MF wires after 100hr duration; (2) the H* value was continuously increased with the reaction time prolongation. The effect of the wire Sn ratio is like this: the T_C of long duration (200hr) nearly remained the same, but the H* value was increased, with the increase of Sn ratio in the composite wire.

Table 5-1 T_C and H* Values for ME wire samples heat-treated at different conditions

sample	**Heat treatment**	**T_C, (K)**	**H*(T), 12K**
SF2	675°C/200hr	16.9	4.1
	700°C/200hr	17.4	5.5
	725°C/200hr	17.5	6.3
SF4	675°C/200hr	15.4	2.6
	700°C/200hr	17.3	6.4
	725°C/200hr	17.3	6.0
SF2	8hr/700°C	14.2	1.6
	32hr/700°C	15.8	2.9
	100hr/700°C	17.1	4.4
	200hr/700°C	17.4	5.5
SF4	8hr/700°C	14.3	1.6
	32hr/700°C	15.8	2.9
	100hr/700°C	17.0	3.6
	200hr/700°C	17.3	6.4
SF1		17.2	4.2
SF2	700°C/200hr	17.4	5.5
SF3		17.3	5.8
SF1		17.2	4.6
SF2	725°C/200hr	17.5	6.3
SF3		17.5	7.3

5.2.3 Discussion

Several differences have been found between ME wire and MF wire in the magnetization measurements. For instance, the superconducting properties of ME wires were continuously improved with the increase of HT temperature and time, but those of MF wires often achieved their maxima before lowering down. These differences are primarily caused by the different configuration designs of the two kinds of wires. There are two important dissimilarities between the two designs. In the first case, the Sn core of ME wire is located inside the Nb filamentary tube, while the Sn core of MF wire is among a bundle of a large number of Nb filaments. Therefore the A15 reaction of ME wire is radially from the Nb tube inside to outside, forming a inner-to-out gradient composition distribution with high Sn concentration at the layer inner part. On the contrary, the MF wire reacts from the Nb filament outside to inside, forming an out-to-inner gradient composition with high Sn concentration at the filament out part. Because of the specific design of the ME wire, the best A15 layer formed during HT can not shield the outer part of lower Sn concentration in magnetization measurement. In other words, various compositions of the gradient A15 layer in ME wire are transparent to the applied field and the magnetization measurement actually reflects the whole situation of the gradient layer. This wire design is similar to that of PIT wire in which the A15 reaction is also progressing from filament inside to outside. So, there have appeared some identical magnetization performances between the ME and PIT wires [134,135].

The other dissimilarity between the two designs is that the Nb filament tube of ME wire has a much larger thickness which is used not only for A15 phase formation, but also as a diffusion barrier. The main purpose of this design was to observe the variation of A15 phase formation progress in a long reaction period and to study the phase formation kinetics. In this way, almost all ME samples did not react through even after 200hr duration, just forming a gradient A15 layer, with the only exception of the 725°C/200hr sample of SF4 wire which had much higher reaction rate. However, the MF wire are usually composed of hundreds of thousands of Nb filaments which are very thin (only 3~5μm) and will be completely reacted in much shorter time. With the progress of heat reaction the formed A15 phase gradient layer in the filament of MF wire will grow and then flatten gradually and its composition will become more and more homogenous. Therefore, it is obvious that in SQUID magnetization

measurement the ME wire mainly reflects the variation of A15 layer quantity with the progress of heat reaction, while the MF wire primarily reveals the growth and homogenizing of A15 phase.

According to the above analysis of the relationship of wire design and magnetization measurement, the results in section 5.2.2 can be interpreted as the followings.

Firstly, the reaction temperature influence is discussed. With the elevation of HT temperature, the gradient A15 layer developed in the ME wire grow faster and faster and its average composition became increased, which was demonstrated in the SQUID measurements. The average composition related properties, such as $T_C(B)$ and T*(B), were improved with the reaction temperature increase. Although the elevation of reaction temperature may coarsen the grain size, the large increase of A15 layer quantity substantially enlarges the grain boundary area, bringing on the large increase of package F_P and then package J_C, as the hysteresis width ΔM is also proportional to the amount of A15 phase. However, as previously known, the package properties are the obtained values divided by the entire wire cross section area, and do not reflect the situations of the A15 layer which is more important for evaluating the phase formation. For this reason, the magnetization properties of A15 layers of ME wires were determined in this study. The obtained results clearly showed that the A15 layer J_C and A15 layer F_P at high field were strengthened more substantially than those at low field with the increase of reaction temperature. This means that the elevated temperature can raise the upper critical field $H_{C2}(T)$ or irreversibility field H*(T), which was confirmed by the values in Table 5-1. It is indeed that the increase of $H_{C2}(T)$ or H*(T) is an effective way to improve the high-field performances of the Nb_3Sn superconductors [55]. Therefore, if the wire is for high-field application, a relatively high temperature should be chosen for heat treatment.

Secondly, the reaction time influence is considered. From section 5.2.2.2 we have shown that with the extension of reaction time, the A15 phase quantity (layer thickness) became increased and the quality (average composition) was improved. These can be demonstrated by the hysteretic loop measurements, although the $T_C(B)$ and T*(B) values could not be tested due to the very thin layer thickness for the samples heat-treated shorter than 32hrs. The package J_C and package F_P had been proved to become enlarged with the reaction time

extension. Even though the long reaction time may coarsen the grain dimension, the grain boundary area is also substantially enlarged because of the ever-increasing of A15 layer thickness, leading to the increase of package F_P and package J_C. Similarly, different characteristics can be found for A15 layer J_C and A15 layer F_P, which were obviously showed to expand to high field direction for long duration sample. In addition, the maximum flux pinning force moves towards high-field direction with the increase of reaction duration. These also mean that the long HT time can raise the H_{C2} (T) or H*(T) values, which can be proved in Table 5-1, and improve the high-field performances of the Nb_3Sn superconductors.

Thirdly, the effect of wire Sn ratio is concerned. It is known that the A15 phase formation rate is dependent not only on the Sn diffusion and reaction rate but also on the amount of Sn source for Sn supplying. At the same HT conditions, the most important factor is thus the amount of Sn provision or the Sn ratio in the composite wire. It is clear that the increase of Sn provision enlarges the formed A15 phase quantity or layer thickness and improves the quantity-related magnetization properties. These can be confirmed by the results in section 5.2.2.3. The SF1, SF2 and SF3 wires have the Sn ratios of 15wt%, 20wt% and 25wt% respectively. The T_C (B) and T*(B) values were increased with the increment of Sn ratio, with even larger variation from 15wt% to 20wt%. The M-T transition curves shifted right-and-down wards, indicating the increase of the A15 amount and the improvement of A15 quality. The package J_C and package F_P were promoted with the Sn ratio increase. A15 layer J_C and A15 layer F_P, the most understandable values of reflecting A15 layer quality, were strengthened more obviously at high field, meaning the increase of H_{C2} (T) or H*(T) (see Table 5-1) and the improvement of high-field performance. However, it should be noticed that too much Sn source actually cannot further improve the superconducting properties. One should carefully balance the Nb/Sn/Cu ratio.

Lastly, the effect of the third element alloying is considered. In the four ME wires, the Sn cores were all alloyed with 2wt%Ti, the same as those of the NIN MF wire. From the measurements of MF wires, we have shown that the Ti alloyed in Sn core can accelerate the Sn diffusion and reaction, improve the A15 phase formation and reduce the A15 reaction temperature, all of which are beneficial to the promotion of superconducting properties. However, the four ME wires have the same Ti alloyed Sn cores, so that the same beneficial

effect on phase formation. It is not necessary to compare the Ti addition in ME wires. The primary consideration in ME wire design is to investigate the effect of Zr addition. The results in section 5.2.2.4 have shown that with 1at%Zr addition the T_C (B) and T*(B) values were largely increased, the M-T transition curves substantially shifted right-and-down wards, and the package J_C and package F_P were significantly enlarged, even if the Sn leakage happens at 725°C/200hr for the SF4 sample wire (see the SEM photograph in section 5.4.2) due to the too fast reaction rate. Furthermore, the A15 layer J_C and A15 layer F_P largely broadened to high field direction with the Zr addition, meaning the increase of H*(T) (see Table 5-1). These obvious effects of Zr alloying may be explained as that the Zr, as a dopant in Nb, lowers the diffusion activation energy and promotes the inter-diffusion between Sn and Nb, resulting in the increase of A15 phase formation rate. Another reason may be that the dopant Zr serves as an additional flux pinning center, increasing the flux pinning force, or forms $Nb(Zr)_3Sn$, improving the superconducting performances.

5.2.4 Conclusion

There are two important dissimilarities between ME and MF wires. One is that the filament of ME wire formed an inner-to-out gradient A15 layer during heat treatment, leaving various A15 compositions apparent to the applied field; while the MF wire formed an out-to-inner gradient A15 layer in which the outer high-Sn part could shield the inner low-Sn part. The other is that the A15 layer of ME wire is continuously growing and always in gradient form, resulting in the ever-increasing of A15 quantity, whereas, the filament of MF wire will react completely and its composition will become uniformly distributed afterwards, so that the A15 quantity will not change any more after reaction through. It is these two dissimilarities that cause the substantial differences of magnetization properties between the two sorts of wires.

The increase of HT temperature and time, the enlargement of Sn ratio in the composite wire and the addition of alloyed Zr all have nearly the same effect on the A15 phase formation of ME wires. They all increase the A15 phase quantity (layer volume) and improve its quality (average composition), but, comparatively, the reaction temperature and the Zr addition have more substantial influence.

In magnetization measurements, the four factors can increase the T_C (B) and T*(B) values, enlarge the package J_C and package F_P, and expand the A15 layer J_C and A15 layer F_P to high field direction and then improve the high-field performance of Nb_3Sn wire.

5.3 Neutron Diffraction Study for Mono-element Nb_3Sn Wires

5.3.1 Sample Preparation and Experiment

Two neutron diffraction techniques have been utilized in ME wire measurement. One is the in-situ examination which has been intensively discussed in the MF wire measurement (see section 4.4.2). The other method is the off-situ examination which will be fully dealt with in the ME wire measurement hereafter.

The ME wires for off-situ neutron diffraction examination were prepared from short length pieces (60 mm high), and 40 of them were sealed in one evacuated quartz tube with ~4Pa of Ar atmosphere before being put inside a tubular furnace for heat treatment. The HT procedures were in accordance with section 5.1. The heat-treated samples can then be used for off-situ measurement. The advantage of this method is that a number of samples of different wires heat-treated at different conditions can be prepared before the expensive neutron diffraction measurement and can be used to compare the phase formation situations of different HT conditions. Obviously, in-situ neutron examination can not do so long such processes (200 hours).

For off-situ neutron detection, 72 samples heat-treated at different conditions were separately fixed in a special sample holder and were exposed vertically to the neutron beam one by one. Neutron diffraction patterns were recorded at room temperature on the D1B diffractometer of the ILL-Grenoble, at a wavelength of 2.524 Å. Refinements were done with the same constraints as those done for in-situ measurement.

5.3.2 Results and Analysis

5.3.2.1 In-Situ Neutron Diffraction Measurement

The SF2 wire (Nb (Cu-20wt%Sn)) was chosen to carry out the in-situ neutron diffraction measurement. The resulted neutron patterns have been depicted in 3D manner, as shown in

Fig.5-27.

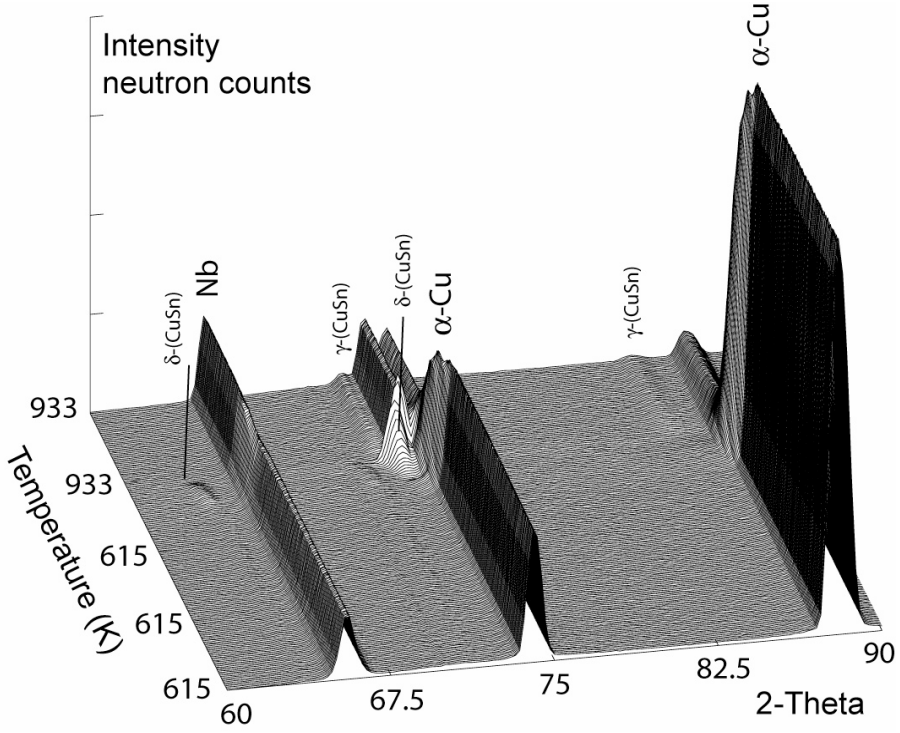

Fig.5-27 the neutron diffraction 3D patterns of SF2 wire

From Fig.5-27 it is seen that the phase formation progress is basically the same as that of MF wires. However, for this time duration at 660°C (24 hours), the quantity of the A15 phase formed is rather low and cannot be measured as neutron diffraction intensity is dependent on the phase volume. The ME wire has one composite element, particularly only one Nb filamentary tube, so that very small available area are available to form phases. Thus, the volumes of various phases are rather small. Specifically, the SEM photograph of the 675°C/32hr sample (higher reaction temperature and longer duration than the in-situ sample) is used to observe the A15 phase formation. As can be seen in Fig.5-28, the developed A15 layer cannot be observed. For observation of such a white A15 layer in Nb see for example figures 5-32(c) and 5-34(a) for longer time experiments.

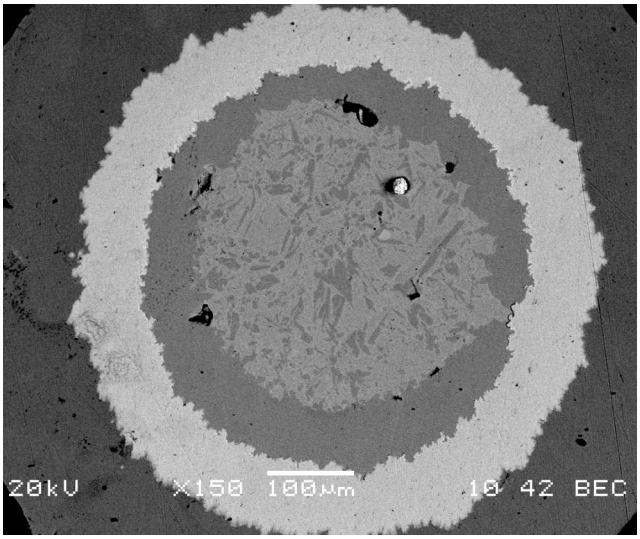

Fig.5-28 The SEM photograph of the 675°C/32hr sample of the SF2 ME wire

5.3.2.2 Off-Situ Neutron Diffraction Measurement

The 72 ME samples heat-treated at different conditions were carried out the off-situ neutron diffraction measurement for the main purpose of observing the A15 phase formation variation with HT conditions.

The SF4 wire samples at 700°C reaction were used as an example to show the reaction time influence, as depicted in Fig.5-29.

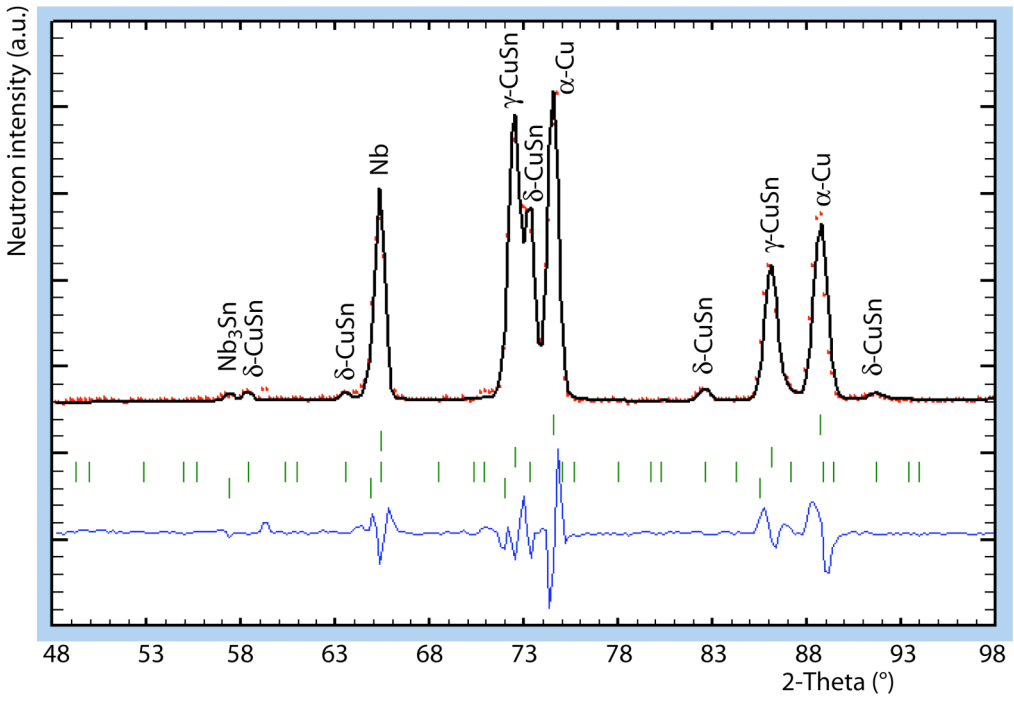

(a) 32hr

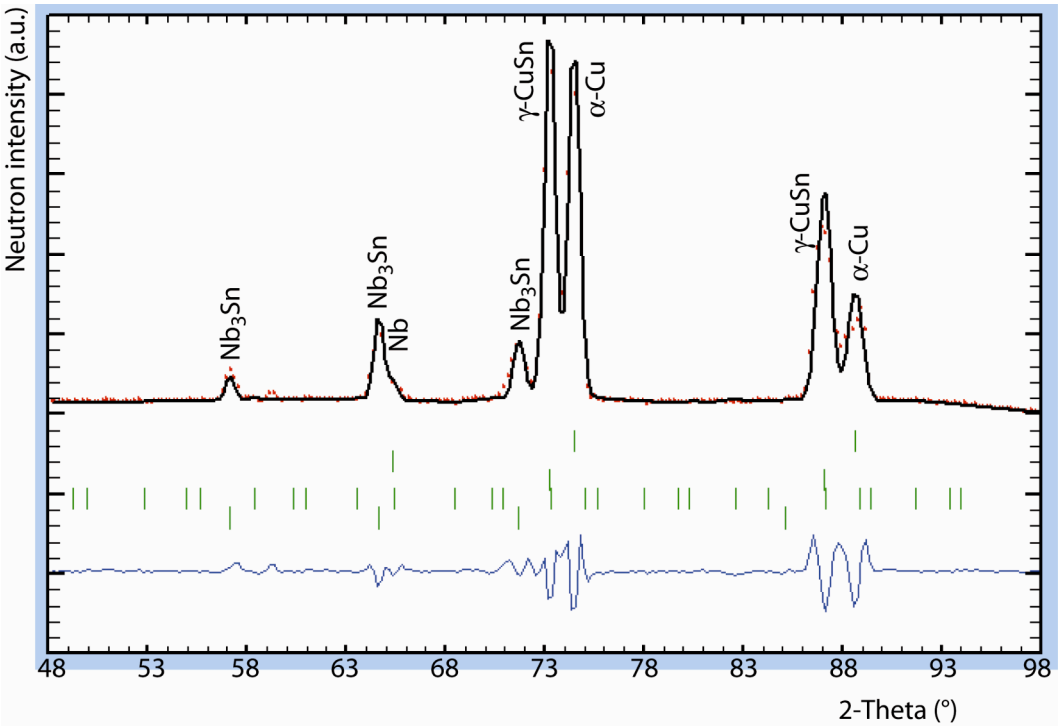

(b) 200hr

Fig.5-29 The neutron diffraction patterns of the SF4 samples of different durations at 700°C

It is clearly seen from Fig.5-29 that the Nb_3Sn phase intensities had a large increase from 32hr to 200hr reaction time.

The four wire samples heat-treated at 725°C for 200hrs were also depicted for the neutron diffraction patterns, as shown in Fig.5-30.

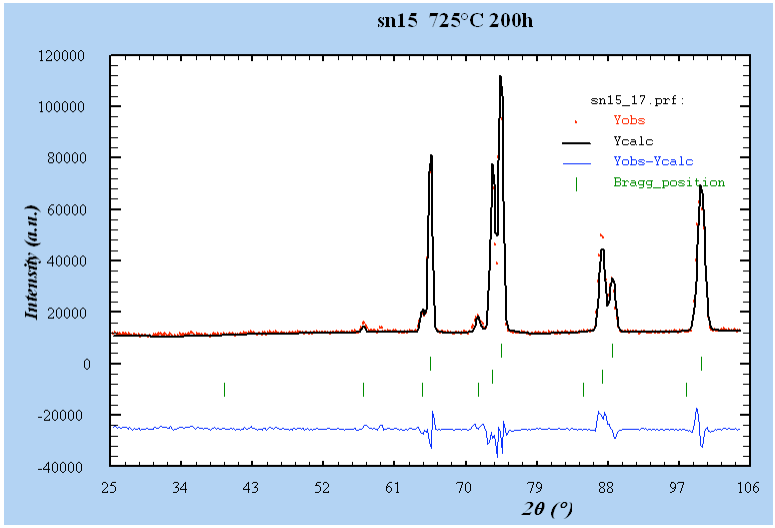

(a) SF1

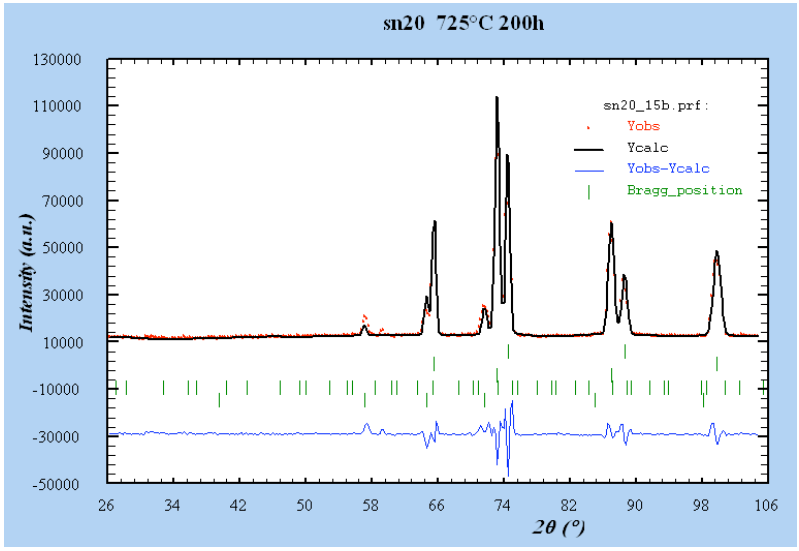

(b) SF2

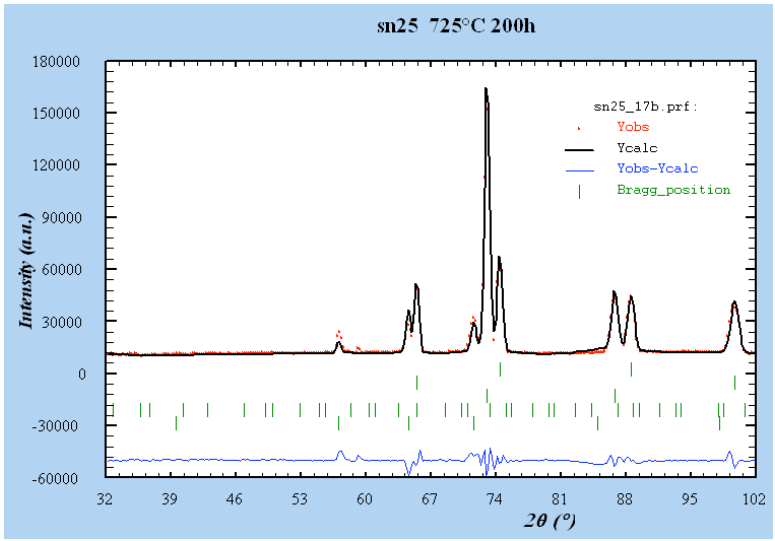

(c) SF3

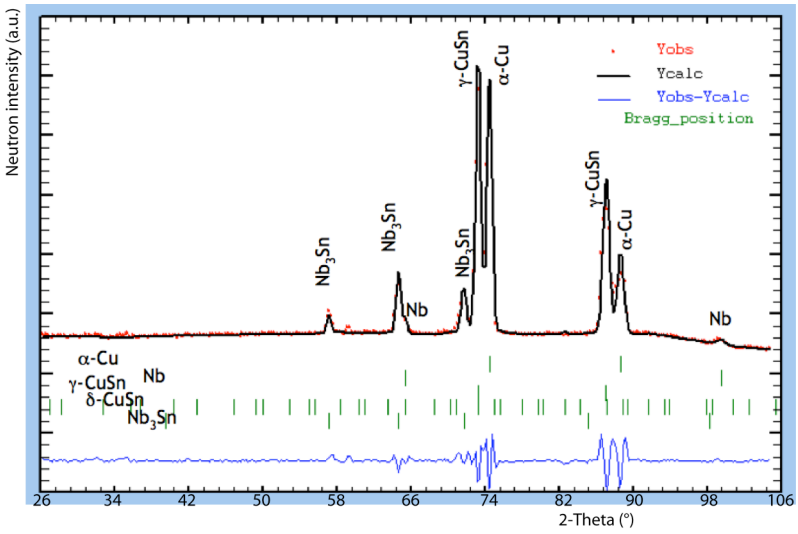

(d) SF4

Fig.5-30 The neutron diffraction patterns of the 725°C/200hrs samples of the four wires

It is found from Fig.5-30 that the SF4 wire had the strongest neutron diffraction intensity of Nb_3Sn phase. Comparing the wires of different Sn ratio, the SF3 wire is seen to behave the most.

In order to systematically compare the 72 samples, their neutron diffraction intensities of Nb_3Sn phase were calculated in percentage, qualitatively reflecting the Nb_3Sn phase content percentage, as plotted in Fig.5-31.

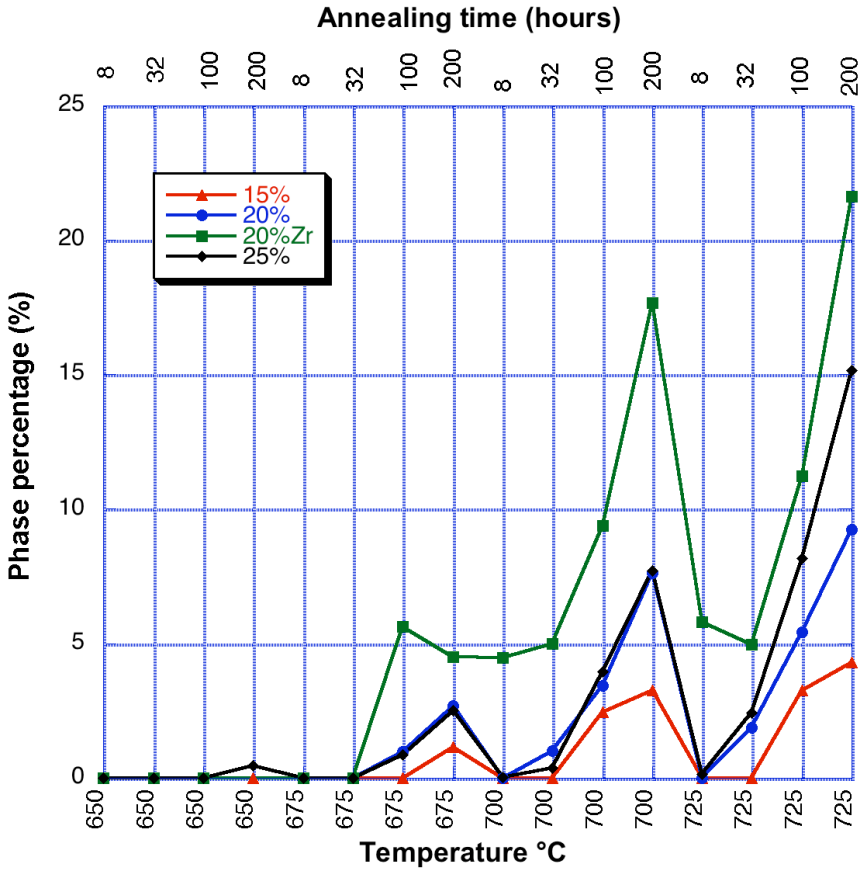

Fig.5-31 The neutron intensity percentages of the Nb_3Sn phase of various ME samples

It is found from Fig.5-31 that the Nb_3Sn phase quantity of SF4 wire shows the most significant increase with the extension of reaction time. Only 8hr duration at 700°C can produce a visible amount of Nb_3Sn phase, and the Nb_3Sn phase quantity had been exceeded 20% after 200hr duration at 725°C .

Comparing the wires of different Sn ratios, the SF3 wire produced an observable amount of Nb_3Sn phase at 700°C for 32hrs. The weakest variation appeared at the SF1 wire, the lowest Sn ratio, in which it is hard to observe a distinguishable Nb_3Sn phase formation even

heat-treated at 675°C for 100hrs. The 700°C/100hr sample of SF1 wire may be comparable to the 700°C/32hr sample of SF3 wire in Nb_3Sn phase formation.

In Fig.5-31, the temperature influence is obvious. All the ME samples heat-treated at 650°C even for 200hr duration are still hard to see detective Nb_3Sn phase formation. With the elevation of temperature to 700°C, the Nb_3Sn phase formation rate is much increased, and until 725°C a substantial increase of Nb_3Sn phase can be found for each ME wire.

5.3.3 Discussion

The in-situ neutron diffraction measurement of SF2 wire has demonstrated that the mechanism of phase formation is the same for the ME wire as for the MF wire. But the amount of the A15 phase formation is low and cannot be visualized for this time duration. This can be attributed to the rather small diffusion and reaction interface area of the ME wire. We have known that a MF wire has 18 or 19 Sn cores and hundreds of thousands of Nb filaments in its composite. The diffusion and reaction interface areas during Cu-Sn alloying and A15 phase formation are very large, resulting in the substantial increase of phase quantity. However, the ME wire has only one Sn core contacted with surrounding Cu matrix and only one Nb filamentary tube offered for A15 phase formation. It is certain that the small diffusion and reaction interface areas will lead to the small phase formation quantity and lower neutron diffraction intensity. This can be illustrated by the phase formation photographs of some ME samples in Fig.5-32.

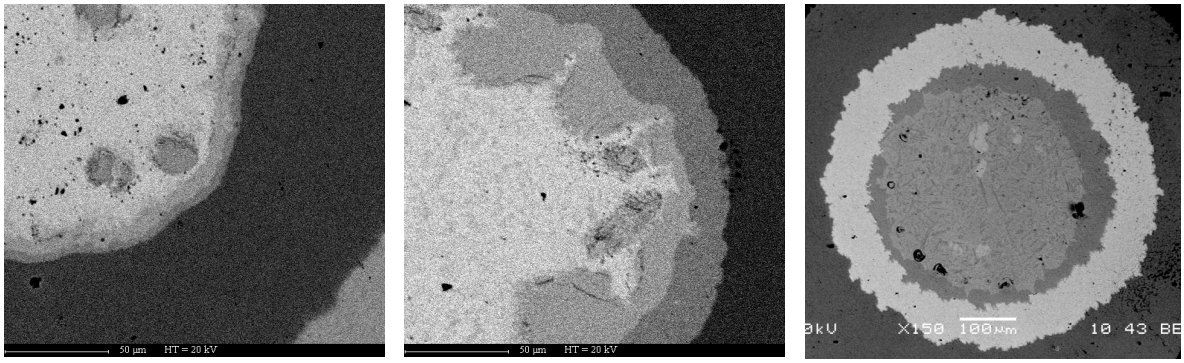

(a) 210°C/50hr (b) 210°C/50hr+340°C/25hr (c) 650°C/32hr

Fig.5-32 The SEM photographs of SF2 samples heat-treated for different periods

In 5-32(a) figure, the sample heat-treated at 210°C for 50hr only developed very thin

layers of η-CuSn phase and ε-CuSn phase. In (b) figure, the sample of 340°C for 25hr still had a large thickness of remained Sn core and Cu matrix, even though there happened liquid-solid diffusion. There was no Sn diffused to the Nb-Cu interface either. The (c) figure shows the situation of the sample heat-treated at 650°C for 32hrs. It is difficult to find the Nb_3Sn phase formation, due to the small reaction interface area.

Hereafter, the off-situ neutron diffraction measurement of ME wires is discussed. In order to investigate the kinetics of Nb_3Sn phase formation, the SF4 wire, which has the fastest reaction rate, was selected to measure the neutron diffraction intensities of Nb_3Sn phase with the variation of reaction time at a fixed temperature. The neutron intensities of Nb_3Sn phase versus reaction time were plotted in logarithmic manner and were linearly fitted, as shown in Fig.5-33.

From Fig.5-33 it can be known that the Nb_3Sn phase formation has a power variation relationship with reaction time and the power index is also varied with reaction temperature.

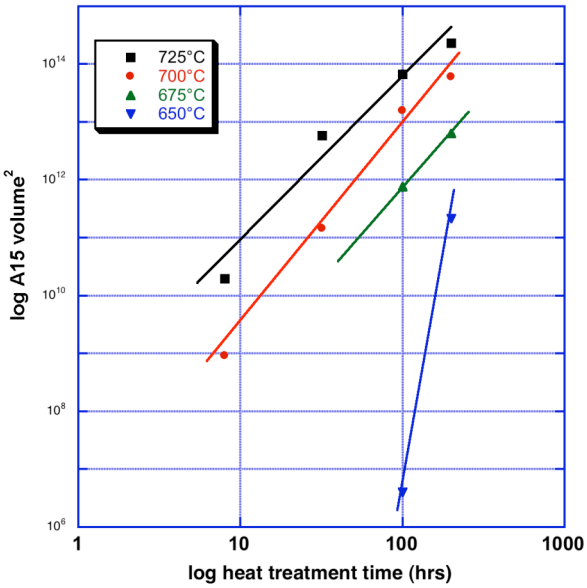

Fig.5-33 The neutron intensities of Nb_3Sn phase versus reaction time for SF4 wire

The volume of Nb_3Sn phase formation is affected by a few factors. The first one is the Sn ratio. Observing the wire samples in Fig.5-31, the SF1 wire has 15wt%Sn contained in its composition, the amount is comparable to that of bronze-processed wire. Its Nb_3Sn reaction rate is lowered because of the shortage of Sn source. It is noticed that the Nb_3Sn volume was still small even heat-treated at as high as 725°C for 200hr duration. With the increase of Sn

ratio to 20wt% of SF2 wire and 25wt% of SF3 wire, the Nb_3Sn quantity had a notable increase. It is seen that the Nb_3Sn neutron intensity was nearly doubled from 15wt% Sn source to 25wt% Sn source.

The second factor is the reaction temperature. At 650°C, all the ME wires had very low Sn diffusion and reaction rate, and the Nb_3Sn volumes formed were rather small, even after 200hr reaction. With the increase of temperature, the Sn diffusion and reaction rate were accelerated. The Nb_3Sn quantity was remarkably increased when the reaction temperature was elevated above 700°C.

The last important factor is the third-element alloying. In the SF4 wire composite, the Nb tubular filament was alloyed with 1at% Zr inside, apart from the 2wt%Ti alloyed in Sn core. It can be clearly found that the combination of alloyed Nb and alloyed Sn is very effective. Comparing SF4 wire with SF2 wire, they have the same Sn ratio and the same 2wt%Ti alloyed Sn cores. However, the Nb_3Sn phase formation rate of SF4 wire was much higher than that of SF2 wire. The explanation is that the Zr dopant reduces the diffusion activation energy and then promotes the inter-diffusion between Sn and Nb, resulting in the large increase of A15 phase quantity.

5.3.4 Conclusion

The in-situ neutron diffraction measurement has demonstrated that the ME wire has weaker neutron diffraction intensities and slower phase formation rates than MF wire does. This is attributed to the rather small diffusion and reaction interface area of ME wires.

The off-situ neutron diffraction measurement has shown that the Nb_3Sn phase formation has a power variation relationship with reaction time and the power index is also varied with reaction temperature.

The Nb_3Sn phase formation is affected by three factors: (1) the higher Sn ratio supplies more sufficient Sn diffusion source, increasing the Nb_3Sn phase quantity; (2) the increase of temperature accelerates the Sn diffusion and reaction rate, especially from 675°C to 700°C; (3) the combination of Ti alloyed Sn and Zr alloyed Nb is very effective in the large promotion of Nb_3Sn phase formation.

5.4 Microstructure Analysis and Phase Formation Kinetics of Mono-element Wires

5.4.1 Sample Preparation and Microscopic Measurement

The ME wire samples heat-treated with the procedure in section 5.1 were cut into small pieces and embedded in resin vertically before polishing. Most of the sample preparation was made in CRETA/CNRS.

The microstructure and microchemistry examinations by SEM and EDS were carried out on a model JEOL A840 in Crystallographe/CNRS and on a model JSM-6460 in the Analysis Center/NIN, respectively. The phase formation profile, phase composition and Sn distribution were analyzed.

5.4.2 Results and Analysis

5.4.2.1 A15 Phase Formation Comparison

According to the composite design of ME wires, the Sn core is located in the centre of Nb tubular filament. After the Cu-Sn alloying progress, the A15 phase layer starts to develop from the inner wall of the Nb tube. With the increasing time or temperature, the A15 phase layer becomes thicker and thicker, which can be obviously observed by SEM examination.

(1) The reaction temperature influence

The SF2 and SF4 wires, which have the same Sn ratio, were used to show the A15 layer variation with reaction temperature. Because the A15 layer is formed very slowly, especially at lower temperature, the samples for 200hr duration were selected to do the SEM observations. Fig.5-34 shows the photographs of SF2 wire.

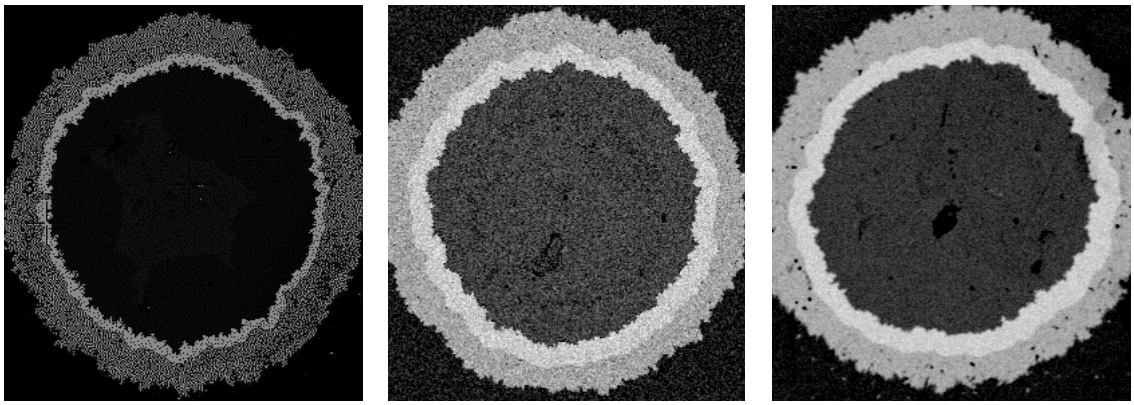

(a) 675°C (b) 700°C (c) 725°C

Fig.5-34 The SEM photographs of SF2 samples heat-treated at different temperatures for 200hrs

Fig.5-35 shows the photographs of SF4 wire.

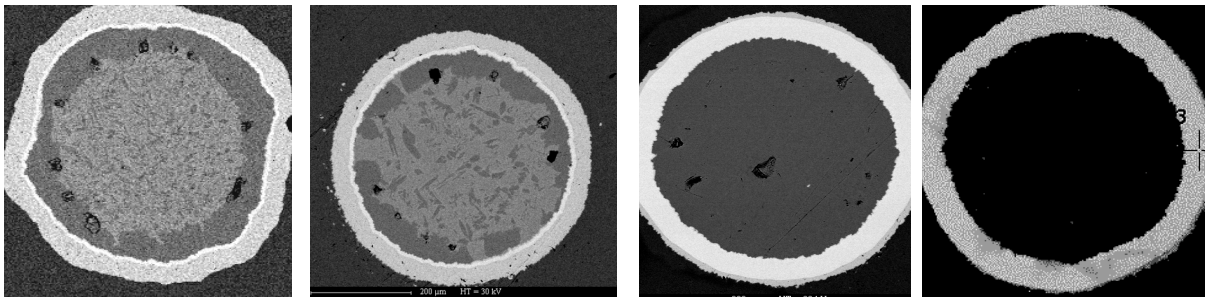

(a) 650°C (b) 675°C (c) 700°C (d) 725°C

Fig.5-35 The SEM photographs of SF4 samples heat-treated at different temperatures for 200hrs

From Figs.5-34 and 5-35 it can be seen that with the increase of reaction temperature, the A15 layer thickness (the light white circle area in the filamentary tube) became increasing, especially a remarkable increase happened at above 675°C. Making a comparison between SF2 and SF4 wires, it is apparent that the one with Zr addition had much faster reaction rate. In Fig.5-34, the filamentary tube had only very thin unreacted part at 700°C for 200hr duration. At 725°C, the filamentary tube had already reacted completely, even with Sn leakage into stabilizing Cu.

(2) The reaction time influence

The SF2 and SF4 wires were also used to show the A15 layer variation with reaction time. Because the A15 layer is formed very slowly at lower temperature, the 700°C reacted samples were selected to do the SEM observations. Fig.5-36 and Fig.5-37 show the

photographs of SF2 wire and SF4 wire respectively.

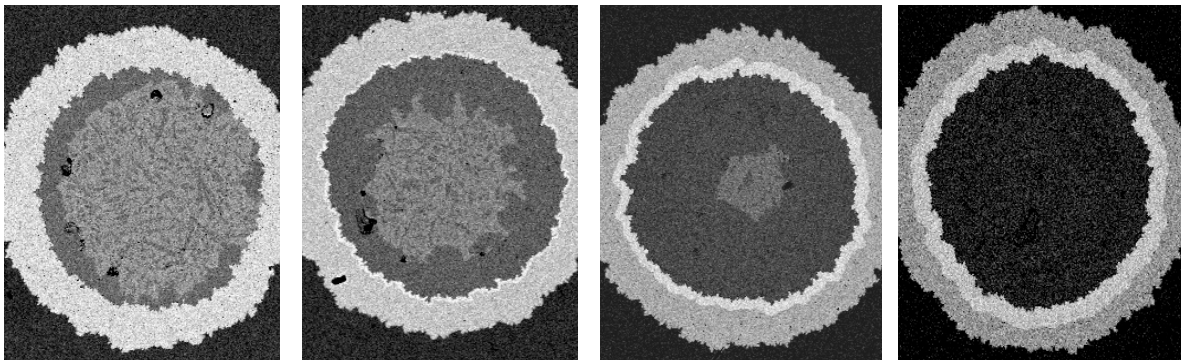

(a) 8hr (b) 32hr (c) 100hr (d) 200hr

Fig.5-36 The SEM photographs of SF2 samples heat-treated at 700°C for different times

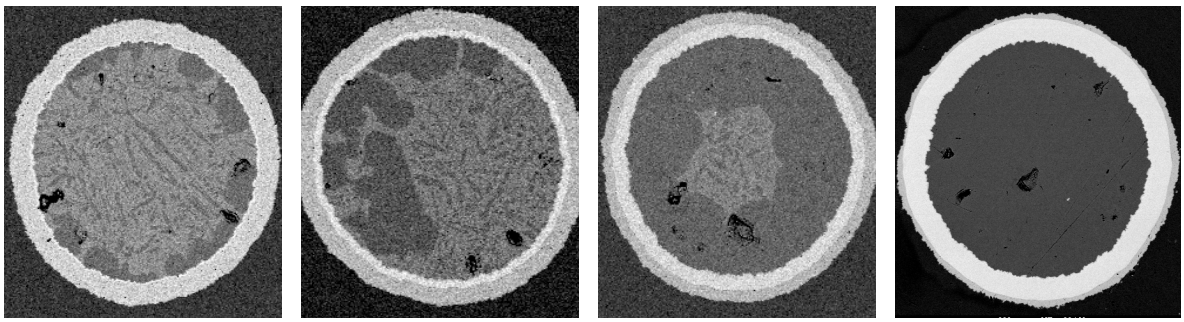

(a) 8hr (b) 32hr (c) 100hr (d) 200hr

Fig.5-37 The SEM photographs of SF4 samples heat-treated at 700°C for different times

From Figs.5-36 and 5-37 it can be seen that with the prolongation of reaction time at 700°C, the A15 layer thickness became increased and the high-Sn area inside the Nb tube (the light area in the middle part, the composition by EDS: Cu 83.04 at%; Sn 16.96 at%) was continuously shrank and disappeared until 200hr reaction. Comparing the SF2 and SF4 wires, the later had much faster reaction rate. The A15 layer thickness of 8hr sample was even larger than that of SF2 sample of 32hr duration. After 200hr reaction the difference was much remarkable.

(3) The Sn ratio influence

The four wire samples heat-treated at 700°C for 200hrs were used to show the Sn ratio and Zr addition effects on A15 phase formation. Fig.5-38 shows the result of SEM observations.

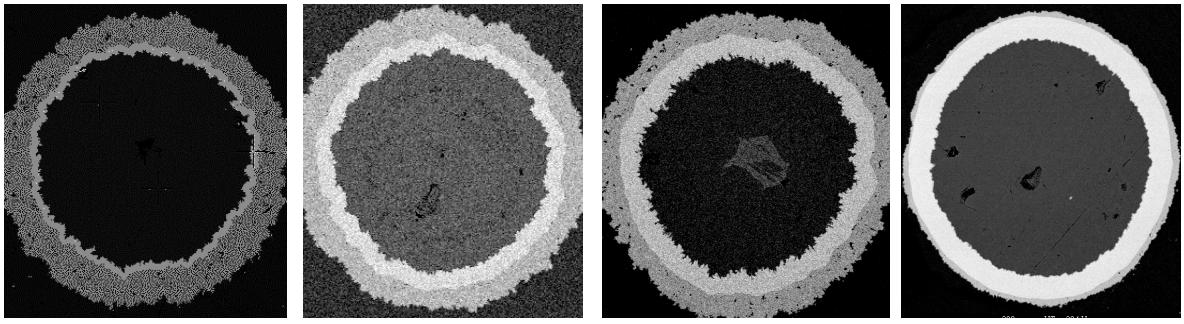

(a) SF1 (b) SF2 (c) SF3 (d) SF4

Fig.5-38 The SEM photographs of the four wire samples heat-treated at 700°C for 200hrs

It can be seen from Figs.5-38 that the A15 layer thickness is increased with the enlargement of Sn ratio. The sample of SF1 wire only developed a thin layer of A15 phase at 700°C for 200hr duration. However, the SF3 wire had reacted over half of the Nb tube at the same HT conditions and there was still enough Sn source remained in the Cu-Sn area (the light high-Sn area).

Observing the SF2 and SF4 wire samples, it is clear that the sample with Zr addition have nearly doubled the A15 layer thickness, demonstrating the substantial promotion effect of the alloyed Zr on A15 phase formation.

5.4.2.2 Sn Distribution Analysis

The selected ME wire samples were measured for the composition distribution by X-ray EDS technique with the SEM of model JEOL A840 in Crystallographe/CNRS. The measurement procedure was like this: dividing the scanning line into 50 or 60 steps (step interval less than 1.5μm) and then measuring the phase composition step by step. The detecting time was 40s and the testing voltage was 30kv at each step.

5.4.2.2.1 *Sn Distribution across A15 layers*

The scanning line was across the Nb filamentary tube from inside to outside. As an example Fig.5-39 shows a scanning line.

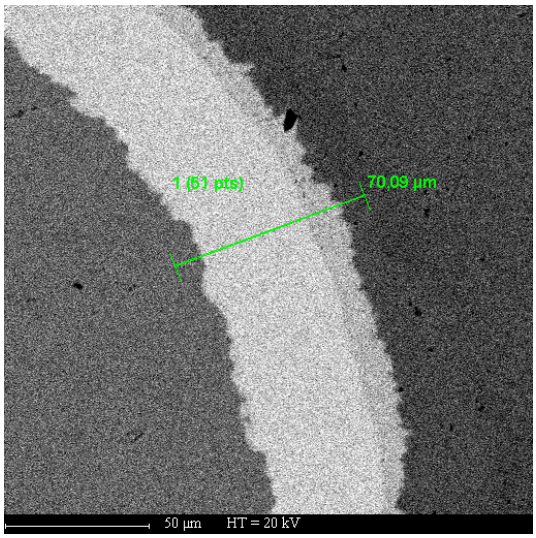

Fig.5-39 An example of the scanning line (the 700°C/200hr sample of SF4 wire)

After measurement step by step, the composition distribution was plotted as element atomic percentage versus the dimension of scanning line. An example is shown in Fig.5-40.

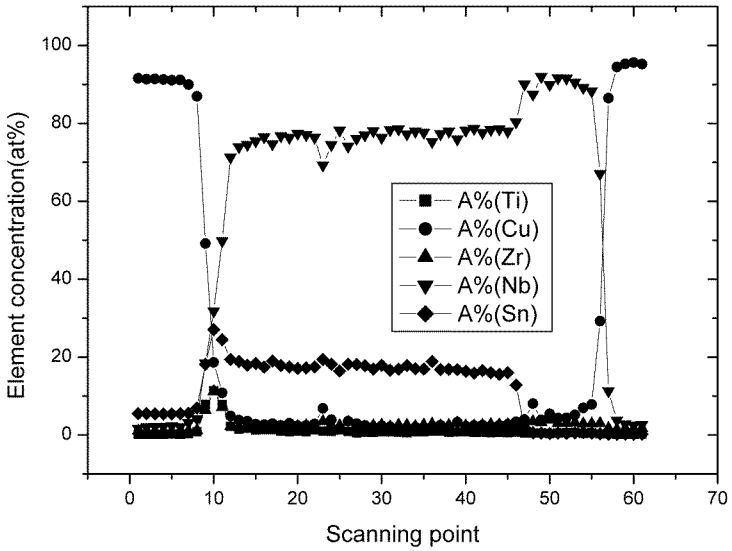

Fig.5-40 An example of the composition distribution (the same sample)

The Sn content distribution was specifically concerned and the results were also sorted into four aspects.

(1) The reaction time influence

The SF2 and SF4 wire samples heat-treated at 700°C for various times were measured for the Sn distribution, with the results shown in Figs.5-41 and 5-42.

From Fig.5-41 it can be seen that at the reaction temperature of 700°C, the SF2 wire

started to gather 5~7at% Sn in the interface between Nb tube and Cu-Sn phases. For 8hr reaction, the formed A15 phase layer was too small to be detected. Until 32hrs, there developed a layer of A15 phase which had an 18at%Sn composition. After 100hr reaction, the formed A15 phase had a nearly stable composition with Sn concentration of ~23at%.

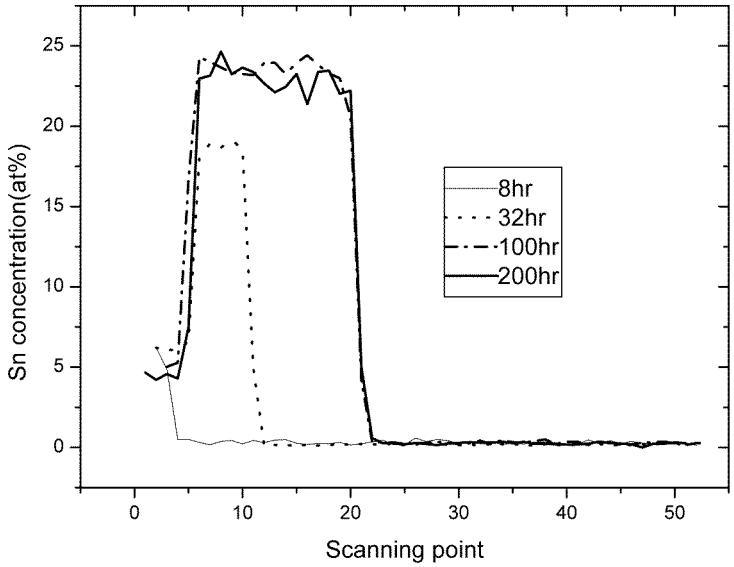

Fig.5-41 The Sn content distribution of SF2 samples heat-treated at 700°C for various times

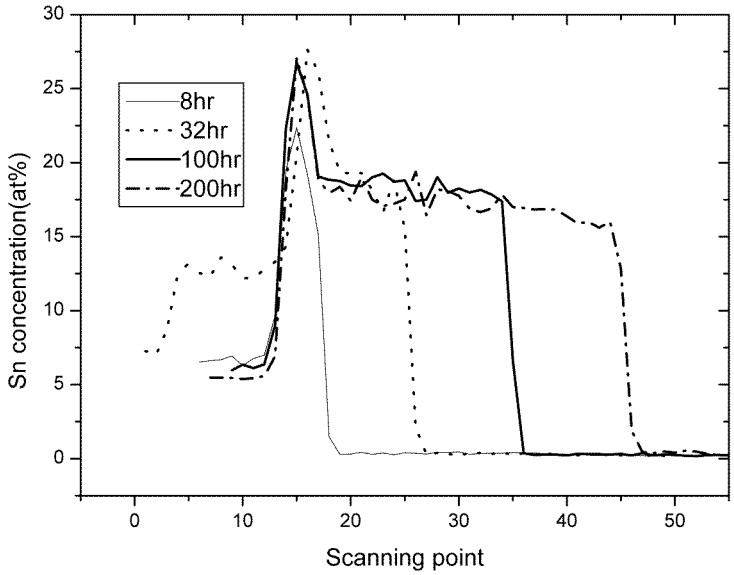

Fig.5-42 The Sn content distribution of SF4 samples heat-treated at 700°C for various times

In Fig.5-42, at the same HT conditions, the SF4 wire also started to gather 5~7at%Sn in the interface, but even further accumulated 13at% Sn for the 32hr sample in the nearby CuSn phases area, and there always accumulated as high as 23~27at% Sn for any HT duration. The

A15 phase formation had a much higher rate. After 8hr reaction a layer of A15 phase can be clearly observed. After 200hrs, the filamentary Nb tube only had a very thin unreacted part. In addition, it is notable that the A15 phase formed an inner-to-out gradient layer with the Sn concentration descending.

(2) The reaction temperature influence

The SF2 and SF4 wire samples reacted at different temperatures for 200hrs were measured for the Sn concentration distribution, with the results shown in Figs.5-43 and 5-44.

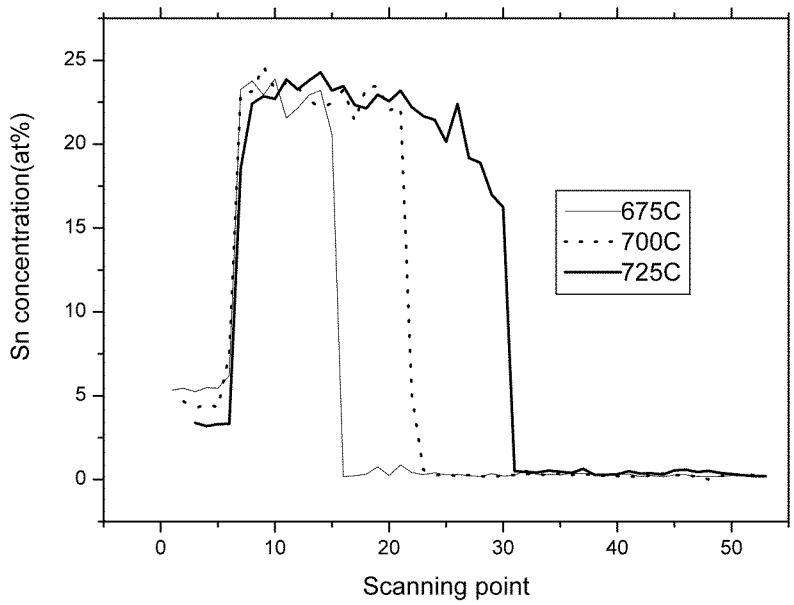

Fig.5-43 The Sn content distribution of SF2 samples heat-treated at different temperatures for200hrs

In Fig.5-43, the SF2 samples had three phase formation characteristics: (a) the Sn concentration in the interface between Nb tube and CuSn phases was reduced from ~5at% to ~3at%, with the increase of reaction temperature from 675°C to 725°C. At the same time, the A15 phase layer was largely thickened. (b) After 200hr reaction, the samples at different temperature nearly had the same average Sn concentration (~23at%). This indicates the A15 composition seems to be temperature-independent. (c) The Sn concentration had a slow gradient distribution, besides a very short sharp decrease at the layer outside.

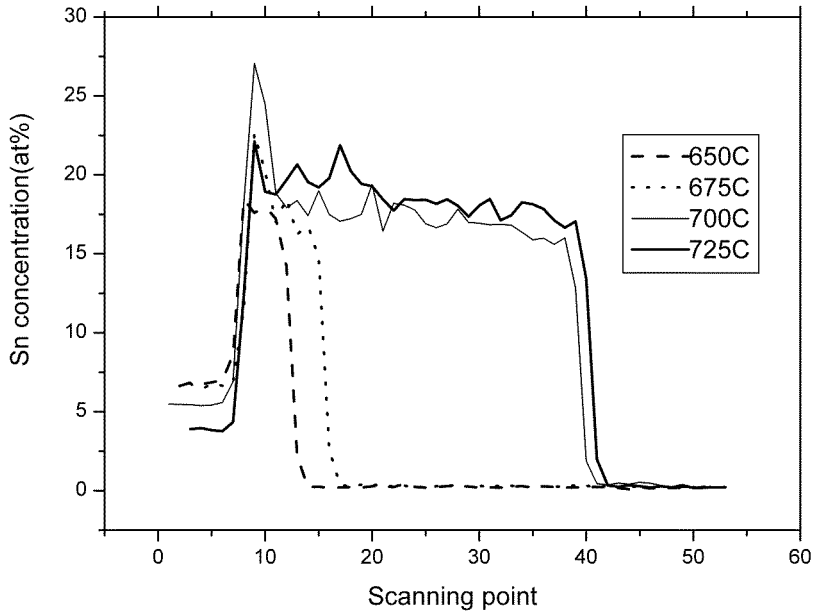

Fig.5-44 The Sn content distribution of SF4 samples heat-treated at different temperatures for200hrs

In Fig.5-44, the SF4 samples showed four characteristics: (a) the Sn concentration in the interface was reduced from ~7at% to ~4at%, with the increase of reaction temperature from 650°C to 725°C. At the same time, the A15 phase layer was substantially thickened, especially at above 700°C. At 725°C, the too fast reaction rate caused the Nb(Zr) tube to react through already, so that the A15 thickness had no much increase. (b) there accumulated a rather high Sn concentration in the interface at each temperature, indicating a sufficient Sn supply of SF4 wire. (c) the Sn concentration had a slow gradient distribution, except for a very short sharp decrease at the layer outside. (d) the average Sn concentrations in the A15 layer were 18~19at%, a lower composition than that of the SF2 wire. This is actually caused by the Zr combining in the A15 phase (see the Zr distribution in Fig.5-45). As for the further decrease of Sn concentration in the 725°C/200hr sample, it was the consequence of Sn leakage into stabilizing Cu.

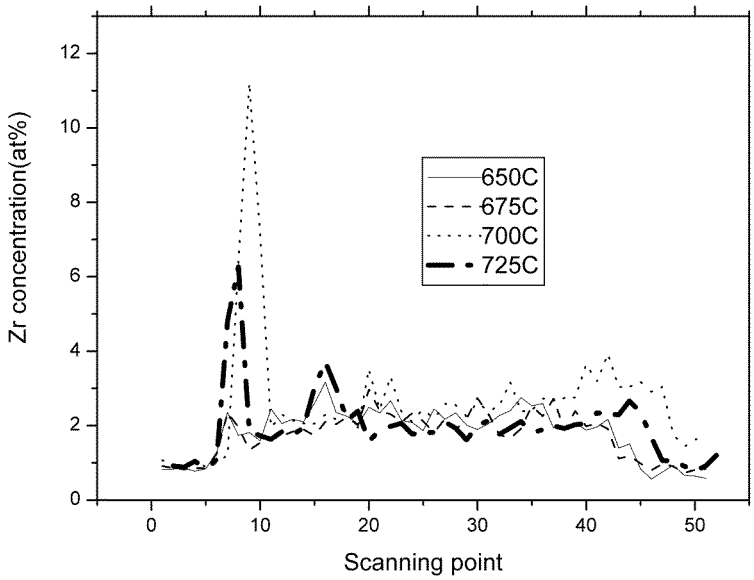

Fig.5-45 The Zr concentration distribution of SF4 samples reacted at different temperatures for 200hrs

(3) The Sn ratio effect

The SF1, SF2 and SF3 wire samples reacted at 700°C for 200hrs were measured for the Sn concentration distribution, as shown in Fig.5-46.

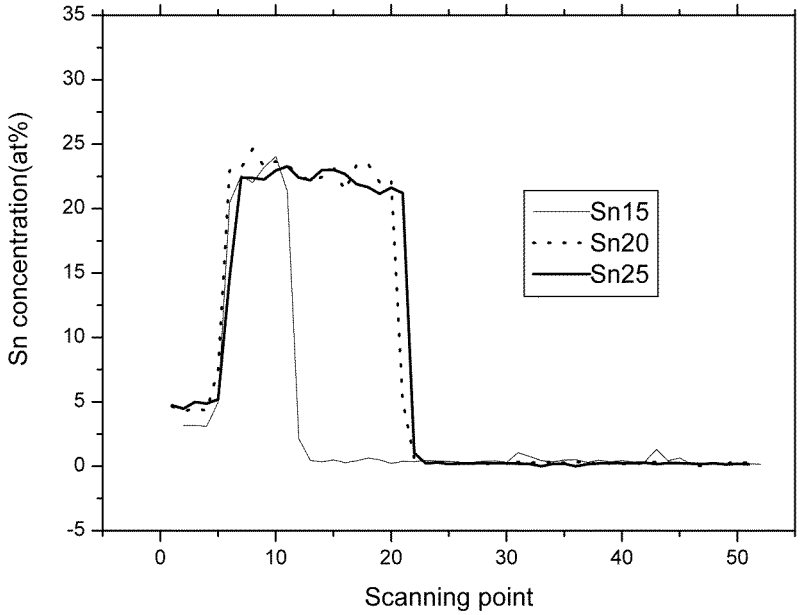

Fig.5-46 The Sn ratio effect on Sn content distribution in A15 layer

It can be found from Fig.5-46 that with the increase of Sn ratio, the A15 layer was largely thickened, especially when the Sn ratio exceeded 15wt%. Furthermore, the A15 phase layer of any Sn ratio wire had nearly the same average Sn concentration of ~23at%.

(4) The Zr alloying effect

The SF2 and SF4 wire samples reacted at 700°C for 200hrs were measured for the Sn concentration distribution, as shown in Fig.5-47.

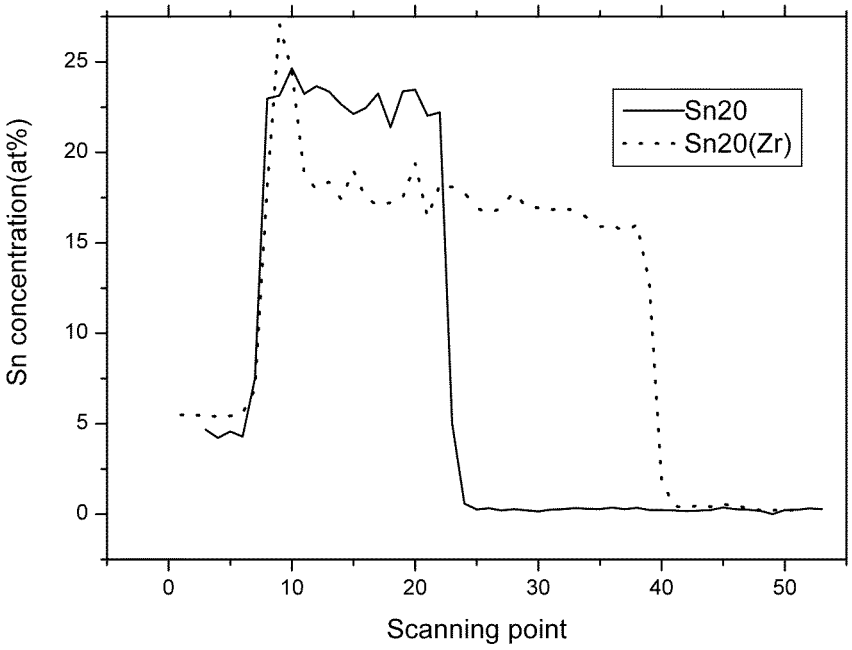

Fig.5-47 The Zr addition effect on Sn content distribution in A15 layer

It can be found from Fig.5-47 that the A15 layer thickness of SF4 sample was over twice as that of SF2 sample and there still accumulated high concentration of Sn in the Nb(Zr)-CuSn interface of SF4 sample. This result indicates that the Zr addition largely promotes the Sn accumulation and improves the A15 phase formation rate. On the other hand, it is noticed that the A15 compositions of SF4 sample and SF2 sample had an average Sn concentration of 16~18at% and 21~23at% respectively. Besides the 2~3at% Zr combined in the Nb_3Sn phase (see Fig.5-45), there was still shortage of Sn content in the A15 layer. This result means that by Zr addition the quantity of A15 phase is largely increased at the expense of A15 phase quality (Sn concentration decrease).

5.4.2.2.2 *Composition Distribution across Cu-Sn Alloying Area*

For the observation of Cu-Sn alloying, two samples were prepared, with one heat-treated at 210°C for 50hrs and the other, at 340°C for 25hrs. The two samples were measured for the composition distribution across the Cu-Sn mixing area. The results are shown in Figs.5-48

and 5-49.

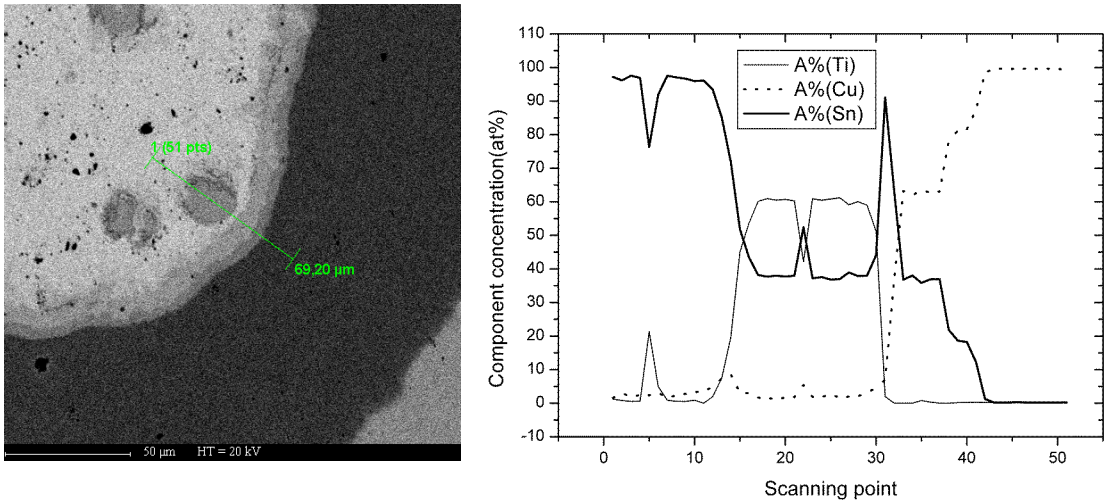

(a) the scanning line (b) composition distribution across the Cu-Sn mixing area.

Fig.5-48 The composition distribution of SF4 sample heat-treated at 210°C for 50hrs

It can be clearly seen from Fig.5-48 that there is formation of an η phase layer (Sn concentration: about 37at%) of ~8μm thick and an ε phase layer (Sn concentration: about 19at%) of ~3μm thick across the Cu-Sn mixing area. Most Sn core area had no change. The scanning line was across a Ti-rich area in the Sn core, which has the Ti concentration as high as 60at%. There also exists much non-alloying Cu in the outside of ε phase.

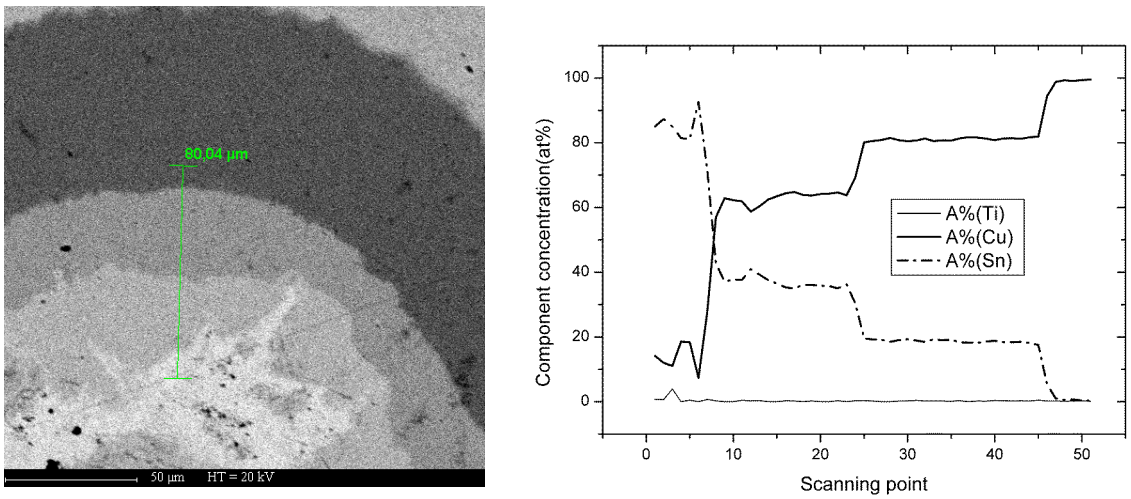

(a) the scanning line (b) composition distribution across the Cu-Sn mixing area.

Fig.5-49 The composition distribution of SF4 sample heat-treated at 340°C for 25hrs

In Fig.5-49 the Cu-Sn mixing area was much enlarged, forming an η phase layer of ~21μm thick and an ε phase layer of ~30μm thick along the scanning line, while the Cu-Sn

mixing area was obviously irregular due to the liquid-solid diffusion. In addition there still exists a large amount of non-alloying Cu.

5.4.2.3 A15 Layer Thickness Measurement

All the 72 wire samples prepared in section 5.1 were examined for the A15 layer thickness by means of the JSM-6460 scanning electronic microscope in the Analysis Center/NIN. Around the filamentary tube, 8 positions were selected and measured for the layer thicknesses. Calculating the average value, the formed A15 phase layer thickness was then determined. All the values are included in Table 5-2.

Table 5-2 A15 layer thickness of all ME wire sample

ME wire	Reaction temperature(°C)	A15 thickness (μm) of different reaction time			
		8hr	32hr	100hr	200hr
SF1	650	---	---	1.1	1.6
	675	---	0.4	1.4	5.2
	700	0.4	1.6	9.4	15.7
	725	0.6	2.4	12.8	20.6
SF2	650	---	0.5	2.2	---
	675	0.4	1.8	6.8	15.6
	700	1.1	4.9	18.9	33.9
	725	1.8	8.9	27.5	41.5
SF3	650	---	0.7	2.8	5.2
	675	0.5	2.3	6.8	15.6
	700	1.5	6.2	20.1	38.3
	725	2.5	10.8	36.3	53.9
SF4	650	0.5	1.8	4.7	7.9
	675	1.0	2.8	8.5	14.6
	700	3.1	12.6	26.8	41.9
	725	6.7	19.4	41.2	50.5

In Table 5-2, it should be noted that some samples cannot be measured for the thickness values because of the too thin A15 layer formed. The value of SF4 725°C/200hr sample is the completely reacted layer thickness, but not the thickness it should develop, because the Nb(Zr) tube was reacted through before 200hrs.

It can be found from Table 5-2 that the Nb or Nb(Zr) tube became thickened after A15 phase formation. For example, the original SF4 wire has the Nb(Zr) tube of 40μm thickness, which became 50.5μm after complete reaction. This is caused by the volume expansion from Nb to Nb_3Sn.

5.4.3 Discussion

5.4.3.1 Effects on Phase Formation of Mono-element Wires

It is known that the heat treatment of internal-Sn superconducting wire includes Cu-Sn alloying process and A15 phase formation process. Although the Cu-Sn alloying process of MF wires has been intensively investigated [85, 127], it is still necessary to analyze the situation of ME wires.

Fig.5-48(a) shows the SEM photograph of SF4 210°C/50hr sample. Since at 210°C the Sn has not molten, its diffusion and reaction with Cu is in solid-solid state and then has a very slow rate. So, one can see very thin layers of η and ε phases in the figure. Fig.5-49 (a) shows the SEM photograph of SF4 340°C/25hr sample. It can be seen that η and ε phases had a substantial increase. This is because at 340°C the Sn is in liquid state, and the liquid-solid diffusion and reaction accelerated the development and transformation of η and ε phases. However, the temperature of 340°C cannot develop other CuSn phases according to the Cu-Sn binary phase diagram. There existed a large amount of non-alloying Cu in the figure.

Hereafter, the A15 phase formation of ME wires is mainly discussed from the following aspects.

Firstly, the HT temperature is concerned. From the microstructure and microchemistry analysis we have known that the reaction temperature is the most significant factor to affect A15 phase formation rate. At 650°C for 200hr treatment, the amount of the formed A15 phase is still small. With the elevation of reaction temperature, the phase formation is accelerated. Especially from 675°C to 700°C, the A15 phase thickness had nearly a double increase.

Obviously, the reason is that the elevation of temperature increases the activities of Sn diffusion and reaction, and reduces the activation energy. However, it is found from Fig.5-43 that after a long time duration (i.e. 200hrs) the ME samples heat-treated at different temperatures nearly had the same average Sn concentration distribution, indicating again the temperature-independence of A15 phase composition. That is to say, the increase of reaction temperature only accelerates the phase formation rate, but does not change the equilibrium phase composition of A15 phase. In addition, comparing the A15 phase formation between ME wire and MF wire (see section 4.5.3.1) it can be seen that the ME wire seems to need higher temperature to form the A15 phase. This is because the ME wire has smaller reaction interface and longer reaction route (see Fig.5-38).

Secondly, the HT time is concerned. The microstructure and microchemistry analysis have demonstrated that with the increase of reaction time the A15 phase layer thickness became enlarged gradually, and the Sn concentration in A15 phase is continuously increasing, tending to be stoichiometric Nb_3Sn. This is actually understandable. It is known that the A15 phase is a Nb-Sn solid solution compound of different Sn concentration. At the early reaction time, the A15 phase quality is poor because of the shortage of Sn supply. With the reaction time elongation, the ever-increasing of Sn supply enriches the Sn concentration in the A15 phase, until achieving an equilibrium state. On the other hand, the increase of the A15 product thickness prolongs the diffusion route within the phase, slowing the A15 phase formation rate. Therefore, the A15 layer thickness cannot be linearly increased.

Thirdly, the Sn ratio effect is considered. From the microstructure and microchemistry analysis, it is known that the A15 layer is thickened with the enlargement of the Sn ratio in the composite wire. This is because the A15 phase quantity is determined by the amount of Sn source. We have known that the bronze-processed wire cannot achieve higher superconducting performance because its available Sn source is small, resulting in the small amount of A15 phase. It is this reason that the bronze process is replaced by internal-Sn process in many applications. In the three ME wires, the ME wire only has 15wt% Sn ratio, the amount comparable to that of the bronze-processed wire, so that the formed A15 phase volume was the smallest. The SF2 and SF3 wires have enough Sn supply, so the A15 quantity was much increased. Additionally, it is found from Fig.5-46 that the average A15 phase

compositions (Sn concentration) of the three ME wires were nearly the same, no matter what Sn ratio was. It can be explained as that at the same HT conditions, the three wires have the same diffusion and reaction activation energy, then the same phase formation dynamics. It is certainly that they should have the same equilibrium A15 composition.

Lastly, the third-element addition effect is considered. The microstructure and microchemistry analysis have exhibited that the A15 layer thickness of SF4 wire was doubled that of SF2 wire, and even larger than that of SF3 wire (25wt% Sn ratio). From the discussion of MF wires we have known that the best alloying way is to alloy Sn and alloy Nb either. SF4 wire has this component design, in which 2wt%Ti was added in Sn and 1at%Zr was alloyed in Nb. The combined effect of Zr and Ti additions not only increases the inter-diffusion and reaction rates of the atoms but also reduces the activation energy, resulting in the doubled A15 phase quantity. In Fig.5-47, a much higher Sn concentration was accumulated on the interface of Nb(Zr) and CuSn phases, and in Fig.5-45 there also gathered a rather large amount of Zr. This fact convincingly demonstrates the promotion effect of Zr and Ti addition on the inter-diffusion and reaction.

Another notable fact is the Sn concentration distribution of ME samples. Although the A15 phase layer has an inner-to-out gradient composition distribution, most of the layer just has a small difference in Sn concentration, except for the small regions on the outer and inner boundaries of the A15 layer where the Sn concentration changed sharply. This fact indicates that at the early time of A15 heat treatment the A15 phase composition may vary largely. When an equilibrium composition is achieved any further HT progress changes the phase composition very little, although the phase quantity may increase largely. This is consistent with the study by C.D. Hawes et al.[136].

5.4.3.2 Kinetics Study of A15 Phase Formation

The A15 phase formation kinetics of Nb_3Sn wire is discussed in detail in this section. We have known that it is very difficult to quantitatively investigate the phase growth of MF wires because of the anfractuous factors from the wire configuration design and from metallurgical processing. However, the ME wire has no most of the difficulties. Since the configuration design of ME composite is very simple, the problem of metallurgical processing

can be ignored. Furthermore, the thickness of the filamentary tube in ME wire has an ample designed dimension, so the A15 phase formation progress can be observed in enough reaction time. It is for this reason that the ME wires are used for quantitative study of the A15 phase formation kinetics.

The Nb_3Sn phase formation belongs to solid reaction. Its kinetics model can be described in two relations. The first one is as

$$Y=k_1(T)t^{n1} \qquad (5\text{-}1)$$

where Y is the A15 layer thickness, k_1 is the growth rate of the A15 layer, t is the reaction time and n1 is the exponent.

The equation (5-1) can be plotted in logarithmic manner and linearly fitted, from which the power index n1 can be conveniently determined. The A15 layer thicknesses of various HT conditions (see Table 5-2 in section 5.4.2.3) have been linearly fitted in the logarithmic manner. Fig.5-50 shows the results.

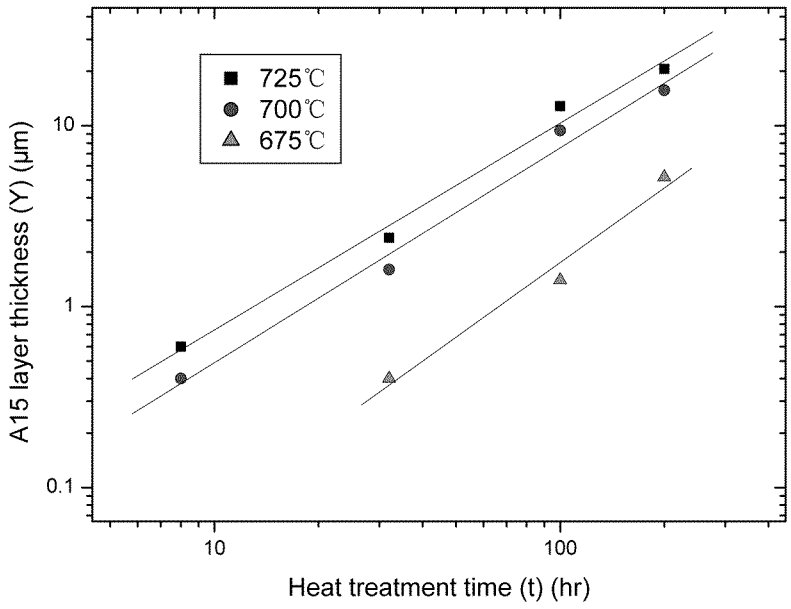

(a) SF1

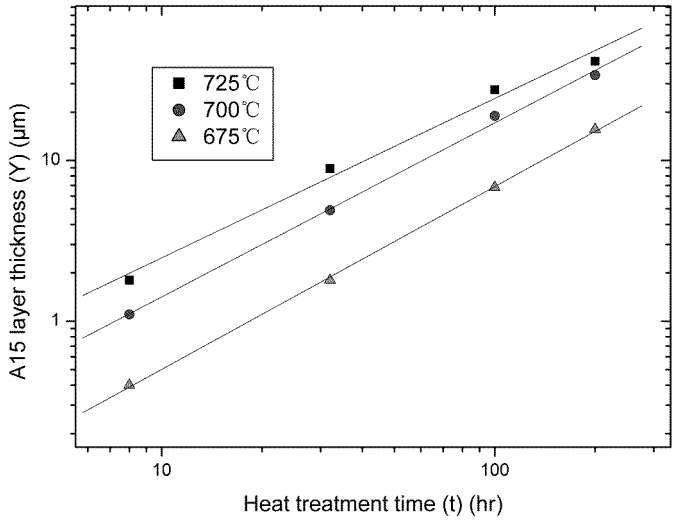

(b) SF2

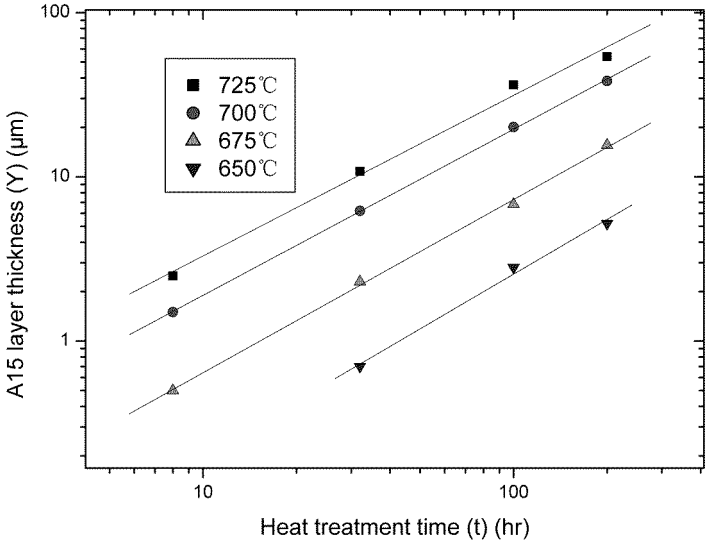

(c) SF3

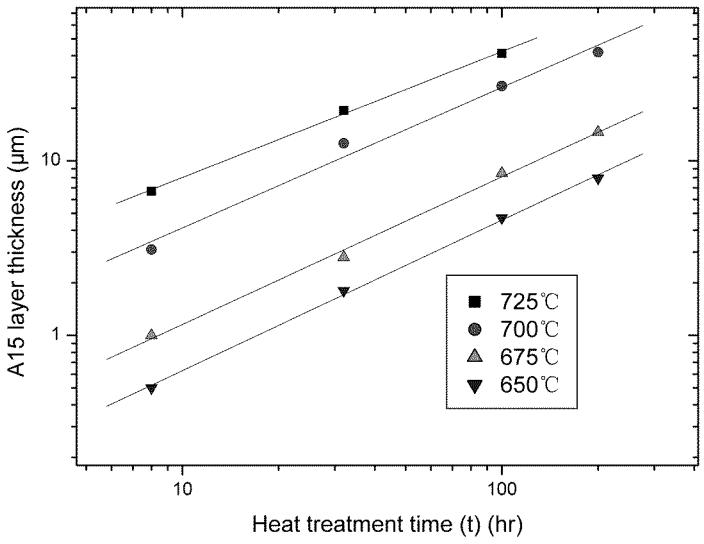

(d) SF4

Fig.5-50 Linear fitness of the A15 layer growth as a function of HT time and temperature for ME wires

The obtained n1 values are exhibited in Table 5-3.

Table 5-3 The n1 values of the four ME wires at different temperatures

ME sample	n1 values at different HT conditions			
	650°C	675°C	700°C	725°C
SF1		1.37	1.19	1.14
SF2		1.14	1.18	0.99
SF3	1.11	1.05	1.01	0.98
SF4	0.86	0.85	0.80	0.72

From Table 5-3 it can be seen that the n1 values was decreased with the increase of reaction temperature.

The second kinetics model of Nb_3Sn phase formation is derived from Fick's first law and described as:

$$Y^n=K(T)t \qquad (5\text{-}2)$$

where Y and t are the same as those of equation (5-1), K and n are A15 layer growth rate and the exponent respectively in this model equation. An exponential dependence of K with the reaction temperature is as the relation:

$$K=K_0\exp(-E/\beta T) \qquad (5\text{-}3)$$

where K_0 is the diffusion frequency, β is the Boltzmann constant, T is the temperature, and E is the activation energy.

The A15 layer thickness of various HT conditions in Table 5-2 have been non-linearly fitted with the equation (5-2), as depicted in Fig.5-51, from which the A15 layer growth rate K and the power index n can be obtained.

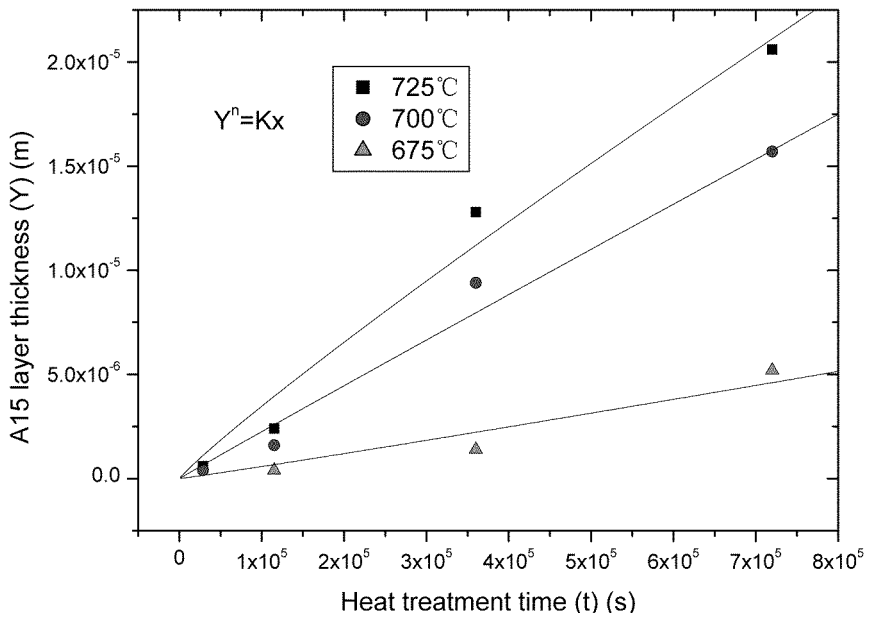
A15 layer thickness (Y) (m)
Heat treatment time (t) (s)
Y^n=Kx
725℃
700℃
675℃
2.0x10^-5
1.5x10^-5
1.0x10^-5
5.0x10^-6
0.0
0
1x10^5
2x10^5
3x10^5
4x10^5
5x10^5
6x10^5
7x10^5
8x10^5

(a) SF1

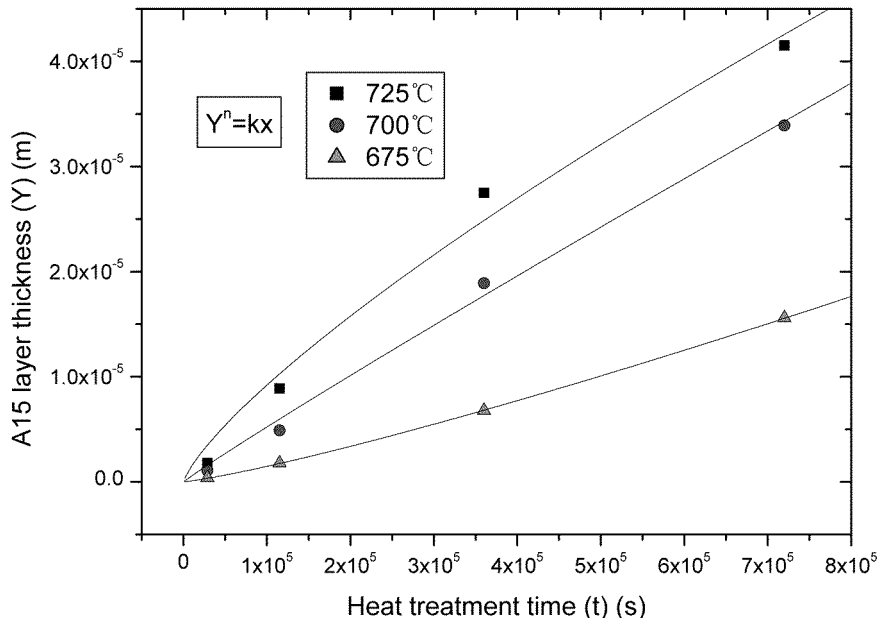
A15 layer thickness (Y) (m)
Heat treatment time (t) (s)
Y^n=kx
725℃
700℃
675℃
4.0x10^-5
3.0x10^-5
2.0x10^-5
1.0x10^-5
0.0
0
1x10^5
2x10^5
3x10^5
4x10^5
5x10^5
6x10^5
7x10^5
8x10^5

(b) SF2

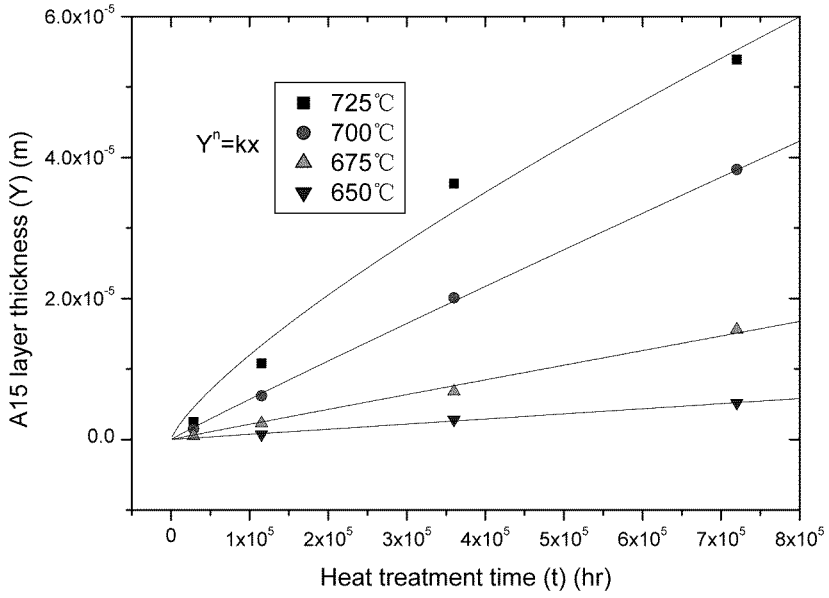

(c) SF3

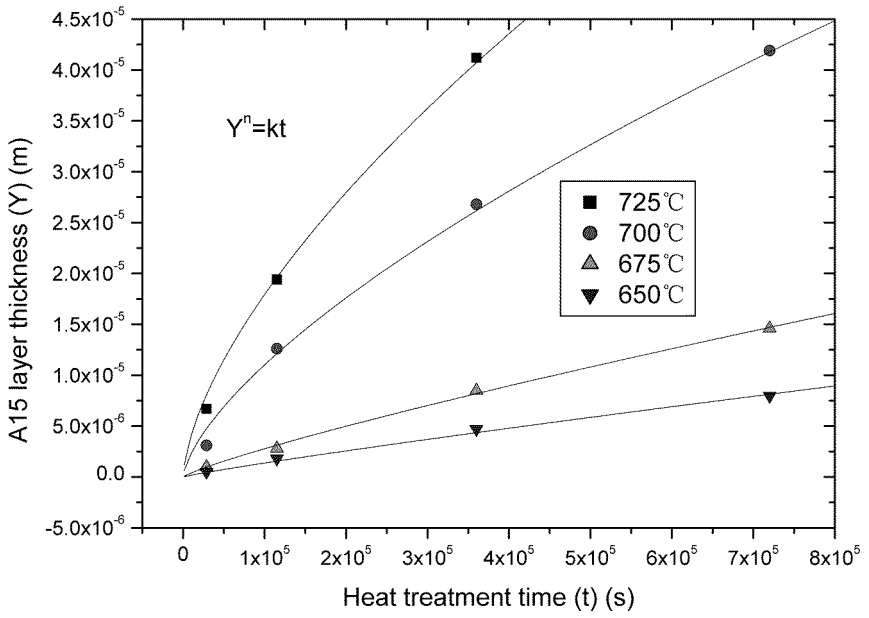

(d) SF4

Fig.5-51 Non-linear fitness of the A15 layer growth as a function of HT time and temperature for ME wires

The obtained K and n values are demonstrated in Table 5-4.

Table 5-4 The K and n values of the four ME wires at different temperatures

ME sample	K and n values at different HT conditions							
	650° C		675° C		700° C		725° C	
	K[m^n/s]	n	K[m^n/s]	n	K[m^n/s]	n	K[m^n/s]	n
SF1	---	---	$1.14*10^{-11}$	0.95	$1.86*10^{-11}$	1.01	$1.07*10^{-11}$	1.09
SF2	---	---	$1.27*10^{-10}$	0.84	$2.86*10^{-11}$	1.05	$3.20*10^{-12}$	1.29
SF3	$7.04*10^{-12}$	1.00	$1.77*10^{-11}$	1.02	$3.60*10^{-11}$	1.04	$4.40*10^{-12}$	1.29
SF4	$3.21*10^{-12}$	1.11	$2.62*10^{-12}$	1.18	$4.50*10^{-13}$	1.48	$3.84*10^{-13}$	1.56

From Fig.5-51 and Table 5-4 it can be seen that the A15 layer growth of ME wires is all right in accordance with the kinetics model of equation (5-2), that is, the n power variation relation [129].

Also from Table 5-4 it is found that the n value is increased with the increase of HT temperature, which seems to be contrary to the n1 variation in Table 5-3. Actually, the n value and n1 value have the same meaning, except that they are in different position of the equations. They all indicate that the A15 phase formation rate is increased with the elevation of reaction temperature.

It is notable from Table 5-3 that the A15 layer growth rate K is associated with the exponent n value. So, from the equation (5-3) one can see that the K_0 is also varied with the n value. The n value is actually determined by the amount of diffusion source. If the diffusion source is invariable, the n value should be constant, the situation as that of the Cu-Sn alloying progress. However, the Sn supply for A15 phase formation is variable because the Sn concentration on the phase boundary is not stable. In this case, the n value is varied and then the K_0 is also not a constant. Therefore, it seems to be impossible to obtain the activation energy E from eqs.5-2 and 5-3. Maybe that is the reason of no any report until now which has acquired the activation energy E of Nb_3Sn superconductors from the A15 layer growth.

5.4.4 Conclusion

The phase microstructures of ME wires are primarily determined by the HT temperature and time, Sn ratio in the composite, and the third-element addition.

The elevation of HT temperature increases the atom diffusion and reaction activity, and reduces the activation energy, resulting in the increase of phase formation rate. However, it only alters the phase quantity, but does not change the A15 phase composition too much.

The prolongation of HT time not only increases the A15 quantity, but also enriches the Sn concentration in the phase until an equilibrium state, which is more closed to stoichiometric Nb_3Sn. Whereas, the ever-increasing layer thickness elongates the Sn diffusion route, so the A15 phase growth rate is not linearly increased.

The enlargement of Sn ratio increases the Sn source supply and then obviously increases the A15 phase quantity, but it also cannot change the equilibrium phase composition.

The Zr addition lowers the activation energy and increases the atom inter-diffusion and reaction rate, and then substantially enlarges the A15 phase quantity, although it cannot vary the equilibrium composition of the formed A15 phase.

6. RESEARCH SUMMARY

Nb_3Sn superconducting wire is one of the most applicable cryogenic superconducting materials and the best choice for high-field magnets exceeding 10T. One of the most significant utilization is the ITER project which is regarded as the hope of future energy source. The magnetic confinement facility of the ITER fusion system needs very strong high-field magnets made with the Nb_3Sn superconducting wires. Systematic research on the internal-Sn Nb_3Sn superconductors to satisfy the ITER's requirement is the main motivation of this thesis.

Since the target of ITER project is the production of AC power, a special requirement is made for the Nb_3Sn wire, modest critical current density J_C, but rather low hysteretic loss. The high-Cu composite designs with smaller number of sub-element and non-reactive diffusion barrier, and the RRP internal-Sn technology are usually applied for the wire manufacturing. Such designed and processed wires were supplied by MSA/Alstom and WST/NIN in this research.

The systematic investigation on internal-Sn superconducting wires includes the optimization of HT conditions, phase formation and its relation with superconductivity, microstructure analysis, and the phase formation kinetics. Because of the anfractuosity of the configuration design and metallurgical processing, the MF wires are not sufficient for studying a sole factor effect on superconductivity, especially for analyzing the A15 phase growth kinetics. Therefore, four sets of ME wires with different Sn ratios and different third-element addition were designed and fabricated in order to explore the relationship between phase formation and superconducting performances, particularly the A15 layer growth kinetics.

In the first place, the two ITER-type MF wires were studied in details. The transport critical current measurements were carried out, from which the engineering J_E, non-Cu J_C and flux pinning force F_P reflected by $J_C \times B$ can be determined as a function of the applied field. And also the irreversibility field H* at different reaction temperature can be obtained by the Krammer extrapolation manner. The in-situ neutron diffraction examination was arranged for

two purposes: one was to dynamically observe the variation of various CuSn phases with the HT progress; the other was to search for the variation rule of Nb_3Sn phase development. Two SQUID magnetization techniques were applied, cycling the temperature at a fixed field and cycling the field at a constant temperature. The former was used to determine T_C (B), irreversibility temperature T*(B) and T_C transition curves. The later was used to obtain hysteretic loops, and then flux pinning force F_P and irreversibility field H*. Microstructure observation and microchemistry analysis were employed in exploring A15 grain configuration, crystalline morphology and Sn concentration distribution. All the above measurement results are generalized as the followings.

The transport critical current measurements showed that both NIN wire and AST wire can achieve nearly the same magnitude of the best non-Cu J_C, which is over the ITER's requirement, although a rather big difference found in J_E values. However, AST wire needs to be heat-treated at higher temperature than NIN wire does in order to realize the best superconductivity. The measurements also demonstrated that the transport critical current and the calculated flux pinning force were promoted to the highest and then reduced with the increase of HT temperature and time. On the contrary, the irreversibility field H* had no such a decrease, indicating the enhancement of high-field performances with the reaction temperature and time increase.

The in-situ neutron diffraction measurement has shown the identical phase formation and transformation rules between the two wires. The Cu-Sn alloying process started to develop η phase at ~210°C, and then transformed into ε phase and δ phase. The γ phase became increasing at the expense of δ phase decrease. The Nb_3Sn phase formation started at ~600°C and kept increasing with the prolongation of reaction time. The results of neutron diffraction intensity also revealed that the variation of Nb_3Sn phase formation is in accordance with the power relationship. In comparison of NIN wire with AST wire, the former showed faster phase formation rate due to the alloyed Ti addition in Sn core.

The SQUID magnetization measurements have demonstrated the following results of NIN and AST wires. The T_C(B) and T*(B) values, the T_C values and M-T transition curves were all increased with the increase of HT time, and maintained nearly no change after complete reaction. These T_C-related superconducting properties had no obvious variation at

different HT temperatures for complete reaction, indicating that the A15 phase composition of Nb_3Sn wire is temperature-independent. The ΔM-B curves and the (ΔM × B)-B curves, determined from the hysteretic loops, were also increased with the increment of HT temperature and time, approached the highest position before lowering down, whereas the irreversibility field H* maintained the high values. This result can be interpreted as that the flux pinning force, which is dependent on A15 grain size and morphology, is strengthened with the reaction temperature and time increase. After reaching the best situation the F_P becomes reduced due to the grain size coarsening. The dissimilarity between NIN wire and AST wire is that the best magnetization properties of NIN wire appeared at lower temperature. This is the effect of Ti alloyed Sn in NIN wire.

The microstructure observation and microchemistry analysis have shown that the NIN wire had faster reaction rate and lower reaction temperature, and developed more equiaxed crystals in its crystalline morphology at the same HT conditions. This is also the effect of Ti addition. Comparatively, AST wire needs a higher reaction temperature to increase the reaction rate and to improve the A15 phase configuration distribution.

From the above measurement results it can be concluded that the NIN wire is suitable to be heat-treated at lower temperature because the Ti alloyed in Sn effectively accelerates the Sn diffusion and reaction rate, reduces the reaction temperature and promotes the phase formation. However, the AST wire must be heat-treated at higher temperature to achieve its best superconducting performances. Indeed, the AST wire had Ta alloyed in Nb. Maybe too much addition retards the A15 phase formation. Therefore, the HT optimization of the two wires has been acquired as: NIN wire, 650°C~675°C for 128hrs and AST wire, 675°C~700°C for 128hrs.

In order to compare the effect of different HT progresses on the wire final superconductivities, two-step and one-step procedures were arranged for the two wires. The measurement results have exhibited that any heat treatment procedures before A15 phase formation only alters the phase formation progress but has no influence on the final superconducting properties of internal-Sn Nb_3Sn wires.

In the second place, the four sets of ME wires were studied basing on MF wire analysis, primarily focusing on sole factor influence on the superconductivities, and especially on

phase formation kinetics. For these purposes, three measurement techniques have been used, including off-situ and in-situ neutron diffraction examination, SQUID magnetization test and SEM and EDS analysis. Specifically, the off-situ neutron diffraction measurement was adapted in order to compare the phase formation situations of different ME wires at different HT conditions. The microstructure and microchemistry analysis of ME wires mainly focused on phase composition distribution examination and A15 layer thickness measurement. The results of all ME wires can be summarized as the followings.

The SQUID magnetization measurement has shown several differences between ME wire and MF wire, i.e. the variations of T_C transition line, ΔM-B and ($\Delta M \times B$)-B curves. These differences are caused by the different configuration designs of the two sorts of wires. The ME wire developed an ever-increasing inner-to-out gradient composition A15 layer with various compositions transparent to the applied magnetic field. On the contrary, the MF wire formed an out-to-inner gradient composition which gradually became uniformly distributed with no change of the A15 phase composition any more after reaction through and the outer part of the filament will shield the inner part in magnetization measurement.

The magnetization measurement also showed that the package F_P and package J_C of ME wires became increasing with the increase of HT temperature and time and the Sn ratio, and with the addition of third-element Zr, while the A15 layer F_P and the A15 layer J_C changed very little at lower field, but expanded to high field. This indicates that the above phase-improving factors only alters the A15 phase quantity and grain configuration, but does not vary the A15 phase quality or equilibrium composition.

The in-situ neutron diffraction measurement has demonstrated that the Cu-Sn alloying progress of ME wire is identical to that of MF wire, only except the small neutron intensities of various phases appeared due to the rather small reaction interface in the ME wire. The off-situ neutron diffraction measurement has shown that the phase formation rate of ME wire is affected by the three factors: (1) the increase of Sn ratio enlarges the Sn source supply and then increases the phase formation rate; (2) the elevation of HT temperature activates the Sn diffusion and reaction and then accelerates the phase formation rate, especially from 675°C to 700°C; (3) the combination of Ti alloyed in Sn and Zr alloyed in Nb is very effective in promoting the A15 phase formation.

The SEM and EDS analysis have exhibited that the microstructure and phase composition variations are also dependent on the HT temperature and time, the Sn ratio and the third-element alloying. The A15 phase amount was obviously increased with the increase of reaction temperature and time and the Sn ratio, and with the addition of Zr. However, the EDS composition distribution analysis really showed that these factors cannot change the equilibrium A15 phase composition.

In particular, the A15 layer thicknesses of various ME samples were measured and carried out linear and non-linear fits by means of two model equations. The results have clearly demonstrated that the phase formation kinetics of Nb_3Sn solid-state reaction is in accordance with an n power relation and the n value is increased with the increase of HT temperature and the Sn ratio in the wire composite.

BIBLIOGRAPHY

[1] S. Hong, M.B. Field, J.A. Parrell and Y. Zhang. Latest improvement of current carrying capacity of niobium tin and its magnet applications. IEEE Trans. Appl. Supercond.,16(2), 1146-51, 2006.

[2] R.M. Scanlan, Recent Progress in Nb_3Sn Superconductors for High Magnetic Field Application. IEEE Trans. Appl. Supercond., 11(1), 2150, 2001.

[3] S. Hong, M.B. Field, J.A. Parrell, and Y. Zhang, Recent progress in Nb3Sn superconductor for high magnetic field application. Presented at CEC-ICMC 2003, Anchorage, Alaska.

[4] J.A. Parrell, M.B. Field, Y. Zhang, and S. Hong, Nb3Sn conductor development for fusion and particle accelerator applications. Presented at CEC-ICMC 2003, Anchorage, Alaska.

[5] E. Gregory, E. Gulko, T. Pyon and L.F. Goodrich. Properties of internal-tin Nb3Sn strand for the International Thermonuclear Experimental Reactor. Advances in Cryogenic Engineering Materials, 42(2), 1319-28, 1997.

[6] N.I. Kozlenkova, V.I. Pantsyrnyi, A.K. Shikov, A.E. Alexandra and A.E. Mitin. Scaling of the V-I characteristics in the ITER type Nb3Sn strands in relation to the applied field and temperature. IEEE Trans. Appl. Supercond., 15(2), 3450, 2005.

[7] A. C. Rose-Innes and E. H. Rhoderick, Introduction to Superconductivity, International Series in Solid State Physics, Vol.6, Second Edition, Pergamon Press, New York, 1988.

[8] Zhang Liyuan. Superconductivity Theory. Science Press, Beijing, 2003.

[9] W.H. Warnes. Principles of Superconductivity. ASM International Metals Handbook. Vol.2, 10^{th} ed., 1990.

[10] Wu Hangsheng, Guan Weiyan and Li Hongcheng. Superconductivity. Science Press, Beijing, 1979.

[11] D.B. Smathers. A15 Superconductors. Metals Handbook. Vol.2, 10^{th} ed., American Society for Metals, 1990.

[12] J.P. Charlesworth, I. Macphail and P.E. Madsen. Experimental work on the Niobium-Tin constitution diagram and related studies. J. Mat. Sci., 5 580-603, 1970.

[13] H. Devantay, J.L. Jorda, M. Decroux, J. Muller and R. Flükiger. The Physical and

structural properties of superconducting A15-type Nb-Sn alloys. J. Mat. Sci., 16, 2145-53, 1981.

[14] G. LeFranc and A. Mulller, Effects of Copper additions to superconducting niobium tin sinter material. J. Less-Common Met., 45, 339-342, 1976.

[15] P. Villars, A. Prince, and H. Okamoto. Handbook of Ternary Alloy Phase Diagrams. eds., ASM International, 1995.

[16] J.D. Livingston. Grain size in A-15 reaction layers. Phys. Stat. Sol. A, 44, 295-301, 1977.

[17] M. Suenaga and M. Jansen. Chemical compositions at and near the grain boundaries in bronze-processed superconducting Nb3Sn. Appl. Phys. Lett. 43(8), 791-793, 1983.

[18] J.E. Kunzler, E. Buehler, L. Hsu and J.Wernick. Superconductivity in Nb3Sn at high current density in a magnetic field of 88Kgauss. Phys. Rev. Letts., 6, 89-91, 1961.

[19] C.D. Hawes. Investigations of the inhomogenenity of a Powder-In-Tube Nb_3Sn conductor. Masters Thesis, University of Wisconsin-Madison, 2000.

[20] A.R. Kaufman and J.J. Picket. Multifilament superconducting wire. Bull. Am. Phys. Soc., 15, 838, 1970.

[21] V. Abacherli, B. Seeber, E. Walker and R. Flukiger. Development of $(Nb,Ta)_3Sn$ multifilament superconductors using Osprey bronze with high tin content. IEEE Trans. Appl. Supercond., 11(1) , 3667-70, 2001.

[22] A. Vorobieva, A. Shikov, A. Silaev, E. Dergunova, V. Lomaev, M. Nasibulin, K. Mareev and S. Kuznetsov. Study of Nb_3Sn with enhanced characteristics for ITER. IEEE Trans. Appl. Supercond., 11(1) , 3588-90, 2001.

[23] M.T. Naus. Optimization of Internal-Sn Nb_3Sn Composites. PhD. Thesis, University of Wisconsin-Madison, 2002.

[24] E.M. Hornsveld, J.D. Elen, C.A.M. van Beijnen and P. Hoogendam. Development of ECN-Type Niobium-Tin wire. Adv. Cryo. Eng., 34, 493-498, 1987.

[25] E. Barzi P.J. Limon, R. Yamada and A.V. Zlobin. Study of Nb_3Sn strands for Fermilab's high field dipole models. IEEE Trans. Appl. Supercond., 3(1) , 1334-1337, 1993.

[26] H. Ten Kate, H. Weijers and J. Van Oort. Critical current degredation in Nb_3Sn cables under transverse pressure. IEEE Trans. Appl. Supercond., 11(1) , 3595-98, 2001.

[27] Y. Hashimoto, K. Yoshizaki and M. Tanka. Processing and properties of superconducting Nb_3Sn filamentary wires. Proc. Of the 5th International Cryogenic Engineering Conference, Kyoto, Japan, 332-335, 1974.

[28] W.K. Mcdonald, C.W. Curtis, R.M. Scanlan, D.C. Larbalestier, K. Marken and D.B. Smathers. IEEE Trans. Mag., MAG-19(3), 1124, 1983.

[29] J.A. Parrel, M.B. Field, Y. Zhang and S. Hong. Advances in Nb3Sn strand for fusion and particle accelerator applications. IEEE Trans. Appl. Supercond., 15(2), 1200-4, 2005.

[30] M. Wake, T. Shintomi, S. Nakayama, K. Egawa, Y. Kubo, T. Nagai, T. Sone, K. Hiramoto and O. Taguchi. Development of high current density Nb3Sn conductor with distributed tin configuration. AIP-Conference-Proceedings, (711):410-16, 2004.

[31] J.A. Parrel, Y. Zhang, M.B. Field, P. Cisek and S. Hong. High field Nb3Sn conductor development at Oxford Superconducting Technology. IEEE Trans. Appl. Supercond., 13(2), 3470-3, 2003.

[32] B.A. Zeitlin, E. Gregory, T. Pyon, R.M. Scanlan, A.A. Polyanskii and P.J. Lee. Progress on the use of internal fins as barriers to reduce magnetization on high current density mono-element internal-tin conductors. AIP Conference Proceedings, (711):417-24, 2004.

[33] E. Gregory, B.A. Zeitlin, M. Tomsic, T. Pyon, M. Sumption, E.W. Collings, E.Barzi, R.M. Scanlin, A.A. Polyanskii and P.J. Lee. Attempts to reduce a.c. losses in high current dencity internal-tin Nb3Sn. AIP-Conference-proceedings. (711): 789-96, 2004.

[34] X. Peng, J. Phillips, M. Tomsic, R. Dhaka, M. Sumption, E.W. Collings and E. Gregory. Progress of Nb3Sn conductors at Hyper Tech Research. Presentation on AIP Conference. Aug. 2006.

[35] C.V. Renaud Jr, T. Wong and L.R. Motowidlo. ITT Nb3S processing and properties. IEEE Trans. Appl. Supercond., 15(2) , 3418-21, 2005.

[36] R.A. Lundy. State of the energy doubler. IEEE Trans. Mag., MAG-17, 709-712, 1981.

[37] M.T. Naus, P.J. Lee, A.A. Squitieri, D.C. Larbalestier. IEEE Trans. Appl. Supercond., 7(2), 1122, 1997.

[38] B.T. Matthias, T.H. Geballe, S. Geller and E. Corenzwit. Superconductivity of Nb3Sn. Physical Review, 95(6), 1435, 1954.

[39] R.L. Cooper. RCA Rev., 25, 405, 1964.

[40] P.R. Bosomworth, and G.W. Cullen. Energy gap of superconducting Nb_3Sn. Physical Review, 160(2), 346-347, 1967.

[41] **Zhou Lian** et al. Critical Current of Multifilament Nb_3Sn Wire in High Magnetic Field, IEEE Trans. On Mag. Vol. MAG-17. No.5, 1981, P2293~2294.

[42] V. Guritanu, W. Goldacker, F. Bouquet, Y.Wang, R. Lortz, G. Goll and A. Junod. Specific heat of Nb3Sn: the case for second energy gap. Physical Review B, 70(18), 184526-1-8, 2004.

[43] J.D. Livingston. Metallurgy of bronze-process A15 superconducting composite. Kristall –und -Technik. 13(12), 1379-1389, 1978.

[44] C.V. Renaud Jr, L.R. Motowidlo, and T. Wang. Status of Powder-in-Tube Nb3Sn conductor development at Supercon. IEEE Trans. Appl. Supercond., 13(2), 3490-93, 2003.

[45] C.V. Renaud Jr, L.R. Motowidlo, and T. Wang. Nb3Sn Powder-in-Tube Superconductor: Processing, design optimization and properties. AIP-Conference-Proceedings, (711):376-81, 2004.

[46] D.C. Welch. Alteration of superconducting properties of A15 compounds and elementary composite superconductors by Non-hydrostatic Elastic Strain. Adv. Cryo. Eng., 26, 48-65, 1980.

[47] A.J. Arko, D.H. Lowndes, F.A. Roeland, J. Wolfrat, A.T. van Kessel, H.W. Myron, F.M. Meuller and G.W. Webb, Phys. Rev. Lett., 40(24), 1590, 1978.

[48] T.P. Orlando, J.A. Alexander, S.J. Bending, J. Kwo, S.J. Poon, R.H. Hammond, M.R. Beasley, E.J. McNiff and S. Foner. IEEE Trans. Mag., MAG-17(1), 368, 1981.

[49] R.Akhama, K. Yasukochi and T. Ogasawara. IEEE Trans. Mag., MAG-13(1), 803, 1977.

[50] M.C. Jewell, A. Godeke, P.J. Lee and D.C. Larbalestier. The upper critical field of stoichiometric and off-stoichiometric bulk, binary Nb3Sn. AIP-conference-proceedings. (711): 474-81, 2004.

[51] R. Flukiger, W.Schauer and W. Goldacker. Superconductivity in d- and f-Band Metals, W.Buckel and W. Weber, eds., Karlsurhe, 1982.

[52] C.Verwaerde, R. Taillard, C.E. Bruzek and Hoang-Gia-Ky, Adv. Cryo. Eng., 42, 1377, 1996.

[53] Y.B. Kim, C.F. Hempstead and A.R. Strnad. Phys. Rev., 139(4A), A1163, 1965.

[54] J. Ekin. Strain effect in superconducting compounds. Adv. Cryo. Eng., 30, 823-836, 1984.

[55] L.D. Cooley, Y.F. Hu, A.R. Moodenbaugh. Enhancement of the upper critical field of Nb3Sn utilizing disorder introduced by ball milling the elements. Applied Physics Letters, 88(14), 142506-1-3, 2006.

[56] E.J. Kramer. J. Appl. Phys., 44(3), 1360, 1973.

[57] A. Godeke, M.C. Jewell, A.A. Golubov, B. Ten-Haken and D.C. Larbalestier. Inconsistencies between extrapolated and actual critical field in Nb_3Sn wires as demonstrated by direct measurements of H_{C2}, H* and T_C. Superconductor Science and Technology, 16(9), 1019-25, 2003.

[58] M.G. Adesso, D. Uglietti, N. Musolino, R. Flükiger and S. Pace. Investigation of magnetic behavior in various Nb_3Sn multifilament wires by means of the 1st and 3rd harmonics of the AC magnetic susceptibility. IEEE Trans. Appl. Supercond., 16(2), 1241-4, 2006.

[59] E. Gregory, E. Gulko, T. Pyon. Improvement in the properties of internal-tin Nb3Sn. IEEE Trans. Appl. Supercond., 7(2), 1498-503, 1997.

[60] **Zhou Lian,** Critical Current of Nb_3Sn Practical Superconductors in High Magnetic Field. IEEE Trans. Mag., MAG-19(3), 280~284, 1983.

[61] C.M. Fischer. Investigation of the Relationships between Superconducting Properties and Nb3Sn Reaction Conditions in Powder-In-Tube Nb3Sn Conductors. Master Thesis, University of Wisconsin-Madison, 2002.

[62] K.R. Marken, S.J. Kwon, P.J. Lee and D.C. Larbalestier. Characterization study of a fully reacted high bronze-to-Nb ratio filamentary Nb3Sn composite. Adv. Cryo. Eng., 32, 967-975, 1986.

[63] E. Gregory, M. Tomsic, M.D. Sumption, X. Peng, X. Wu, E.W. Collings and B.A. Zeitlin. The introduction of titanium into internal-tin Nb3Sn by a variety of procedures. IEEE Trans. Appl. Supercond., 15(2) , 3478-81, 2005.

[64] A. Godeke, M. C. Jewell, C. M. Fischer, A. A. Squitieri, P. J. Lee, and D. C. Larbalestier, The upper critical field of filamentary Nb3Sn conductors, J. Appl. Phys. vol. 97, 093909,

2005.

[65] M. Suenaga, A.K. Ghosh, Yuwen XU, and D.O. Welch, *Phys. Rev. Letters*, 66, 1777(1991).

[66]Zhang Chaowu, A. Sulpice, Zhou Lian, J.L. Soubeyroux, C. Verwaerde, G. K. Hoang.Investigation of ITER Use Internal-Sn Nb_3Sn Superconducting Wire through Irreversibility Temperature Measurement. IEEE Trans. Appl. Supercond., 17(1), 2007.

[67] Zhang Chaowu , A. Sulpice, Zhou Lian, Tang Xiande, J.L. Soubeyroux, Zhang Pingxiang, Lu Yafeng. Irreversibility Temperature Investigation of ITER Nb_3Sn Wire by Internal-Sn Process. Chinese Journal of Low Temperature Physics. 28 (4), 2006.

[68] J.A. Parrell, M.B. Field, Y. Zhang, and S. Hong. Advances in Nb3Sn conductor development for fusion and particle accelerator applications. IEEE Trans. Appl. Supercond., 15(2) , 1200-4, 2005.

[69] T. Pyon and E. Gregory. Nb3Sn conductors for high energy physics and fusion applications. IEEE Trans. Appl. Supercond., 11(1), 3688-91, 2001.

[70] A. Godeke. A review of the properties of Nb3Sn and their variation with A15 composition, morphology and strain state. Superconductor Science and Technology, 19(8), R68-80, 2006.

[71] X. Peng, M.D. Sumption, and E.W. Collings. Magnetization and D_{eff} in multifilamentary Nb_3Sn strands. IEEE Trans. Appl. Supercond., 15(2), 3498-3501, 2005.

[72] M.D. Sumption, X. Peng, and E.W. Collings. Magnetization and D_{eff} in HEP relevant RIT type Nb_3Sn strands influence of internal barriers. AIP-Conference-Proceedings, (711):836-43, 2004.

[73] M.D. Sumption, X. Peng, E. Lee, X. Wu, E.W. Collings. Analysis of magnetization, ac loss and D_{eff} for various internal-Sn based Nb3Sn multi-filamentary strands with and without subelement splitting. Cryogenics, 44(10), 711-25, 2004.

[74] A.K. Ghosh, L.D. Cooly, A.R. Moodenbaugh, J.A. Parrell, M.B. Field, Y. Zhang and S. Hong. IEEE Trans. Appl. Supercond., 15(2) , 3494-97, 2005.

[75] M.B. Field, R. Hentges, J.A. Parrell, Y. Zhang and S. Hong. Progress with Nb3Sn conductors at Oxford Instruments, Superconducting Technology. Presented at CEC-ICMC, Anchorage, Alaska. 2003.

[76] T. Pyon and E. Gregory. Niobium-Tin for fusion, high energy physics and other applications. IEEE Trans. Appl. Supercond., 9(2) , 2509-12, 1999.

[77] X. Peng, M.D. Sumption, M. Tomsic, E. Gregory, E.W. Collings. Microstructural investigation of internal-tin Nb3Sn strands. IEEE Trans. Appl. Supercond., 15(2), 3422-5, 2005.

[78] R. Flukiger, R. Isernhagen, W. Goldacker and W. Specking. Long-range atomic order, crystalographical changes and strain sensitivity of Jc in wires based on Nb_3Sn and other A15 compounds. Adv. Cryo. Eng., 30, 851-858, 1984.

[79] A. Godeke, H.J.G. Krooshoop, H.G. Knoopers, B. Ten-Haken, and H.H.J. Ten-Kate. Experimental verification of temperature and strain dependence of the critical properties in Nb3Sn wires. IEEE Trans. Appl. Supercond., 11(1) , 1526-9, 2001.

[80] A. Godeke, B. Ten-Haken, and H.H.J. Ten-Kate. Scaling of the critical current in ITER type niobium-tin superconductors in relation to the applied field, temperature and uni-axial applied strain. IEEE Trans. Appl. Supercond., 9(2), 161-4, 1999.

[81] J.W. Ekin, N. Cheggour, C. Clickner, M. Field, H. Seung, J. Parrel and Y. Zhang. Progressive pre-strain in high-iobium-fraction Nb3Sn superconductors. IEEE Trans. Appl. Supercond., 15(2) , 3560-3, 2005.

[82] R.M. Scanlan, W.A. Feitz and E.F. Koch. Flux pinning centers in superconducting Nb3Sn. J. Appl. Phys. 46(5), 2244-2249, 1974.

[83] M. Suenaga, in Superconductor Materials Science-Metallurgy, Fabrication and Applications. S. Foner and B. Schwartz, Ed., Plenum Press, 1980.

[84] S. Ochiai, and L. Osamura. Influence of grain size and upper critical field on global pinning force of bronze-processed Nb3Sn compound. Acta Metall. 34(12), 2425-2433, 1986.

[85] M.T. Naus, P.J. Lee and D.C. Larbalestier. The interdiffusion of Cu and Sn in internal-Sn Nb_3Sn superconductors. IEEE Trans. Appl. Supercond., 10(1) , 2000.

[86] Zhang Chaowu, L. Zhou, X. Tang, J.L. Soubeyroux, A. Sulpice, P. Zhang, Y. Lu. Neutron Diffraction Investigation of ITER Internal-Sn Nb_3Sn Superconducting Wires. Rare Metal Materials and Engineering, 36(9), 2006.

[87]Jean-Louis Soubeyroux**,** Andre Sulpice, Chaowu Zhang, Lian Zhou. In-situ neutron

diffraction study of a heating treatment for Nb_3Sn ITER superconducting Wires. J. Phys.: Conference Series 43, 39-42, 2006

[88] M. Hansen. Constitution of Binary Alloys (McGraw-Hill), 643, 1958.

[89] M.T. Naus, P.J. Lee and D.C. Larbalestier. The influence of the starting Cu-Sn phase on the superconducting properties of subsequently reacted internal-Sn Nb3Sn conductors. IEEE Trans. Appl. Supercond., 11(1) , 3569-72, 2001.

[90] D.R. Dietderich, J. Glazer, C. Lea, W.V. Hasenzahl and J.W. Morris, Jr., IEEE Trans. Mag., MAG-21(2), 297, 1985.

[91] C.E. Bruzek, P. Sultan, P. Mocaer, P. Mougenot, f. Peltier and G. Grunblutt. Adv. Cryo. Eng., 42, 1369, 1996.

[92] E. Barzi, E. Gregory and T. Pyon. Heat treatment optimization of internal tin Nb3Sn strands. IEEE Trans. Appl. Supercond., 11(1), 3573, 2001.

[93] M.T. Naus, M. C. Jewell, P.J. Lee, and D.C. Larbalestier. Lack of influence of the Cu-Sn mixing heat treatments on the superconducting properties of two high-Nb, internal-Sn Nb3Sn conductors. AIP Conference Proceedings, (614B):1016-22, 2002.

[94] C.M. Fischer, P.J. Lee and D.C. Larbalestier. Irreversibility field and critical current density as a function of heat treatment time and temperature for a pure niobium Powder-In-Tube Nb3Sn conductor. Proceedings of ICMC, 48, 1008-1015, 2002.

[95] R. Tailard, C. Verwaerde, C.E. Bruzek and P. Sulten. Heat treatments, microstructure and properties of internal-tin Nb3Sn. IEEE Trans. Appl. Supercond., 7(2) , 1504-7, 1997.

[96] Zhang Chaowu, Zhou Lian, A. Sulpice, J.L. Soubeyroux, C. Verwaerde, G. K. Hoang，Zhang Pingxiang, Lu Yafeng, Tang Xiande, Magnetization Study of ITER-type Internal-Sn Nb_3Sn Superconductor Wire. Chinese Physics, 16(6), 2007.

[97] Zhang Chaowu, A. Sulpice**,** J.L. Soubeyroux, Lian Zhou, Xiande Tang, C. Verwaerde, G. K. Hoang, Robert Tournier. Critical and irreversibility temperatures study of internal-Sn Nb_3Sn superconducting wires. Presentation on 2006 ICSM Beijing Conference and published on Materials Science Forum, Vols. 546-549, Part 4.

[98] L.D. Cooly, P.J. Lee and D.C. Larbalestier. Changes in flux pinning curve shape for flux-line separations comparable to grain size in Nb3Sn wires. AIP Conference Proceedings, (614B):925-32, 2002.

[99] D.R. Dietderich, D. Tribula, J.W. Jr Morris. The Nb3Sn grain structure evolution in bronze-processed multifilamentary superconducting wire. Journal of the Less Common Metals, 139(1), 79-85, 1988.

[100] P.J. Lee, D.C. Larbalestier. Microstructure, microchemistry and the development of very high Nb3Sn layer critical current density. IEEE Trans. Appl. Supercond., 15(2) , 3474-7, 2005.

[101] P.J. Lee, C.M. Fischer, M.T. Naus, A.A. Squitieri and D.C. Larbalestier. The microstructure and microchemistry of high critical current Nb3Sn strands manufactured by the bronze, internal-Sn and PIT techniques. IEEE Trans. Appl. Supercond., 13(2) , 3422-25, 2003.

[102] P.J. Lee, and D.C. Larbalestier. Compositional and micro-structural profiles across Nb3Sn filaments produced by different fabrication methods. IEEE Trans. Appl. Supercond., 11(1), 3671-74, 2001.

[103] P.J. Lee, A.A. Squitieri, and D.C. Larbalestier. Nb3Sn: macrostructure, microstrcture and property comparisons for bronze and internal-Sn process strands. IEEE Trans. Appl. Supercond., 10(1), 979-982, 2000.

[104] P.J. Lee, J.R. Ruess, and D.C. Larbalestier. Quantitative image analysis of filament coupling and grain size in ITER Nb(Ti)3Sn strands manufactured by the internal-Sn process. IEEE Trans. Appl. Supercond., 7(2) , 1516-19, 1997.

[105] H. Oikawa, and A. Hosoi. Scr. Metal., 9, 823, 1975.

[106] D.S. Easton and D.M. Kroeger. IEEE Trans. Mag., MAG-15(1), 178, 1979.

[107] M. C. Jewell, P.J. Lee, and D.C. Larbalestier. Poster presented at the Applied Superconductivity Conference, Madison, WI (2000).

[108] M. Suenaga, D.O. Welch, R.L. Sabatini, O.F. Kammerer and S. Okuda. J. Appl. Phys., 59(3), 840, 1986.

[109] T. Wong, and C.V. Renaud. Ti and Ta additions to Nb_3Sn by powder-in-tube process. IEEE Trans. Appl. Supercond., 11(1), 3584-87, 2001.

[110] R. Akihama, K. Yasukochi and T. Ogasawara. IEEE Trans. Mag., MAG-13(1), 803, 1977.

[111] H. Kurahashi, K. Itoh, S. Matsumoto, T. Kiyoshi, H. Wada, Y. Murakami, H. Yasunaka,

S. Hayashi, and Y. Otani. Effect of third-element additions on the upper critical field of bronze-processed Nb_3Sn. IEEE Trans. Appl. Supercond., 15(2), 3385-89, 2005.

[112] X. Wu, X. Peng, M.D. Sumption, M. Tomsic, E. Gregory, E.W. Collings. Ti and Sn diffusion and its influence on phase formation in internal-Sn Nb3Sn superconductor strands. IEEE Trans. Appl. Supercond., 15(2) , 3399-402, 2005.

[113] D. Jr Rodrigues, C.L.H. Thieme, D.G. Pinatti, S. Fonet. Grain boundary compositions, transport and flux pinning of multifilament Nb_3Sn wires. IEEE Trans. Appl. Supercond., 5(2), 1607-10, 1995.

[114] B.A. Zeitlin, E. Gregory, J. Marte, M. Benz, Tae-Pyon, R. Scanlan, D. Dietderich. Results on mono element internal tin Nb3Sn conductors (MEIT) with Nb7.5Ta and Nb(1Zr+O_x) filament. IEEE Trans. Appl. Supercond., 15(2), 3393-98, 2005.

[115] B.A. Zeitlin, J. Marte, D. Ellis, M. Benz, E. Gregory. Some effects of the addition of 1at% Zr to Nb on the properties and ease of manufacture of internal-tin Nb3Sn. AIP Conference Proceedings, (711):395-402, 2004.

[116] J.L. Soubeyroux**,** C. Zhang, A. Sulpice, L. Zhou, X. Tang and R.Tournier. Neutron diffraction studies of the Zr/Nb effects on the Nb_3Sn phase formation of monofilament wires. Presented on ICSM Conference, Beijing, 2006.

[117] K. DeMoranville, D. Yu and J. Wong. Adv. Cryo. Eng., 40, 931, 1994.

[118] K. Tachikowa, T. Asano and T. Takeuchi. Appl. Phys. Lett., 39(9), 766, 1981.

[119] J.C. McKinnel, M.B. Siddal, P.M. Olarey and D.B. Smathers. Adv. Cryo. Eng., 40, 945, 1994.

[120] H. Sekine, Y. Ijima, K. Itoh and K. Tachihama. Improvement of high field performances of bronze-processed Nb3Sn superconductors by titanium addition to the matrix. Journal of the Japan Institute of Metals. 49(10), 913-20, 1985.

[121] E. Gregory, M. Tomsic, M.D. Sumption, X. Peng, X. Wu, E.W. Collings, B.A. Zeitlin. The introduction of titanium into internal-tin Nb_3Sn by a variety of procedures. IEEE Trans. Appl. Supercond., 15(2), 3478-81, 2005.

[122] M. Onishi, and H. Fujibuchi. Reaction diffusion in the Cu-Sn system. Transations of Japanese Institute of Metals. 16, 539, 1975.

[123] K. Hoshino, Y. Iijima and K. Hirano. Interdiffusion and Kirkendall effects in Cu-Sn

alloys. Trans. J. Inst. Metals, 21, 674, 1980.

[124] J.D. Verhoeven, K. Heimes and A. Efron. Analysis of the tin diffusion in Nb_3Sn-Cu superconducting wire produced by the external tin process. J. Appl. Phys. 59, 2096, 1986.

[125] J.D. Verhoeven, A. Efron, E.D. Jibson C.C. Cheng. Void formation in Nb3Sn-Cu superconducting wire produced by the external tin process. J. Appl. Phys. 59, 2105, 1986.

[126] S. Mattafirri, E. Barzi, F. Fineschi and J.M. Rey. Kinetics of phase growth in the Cu-Sn system and application to composite Nb3Sn strands. IEEE Trans. Appl. Supercond., 13(2) , 3418-21, 2003.

[127] J. M. Rey, E. Barzi, S. Mattafirri, J. Hoffman and R. Yamada. Effect of partially reacting Nb_3Sn before magnet winding on the strand critical current. Presented at ICMC 2001-Madison-WI.

[128] X. Tang D. Shan and M. Li. Metallurgical and superconducting properties of the bronze-MF Nb_3Sn conductor able to produce 15T field. Chinese Journal of Low Temperature Physics. 10(2), 116-121, 1988.

[129] E. Barzi, and S. Mattafirri. Nb3Sn phase growth and superconducting properties during heat treatment. IEEE Trans. Appl. Supercond., 13(2), 3414-17, 2003.

[130] Ding Shiying，Marvelous Superconducting Materials, Science Press, Beijing, 2003.

[131] Jean-Louis Soubeyroux, et al. Report in NIN, Xi'an, 2005.

[132] J.D. Livingston. Structure and Properties of High Field Superconductors. IEEE Trans. Magnetics, 19(3), 773, 1983.

[133] J.E. Evetts and P.H. Kes. Magnetic and Superconducting Materials, pp. 95-102, 1992.

[134] C.D. Hawes, P.J. Lee and D. C. Larbalestier. Measurements of the critical temperature transition and composition gradient in powder-in-tube Nb3Sn composite wire. IEEE Trans. Appl. Supercon., 10(1), 988-91, 2000.

[135] L.D. Cooley, C.M. Fischer, P.J. Lee, D. C. Larbalestier. Simulations of the effects of tin composition gradients on the superconducting properties of Nb3Sn conductors. Journal of the Applied Physics, 96(4), 2122-30, 2004.

[136] C.D. Hawes, P.J. Lee and D. C. Larbalestier. Measurements of the microstructure, microchemical and transition temperature gradients of A15 layers in a high-performance Nb3Sn powder-in-tube superconducting strand. Superconductor Science and Technology,

19(3), S27-37, 2006.

[137] Testing Procedures for Superconductor Properties, DRG1 Annex, Superconducting Material Database, Article 4.

PUBLICATIONS

1. **Zhang Chaowu**，Zhou Lian，Tang Xiande，Jean-Louis Soubeyroux, Andre Sulpice，Zhang Ping Xiang，Lu Yafeng. “Phase formation investigation of internal-Sn Nb_3Sn by in-situ neutron diffraction”, Rare Metal Materials and Engineering，35(9), 2006.
2. **Zhang Chaowu,** Andre Sulpice, Zhou Lian, Jean-Louis Soubeyroux, Christophe Verwaerde, Gia Ky Hoang. “Investigation of ITER Use Internal-Sn Nb_3Sn Superconducting Wire through Irreversibility Temperature Measurement”， IEEE Transaction on Applied Superconductivity，17(1), 2007.
3. **Zhang Chaowu,** Zhou Lian, Andre Sulpice, Jean-Louis Soubeyroux, Christophe Verwaerde, Gia Ky Hoang，Zhang Pingxiang, Lu Yafeng, Tang Xiande “Magnetization Study of ITER-type Internal-Sn Nb_3Sn Superconductor Wire”, Chinese Physics, 16(6), 2007.
4. **Zhang Chaowu,** Wang Fen,“Structure and Coordination Investigation of Iron-ion Tinting Principle in Ferreous Glass”，Journal of Wuhan University of Technology—Materials Science Edition，20(2)，2005.
5. **Zhang Chaowu ,** Andre Sulpice, Zhou Lian, Tang Xiande, Jean-Louis Soubeyroux, Zhang Pingxiang, Lu Yafeng.“Irreversibility Temperature Investigation of ITER Nb_3Sn Wire by Internal-Sn Process”，Chinese Journal of Low Temperature Physics, 28(4), 2006.
6. **Zhang Chaowu**, André Sulpice**,** Jean-Louis Soubeyroux, Lian Zhou, Xiande Tang, Christophe Verwaerde, Gia Ky Hoang, Robert Tournier “Critical and irreversibility temperatures study of internal-Sn Nb_3Sn superconducting wires” Presentation on 2006 ICSM Beijing Conference, published on Materials Science Forum, Vols. 546-549, Part 4.
7. J.L. Soubeyroux**, C. Zhang ,** A. Sulpice, Lian Zhou, Xiande Tang and Robert Tournier. “Neutron diffraction studies of the Zr/Nb effects on the Nb_3Sn phase formation of monofilament wires”，Presentation on 2006 ICSM Beijing Conference, published on Materials Science Forum, Vols. 546-549, Part 4.
8. Jean-Louis Soubeyroux**,** Andre Sulpice, **Chaowu Zhang,** Lian Zhou.“In-situ neutron diffraction study of a heating treatment for Nb_3Sn ITER superconducting Wires”, Journal

of Physics : Conference Series 43, 39-42, 2006.

9. Tang Xiande, Zhou Lian, **Zhang Chaowu**, “Manufacturing and Performance of Multifilament Nb3Sn Superconducting wires and tapes”，Presentation on France-China Workshop of Superconducting and Magnetic Materials，Sept. 2004.

Résumé : Les fils supraconducteurs Nb_3Sn sont, parmi les matériaux, ceux qui présentent le plus d'applications possibles pour produire des champs magnétiques supérieurs à 10 Tesla. L'utilisation la plus immédiate se place dans le cadre du projet ITER, qui est considéré comme un grand espoir de source d'énergie dans le futur. La conception composite avec beaucoup de cuivre, un petit nombre de sous-éléments, une barrière de diffusion non réactive et la technologie de l'étain interne RRP (Restacked Rod Process) est généralement utilisée pour la fabrication des fils. Des spécifications particulières sont nécessaires pour cette utilisation. Elles peuvent être obtenues par une conception particulière de l'assemblage des filaments, la méthode de formation de la phase A15 Nb_3Sn (ici le procédé de l'étain interne), les traitements thermiques. De tels fils ont été fournis par les sociétés MSA/Alstom et WST/NIN pour cette étude. Pour déterminer de manière précise les conditions de formation et les cinétiques de réaction, des filaments plus simples ont été préparés (4 formulations avec des rapports Cu/Sn différents et des additifs différents). Pour cela différentes techniques de caractérisation ont été mises en œuvre, mesures d'aimantation sous champ magnétique, diffraction neutronique, microscopies électroniques (MEB/EDEX, TEM).
L'épaisseur de la couche de la phase A15 mesurée dans différents monofilaments a permis de déterminer la loi de cinétique de formation selon deux modèles. Les résultats ont clairement montré que le modèle de diffusion en phase solide est en accord avec une loi de puissance n et que la valeur de n augmente avec la température de traitement et le taux d'étain dans le fil composite.

Mots-clés : conducteurs Nb_3Sn, matériaux supraconducteurs, courant critique, aimantation, champ critique.

Abstract : Superconductors Nb_3Sn wires are one of the most applicable cryogenic superconducting materials and the best choice for high-field magnets exceeding 10T. One of the most significant utilization is the ITER project which is regarded as the hope of future energy source. The high-Cu composite designs with smaller number of sub-element and non-reactive diffusion barrier, and the RRP (Restacked Rod Process) internal-Sn technology are usually applied for the wire manufacturing. Such designed and processed wires were supplied by MSA/Alstom and WST/NIN in this research. The systematic investigation on internal-Sn superconducting wires includes the optimization of HT conditions, phase formation and its relation with superconductivity, microstructure analysis, and the phase formation kinetics. Because of the anfractuosity of the configuration design and metallurgical processing, the MF wires are not sufficient for studying a sole factor effect on superconductivity. Therefore, four sets of ME wires with different Sn ratios and different third-element addition were designed and fabricated in order to explore the relationship between phase formation and superconducting performances, particularly the A15 layer growth kinetics. Different characterization technics have been used (magnetization measurements, neutron diffraction and SEM/TEM/EDX analysis)
The A15 layer thicknesses of various ME samples were measured and carried out linear and non-linear fits by means of two model equations. The results have clearly demonstrated that the phase formation kinetics of Nb_3Sn solid-state reaction is in accordance with an n power relation and the n value is increased with the increase of HT temperature and the Sn ratio in the wire composite.

Keywords : Nb3Sn wires, superconducting materials, critical current, magnetization, critical field.

摘要：Nb_3Sn超导线材是最实用的低温超导材料之一，是10T以上高场磁体的最佳选择。一种最有意义的重大应用是被称之为未来能源希望之所在的ITER计划。高Cu复合体、亚组元数量少、非反应型扩散阻隔层的设计，以及RRP内锡法工艺常常用于多芯导线的制备。在本研究中按照这种设计和工艺制备的导线由MSA/Alstom 和 WST/NIN提供。对内锡法超导线的系统研究包括热处理制度的优化、成相及其与超导性能的关系、显微结构分析和成相动力学。由于多芯线结构设计与冶金过程的复杂性，常常不足以研究单一因素对超导性能的影响。因此，设计并制备了四组具有不同含Sn率和不同合金化掺杂元素的单芯线，以探讨成相与超导性能的关系，特别是A15层生长动力学。研究中采用了不同的现代测试分析技术，包括磁化性能测定、中子衍射技术和SEM/TEM/EDX分析。
对各种单芯线样品的A15层厚度进行了测定，并采用两种模型关系进行了线性和非线性拟合。所得结果清楚表明Nb_3Sn固相反应的成相动力学符合n指数变化规律，并且n值随热处理温度以及导线复合体含Sn率的增加而增大。

关键词：Nb_3Sn导线，超导材料，临界电流，磁化强度，临界场.